VOLUME 48 • SPECIAL ISSUE • NO. 1 • September 2025

ISSN 0971-3034

THE INDIAN JOURNAL OF TECHNICAL EDUCATION

Published by
INDIAN SOCIETY FOR TECHNICAL EDUCATION
Near Katwaria Sarai, Shaheed Jeet Singh Marg,
New Delhi - 110 016

INDIAN JOURNAL OF TECHNICAL EDUCATION

Volume 48 • Special Issue • No. 1 • September 2025

Editorial Advisory Committee

Prof. Pratapsinh K. Desai - Chairman
President, ISTE

Prof. N. R. Shetty
Former President, ISTE, New Delhi

Prof. (Dr.) Buta Singh Sidhu
Former Vice Chancellor, Maharaja Ranjit Singh Punjab Technical University, Bathinda

Prof. G. Ranga Janardhana
Former Vice Chancellor
JNTU Anantapur, Ananthapuramu

Prof. D. N. Reddy
Former Chairman
Recruitment & Assessment Centre
DRDO, Ministry of Defence, Govt. of India
New Delhi

Prof G. D. Yadav
Vice Chancellor
Institute of Chemical Technology, Mumbai

Dr. Akshai Aggarwal
Former Vice Chancellor
Gujarat Technological University,
Gandhinagar

Prof. M. S. Palanichamy
Former Vice Chancellor
Tamil Nadu Open University, Chennai

Prof Amiya Kumar Rath
Vice Chancellor, BPUT
Rourkela

Prof Raghu B Korrapati
Fulbright Scholar & Senior Professor
Walden University, USA & Former
Commissioner for Higher Education, USA

Editorial Board

Dr. Vivek B. Kamat
Director of Technical Education
Government of Goa, Goa

Dr. Ishrat Meera Mirzana
Professor, MED, & Director, RDC
Muffakham Jah College of Engineering and Technology
Hyderabad, Telangana

Prof. (Dr.) CH V K N S N Moorthy
Director R&D
Vasavi College of Engineering
Hyderabad, Telangana

Prof. C. C. Handa
Professor & Head, Dept. of Mech.Engg.
KDK College of Engineering, Nagpur

Prof. (Dr.) Bijaya Panigrahi
Dept. Electrical Engineering
Indian Institute of Technology, Delhi
New Delhi

Prof. Y. Vrushabhendrappa
Director
Bapuji Institute of Engg. & Technology, Davangere

Dr. Anant I Dhatrak
Associate Professor, Civil Engineering Department, Government College of Engineering, Amravati, Maharashtra

Dr. Jyoti Sekhar Banerjee
Associate Editor

Dr. Rajeshree D. Raut
Associate Editor

Dr. Y. R. M. Rao
Editor

Copyright (c) Indian Society for Technical Education, The Journal articles or any part of it may not be reproduced in any form without the written permission of the Publisher.

INDIAN JOURNAL OF TECHNICAL EDUCATION

Published by
INDIAN SOCIETY FOR TECHNICAL EDUCATION
Near Katwaria Sarai, Shaheed Jeet Singh Marg
New Delhi - 110 016

Editorial

From Choice to Necessity: AI and ML in Higher Education: Artificial Intelligence (AI) and Machine Learning (ML) are no longer futuristic ideas, they are powerful forces shaping today's world. From healthcare and manufacturing to education and governance, these technologies are redefining how we live, work, and learn. For engineering faculty, engaging with AI and ML is no longer optional; it has become an essential for professional growth and institutional advancement.

AI and ML provide fertile ground for research, innovation, and interdisciplinary collaboration. Their applications such as intelligent diagnostics in healthcare, autonomous vehicles, smart farming, natural language processing, robotics, and personalized education, are few to mention. By aligning their work with these fast-growing domains, faculty can strengthen academic profiles while also opening doors to industry collaborations, patents, and consultancy opportunities.

For career development, AI/ML research offers high visibility. Publications in reputed journals, presentations at international conferences, and strong citation records all contribute to academic recognition. Funded projects in AI-related fields add further credibility, while mentoring students in areas such as predictive modelling, data-driven systems, or AI-enabled product design ensures graduates are well-prepared for a competitive global workforce.

AI and ML also enrich classroom teaching. Faculty who integrates AI research into their lectures move beyond textbook knowledge. Real-world case studies, live demonstrations of machine learning models, and project-based learning inspired by ongoing faculty research create an engaging, application-oriented learning environment. This, in turn, enhances student employability and strengthens the institution's reputation. However, pursuing AI/ML research demands continuous learning. Faculty must spend time in learning master programming languages like Python and R, and deepen knowledge of data science and neural networks.

Institutions must also take an active role by offering access to high-performance computing resources, advanced laboratories, and continuous training opportunities. AI and ML are reshaping academia. For faculty, they represent not just tools of research but pathways to excellence, relevance, and leadership in the rapidly evolving world of higher education.

"From classrooms to research labs, AI and ML are the catalysts of academic transformation."

New Delhi **Editor**

15th September 2025

N S S COLLEGE OF ENGINEERING

Palakkad 678008, Kerala, India
(A Government Aided Institution Established in 1960)
Affiliated to APJ Abdul Kalam Technological University and approved by AICTE
An Institution of Nair Service Society
www.nssce.ac.in, nssce@nssce.ac.in

Chief Patron

Patron

Editorial Advisory Committee

Editorial Board

Contents

Seismic Performance of Conventional Vs. Tubular RC Frame Structures With Shear Walls

Anjala Gafoor K
PG Scholar
Department of Civil Engineering
NSS College of Engineering
Palakkad, Kerala
✉ anjalagafoork@gmail.com

Praseeda K I
Assistant Professor
Department of Civil Engineering
NSS College of Engineering
Palakkad, Kerala
✉ praseedaki@nssce.ac.in

ABSTRACT

The structural integrity of buildings is crucial for protecting occupants during earthquakes and reducing damage in areas that are prone to seismic activity. The purpose of this project is to evaluate and compare the seismic performance of tubular reinforced concrete frame structures with shear walls with that of conventional Reinforced Concrete (RC) frame structures. In order to ascertain the relative seismic performance of these structural systems, the analysis concentrates on important parameters like time period, base shear, lateral story displacement, and story drift. ETABS software, an advanced computational modeling and seismic analysis method, examines how both kinds of structures react dynamically to different seismic loads. The objective is to provide insights into the effectiveness of conventional RC frame structures with shear walls in resisting seismic forces when compared to tubular RC frame structures through comprehensive numerical simulations and performance assessments. In addition, the study investigates how adding dampers to traditional RC frame buildings affects their seismic performance, to compare it with the seismic performance of tubular RC frame buildings that have shear walls. The findings will contribute to enhancing the understanding of the seismic behavior of conventional with or without damper and tubular RC frame structures with shear walls, thereby assisting engineers and designers in making informed decisions regarding structural design and retrofitting strategies to mitigate the effects of seismic events on buildings and infrastructure. Understanding structural behavior under seismic loading conditions will be improved by the researcher's insights, which will also guide the design and construction of more resilient buildings in earthquake-prone areas.

KEYWORDS: *Seismic performance, Reinforced concrete frame structures, Tubular structures.*

INTRODUCTION

High rise buildings are commonly used due to urbanization and high land cost. In high rise buildings, tubular structures are commonly used because of their better structural performance and seismic resistance. Tubular structures have advantages over tall Reinforced Concrete (RC) Moment-Resisting Frame Structures (MRFS) in seismic performance. The tube-in-tube structures shows high seismic resistance to the structure and it is superior while compared to other tubular structures. Tube-in-tube structures have inner and outer tubes with closely spaced columns to enhance the seismic performance of the structure. Through its inner tube the lateral loads such as wind loads and seismic loads are distributed to the ground and the lateral stability is achieved through the interaction between the inner and outer tubes. The outer tube acts as a load-bearing element, it transfers the vertical loads to the foundation. The inner tube provides additional lateral support. Fig 1 shows the tube in tube structure.

Moment-resisting frame's seismic performance can be enhanced by installing Dampers to the existing structures. There are several types of dampers such as Fluid viscous damper, Friction damper, mass damper etc. Moment resisting frames with Fluid Viscous Dampers (FVDs) effectively enhance seismic behavior rather than other dampers. The fluid viscous damper consists of a piston within a cylinder filled with the damping fluid shown in Fig 2. The fluid viscous damper works on the principle of dissipating energy by forcing a fluid which is a high-viscosity oil, through an orifice. By placing the fluid viscous damper in each story of the building, the structure shows better performance on seismic resistance than dampers placed in the other positions. This results in decreased maximum story displacement, maximum story drift, and increased shear values, helps to improve the seismic resilience.

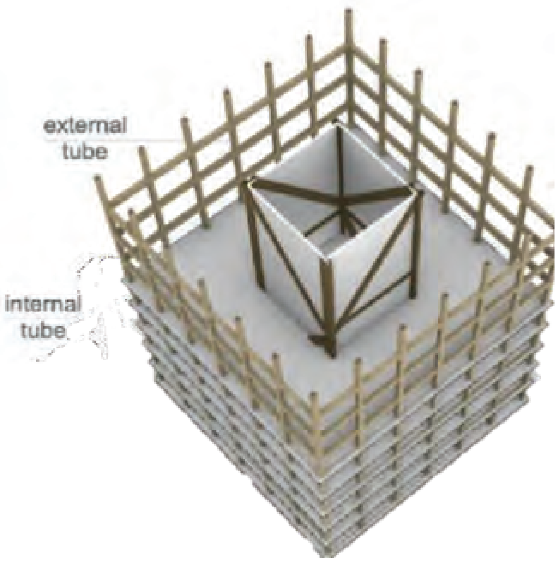

Fig. 1. Tube in tube structure

Fig. 2. Fluid viscous damper

This study compares the seismic performance of a Conventional Moment Resisting Frame (CMRF) structure and Tubular Reinforced Concrete Structure (TRFS) with shear walls. Key parameters such as base shear, lateral story displacement and lateral story drift, are examined to understand the seismic behavior under different loading conditions of the structure.

The study aims to identify the similarities of the structural properties of the conventional RC frame structures with and without damper to the tube in tube structure. Model analysis provides a clear understanding on effect of seismic properties on the structure and helps to identify the most effective model for the seismic prone areas. Seismic zone IV and zone V are considered in this design and the seismic properties such as maximum story displacement; maximum story shear and maximum story drift of the structure are analyzed using ETABS software.

MODELLING OF STRUCTURE

Structural systems used in the study conducted by Bhavanishankar et al. in 2021, was adopted for the present study. The details of different models are given in the following sections.

Material properties from the journal

The material properties shown in Table 1 are considered by the author:

Table 1. Material properties from the journal

Properties	Values
Concrete compressive strength (fck)	25 N/mm^2
Reinforcing yield stress (fy)	415 N/mm^2
Concrete modulus of elasticity (E)	20000 N/mm^2
Shear modulus (G)	10000 N/mm^2

Loads and intensities from the journal

Loads and intensities considered by the author are shown in Table 2.

Table 2. Loads and intensities of building from the journal

Live load on each floor	4 kN/m^2
Live load on terrace	1 kN/m^2
Floor finish	1 kN/m^2
Terrace finish	1 kN/m^2
Wall load	10.5 kN/m^2
Parapet wall load	2.85 kN/m^2

Details of building for modelling

The building is a 30 x 30m commercial structure located in seismic zones 4 and 5. It consists of 21 stories, with each story having a height of 3 meters. The slab and shear wall thickness adopted for the structures are 150mm and 300mm respectively. The structural modelling was based on the parameters listed in Table 3.

Table 3. Detailing of building for modelling purpose

Size of beam	300*650 mm
Size of column	700*700 mm
Grade of concrete	M30

Seismic properties from IS 1893-2016 for modelling

The seismic properties shown in table 4 are considered for the modelling of the structure in medium soil type.

Table 4. Seismic properties from IS 1893-2016 code for modelling

Zone factor	0.24 (zone4), 0.36 (zone 5)
Importance factor	1.2
Response reduction factor	5

Building models

The following models given in Table 5 are modelled in the ETABS software for studying the seismic performance of structures.

Table 5. Building models used for the study

Sl. No	Model Code	Model Description
1	CMRF	Conventional Moment Resisting Frame (CMRF) building with shear walls
2	TITS	Tube In Tube RC Frame Building with Shear Wall - A structure with two concentric tubes (inner core and outer perimeter) connected by horizontal and vertical members.
3	SDTS	Single Damper in Three Stories - One damper placed in each of the top, middle, and bottom storeys.
4	SDCS	Single Damper in Consecutive Stories - One damper placed in three consecutive stories in the top, middle, and bottom regions.
5	SDAS	Single Damper in Alternative Stories - One damper placed in alternate stories throughout the building.
6	SDES	Single Damper in Each Story - One damper placed in each story of the structure.
7	DDTS	Double Damper in Three Stories - Two dampers placed in each of the top, middle, and bottom stories.
8	DDCS	Double Damper in Consecutive Stories - Two dampers placed in three consecutive stories in the top, middle, and bottom regions.
9	DDAS	Double Damper in Alternative Stories - Two dampers placed in alternate stories throughout the building.
10	DDES	Double Damper in Each Story - Two dampers placed in each story of the structure.

The following figures illustrate the different structural models considered in the study. Fig 3 shows the plan of the Conventional RC Frame Building with Shear Wall (CMRF) modeled in ETABS. Fig 4 presents the plan of the Tube in Tube RC Frame Building with Shear Wall (TITS). Fig 5 illustrates the elevation view of the structure with a Single Damper in each of the top, middle, and bottom stories (SDTS). Fig 6 displays the elevation view with a Single Damper in 3 Consecutive Stories at the top, middle, and bottom regions (SDCS). Fig 7 depicts the elevation with a Single Damper in Alternative Stories (SDAS). Fig 8 presents the elevation with a Single Damper in Each Story (SDES). Fig 9 shows the elevation with Two Dampers in the top, middle, and bottom stories (DDTS). Fig 10 illustrates the elevation with Two Dampers in 3 Consecutive Stories at the top, middle, and bottom regions (DDCS). Fig 11 displays the elevation with Two Dampers in Alternative Stories (DDAS). Fig 12 shows the elevation with Two Dampers in Each Story (DDES).

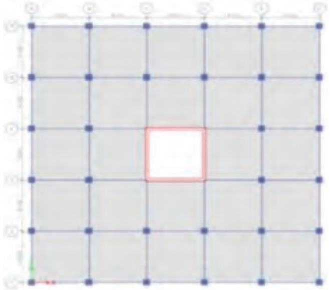

Fig. 3. Plan of CMRF in ETABS software

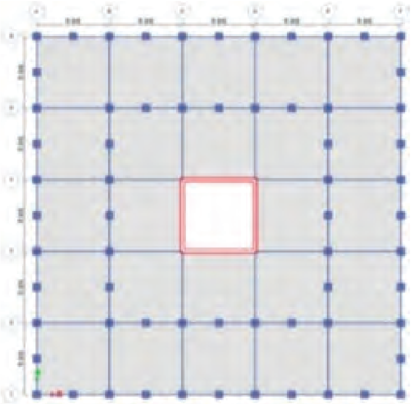

Fig. 4. Plan of TITS in ETABS software

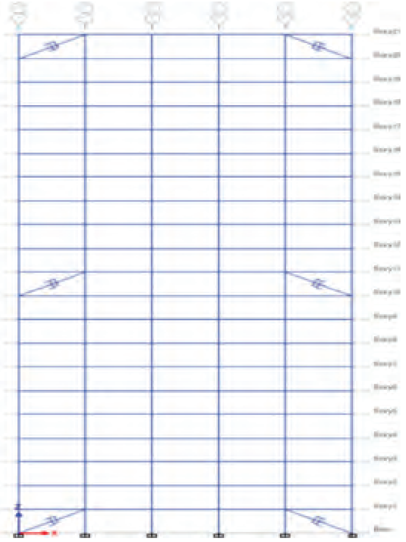

Fig 5. Elevation of SDTS

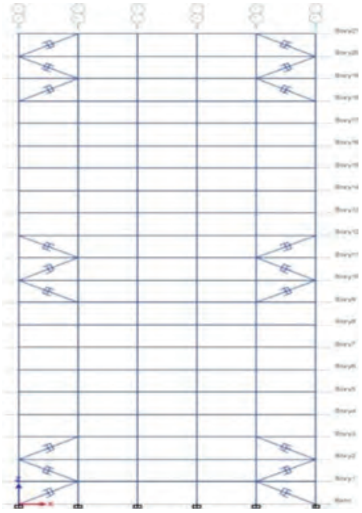

Fig 6. Elevation of SDCS

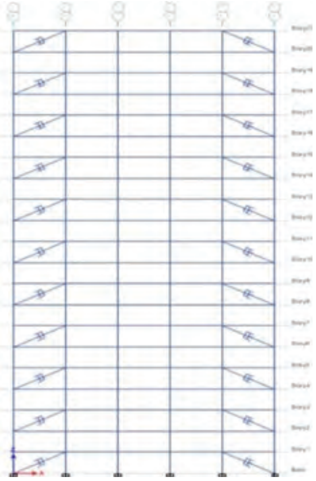

Fig 7. Elevation of SDAS

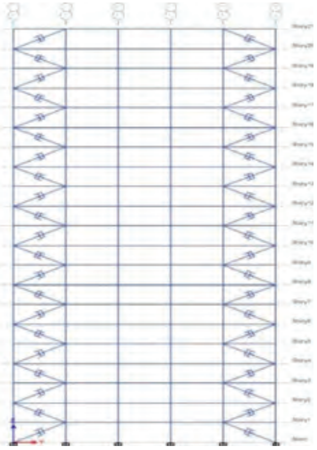

Fig 8. Elevation of SDES

Fig 9. Elevation of DDTS

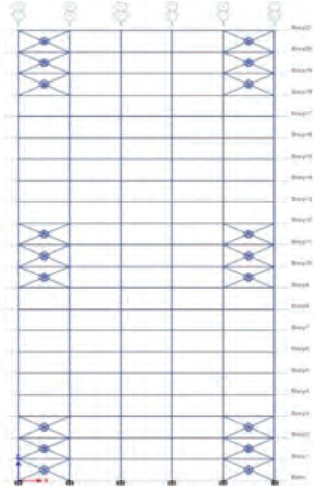

Fig 10. Elevation of DDCS

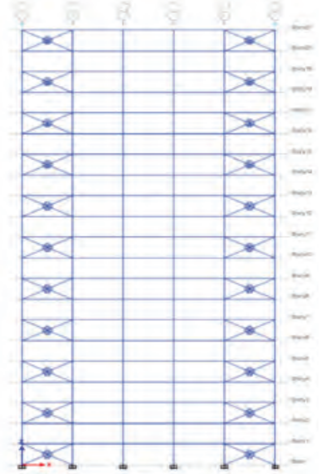

Fig 11. Elevation of DDAS

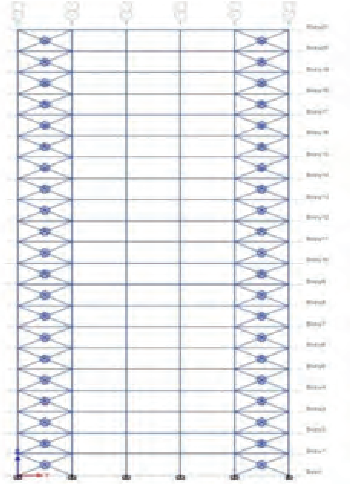

Fig 12. Elevation of DDES

RESULTS AND DISCUSSIONS

Maximum story displacement, maximum story shear and maximum story drift are calculated for the modelled structures using ETABS software in seismic zone IV and zone V. The analysis of the results and comparison are presented in the following sections.

Maximum story displacement

Maximum story displacement is the displacement which occurs in the stories of the structure due to seismic excitation on top of the structure. Fig 13 shows the bar charts of maximum story displacement of Conventional Moment Resistant Frame structure (CMRF) and Tube In Tube Structure (TITS). And Fig 14 shows the bar chart of max story displacement of damper added models (SDTS, SDCS, SDAS, SDES, DDTS, DDCS, DDAS and DDES). The DDES shows lower max displacement compared to other damper structures. Fig 15 shows the bar chart of Max story displacement of DDES and TITS.

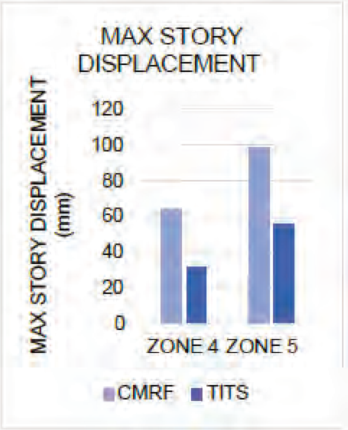

Fig 13. Bar chart of Max story displacement of CMRF and TITS

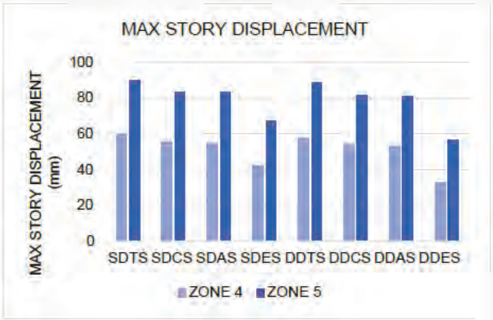

Fig 14. Bar chart of max story displacement of damper added models

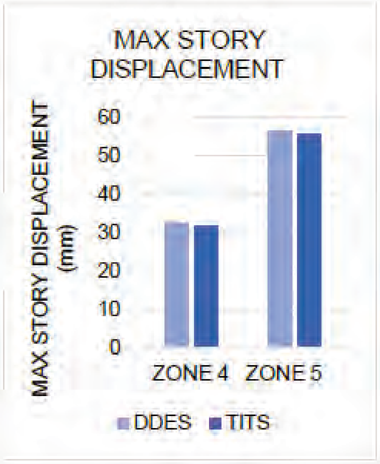

Fig 15. Bar chart of Max story displacement of DDES and TITS

Maximum story drift

Maximum story drift is the ratio of relative displacement between adjacent stories of the building to the height between two consecutive stories of the building. It is the displacement or movement in each story of building relative to its original position due to earthquake. Fig 16 shows the bar charts of maximum story drift of CMRF and TITS. And Fig 17 shows the bar chart of max story drift of damper added models (SDTS, SDCS, SDAS, SDES, DDTS, DDCS, DDAS and DDES). The DDES shows lower max story drift compared to other damper structures. Fig 18 shows the bar chart of Max story drift of DDES and TITS.

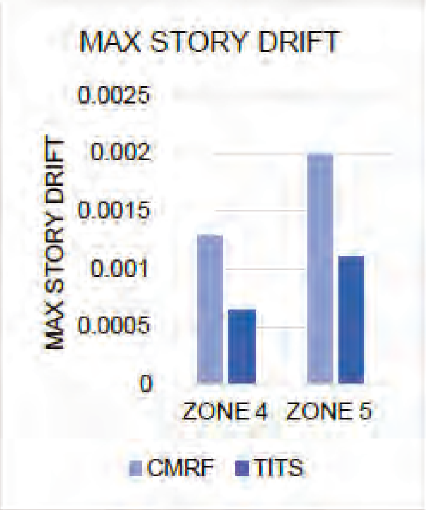

Fig 16. Bar chart of Max story drift of CMRF and TITS

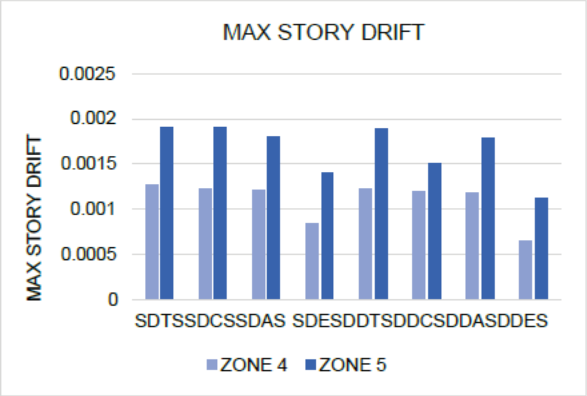

Fig 17. Bar chart of max story drift of damper added models

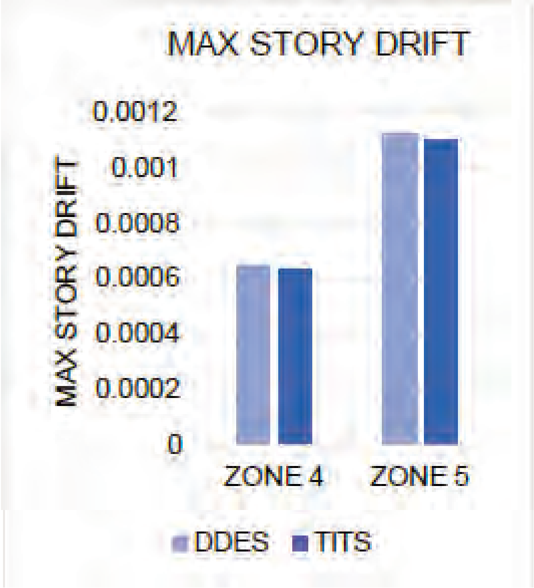

Fig 18. Bar chart of Max story drift of DDES and TITS

Maximum story shear

Base shear is the maximum lateral force resistance at the base of building due to seismic loading. Maximum story shear is the maximum lateral force resistance in the entire structure. It should be higher in value for the better performance of the structure. Fig 19 shows the bar charts of maximum story shear of CMRF and TITS. And Fig 20 shows the bar chart of max story shear of damper added models (SDTS, SDCS, SDAS, SDES, DDTS, DDCS, DDAS and DDES). The DDES shows higher value of max story shear compared to other damper structures. Fig 21 shows the bar chart of Max story shear of DDES and TITS.

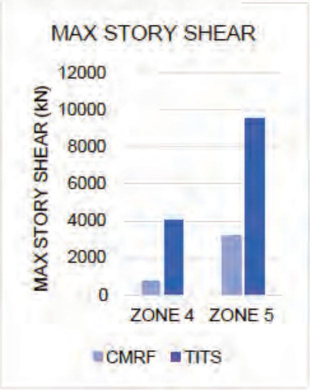

Fig 19. Bar chart of Max story shear of CMRF and TITS

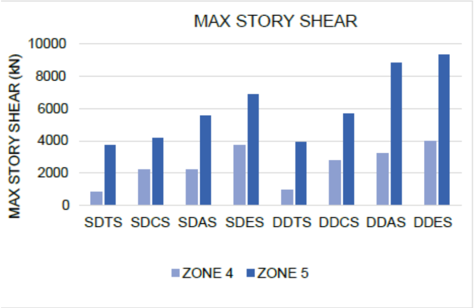

Fig 20. Bar chart of max story shear of damper added models

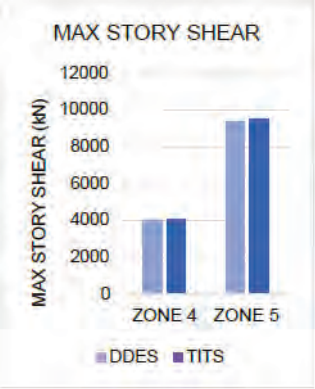

Fig 21. Bar chart of Max story shear of DDES and TITS

Comparison of results

The comparison between the conventional moment resisting frame structure and tube in tube structure is shown in table 6. The Double Damper in Each Story (DDES) model shows better seismic performance compared to the other model. So, this model taken for final comparison with Tube in Tube structure model to evaluate structural model seismic performance. Table 7 shows the percentage variation in the key parameters on comparison of DDES and TITS in zone IV and zone V.

Table 6. Comparison of results of Conventional RC frame and Tube in tube structures

Zones	Parameters	Conventional Moment Resisting Frame structure (CMRF)	Tube In Tube Structure (TITS)	Percentage variation
Zone IV	Max story displacement (mm)	63.7952	31.84	50.09%
	Max story drift	0.00128	0.000636	50.31%
	Max story shear (kN)	756	4054.943	65.96 %
Zone V	Max story displacement (mm)	98.47	55.93	43.2%
	Max story drift	0.001972	0.001099	44.26%
	Max story shear (kN)	3233.7	9524.947	66.05 %

Table 7. Percentage variation of DDES and TITS seismic performance

Zones	Parameters	Double Damper in Each Story (DDES)	Tube in Tube building (TITS)	Percentage variation
zone IV	Max story displacement (mm)	32.6558	31.84	2.49 %
	Max story drift	0.000647	0.000636	1.7 %
	Max story shear (kN)	3990.54	4054.94	1.58 %
zone V	Max story displacement (mm)	56.7438	55.9398	1.41 %
	Max story drift	0.001123	0.001099	2.13 %
	Max story shear (kN)	9332.91	9524.94	2.01 %

CONCLUSIONS

Tube-in-tube RC frame structure with shear wall shows higher seismic resistance compared to other structural models. Conventional buildings with dampers show higher seismic performance compared to conventional buildings without dampers. Dampers are devices installed in buildings to absorb and dissipate seismic energy, reducing the impact of earthquakes on the structure. Conventional buildings with 2 dampers in each story exhibit less maximum story displacement, less maximum story drift, and high maximum story shear compared to other damper models. Having two dampers per story enhances the building's ability to dissipate seismic energy effectively. By comparing the DDES and TITS the following percentage variations are obtained.

- ➢ Percentage variation in Maximum story displacement as 2.49% for Zone IV and 1.41% for Zone V
- ➢ Percentage variation in Maximum story drift as 1.7% for Zone IV and 2.13% for Zone V
- ➢ percentage variation in Maximum story shear as 1.58% for Zone IV and 2.01% for Zone V

By comparing the DDES and TITS seismic performance, they show negligible variations in story displacement, story shear and story drift. This implies that both structural systems offer comparable levels of resilience against seismic events. In other words, when dampers are installed on all stories of a conventional moment resisting frame, the resulting seismic performance is observed to be equivalent to that of a tube in tube structure.

REFERENCES

1. Balakrishnan S, James R M. 2019. Comparative Study of Tube in Tube Structures and Tubed Mega Frames. International Journal of Recent Trends in Engineering and Research, 4(6), 18–26.
2. Bhavanishankar S, Vinod. 2021. Comparative Analysis of Tubular Structures with Conventional Tall RC Structure. International research journal for engineering and technology, 8(3).
3. Del Gobbo G M, Blakeborough A., and Williams M S. 2018. Improving total-building seismic performance using linear fluid viscous dampers. Bulletin of Earthquake Engineering, 16, 4249-4272.
4. Elwardany H, Jankowski R., and Seleemah A. 2021. Mitigating the seismic pounding of multi-story buildings in series using linear and nonlinear fluid viscous dampers. Archives of Civil and Mechanical Engineering, 21(4), 137.
5. Ijmulwar S S, Patro S K. 2024. Seismic design of reinforced concrete buildings equipped with viscous dampers using simplified performance-based approach. In Structures, (Vol. 61, p. 106020).
6. Khatri A G, Goud R., and Awasthi G. 2019. Performance of tube in tube structures: A review. In AIP Conference Proceedings, (Vol. 2158, No. 1).
7. Mirzahosseini H. 2014. Optimal design of tube in tube systems. Indian Journal of Fundamental and Applied Life Sciences, ISSN, 2231-6345.
8. Nkurey A, Vhajage S., Gawand S., Jchause M., and Nkondekar A R. 2021. Comparative Study of Tube in Tube System and Bundled Tube System for High Rise Building. International Journal of Innovative Research in Science, Engineering and Technology, 11(10).
9. Sarcheshmehpour M, Estekanchi H E., and Moosavian H. 2020. Optimum seismic design of steel framed-tube and tube-in-tube tall buildings. The Structural Design of Tall and Special Buildings, 29(14).
10. Sharma K V, Parmar V., Gautam L., Choudhary S., and Gohil J. 2023. Modelling efficiency of fluid viscous dampers positioning for increasing tall buildings Resilience to earthquakes induced structural vibrations. Soil Dynamics and Earthquake Engineering, 173, 108108.
11. Wadagule S R, Charantimath V R. 2019. Comparative study of tube in tube structure and frame tube structure. Int. Res. J. Eng. Technol, (IRJET), 6(07), 2395-0056.
12. Zhang S, Zhou J., and Hao Y. 2020. Seismic Vulnerability Analysis of High-Rise Composite Frame Concrete Tube Composite Structure. IOP Conference Series: Earth and Environmental Science, 455(1), 012010. https://doi.org/10.1088/1755-1315/455/1/012010.

Seismic Analysis of Diagrid Structures Having Steel Shear Wall with Different Angles

Gopika N
PG Scholar
Department of Civil Engineering
NSS College of Engineering
Palakkad, Kerala
🖂 gopikan831@gmail.com

Krishnachandran V N
Assistant Professor
Department of Civil Engineering
NSS College of Engineering
Palakkad, Kerala
🖂 vnkrishnachandran@nssce.ac.in

ABSTRACT

With rapid growth in vertical development and increasing probabilities of earthquake occurrences, the need to make any structure earthquake resistant has become vital. Diagrids are supporting framework in a building formed with diagonally intersecting ribs of metal or concrete and is considered an excellent lateral force resisting system. By applying the finite element analysis program ETABS, this study examines the seismic performance of diagrid structures with different angles. The study utilizes linear static analysis for the evaluation of a 60 storied steel building and aims to determine the best configuration of diagrids with steel shear wall. The angles with which diagrids placed are 49o, 67o, 74o, 78o, 80o and 82o. The study evaluates how well diagrids along with steel shear wall reduces the effect of earthquakes on tall buildings. Maximum Storey displacement, maximum storey drift and maximum storey stiffness are the main parameters of interest. Hence the study addresses the critical need for earthquake-resistant structures in the context of increasing vertical development and seismic risks, comparing various diagrid angles to identify the optimal configuration for seismic resistance. The study's conclusions show that integrating diagrids to a conventional building enhances the structure's seismic performance. After thorough consideration, the most suitable angle for diagrid placement is determined to be between 670 and 780.

KEYWORDS: *Diagrids, Shear wall, Seismic performance.*

INTRODUCTION

The term diagrid originated from the combination of diagonals and grids. Diagrids are considered a major advent of the century as it outperforms the existing structural systems. Diagrids are structural framework arranged diagonally on the periphery of the structure and the material can be steel, concrete, timber etc. Steel diagrids are more popular than concrete and timber, as steel can contribute to the ductility aspect. These are made of diamond modules with diagonal members and provides more lateral stiffness than conventional building. They are capable of carrying both lateral as well as gravity loads which in turn leads to the elimination of vertical columns at the periphery of the building. As the diagrid structure minimizes the number of columns in the building, it gives more freedom for the architects to enhance the flexibility of design. A comparison of diagrid structure with various other lateral force resisting systems has pointed out the advantages that diagrids possess. While braced system can carry only lateral loads, diagrids are capable of resisting and transferring lateral and gravity loads respectively. Diagrids are effective in minimizing shear deformation (change in shape) as they carry shear by axial action of diagonal members, whereas for conventional structures, they carry shear by bending of the columns. When compared to outrigger structures, diagrid structures offer both bending and shear rigidity whereas outriggers offer bending rigidity by reducing moment, but does not provide shear rigidity. Since steel is the most commonly used material for diagrid, it can create long spanning members without reinforcement. As incorporation of diagrids in building eliminates the need for outer and corner columns, it leads to material efficiency in construction. Fig. 1 depicts the Tornado tower situated in Doha, Qatar, which is a diagrid building. Fig. 2 depicts the Gherkin situated in London, which is a diagrid building.

Fig. 1. Tornado tower, Qatar

Fig. 2. The Gherkin, London

BACKGROUND SUMMARY

Kadekar and Thorat [1] conducted seismic investigation of diagrid structures and identified a number of metrics in seismic zone III, including story shear and storey displacement. The findings demonstrated that, in comparison to RCC buildings, structural systems with diagrids performed better. The incorporation of diagrids also resulted in reduction of displacement by 43.78%, which is almost similar to that of braced model (Touseef and Patil [2])Other design studies have been made. Several types of structures were taken into consideration, including bare frames, structures with shear walls at their core, structures with irregular masses, structures with diagrids, and structures that combined diagrids and shear walls and found that the diagrid structure seemed to have the least amount of storey displacement based on the results (Jaiswal and Mahajan [3]). Vishali et al. [4] conducted a comparative study on the seismic behaviour of diagrid structures with dampers. The study concluded that diagrid building with damper showed improved strength and lateral load resisting capacity when subjected to earthquake forces. The traditional structure's storey stiffness exhibited lower values in comparison to the diagrid construction. Diagrid constructions withstand horizontal forces more effectively and efficiently than regular buildings (Teja et al. [5]). Chowdari et al. [6] performed a seismic analysis of a tall concrete and steel diagrid structure employing response spectrum and time history methods in e-tabs. The objective of the study was to optimize the placement of the diagrid in two distinct G+20 storey structures and assessed the seismic behaviour of 20 storied concrete as well as steel diagrid structures. The study discovered that the basic time period in concrete diagrid was shorter than in steel diagrid.

While comparing diagrid building with a shear wall system, the analysis results indicated that the diagrid structure exhibited a shorter modal time period than the shear wall structure in all significant directions (Abedin and Autade [7]). Bhat and Danish [8] analyzed different configurations of variable angle diagrid structures. The study included two strategies in which the first one was placing diagrids in the building such that there are two varying angles of diagrids in the ratios 1:1, 1:2, 2:1. The second strategy was placing diagrids with three varying angles in the same structure in the ratio 1:1:1. The study concluded that constant angle diagrids are much more material efficient when compared to varying angle diagrids. Analysis of a 45 storied steel frame with a diagrid angle of 67.32, comparing it to two other frames using x-bracing and dampers showed diagrid structure showcased lower story drift values and higher stiffness values when compared to other models (Yadav and Bajpai [9]). Jani and Patel [10] performed seismic analysis and design of diagrid buildings in steel buildings. The study found out that most of the lateral loads were resisted by diagrids and gravity loads by internal columns as well as diagrids on the periphery.

For high rise buildings subjected to horizontal forces like seismic and wind forces, optimizing lateral load resisting system is of greater importance. Diagrids are considered a new advent in this century which outperforms the existing lateral force resisting structures. Incorporating diagrids in tall buildings has shown better results when the structure is subjected to earthquake loading. The seismic analysis of diagrid structures showed lower displacement, storey drift etc. when compared to conventional building, indicating its efficiency. Also, diagrid buildings have proved to be cost effective as it reduces the consumption of steel when compared to ordinary building.

METHODS

Several kinds of analysis can be done in order to study the response of the structure and assess how well the structures work. Analyses that are both linear and nonlinear can be used to determine the response of the structure. The three types of linear analysis are time history, linear dynamic (eg. response spectrum), and linear static (eg. equivalent static). Response spectrum analysis and equivalent static analysis are part of linear analysis, with former being static and latter being dynamic in nature of analysis. Push-over analysis, which is a non-linear static and non-linear time history analysis are examples of non-linear analysis.

Equivalent static method

Using this method, the building's overall design base shear (VB) is calculated initially. The base shear will then be dispersed to the different levels of the floor at the appropriate centers of mass. In conclusion, the seismic force at each floor level will be allocated to certain materials that can withstand lateral loads by means of structural analysis, taking into account the diaphragm action of the floor. The equivalent static method is a simplified method used in seismic analysis and design, which converts dynamic earthquake forces into equivalent static loads. This method involves placing static loads on a structure similar to dynamic loading from earthquakes, focusing on floor and roof levels, where the mass concentration is highest, resulting in the greatest lateral displacements. The formula for calculating the design base shear, or VB, along any principal direction of a building is as follows:

$V_B = A_h * W$,

where Ah is the design horizontal acceleration coefficient value and W is the building's seismic weight.

Fig. 3 depicts the relationship between top story displacement and base shear in a building.

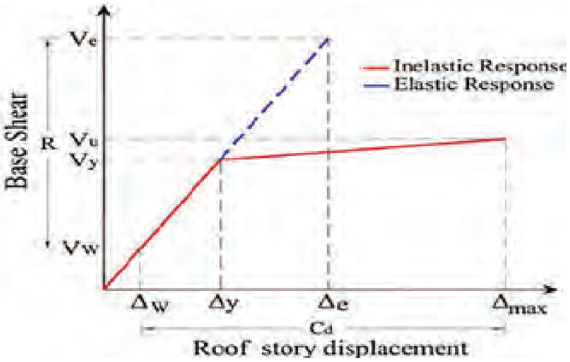

Fig. 3. Relation between roof storey displacement and base shear

METHODOLOGY

The study is conducted with a proper methodology which involves a series of sequences. Initially, an extensive literature survey has been carried out and objectives were formulated. Following this, in the model validation phase, a 60 storied building is taken for validation purpose. This involves creating a model with diagrids at the periphery. In the next stage, buildings with different angles of diagrids are modelled and analysed using ETABS. Critical parameters like maximum displacement, storey drift and stiffness are evaluated.

The scope of this project is to analyse a 60 storied steel building with diagrids of different angles using ETABS software. The plan dimension of the building is 36m x 36m and each floor height is 3.5m. Equivalent lateral load method, which is a linear static method of analysis, is made use for the study. For seismic analysis IS 1893 (Part 1):2016 [11], has been used. A total of seven models are included in the present study, with first model being conventional building with steel shear wall and the remaining models having different diagrid angles namely 49o, 67o, 74o, 78o, 80o and 82o. Separate analysis is carried out for each model. The angles are selected based on the module arrangement of diagrids. The seismic performance results were analysed in terms of maximum storey displacement, maximum drift and maximum stiffness. The scope of the study is limited to constant angle diagrids with steel as their material. Future studies are possible for variable angle diagrids, incorporating composite materials, design of diagrid nodes.

MODELLING AND ANALYSIS

Diagrid structure of 60 stories and six different grid angles were considered. The angles taken into consideration are 49°, 67°, 74°, 78°, 80° and 82°. Fig. 4 shows the building plan of the structure.

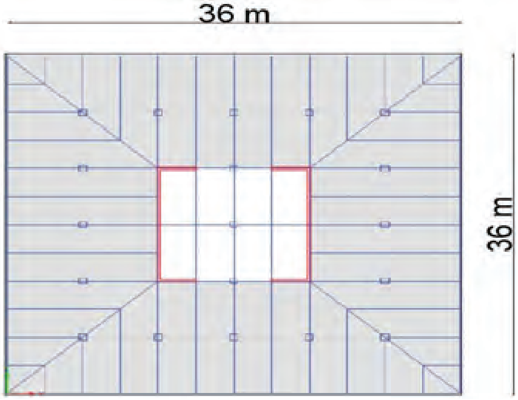

Fig. 4. Building plan of the structure

The modelled structures have a plan dimension of 36 × 36 m and inner core of dimension 12 × 12 m. The height of the all the stories is 3.5 m. Fig 5 to 10 shows the elevations of the diagrid structure. The dead load and live load taken for the analysis are 5 kN/m2 and 5 kN/m2. For seismic analysis, building is assumed to be located at zone V.Response reduction factor corresponding to special moment resisting frame in steel buildings is taken and the value is taken as 5.0 as per IS 1893(part 1):2016 [11]. The type of the soil if taken as medium (Type II) and the damping ratio is assumed as 5%. Modelling and analysis of diagrid structure is the core of the project, therefore, an important phase. In this phase, the structural components of the building are carefully represented within a digital framework using ETABS software. Table 1 and table 2 lists the seismic parameters and structural details respectively that are taken into consideration for the analysis. Table 3 lists the models and the abbreviations.

Table 1

Seismic zone	V
Zone factor (Z)	0.36
Importance factor (I)	1
Response reduction factor (R)	5
Type of soil	Medium
Damping ratio	5 %

Table 2

Total height	210 m
No of stories	60
Beam size, B1	ISMB 550
Beam size, B2	ISMB 600 & cover plates on top & bottom of dimension 250 x 50mm
Column size	600mm x 600mm x 16mm steel tube
Diagrid size	375mm pipe section with 12mm thickness

Table 3

Models	Diagrid module	Abbreviations
60 storied conventional building	-	CB - SW
60 storied building with diagrid angle 49°	2 storey modules	D 49
60 storied building with diagrid angle 67°	4 storey modules	D 67
60 storied building with diagrid angle 74°	6 storey modules	D 74
60 storied building with diagrid angle 78°	8 storey modules	D 78
60 storied building with diagrid angle 80°	10 storey modules	D 80
60 storied building with diagrid angle 82°	12 storey modules	D 82

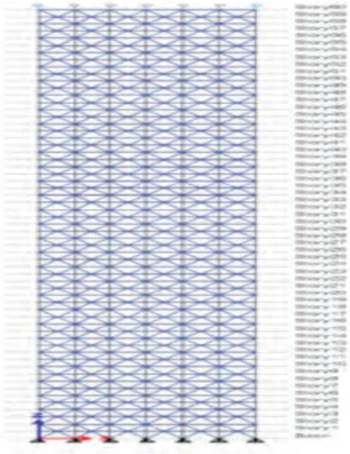

Fig. 5: Elevation of D 49

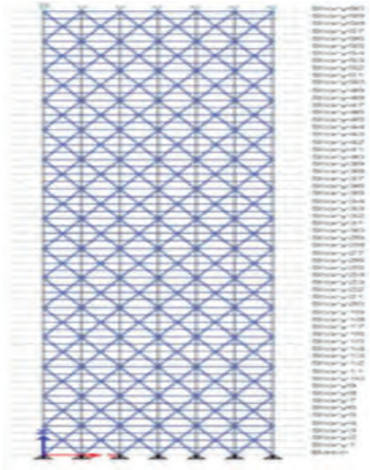

Fig. 6: Elevation of D 67

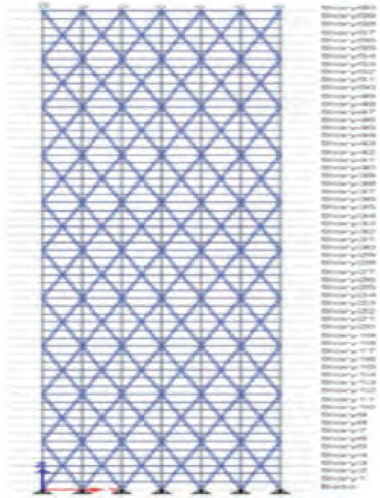

Fig. 7: Elevation of D 74

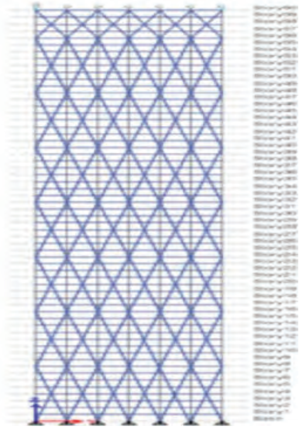

Fig. 8: Elevation of D 78

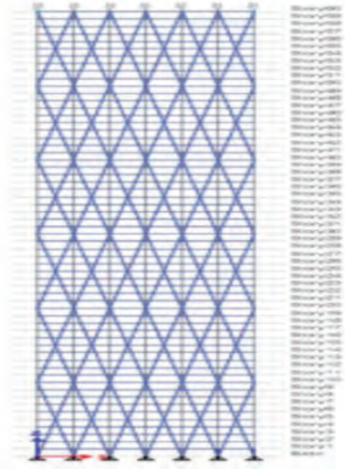

Fig. 9: Elevation of D 80

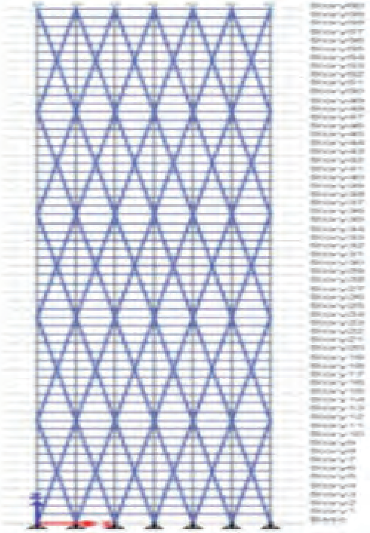

Fig 10: Elevation of D 82

Diagrids are featured based on the diagonal arrangement of the inclined members. This diagonal arrangement is referred to as modules. When a single diagonal module covers two floors, then it is a two-storey module diagrid building and the corresponding angle in which diagrids placed will be 490.

When a single diagonal module covers four floors, then it is a four-storey module diagrid building and the corresponding angle in which diagrids placed will be 670. When a single diagonal module covers six floors, then it is a six-storey module diagrid building and the corresponding angle in which diagrids placed will be 740. When a single diagonal module covers eight floors, then it is an eight-storey module diagrid building and the corresponding angle in which diagrids placed will be 780. Similar logic is applied to further angles of diagrid as well.

Response parameters included in the study are maximum storey displacement, storey drift and storey stiffness. Storey displacement is an important parameter in earthquake analysis as it measures the lateral movement within the building when subjected to lateral forces like earthquakes, wind etc. Excessive storey displacement can harm the structure and may compromise the functionality of the building and safety of its occupants. Storey displacement of any building should be within the permissible limit prescribed as per IS 456:2000 [12]. The displacement value for a building should not exceed H/500, where H is the height of the building.

Storey drift is a measure of the relative lateral displacement between adjacent floors or levels within a building. It signifies the capacity of the building to endure and dissipate these lateral forces while upholding the structural integrity. As per IS 1893:2016, maximum storey drift for a building should not exceed 0.004 times the height of a storey.

Storey stiffness in multi-storey buildings is a crucial factor that influences their dynamic behaviour during earthquakes. It measures the lateral translational stiffness of each storey in a building, indicating its resistance to lateral deflection under lateral forces. Buildings with higher stiffness values is desirable in seismic point of view. Stiffness irregularities in the building will lead to worsened effects when earthquakes hit the building.

RESULTS AND DISCUSSIONS

The study compares maximum displacement, maximum storey drift and maximum storey stiffness across different models, providing a comprehensive analysis of their respective performance.

Maximum storey displacement

When comparing with conventional building, all the other models showed lower values of storey displacement. The comparison and the percentage reduction in displacement and drift is shown in table 4. Conventional steel building is compared with various diagrid models with different angles and the results are represented in a tabular format, complemented by graphical representations, offering a comprehensive visualization of the results.

Table 4

Building Models	Percentage reduction in displacement (%)	Percentage reduction in drift (%)
CB - SW	-	-
D 49	46.01	45.94
D 67	51.65	51.88
D 74	52.05	55.63
D 78	64.03	65.00
D 80	61.55	62.81
D 82	37.72	39.69

The incorporation of diagrids into a conventional building drastically improves the storey displacement values. Maximum percentage reduction of 64.03% is obtained for D 78 model. As the angle in which diagrids are placed increases, storey displacement decreases, but only up to a point where the trend reverses and the values goes up. As per IS 456:2000, the permissible displacement value for this particular building is 420mm (H/500 = 210000/500 = 420 mm) and all the diagrid models exhibits displacement values within the limits prescribed by the code. Fig. 11 depicts the variation in displacement of all the models across different stories.

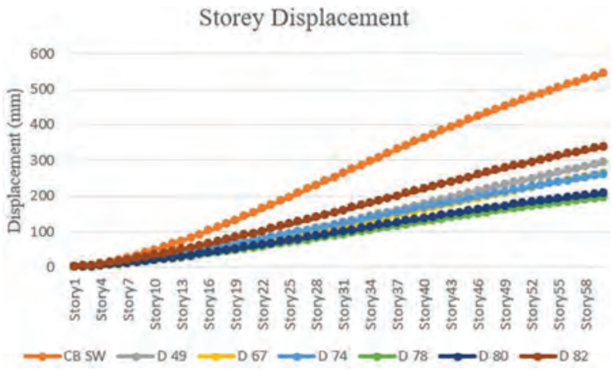

Fig. 11. Comparison of displacement values

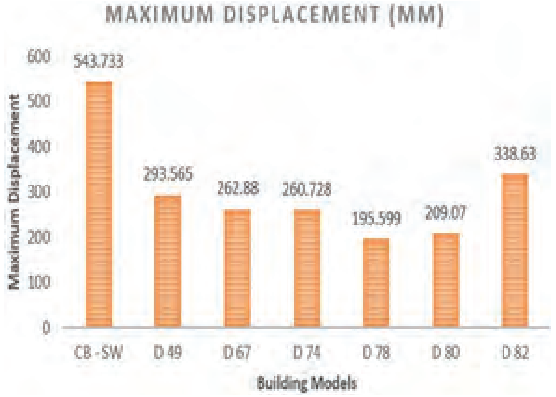

Fig. 12. Maximum storey displacement

From figure 11, it is clear that, conventional building with steel shear wall shows highest displacement values, which implies poor seismic performance. Diagrid buildings are exhibiting much lesser values, showcasing the efficacy of diagrid buildings in resisting seismic forces. Fig. 12 shows the maximum storey displacement for the respective models.

Maximum storey drift

Maximum drift value follows the same trend as that of displacement, where the drift value decreases up to D 78 and thereafter starts rising up. From table 4, maximum percentage reduction of 65 % is obtained for the model D 78. Fig. 13 depicts the variation in drift of all the models across different stories. Fig. 14 shows the maximum storey drift values of all the respective models.

From figure 13, it is evident that, conventional building with steel shear wall exhibited maximum storey drift when compared to diagrid models. The best performance is exhibited by D 78 model followed by D 80, D 74, D 67, D 49 and finally D 82. Storey drift is one of the important parameters that determines the seismic resilience of the structure. The model D78 showed least value of 0.00112.

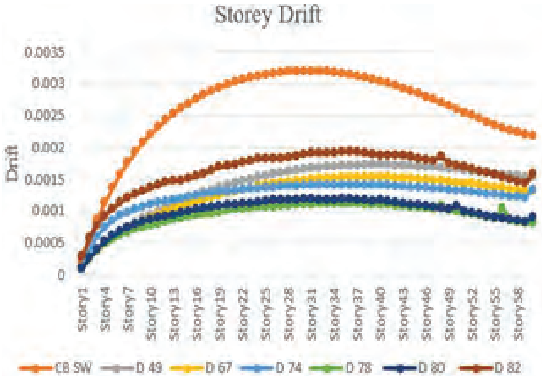

Fig. 13. Maximum storey drift

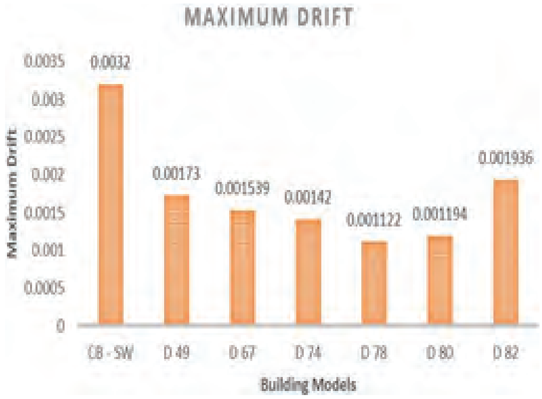

Fig. 14. Maximum storey drift

Maximum storey stiffness

Maximum storey stiffness is found to be for D 78 and the stiffness is approximately 6 times higher than conventional structure. The stiffness value increases as the diagrid angle increases and starts dropping down when it is placed beyond an angle of 78. Fig. 15 depicts the maximum storey stiffness for respective models.

Stiffness of a building is important to resist the displacement that might happen to a structure when it is subjected to lateral forces. Model D 78 obtained a maximum storey stiffness of 49.75 x 106 amongst all the models. Such a remarkable increase in the stiffness implies the capability of diagrid buildings in resisting the lateral forces.

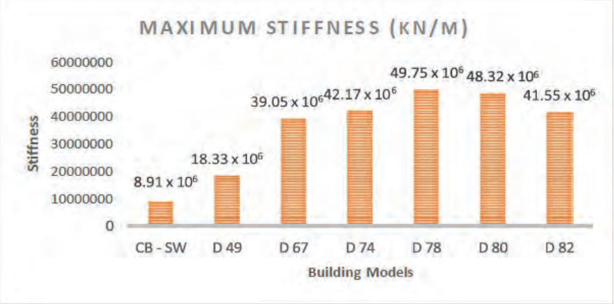

Fig. 15. Maximum storey stiffness

CONCLUSIONS

ETABS software was used to model and analyse a 60-storied conventional steel building with steel shear wall as well as various diagrid structures with diagrids positioned at angles of 49, 67, 74, 78, 80, and 82 degrees. Results were compared in terms of storey displacement, storey drift and storey stiffness. The main failure mode of diagrid buildings is due to the cumulative damage of column hinge. It is difficult to realize the beam hinge in diagrid structures. Following conclusions were drawn from the analysis.

- The seismic behaviour of a diagrid structure featuring a steel shear wall is superior to that of its conventional counterpart.
- The analysis shows that the D 78 model, with a notable decrease of 64.03%, shows the greatest reduction in maximum displacement. The displacement values of all the diagrid models are within the limits prescribed in the code. The results hence reveals that the maximum displacement of all the diagrid model falls within the limit. Furthermore, the maximum storey drift is impressively reduced by 65% in the same model.
- It is worth to note that the stiffest model is the D 78 and the stiffness is 6 times higher than the conventional structure. This suggests that the structure is more resilient to relative displacement and drift.
- The pattern followed by storey drift and storey displacement in diagrid systems is similar. When the angle of the diagonal increases, the values decline until they abruptly begin to grow at a break point. Simultaneously, storey stiffness exhibit a similar pattern, with initial increase in values followed by a decline.
- The best suited angle for diagrid placement is determined by meticulous analysis. As the diagrid is oriented at angles between 67 and 78, the analysis yields remarkable results. Consequently, the suitable angle may be between 67 and 78 degrees. The study's conclusions highlight the ideal angle at which to position diagrids to improve the building's seismic performance.

REFERENCES

1. Kadekar, M.A.M. and Thorat, V.S., 2023. "Comparative seismic analysis of diagrid structure and RCC frame structure using ETABS". International Research Journal of Modernization in Engineering Technology and Science, pp 3587-3593.
2. Touseef, M. and Patil, A.S., 2023. "Seismic evaluation of braced and diagrid structures". Journal of Scientific Research and Technology, pp.40-50.
3. Jaiswal, R. and Mahajan, A., 2023. "Comparative analysis of building with shear wall & diagrid structure". In IOP Conference Series: Earth and Environmental Science, Vol. 1110, No. 1, pp 12-33. IOP Publishing.
4. Vishali, M., Pradeep, S. and Satyanarayanan, K.S., 2022. "Comparative Study on Seismic Performance of Steel Diagrid Structures with and Without Dampers". In Sustainable Construction Materials: Select Proceedings of ACMM 2021, pp. 387-395. Springer Singapore.
5. Teja, B.S., Vasugi, V. and Jagen, V., 2022. "Comparative Analysis of Diagrid Structural System with Conventional Systems for Tall Buildings". In Recent Trends in Civil Engineering: Select Proceedings of ICRACE 2021, pp. 203-216. Singapore: Springer Nature Singapore.
6. Chowdary, M.S.S.K., Kumar, Y.H. and Lingeshwaran, N., 2021. "Seismic analysis of tall concrete and steel diagrid structure using response spectrum and time history method in e-tabs". In IOP Conference Series: Materials Science and Engineering, Vol. 1136, No. 1, pp. 12-35. IOP Publishing.
7. Abedin, S.A.S.M. and Autade, P., 2021. "Study the Behaviour of the RCC Structure with different Grid pattern against Earthquake". IOSR Journal of Mechanical and Civil Engineering (IOSR-JMCE), pp 01- 06.

8. Bhat, K.A. and Danish, P., 2021. “Analyzing different configurations of variable angle diagrid structures”. Materials Today: Proceedings, 42, pp 821-826.

9. Yadav, V. and Bajpai, A., 2020. “Seismic study of diagrid structure with brace frame and damper frame system of different arrangement”. Journal of Civil Engineering and Environmental Technology, 7(2), pp.174-178.

10. Jani, K. and Patel, P.V., 2013. “Analysis and design of diagrid structural system for high rise steel buildings”. Procedia Engineering, 51, pp 92-100.

11. Indian Standard for Code of Practice for Criteria of Earthquake Resistant Design of Structures-IS 1893:2016 Bureau of Indian Standards, New Delhi.

12. Indian Standard for Code of Practice Plain and Reinforced Concrete-IS 456:2000 Bureau of Indian Standards, New Delhi.

Seismic Performance of High-Rise Building with and Without Oblique Columns

Anjana Vijayan
PG Scholar
Department of Civil Engineering
NSS College of Engineering
Palakkad, Kerala
✉ anjanavijayan2310@gmail.com

Bharati Raj J
Assistant Professor
Department of Civil Engineering
NSS College of Engineering
Palakkad, Kerala
✉ bharatiraj@nssce.ac.in,

ABSTRACT

Finite Element Analysis is critical in understanding and enhancing the seismic performance of structures with oblique columns. The aim of this study is to investigate the seismic performance of oblique columns using the finite element analysis application ETABS and to evaluate how well the effects of earthquakes are reduced on tall buildings with oblique columns rather than normal columns. Understanding the seismic performance of structures is critical to guaranteeing the safety and resilience of buildings in earthquake prone areas. Oblique columns are a promising method for reducing earthquake forces. Maximum storey displacement, maximum storey drift and maximum storey shear are the main parameters of interest. The analysis involves a comparison of oblique columns at various angles that are subjected to seismic loads. In addition, the results support the optimization of tall building design and retrofitting to improve seismic resilience and reduce possible earthquake damage. In structures with oblique columns, the seismic performance is found better than buildings with conventional columns. Storey displacement and drift is found to be reduced while the storey shear is improved, providing a strong structure.

KEYWORDS: *Seismic performance, Oblique columns, Finite element analysis.*

INTRODUCTION

Building seismic performance is an important design consideration in structural engineering, particularly in earthquake- prone areas. This study uses the finite element analysis programme ETABS to assess the seismic performance of a building with oblique columns. When oblique columns are used instead of typical vertical columns, a unique structural system is produced with benefits including better load distribution and higher lateral stiffness. This study's main goals are to examine the structure's seismic response to different seismic loading scenarios and to evaluate important performance metrics such as overturning moment, maximum storey displacement, maximum storey drift, and maximum storey shear. The results of this study will provide significant insights on how well oblique columns might improve a building's seismic performance.

High-rise building design and construction have always been at the forefront of advances in engineering and architecture. An increasingly popular method is to use slant columns in high-rise structures. These raked or inclined columns offer distinct opportunities for structural behavior and architectural design since they depart from the traditional vertical orientation. The custom of using just vertical columns and beams has been abandoned in favor of oblique columns in high-rise constructions. There are several advantages for engineers and architects when the columns are inclined at particular angles. From a structural perspective, oblique columns can improve stability, optimize load distribution, and boost the building's overall performance. These columns' slant facilitates more effective load transmission, distributing forces and reducing the requirement for extra structural components. This could improve the structural integrity and resistance to lateral forces like wing or earthquake loads in addition to reducing the amount of material used.

OBJECTIVES

To analyze the seismic performance of structures with oblique columns at varying angles.

Scope of the study

To study the effect of inclination of the oblique column on the behavior of the structure and to understand the structural behavior of the oblique column, under earthquake forces. Response Spectrum Analysis is done in G+19 storied buildings having oblique columns with different angles such as 80°, 82°, 85°,88°, 90°, 100°, 120°. The modeling and analysis are done by using ETABS 2015 software.

Fig. 1 Oblique Columns

BACKGROUND SUMMARY

The seismic performance of high-rise structures with oblique columns has attracted a lot of attention because of its possible effects on safety and structural integrity. To improve their design and reduce the hazards connected with earthquakes, a significant amount of research has been done to understand how these kinds of structures behave under seismic loading conditions.

Structures with oblique columns have much better seismic performance than those with regular columns. The storey displacement decreases as the angle of the column lowers, when compared to standard columns. Furthermore, the storey drift increases with the angle of the column. Maximum storey shear and stiffness values fluctuate with column angle, demonstrating the effect of oblique columns on structural behavior under seismic loading circumstances [1]. When seismic performance study of multi-storied buildings with oblique columns was carried out by using ETABS The storey displacement in oblique constructions was found to much smaller than in simple RC frame buildings, indicating the effectiveness of oblique columns in seismic performance of the structure [2]. Using ETABS, SAP2000, MIDAS/GEN, and SATWE, research on high-rise structures with oblique columns is being implemented. Response spectrum, time history, and in-plane slab stress analysis are all included. The results demonstrated that MIDAS/GEN was better at post-processing, particularly for slab stress analysis, whereas ETABS was better at preprocessing. The study emphasized how crucial it is to assess slab stress in intricate structures, especially at weak places [3].

In a 20-storey simple frame building against a diagrid structural system, the advantages of oblique columns in decreasing top storey movement, demonstrating their lower mass and increased rigidity when compared to conventional designs, the oblique structure was found to have higher resistance and efficiency, especially in lateral load distribution and overall structural performance [4]. On reviewing seismic behavior of multistoried buildings with oblique columns and its height optimization, the seismic performance of multi-story buildings with oblique columns shows significant improvements in structural behavior. The oblique column system significantly reduces the effects of seismic stresses on the building, hence improving its overall performance [5]. The seismic performance of Y-shaped oblique columns in symmetrical and asymmetrical high-rise buildings compared to conventional column building on analysis, Y shaped columns show better performance compared to vertical columns [6].Constructions with oblique columns show much higher seismic resistance and lower lateral displacements compared to buildings with standard vertical columns, highlighting the usefulness of oblique columns in lateral load-resisting systems for tall buildings, demonstrating their potential to improve structural efficiency and seismic resistance in high-rise structures [7]. The inclined columns generally improve the structural stability by redistributing forces and increasing load-bearing capacity. These columns are very much useful in seismic zones to enhance building safety by resisting lateral stresses [8].

The seismic performance of a multi-story podium structural building with normal and oblique columns when evaluated using Response Spectrum and Time History analysis, it revealed that oblique columns and dampers improves the stability and seismic resistance of the constructions and podium constructions have been shown to improve stability and space optimization in congested metropolitan environments [9]. The primary determinants of the overall stiffness of the building structure are the selection of columns with the proper shape, size, and orientation, particularly in rectangular plan buildings. The impact of rectangular column design, size, and orientation on the building structure's seismic reaction are governed [10].

MODELLING OF STRUCTURE

The study involved creating detailed structural models in ETABS of a G+19 storeyed building and the seismic performance analysis is done.The building is modeled using oblique columns and conventional columns.

The structural details are provided in Table 1. Structural systems occurred in the study conducted by Santhosh et al. in 2021, was adopted for the present study. The details of different models are given in the following sections.

Details of the model from the journal

Following details of the models are shown in Table 1 considered by the author:

Table 1 Model details from the journal

No. of stories	G+19
Floor height & Depth of slab	3 m, 200 mm
Size of beam & columns	350 x 650 mm, 750 x 750 mm
Seismic zone & Seismic zone factor	111, 0.16
Materials	M30 concrete, Fe500 steel
Support condition	Fixed support
Soil type	Zone -II

Loads and intensities from the journal

Dead load, Live load and floor finishes are considered while modeling the structure. Dead load is considered using IS 875 Part 1. Live loads are considered using IS 875 Part 2. Live load can be considered separately for different buildings based on the purpose of the building.

Table 2 Loads and intensities of building from the journal

Live load on each floor	3kN/m^2
Dead load	2kN/m^2
Floor finishes	1kN/m^2

Details of building for modeling

Following building details shows in Table 3 considered for the modeling of the structure.

Table 3 Detailing of building for modeling purpose

Number of Stories	G+19
Floor height & Depth of slab	3 m, 200 mm
Size of beam & columns	350 x 650 mm, 750 x 750 mm
Oblique columns	80°, 82°, 85°, 88°,100°, 120°
Seismic zone & Seismic zone factor	111, 0.16
Materials	M30 Concrete, Fe500 steel
Support conditions	Fixed support

Building models

G+19-storeyed buildings are considered for modelling, and different models are made using ETABS for buildings with and without oblique columns. The modelling includes assigning various material and section properties such as beams and columns and assigning various loading conditions, along with seismic considerations. Different models with oblique columns at varying angles are considered for modelling.

6 Models have been created by providing oblique columns at varying angles 80°, 82°, 85°,88°, 100°, 120° and 1 model has been created by providing conventional columns (90°).

This range of angles allows for a thorough analysis of how the orientation of oblique columns affects the seismic performance of structures. Because oblique columns are stiffer, the initial stiffness of the reinforced concrete frames is mostly determined by their stiffness. As we move up to the upper stories, the plan dimensions will decrease for oblique columns that are less than 90° and increase for those that are more than 90°. Furthermore, the analysis considers performance indicators linked to occupant safety and building operation, like inter- story drift, in addition to structural reaction parameters like displacement drift and storey shear. To do seismic analysis in ETABS, the structural model is put under seismic loading conditions that are indicative of the seismic hazard at the location. Critical response characteristics, including maximum storey displacement, maximum storey drift, maximum storey shear are assessed during the analysis phase. The following models are modeled in the ETABS software for finding the seismic performance of structures.

MODEL 1: Multi-storeyed building with oblique columns (80°) MODEL

2: Multi-storeyed building with oblique columns (82°) MODEL

3: Multi-storeyed building with oblique columns (85°) MODEL

4: Multi-storeyed building with oblique columns (88°) MODEL

5: Multi-storeyed building with conventional columns (90°) MODEL

6: Multi-storeyed building with oblique columns (100°) MODEL

7: Multi-storeyed building with oblique columns (120°)

Fig. 2. Structural plan of G+19 storeyed building

The structural plan of the building is provided. Similar plan is considered for 20 floors, and vertical columns are replaced with oblique columns in which oblique columns are provided at varying angles. A G+19 storey building (32m x 32m) with an oblique column is modeled using ETABS. Structural plan is provided in Fig. 2.

The modeling includes assigning various material and section properties such as beams and columns and assigning various loading conditions, along with seismic considerations. Different models with oblique columns at varying angles are considered for modeling. This allows for a proper comparison of the performance of buildings with oblique columns by providing oblique columns at varying angles.

Fig 3 Multi-storeyed building with oblique columns (80°)

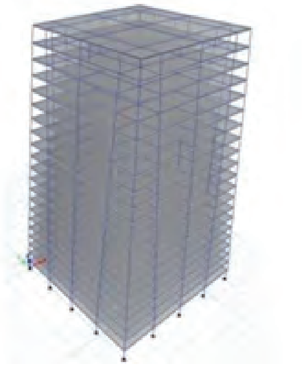

Fig 4. Multi-storeyed building with oblique columns (82°)

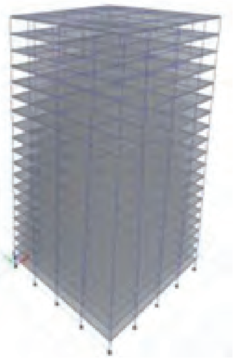

Fig. 5. Multi-storeyed building with oblique columns (85°)

Fig. 6 Multi-storeyed building with oblique columns (88°)

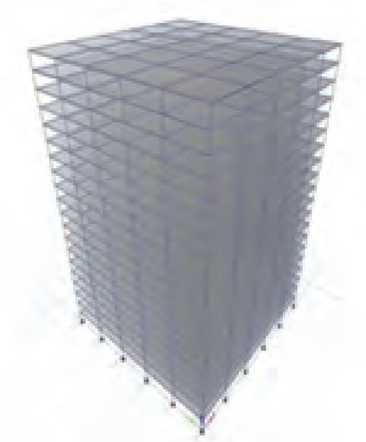

Fig. 7 Multi-storeyed building with conventional columns (90°)

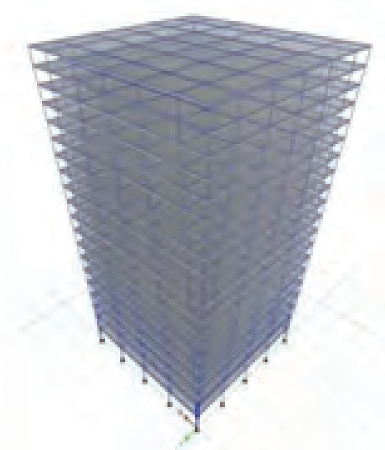

Fig. 8 Multi-storeyed building with oblique columns (7 00°)

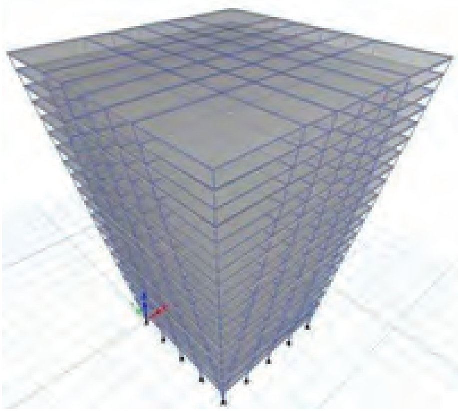

Fig. 9 Multi- storeyed building with oblique columns (7 20°)

Referring to Figure 3, oblique columns at an angle of 80° create a distinct structural structure when compared to other models with varying column angles. The exact angle of the oblique columns influences the building's structural stability and behavior, which affects load distribution, lateral stiffness, and overall structural reaction to seismic forces.

Referring to Figure 4, the overall response to seismic stresses may be affected by a minor redistribution of stiffness and strength throughout the structural parts with an increase in angle from 80° to 82°.During seismic occurrences, the inclination may cause a certain amount of force redistribution within the structure.

The distribution and size of inter-story drifts may vary slightly with a little angle increase from 80° to 82°, which could have an impact on the structure's overall stability and integrity.

Referring to Figure 5, because of the decreased lateral stiffness that comes with a larger angle, oblique columns at 85° may exhibit somewhat larger lateral deformations than those at 80° and 82°. As the angle is increasing the stability of the structure to lateral deformations keep on varying. During seismic occurrences, the structure with columns at an angle of 85° may undergo mild displacement and inter story drift.

Referring to Figure 6, lower story shear demands could arise from a more direct transfer of lateral forces due to the columns' more vertical position at 88°. In the construction with 88° columns, the displacement and inter-story drift may be greater because the oblique columns are less effective at withstanding lateral stresses. On the other hand, because there is less effective lateral force resistance in the building with oblique columns placed at 88°, the storey shear may be lower.

Referring to Figure 7, while angled columns may give more optimal resistance, conventional 90° columns usually provide symmetrical lateral force resistance. When using standard columns alone, a structure may experience moderate displacement and inter storey drift. When columns are oriented at a 90° angle, the structure might not be able to withstand lateral forces as well, which could lead to more displacement and drift than when columns are oriented at an angle smaller than 90°.

Referring to Figure 8, when compared to more vertical columns, columns at an angle of 100° may generally provide moderate to strong resistance against lateral forces, resulting in less displacement and drift; however, they may not be as optimized as columns at angles lower than 90°. When compared to columns at angles less than 90°, columns at 100° may cause a slightly different distribution of lateral forces and, as a result, storey shear.

Referring to Figure 9, comparing 120° columns to more vertical or oblique columns, they would probably provide less resistance against lateral forces also, columns positioned at a 120° angle from the vertical axis would provide a more acute angle.

In comparison to constructions with more vertical or oblique columns, the structure may experience increased displacement and inter-story drift because of the less favorable orientation of its columns.

RESULTS AND DISCUSSIONS

The work focusses on using ETABS software to perform seismic analysis of building models in seismic zone 111, both with and without oblique columns. The Response Spectrum Analysis approach is used to evaluate the behavior of the structure under dynamic seismic forces. To comprehend how seismic pressures impact various levels of the structure, key response metrics like storey displacement, storey shear, and storey drift are assessed. The research emphasizes the significance of storey shear in finding stress concentration zones that might require reinforcement and storey displacement in determining lateral movements. It has been demonstrated that an appropriate shear force distribution improves a building's resistance to seismic activity. To provide insight into structural performance and direct essential design adjustments, the maximum values of storey displacement, shear, and drift are computed and compared.

Maximum story displacement

The results include a tabulation as shown in Table 4 showing the comparison of the maximum storey displacements within the various models. Additionally, the results are visually depicted through graphs in Figure 10, providing a detailed and comprehensive view of the findings.

Table 4 Maximum storey displacement

Model	**Multi-storeyed building with** oblique columns
80°	24.216154
82°	32.716531
85°	40.215673
88°	42.073541
goo	42.514522
100°	48.316814
120°	54.713562

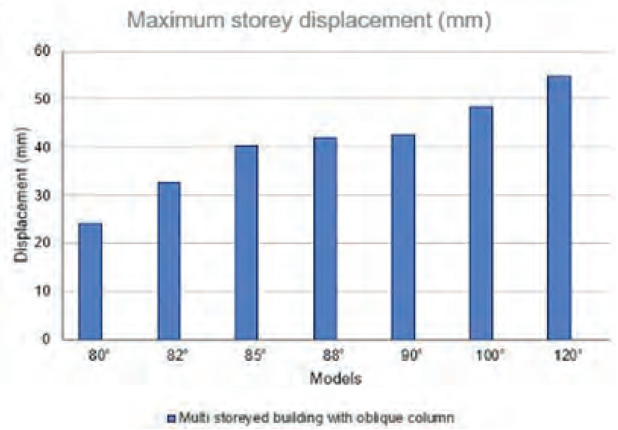

Fig. 10 Maximum storey displacement

Compared to structure with conventional columns and structures with oblique columns greater than go0, lesser displacement is shown for structures with oblique columns at angles lesser than go0

Maximum story drift

The results include a tabulation as shown in Table 5 showing the comparison of the maximum storey drift within the various models. Additionally, the results are visually depicted through graphs in Figure 11.

Providing a detailed and comprehensive view of the findings

Table 5 Maximum storey drift

Model	Multi-storeyed building with oblique columns
80°	0.000773
82°	0.000944
85°	0.001011
88°	0.001048
goo	0.001059
100°	0.001179
120°	0.001243

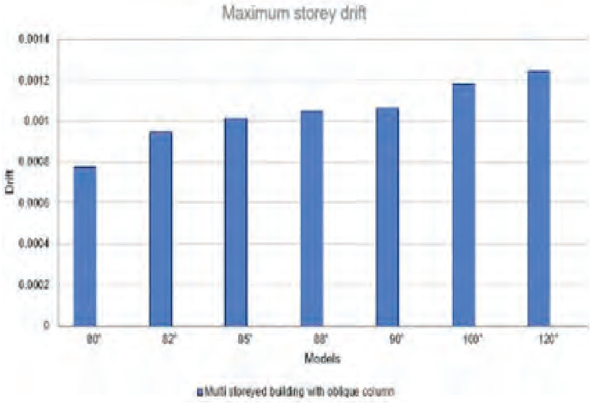

Fig. 11 Maximum storey drift

Compared to structure with conventional columns and structures with oblique columns greater than 90°, lesser drift is shown for structures with oblique columns at angles lesser than 90°

Maximum story shear

The results include a tabulation as shown in Table 6 showing the comparison of the maximum storey shear within the various models. Additionally, the results are visually depicted through graphs in Figure 12, providing a detailed and comprehensive view of the findings.

Table 6 Maximum storey shear

Model	Multi-storeyed building with oblique columns
80°	2789.874
82°	2167.218
85°	1767.506
88°	1586.506
goo	1492.382
100°	1367.217
120°	1234.688

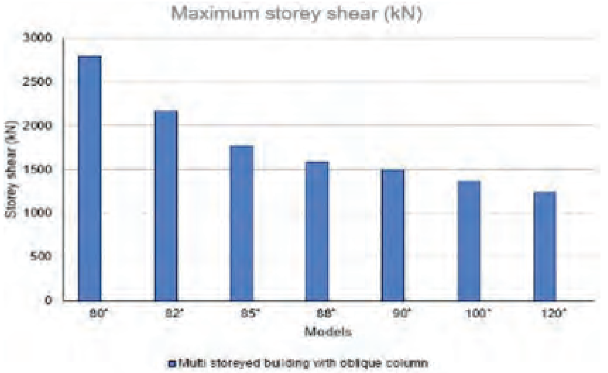

Fig. 12 Maximum storey shear

Compared to structure with conventional columns and structures with oblique columns lesser than 90°, increase in shear is shown for structures with oblique columns at angles greater than 90°

CONCLUSIONS

Based on the findings, the parameters like maximum storey displacement, maximum storey drift and maximum storey shear were analyzed, and the following conclusions were made: -

- Structures with oblique columns show lesser displacement compared to structures with conventional columns. Structures with oblique columns at 80° have shown lesser displacement compared to structures with conventional columns and with columns higher than go0.Structures with oblique columns show less drift compared to structures with vertical columns. Structures with oblique columns at 80° have shown lesser drift compared to structures with conventional columns and with columns higher than go0• Structures with oblique columns show an increase in shear.

Structures with oblique columns at 80° have shown improved shear compared to structures with conventional columns and with columns higher than go0•

- Structures with oblique columns at 80° show 55.7% lesser displacement compared to structures with oblique columns at 120° and 43.03% lesser displacement com- pared to oblique columns at go0•
- Structures with oblique columns at 80° show 37.81% lesser drift compared to structures with oblique columns at 120° and 27% lesser drift compared to oblique columns at go0•
- Structures with oblique columns at 80° show 55.74% increase in shear compared to structures with oblique columns at 120° and 46.5% increase compared to oblique columns at go0•

The structure incorporated with an oblique column is found to show better seismic performance compared to structure with conventional column. As a result, the structure becomes stronger and more resilient, better able to endure the effects of earthquakes and safeguard people and property.

REFERENCES

1. Geethu Krishna K V and Lekshmi L, “Study on Seismic Performance of Multistoried building with Oblique Columns”, International Journal of Applied Engineering Research, Vol. 14, pp. 186-190, 2019
2. Girish Kumar G.M and S M Maheswarappa, “Seismic Performance Study of Multistoried Buildings with Oblique Columns by using ETABS”, International Journal of Engineer- ing Research and Advanced Technology, Vol. 4, pp. 15-20, 2018
3. Kai Hu, Yimeng Yang, Suifeng Mu, Ge Qu, “Study on High rise Structure with Oblique Columns by ETABS, SAP2000, MIDAS/GEN and SATWE”, Elsevier, pp. 474 480, 2012
4. Kona Narayana Reddy and Dr.E.Arunakanthi, “Study on Multi-Storeyed Building with Oblique Columns by using ETABS”, International Journal of Innovative Research in Science Engineering and Technology, Vol. 6, pp.1968 1974, 2017
5. Navaneeth Krishna and Abhishek C V, “Seismic Behaviour of Multi Storied Building with Oblique Column and its Height Optimization”, International Research Journal of Engineering and Technology, Vol. 2, pp.2579 2585, 2020
6. Nikha Santhosh and Gayathri Krishna Kumar., 2021. Seismic Performance of Oblique Columns in High Rise Building. In Proceedings of SECON 2020: Structural Engineering and Construction Management 4 (pp. 131-139). Springer International Publishing.
7. Rohan Singh and Vikas Prabhakar., Study of Multistoried Buildings with Oblique Columns.
8. Spoorthi L, and Naveen Kumar S., 2023. Seismic Performance of Multi-Story Buildings with Oblique Columns of Different Shapes.
9. Vivek Narayanan and Aiswarya S, “Effect of Oblique Column and Viscous Damper on Podium Structure using ETABS”, International Research Journal of Engineering and Technology, Vol. 4, pp. 1899-1903, 2017
10. Vimlesh V. Agrawal and Jawid Ahmad T, “Effect of Column Size, Shape and Orientation on Seismic Performance of RC Building”, Journal of Emerging Technologies and Innovative Research, Vol. 6, pp. 33-38, 2019.

Pushover Analysis of Structures with Concentric Steel Braced Frames having Various Aspect Ratios

Shabna Shirin K
PG Scholar
Department of Civil Engineering
NSS College of Engineering
Palakkad, Kerala
✉ shirinshabna435@gmail.com

Arya B
Assistant Professor
Department of Civil Engineering
NSS College of Engineering
Palakkad, Kerala
✉ aryazarya68@gmail.com

ABSTRACT

In earthquake prone areas, lateral loads on structure are considered in addition to the gravity load. Braced frames are the structural members that is used to resist the lateral load rendering on the structure. Also, the braced frames are used to improve the energy dissipation capability of steel frames to overcome seismic forces. This study delves into the impact of varying aspect ratios (H/B ratio), where H shows the building frames total height and B denotes the base width, on the seismic resilience of steel frame structures. The study explores seven various aspect ratios, differing from 1.5 to 6, across buildings with varying heights while maintaining a constant base width. Nonlinear static pushover analyses are conducted to evaluate how different bracing systems perform in high- rise steel buildings differing from 10 to 40 stories in height with five structural configurations: moment resisting frames, chevron, V, X and zipper braced frames. SAP2000 software is used for the analysis. The study investigates the influence of some parameters like type of the bracing system, building height and lateral load pattern. The structural performance of bare frame and braced frame with different aspect ratio is assessed by using the parameters like base shear and roof displacement. The results show that the aspect ratio increases then the roof displacement and base shear is increased. And the different braced frames perform well relating to of roof displacement and base shear when compared to moment resisting frames in high rise steel buildings. It can be finalized that, ZBF, VBF and CBF for all aspect ratios has higher seismic performance than moment resisting frames and it has enhanced the structural performance in high rise steel structures.

KEYWORDS: *Aspect ratio, X-braced frame (XBF), V-braced frame (VBF), Chevron braced frame (CBF), Zipper braced frame (ZBF), Base shear, Roof displacement.*

INTRODUCTION

The buildings are subjected to unique structural demands in earthquake prone regions. Aside from bearing the primary vertical gravity loads these structures must also undergo lateral loads due to external forces like earthquakes and wind. For high- rise buildings in these regions, stiffness plays an important factor than strength, as a result it helps to maintain stability and reduces sway during seismic events. Here, the selection of structural systems, which includes moment resistant frames (MRFs) and braced frames, is essential for ensure the stability and safety of a structure.

Moment resistant frames (MRFs) and braced frames are two common structural designs that oppose lateral stresses in steel buildings. Moment- resisting frames shows ductility by absorbing energy during earthquakes by providing controlled yielding. This ductility gives MRFs a certain level of safety by allowing them to yield without quickly failing during intense earthquake activity. Sometimes, the flexibility of MRF also be a demerit because they don’t always accomplish the stiffness standards required for tall buildings in seismic regions. On the contrary, braced frames employ vertical or diagonal bracing to effectively transfer lateral loads to the foundation, they are known for their notable stiffness. Their ductility is more constrained when compared to MRFs. There is variousness of braced frames, each with distinctive configurations that affect how the frame behaves during seismic activity.

Concentric braced frames (CBFs) are rigorous and stable structures construct of braces that cross at a single node. The concentric braced frame is shown in Fig 1. Even though it provides less ductility than eccentric braced frames (EBFs), which traits eccentricity or a gap between the frames and the braces, this structure is efficient at tolerating lateral loads. The eccentric braced frame is shown in Fig 2. The ductility of the structure is boosted by this eccentricity, which grants increased energy dissipation. Furtherly, there are wide variety of structural configurations for braced frames, each with an ideal geometric model. By producing a “X” shape, the X-braced frame (XBF) properly divided lateral forces. The V-braced frame (VBF) has “V”-shaped and the similar-twinning chevron braced frame (CBF) have braces facing downward. The zipper braced frame (ZBF) improves energy distribution during seismic activity by connecting multiple stories with a “zipper-like” bracing mechanism. To judge the seismic interpretation of structures with concentric steel braced frames with different aspect ratios, nonlinear static pushover analysis is utilized. In non- linear static pushover analysis, the seismic behaviour of structures with concentric steel braced frames and different aspect ratios is investigated. A buildings height-to-width ratio (H/B) that is the aspect ratio can have a vast effect on how stable it is during seismic activity. Pushover analysis can provide valuable insights into how these structures react to seismic challenges in order to make wise judgments about reinforcement, general safety and design in seismically active zones.

Fig. 1. Concentric braced frame

Fig. 2. Eccentric braced frame

BACKGROUND SUMMARY

The seismic behavior and structural performance of reinforced concrete (RC) and commercial steel buildings are significantly enhanced by incorporating bracing systems. Using software tools such as STAAD Pro, SAP2000, and ETABS, key parameters including base shear, inter-storey drift, spectral acceleration, and time period have been evaluated. Bracing systems, like X, V, inverted V, and Chevron configurations, are critical in providing lateral stability and improving earthquake resistance.

Braced structures exhibit superior seismic performance compared to unbraced ones, with notable improvements in base shear, inter-storey drift, and overall structural integrity. Different bracing patterns demonstrate significant benefits in maintaining structural stability during earthquakes. Static pushover and nonlinear time-history analyses reveal the positive effects of these bracing systems, focusing on capacity curves, drift ratios, and displacements.

In high-rise steel buildings, bracing systems like concentric, V, and Z-braced frames outperform moment-resisting frames in terms of seismic performance. These bracing configurations improve base shear, performance point, inter-storey drift ratio, and storey displacement. For mid-rise structures, Chevron braced frames provide good seismic performance than suspended-zipper braced frames, although both perform similarly in low-rise buildings.

Strengthening existing RC frame buildings with steel braces through seismic retrofitting is identified as a highly effective strategy for enhancing earthquake resilience. Bracing systems significantly boost in-plane shear strength and lateral resistance, crucial for maintaining structural stability against both seismic and wind forces. The research highlights the importance of bracing in improving the deformation capacity and ductility of buildings, ensuring they can undergo significant deformation without collapsing. Overall, the critical role of bracing systems in enhancing the safety and resilience of buildings in seismically active regions is underscored, with braced steel buildings providing better lateral stability and seismic resistance compared to unbraced structures.

MODELLING OF STRUCTURE

In this study, the concentric steel frames with different aspect ratios such as 1.5, 2.25, 3, 3.75, 4.5, 5.25 and 6 and structural configurations like MRF, XBF, VBF, CBF and ZBF are modelled using SAP200 software. The fig 1. shows the structural plan of building.

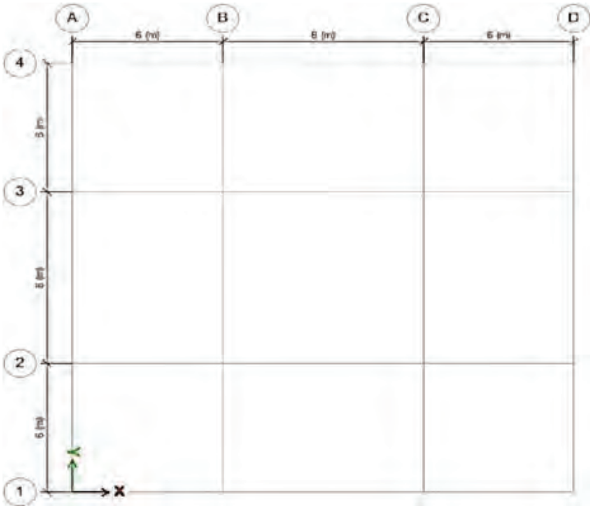

Fig. 3. Structural plan of the building

The load on the frames were determined using IS 875 part 1, part 2. The analysis and modelling of frames are done by using SAP2000 software. The aspect ratio of different height of buildings and steel sections of all frames are given in Table 1 and 2 respectively.

The fig 4 represents the concentric steel frames with aspect ratio 1.5 and structural configurations are MRF, XBF, CBF and ZBF.

Table 1. Aspect ratio for different height of building

Height of the building (m)	Base width(m)	Aspect ratio(H/B)
30	20	1.5
45	20	2.25
60	20	3
75	20	3.75
90	20	4.5
105	20	5.25
120	20	6

Table 2. Steel sections for all frames

Aspect Ratio	Column section	Beam section	Bracing section
1.5	ISHB200	ISMB350	ISLB300
2.25	ISHB250	ISMB350	ISLB300
3	ISHB300	ISMB450	ISLB300
3.75	ISHB350	ISMB500	ISLB300
4.5	ISHB400	ISMB550	ISLB300
5.25	ISHB450	ISMB600	ISLB300
6	ISHB450	ISMB600	ISLB300

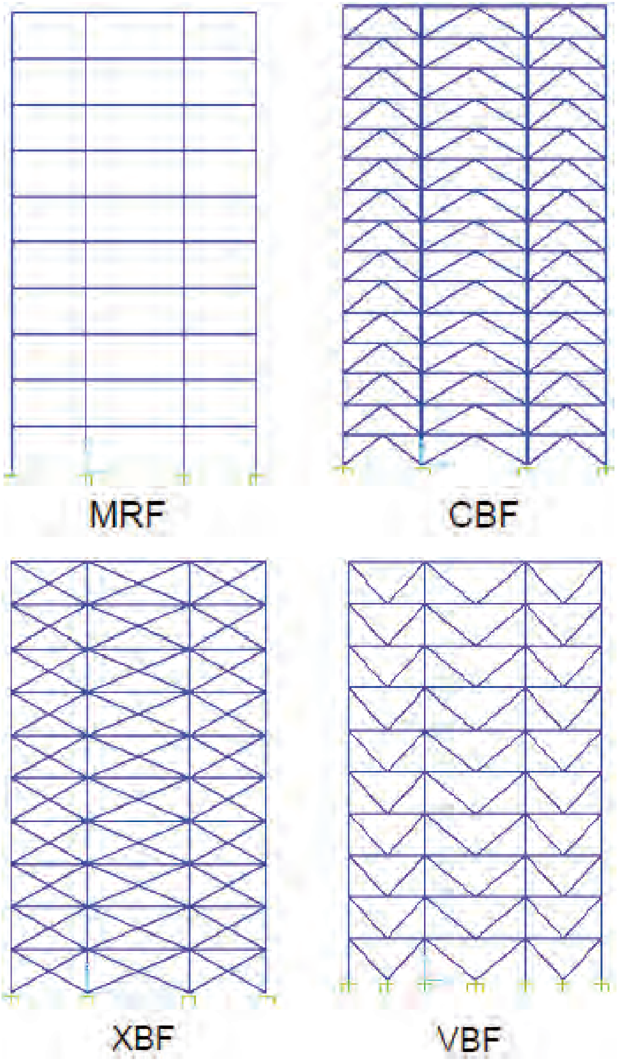

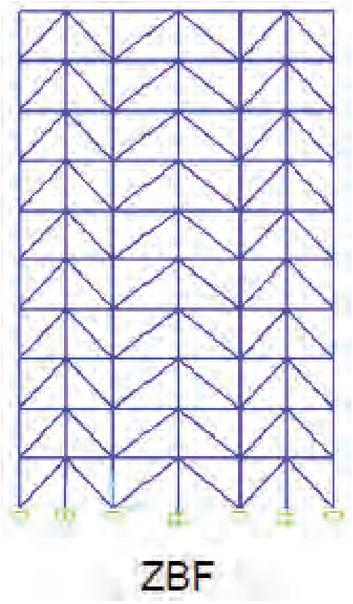

Fig 4. Frames for aspect ratio 1.5

CONCLUSIONS

In this investigation the seismic analysis of buildings with different aspect ratios which are modelled using SAP2000 software. The study mainly determines the structural behaviour of building with concentric steel frame under seismic forces. By properly analyzing the models in SAP2000 software, how different structural configurations including MRF, XBF, VBF, CBF and ZBF respond to seismic events are studied. This analysis provides very valuable details regarding roof displacement and base shear in these modelled structures. While linear elastic analysis can be used to find the structure's elastic capacity and determine the location of the first yielding, it is not able to predict failure mechanisms or take into account the forces that are redistributed as a result of progressive yielding. Among the various methods covered in ATC-40, nonlinear static pushover analysis is especially introduced due to its convenient.

As well as force-controlled pushover analysis is the name used for the analysis when the lateral forces are mandatory. The greatest displacement or maximum force that the structure is predicted to be suitable to withstand during the design earthquake is represented by the target displacement or target force, which is projected. The only way to bend a structure beyond its maximum strength is through displacement-controlled pushover analysis. Therefore, the displacement-controlled pushover method is employed in this work to analyze the structural steel frames. This analysis yields a map of a buildings total base shear v/s top roof displacement, which would identify any failure or weakness. The analysis is performed up till failure, allowing for the purposes of ductility capacity and collapse load. Pushover analysis is a static, nonlinear process where a predetermined pattern is followed to gradually raise the structural loading magnitude. It is also called displacement-controlled pushover analysis if the building moves laterally, and the forces are identified by the equilibrium of the structure. This analysis is limited to identifying the initial local mechanism that forms during an earthquake.

Max. Base Shear and Roof Displacement

The maximum base shear and roof displacement for various aspect ratio corresponding to each structural configuration are shown in Table 3. Additionally, the results are visually depicted through bar charts as shown in Figure 5 and 6.

Aspect Ratio	Frames	Max. Roof Displacement (m)	Max. Base Shear (KN)
1.5	MRF	0.3405	89.736
	XBF	0.214	1029.15
	CBF	0.072	1143.828
	VBF	0.1112	1143.538
	ZBF	0.0578	1187.842
2.25	MRF	0.36	105.298
	XBF	0.3214	1064.89
	CBF	0.1023	1188.965
	VBF	0.1632	1178.562
	ZBF	0.097	1263.601
3	MRF	0.506	227.063
	XBF	0.4132	1264.8
	CBF	0.2351	1358.7
	VBF	0.2276	1304.12
	ZBF	0.1834	1574.992
3.75	MRF	0.646	291.138
	XBF	0.424	1411.54

3.75	CBF	0.418	1424.48
	VBF	0.356	1419.633
	ZBF	0.271	1577.378
4.5	MRF	0.747	665.376
	XBF	0.482	1532.5
	CBF	0.3081	1659.29
	VBF	0.426	1604.37
	ZBF	0.3592	1637.342
5.25	MRF	1.71	872.38
	XBF	0.547	1415.14
	CBF	0.394	1575.404
	VBF	0.432	1605.011
	ZBF	0.365	1687.16
6	MRF	1.738	1121.12
	XBF	0.6134	1528.5
	CBF	0.529	1622.455
	VBF	0.576	1702.191
	ZBF	0.493	1752.342

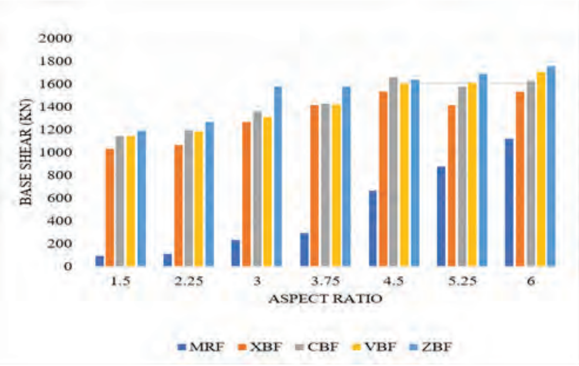

Fig 5. Bar chart representing base shear for different aspect ratios

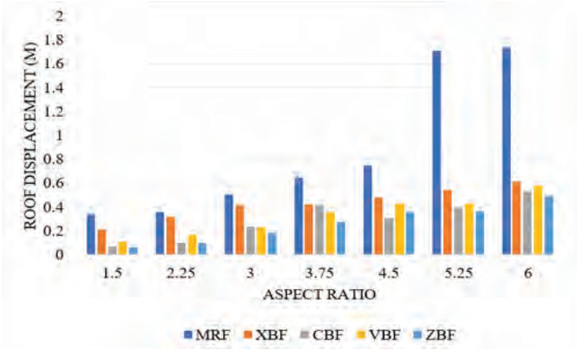

Fig 6. Bar chart representing roof displacement for different aspect ratios

For aspect ratio 1.5, the MRF have 43%, XBF have27%, CBF have 9%, VBF have 14% and ZBF have 7% roof displacement is occurred. Similarly, the MRF have 2%, XBF have 22%, CBF have 25%, VBF have 25% and ZBF have 26% base shear is occurred.

For aspect ratio 2.25, the MRF have 34%, XBF have 31%, CBF have 10%, VBF have 16% and ZBF have9% roof displacement is occurred. Similarly, the MRF have 2%, XBF have 22%, CBF have 25%, VBF have 25% and ZBF have 26% base shear is occurred.

For aspect ratio 3, the MRF have 32%, XBF have 26%, CBF have 15%, VBF have 15% and ZBF have 12% roof displacement is occurred. Similarly, the MRF have 4%, XBF have 22%, CBF have 24%, VBF have 23% and ZBF have 27% base shear is occurred.

For aspect ratio 3.75, the MRF have 30%, XBF have 23%, CBF have 23%, VBF have 17% and ZBF have 13% roof displacement is occurred. Similarly, the MRF have 5%, XBF have 23%, CBF have 23%, VBF have 23% and ZBF have 26% base shear is occurred.

For aspect ratio 4.5, the MRF have 32%, XBF have 22%, CBF have 23%, VBF have 23% and ZBF have 23% roof displacement is occurred. Similarly, the MRF have 9%, XBF have 22%, CBF have 23%, VBF have 23% and ZBF have 23% base shear is occurred.

For aspect ratio 5.25, the MRF have 50%, XBF have 16%, CBF have 11%, VBF have 12% and ZBF have 11% roof displacement is occurred. Similarly, the MRF have 12%, XBF have 20%, CBF have 22%,VBF have 22% and ZBF have 24% base shear is occurred.

For aspect ratio 6, the MRF have 44%, XBF have20%, CBF have 21%, VBF have 22% and ZBF have 23% roof displacement is occurred. Similarly, the MRF have 14%, XBF have 20%, CBF have 21%, VBF have 22% and ZBF have 23% base shear is occurred.

CONCLUSIONS

- Taller buildings with higher aspect ratios are prone to experiencing higher base shears and greater roof displacements under lateral loads. This is primarily attributed to their increased vulnerability to lateral forces due to larger masses, leading to greater overturning moments and their greater flexibility compared to shorter buildings.

- MRF buildings show higher roof displacement representing that MRF buildings are more resilient than other buildings with bracings, so liable to extreme harm in seismic events.
- Seismic activity of CBF and VBF is nearly identical as regards of base shear and roof displacement for all aspect ratios.
- Similarly, ZBF gives higher base shear and minimum roof displacement than other systems.
- ZBF, VBF and CBF have large seismic activity referring to various seismic parameters like base shear and roof displacement than XBF and MRF. In other way, due to their greater stiffness, CBFs, VBFs, and ZBFs may continue less overall structural damage but larger base shear forces.

REFERENCES

1. Ahiwale, D.D., Kontoni, D.N. and Darekar, P.L. (2023). "Seismic performance assessment of reinforced concrete frames with different bracing system". Innovative Infrastructure solution, 8,102.
2. ATC-40 seismic evaluation and retrofit ofconcrete buildings. Applied Technical Council; 1996.
3. Kadid, A. and Yahiaoui, D., (2011). "Seismic assessment of braced RC frames". Procedia Engineering, 14, pp.2899-2905.
4. Maheri, M.R. and Sahebi, A. (1997). "Use of steel bracing in reinforced concrete frames". Engineering Structures, 19(12), pp.1018-1024.
5. Nassani, D.E., Hussein, A.K. and Mohammed, A.H. (2017). "Comparative response assessment of steel frames with different bracings systems under seismic effect". Structures, 11, pp.229-242.
6. Nayak, J.B. (2023). "Pushover analysis of two-dimensional steel braced structure with two storey height bracing". Journal of Emerging Technologies and Innovative Research, 10 (7).
7. Ozcelik, Y., Saritas, A. and Clayton, P.M. (2016). "Comparison of chevron and suspended zipper braced steel frames". Journal of Constructional Steel Research, 119, pp.169-175.
8. Patil, D.M. and Sangle, K.K. (2015). "Seismic behaviour of different bracing systems in high rise 2 D steel buildings". Structures, 3, pp.282- 305.
9. Raja, M.V. and Krishna, K.V. (2018). "Pushover analysis of high-rise buildings with and without bracings by using SAP2000". Journal of Emerging Technologies and Innovative Research, 5 (7).
10. Rangaraj, B., Nalinaa, K., Ashokkumar, M., Deepalakshmi, P. and Rishika (2023). "Comparative analysis of unbraced and chevron braced steel buildings of different storeys". Materials Today: Proceedings.
11. Seki, A., Inoue, K., Okazaki, T., Hashioka, S. and Asada H. (2022). "Seismic performance of steel chevron braced frames designed according to Japanese practice". Journal of Constructional Steel Research, 189.

Reinforced Concrete Frames Subjected to Blast Loading

Navya Eliswa
PG Scholar
Department of Civil Engineering
NSS College of Engineering
Palakkad, Kerala
✉ navyaeliswa@gmail.com

Rohini G Nair
Assistant Professor
Department of Civil Engineering
NSS College of Engineering
Palakkad, Kerala
✉ rohinignair@nssce.ac.in

ABSTRACT

Terrorists generally focus on high occupancy buildings in order to insist maximum number of lives and cause extensive damage to the property. Gas-chemical explosions can create large dynamic loads which lay significant strain on structures beyond their original design limits. But most of these structures have been built without considering their vulnerability to such extreme events. Therefore, the vulnerability assessment of buildings under blast loading is important while designing. To construct these structures to withstand blast loading, the impacts of this explosion must be measured. Shear walls are structural elements in buildings which helps to resist sideways movements caused by wind, earthquakes, or explosions. The purpose of the study is analyse and compare the RC frame structures with and without shear walls under blast loading. Using finite element software (ABAQUS) the response of RC framed structures with and without shear walls while keeping blast load at various locations will be analysed. Various parameters such as stresses in concrete, stresses in steel, deflection and compression damage in concrete were determined and compared. The findings revealed that the structures with shear wall offers better blast resistance compared to the structures without shear wall.

KEYWORDS: *RC frame structure, Explosion, Shear wall, ABAQUS software, Blast resistance.*

INTRODUCTION

The number of terrorist strikes is rising daily these days, resulting in both fatalities and property damage. Therefore, it is crucial to take into account how the blast load affects the structures. Buildings and other structures are frequently constructed using reinforced concrete (RC) frames because of its strength, adaptability, and durability. When subjected to blast loading, RC frames may experience significant deformations, stresses, and potential failure modes, depending on factors such as the magnitude and proximity of the blast, the structural configuration, and the material properties. The incorporation of shear walls into RC frames can significantly influence the response of structures to blast loading. Shear walls provide additional stiffness and strength in the lateral direction and thus enhance the overall stability of RC frames, reducing the risk of progressive collapse and minimizing damage during blast events.

The main goal of the study is to analyse the reinforced concrete frame structures with and without shear wall while keeping blast load at various locations. The various parameters such as stresses in concrete, stresses in steel, maximum deflection and compression damage in concrete were analysed in the project. The main goal is to determine whether the incorporation of shear wall induces better resistance to RC structures against blast loading. The analysis of various parameters shows the percentage reduction of damages that occurs on the buildings and provide us better understanding how to improve the structural stability of the buildings. The analysis here done is using ABAQUS /CAE as the software is known for its reliability for modelling complex systems. ABAQUS offers a wide range of analyses, such as linear and non-linear analyses, static and dynamic analyses etc. which is crucial for understanding the structural behaviour under different loading conditions. It can help the engineers to understand a structures' problems and vulnerability and provide proper enhancing structures.

BACKGROUND SUMMARY

Increasing the member capacities, utilizing dispersed shear walls, and strategic placement of shear walls can enhance structural resilience against blast events. The stand-off distance and location of blast had a greater influence in the prevention of structural failure. Increasing the standoff distance allows the blast wave to dissipate energy before reaching the structure. This reduces the peak pressure and impulse experienced by the building, minimizing the risk of structural deformation, cracking, or collapse. Depending on the blast location, critical structural components such as columns, walls, and floor slabs may experience varying levels of loading and stress.

Sevim et al. highlighted the varying degrees of structural response and damage under different blast loads, emphasizing the importance of understanding blast effects for designing resilient structures. Kasilingam et al. highlighted the importance of blast location, standoff distance, and structural configuration in determining the response of reinforced concrete structures to blast loads. For simulations, ABAQUS/CAE was used to develop concrete damage plasticity model that incorporates inelastic behaviour of concrete. The Johnson-Cook model simulated the elastic and plastic behaviour of the steel reinforcement while accounting for the impacts of temperature, strain rate, and stress state. To evaluate the building's resistance, simulations looked at changes in standoff distance, TNT mass, blast origin locations, and roof slab thickness. The analysis of structural responses included consideration of deflection, impulsive velocity, von-Mises stresses, and damage to concrete under tension and compression. Notably, the study demonstrated the critical role that blast-resistant design considerations have in structural engineering by highlighting the substantial impact that standoff distance has on the durability of the reinforced concrete slab and wall. Kumar et al. provided insights into the behaviour of building frames under different blast loads and highlighted the importance of understanding blast effects on structural integrity for mitigating progressive collapse risks. The study uses ConWep blast load method to evaluate the RC framed structures under different blast loads. The findings reveal a critical gap in current building codes, which lack sufficient design considerations to mitigate blast impacts, especially in iconic structures often targeted by terrorist attacks.

MODELLING OF STRUCTURE

A 3-storied Reinforced Concrete framed structure with and without shear wall is used for the analysis. The analysis was performed using ABAQUS/CAE. The RC framed structure is a three storied building with 3m height for each storey and a TNT of 20 kg is applied as surface blast keeping TNT at various locations in buildings. The structural details are given in Table 1: -

Table 1 Structural Properties

Parameters	Values
Slab Thickness	100mm
Beam	250mmx500mm
Internal and external column	250mmx250mm
Main reinforcement for columns	4 bar, 16mm dia
Main reinforcement for beams	3 bar, 16mm dia
Secondary reinforcement for beam	2 bar, 12mm dia
Stirrups for beam and column	8mmdia,200mmc/c
Slab Reinforcement on both directions	10mmdia,200mmc/c
Shear wall Reinforcement on both directions	10mmdia,150mmc/c

Material Properties

The properties in the present study are adopted from study carried by K. Senthil et al. in 2018

i. Concrete Damage Plasticity (CDP) model

CDP incorporates plastic nature of concrete into finite element simulation and provides a broad spectrum of modelling possibilities. The plastic damage variable 'K' in the plasticity theory is non-dimensional and ranges from 0 to 1. The value of 'K' increases if plastic deformation takes place and when it reaches a maximum value representing total damage, it can be interpreted as formation of macroscopic crack. The compression and tension damage variables for CDP model are shown in tables 2 and 3. The yield stress is the point where the material shows transition from elastic behaviour to plastic behaviour. The compression and tension damage variables are represented as dc and dt respectively. The inelastic strain is the permanent deformation that occurs in the material beyond elastic limit. The cracking strain is the point where the material begins to exhibit visible cracking or failure under applied load. The concrete damage plasticity model values for concrete are shown in table 4.

Table 2 Compression Damage Variables for CDP Model

Yield stress (MPa)	Inelastic strain	Damage parameter (dc)
20	0	0
15	0.0011	0.2
12	0.004	0.24

Table 3 Tension Damage Variables for CDP Model

Yield stress (MPa)	Cracking strain	Damage parameter(dt)
3.3	0	0
3.2	0.003	0.15
3.1	0.005	0.21
3.0	0.007	0.28
2.95	0.01	0.30

Table 4 Concrete Damage Plasticity Model Values for Concrete

Elastic Modulus (GPa)	24
Dilation angle	30
Flow potential eccentricity	1
Viscosity parameter	0.1
Bulk modulus	0.666
fb_o/fc_o	1.16

Jhonson cook model for reinforcement bars

The J.cook elastic-viscoelastic material model used for this study includes the effects of linear thermo-elasticity, yielding, plastic flow, isotropic strain hardening, strain rate hardening, softening due to damage and adiabatic heating. The von-Mises yield criterion and related flow rules served as a framework for the material model. The ultimate tensile strength of the steel was taken as 250 MPa for the model. The table 5 shows values of steel bars for J.cook damage model. Strain hardening constant (n) is used in plasticity model to describe material resistance to plastic deformation after yielding. Viscous effect (C) represents influence of strain rate on materials plastic response. Thermal softening constant (m) represents the softening behaviour of material's influence of temperature on materials strength and stiffness. Reference strain rate represents the reference point for defining the material's rate dependent behaviour and also used to calibrate the model.

Table 5 Values of steel bar for damage model

Modulus of elasticity (N/mm^2)	203000
Poisson's ratio	0.33
Density (kg/m^3)	7850
Yield stress constant (N/mm^2)	
A	304.330
B	422.007
Strain hardening constant, n	0.345
Viscous effect, C	0.0156
Thermal softening, m	0.87
Reference strain rate	0.0001
Melting temperature, K	1800
Transition temperature, K	293
Fraction strain constants	
D1	0.1152
D2	1.0116
D3	-1.7684
D4	-0.05279
D5	0.5262

Finite Element Modelling of RC Frame Structure

Reinforced Concrete Framed Structure Without Shear Wall

In a RC framed structure without shear walls, beams distribute the loads horizontally, dispersing them to the columns and finally to the foundation, while the columns support the vertical loads. In order to preserve structural integrity and stability under a range of stress scenarios, design concerns include making sure that the vertical and horizontal parts have enough stiffness and strength.

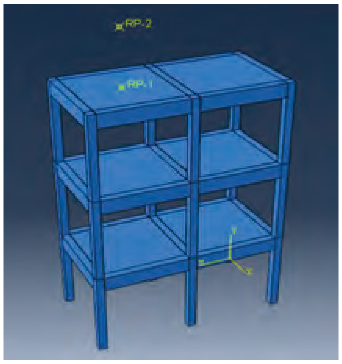

Fig. 1 RC frame with blast load at 2m from the top of the building

Concrete's geometry was represented as a solid deformed body, whereas steel reinforcement's geometry was modelled as a wire deformable body. The constraint embedded region option was used to model the interaction between steel and concrete. The steel was chosen as the embedded region and the concrete as the host region. The blast origin was maintained two meters from the slab above the building, side of the building and inside the building. The interaction module was used to define the blast load. The program's CONWEP definition was used to create the blast load, and two reference points that were assigned depending on the standoff distance from the point of response were used to determine the surface blast. The RC frame structure with blast load kept 2m above the building, reinforcement detailing of RC frame, RC frame with boundary condition, RC frame showing interaction between different structural components, meshing of the building model and RC frame with blast load at various locations are depicted in the figure. 1, 2,3,4,5 and 6 respectively.

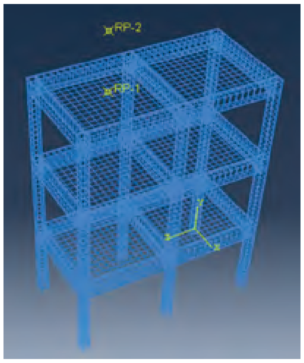

Fig. 2 Reinforcement Detailing of a RC frame

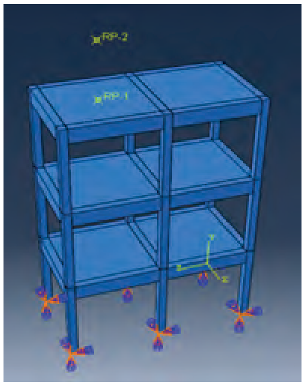

Fig. 3 RC frame with fixed boundary condition at column ends

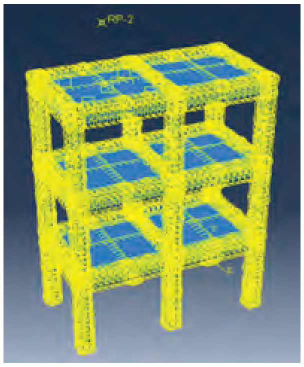

Fig. 4. RC frame showing interaction between different structural elements

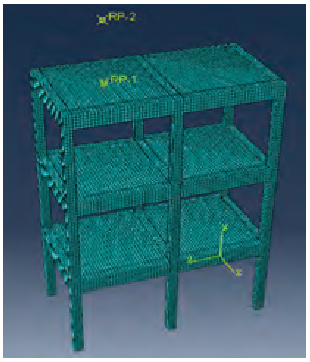

Fig 5 RC frame meshed with 100mm size

Reinforced Concrete framed structure with shear wall

A Reinforced Concrete framed structure incorporated with shear wall improve the overall strength as well as stability of the structure. Shear walls are positioned strategically throughout the building to withstand lateral forces like wind or seismic loads. They are usually made of reinforced concrete or masonry and the structure becomes more rigid and resistant to horizontal movements when shear walls are incorporated into the frame system. In this study, shear wall is incorporated at the centre of the building which helps to distribute the loads uniformly. The incorporation of shear wall helps to reduce the effect of blast load on the structure especially damages to the columns. As shear wall takes the load and distribute the same efficiently, incorporation of shear wall is vital for blast resistant structures. The figure below (fig 7) shows the RC frame with shear wall and blast load kept at 2m from top of the building. The blast load is provided using surface blast option with the help of reference points. The reinforcement detailing of the RC frame with shear wall, RC frame with fixed boundary conditions, RC frame with shear wall showing interaction between different structural components, meshing of RC frame with shear wall and the RC frame with shear wall keeping blast load at various locations are shown in figure 7,8,9,10,11& 12respectively.

Fig. 7 RC frame with shear wall and frame with shear wall

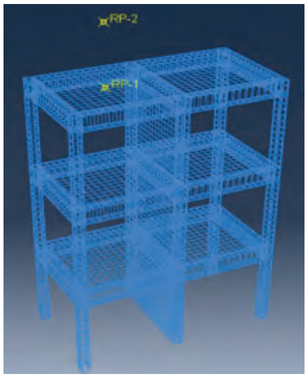

Fig 8 Reinforcement Detailing of a RC blast load at 2m from the top of the building

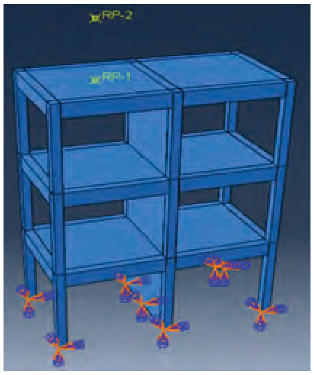

Fig. 9 RC frame with shear wall and fixed boundary condition at ends of column and shear wall.

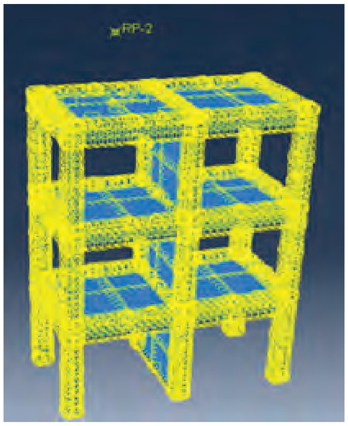

Fig 10 RC frame with shear wall showing interaction between different structural elements

Fig 11 RC frame with shear walls meshed with 100mm si ze

RESULTS AND DISCUSSIONS

The results obtained from the analysis of Reinforced Concrete frames subjected to blast loading with and without shear wall are tabulated. The comparison between the stresses in concrete, stresses in steel, deflection and compression damage while keeping blast at various locations of building were tabulated and represented graphically using bar chart.

Maximum Stresses in Concrete

In the case of three storied framed structure with and without shear wall, whether the blast kept at top of the building, front of the building or inside of the building, buildings with shear wall shows less stresses in concrete compared to buildings without shear wall shown in figure 13.

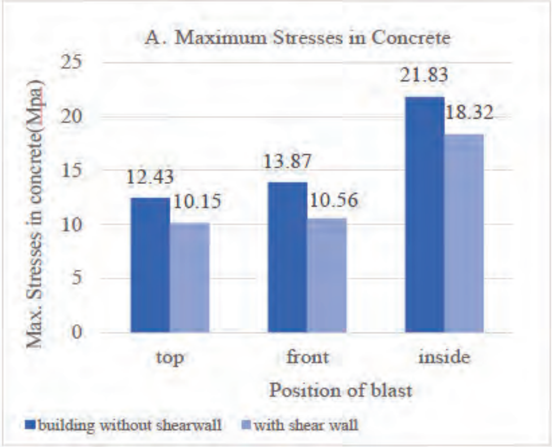

Fig. 13. Comparison of maximum stresses in concrete with and without shear wall

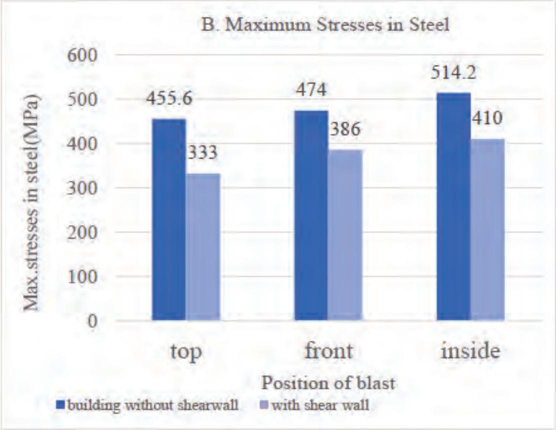

Fig. 14. Comparison of maximum stresses in steel with and without shear wall

Maximum Stresses in Steel

In the case of three storied framed structure with and without shear wall, whether the blast kept at top of the building, front of the building or inside of the building, buildings with shear wall shows less stresses in steel compared to buildings without shear wall as shown in figure 14.

Maximum Deflection

In the case of three storied framed structure with and without shear wall, whether the blast kept at top of the building, front of the building or inside of the building, buildings with shear wall shows less deflection compared to buildings without shear wall as shown in figure 15.

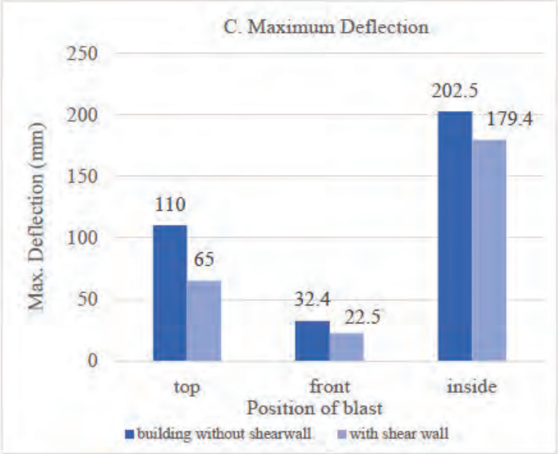

Fig. 15. Comparison of maximum deflection with and without shear wall

Compression Damage

In the case of three storied framed structure with and without shear wall, whether the blast kept at top of the building, front of the building or inside of the building, buildings with shear wall shows less compression damage compared to buildings without shear wall as shown in figure 16.

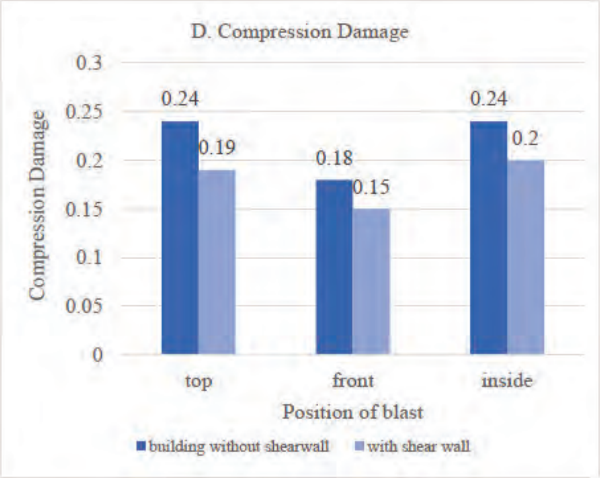

Fig. 16. Comparison of compression damage with and without shear wall

CONCLUSIONS

The comprehensive analysis is conducted on RC framed structure with and without shear wall under blast loading under various blast locations. The study aimed to evaluate the maximum stresses in concrete, steel, maximum deflection and compression damage in the buildings with and without shear wall under various blast locations. The results showed that the building with shear wall offers better resistance to blast loading compared to building without shear wall. The conclusions drawn from the study is as follows: -

- RC framed structures with shear wall offers less stresses in concrete approximately 20% compared to RC framed structure without shear wall, thus reducing the extent of localized damage in the structures.
- The maximum stresses in steel are also reduced by approximately 22% by the incorporation of shear wall into the structure compared to building without shear wall, which also reduces the extent of damages in the structures.
- Maximum deflection occurs in the building is also less compared to building without shear wall, which increases stability of the building's structure.
- Severity of compression damage is more in buildings without shear wall compared to buildings with shear wall.

REFERENCES

1. Chehab, A. I., Eamon, C. D., & Griffin, J. (2017). Collapse resistance of RC Moment-Resisting frame and shear wall structural systems exposed to blast. Journal of Performance of Constructed Facilities, 31(2). https://doi.org/10.1061/(asce)cf.1943-5509.0000957
2. Hao, H., Hao, Y., Li, J., & Chen, W. (2016). Review of the current practices in blast-resistant analysis and design of concrete structures. Advances in Structural Engineering, 19(8), 1193–1223. https://doi.org/10.1177/1369433216656430
3. Ibrahim, Y. E., Ismail, M., & Nabil, M. (2017). Response of Reinforced Concrete Frame Structures under Blast Loading. Procedia Engineering, 171, 890–898. https://doi.org/10.1016/j.proeng.2017.01.384
4. Kumar, D. S., Rai, P., Kumar, R., Karmakar, S., & Saha, S. (2016). Behaviour of reinforced concrete building frame subjected to different types of blast loading. Indian Journal of Science and Technology, 9(23). https://doi.org/10.17485/ijst/2016/v9i23/95966
5. Sevim, B., & Toy, A. T. (2019). Blasting response of a Two-Storey RC building under different charge weight of TNT explosives. Iranian Journal of Science and Technology, Transactions of Civil Engineering, 44(2), 565–577. https://doi.org/10.1007/s40996-019-00256-0
6. Senthil, K., Rupali, S., & Kaur, N. (2018). The Performance of Monolithic Reinforced Concrete Structure Includes Slab, Beam and Column against Blast Load. Journal of Materials and Engineering Structures « JMES », 5(2), 137–151. http://revue.ummto.dz/index.php/JMES/article/view/1722
7. Syed, Z. I., Mohamed, O. A., Murad, K., & Kewalramani, M. (2017). Performance of Earthquake-resistant RCC Frame Structures under Blast Explosions. Procedia Engineering, 180, 82–90. https://doi.org/10.1016/j.proeng.2017.04.167
8. Shi, Y., Li, Z., & Hao, H. (2010). A new method for progressive collapse analysis of RC frames under blast loading. Engineering Structures, 32(6), 1691–1703. https://doi.org/10.1016/j.engstruct.2010.02.017
9. Talaat, M., Yehia, E., Mazek, S. A., Genidi, M. M., & Sherif, A. G. (2022). Finite element analysis of RC buildings subjected to blast loading. Ain Shams Engineering Journal, 13(4), https://doi.org/10.1016/j.asej.2021.101689
10. Xiao, L., Qu, W. Z., & Wang, J. G. (2012). Experimental and numerical studies on the reinforced concrete frames subjected to blast loads. Applied Mechanics and Materials, 157–158, 1173–1177. https://doi.org/10.4028/www.scientific.net/amm.157-158.1173

Influence of Rotational Components of Earthquake on Seismic Performance of Tall Steel Buildings

Jeena S
PG Scholar
Department of Civil Engineering
NSS College of Engineering
Palakkad, Kerala
✉ jeenasanthakumar2000@gmail.com

Nisha A S
Assistant Professor
Department of Civil Engineering
NSS College of Engineering
Palakkad, Kerala
✉ asnisha@nssce.ac.in

ABSTRACT

Earthquake is one of the major natural disasters. Earthquake comprises of 6 components; 3 translation components and 3 rotational components. The translational components are effortlessly measurable; hence, these accelerometers are installed in almost every seismic-prone region. One of the most notable points is that the earthquakes' rotation components are not considered in seismic analysis and design. Maybe because of this reason, only in a few regions, the rotation sensors are installed in seismic-prone regions. In this study, a 20-storey-steel (Tall building) structure is subjected to 30 unique combinations of 6 components of the earthquake, which has its unique combination, employed by linear time history analysis. The findings offer valuable insights into the complex interactions between rotational and translational dynamics in high-rise structures. The maximum structural responses of the steel structure are shown by the 6-component earthquake.

KEYWORDS: *Seismic performance, Tall buildings, Steel structure.*

INTRODUCTION

Earthquake ground motions include both translational and rotational components, though the latter are often overlooked due to their lower amplitudes and the difficulty in measuring them. Despite this, rotational motions can have a significant impact on structural behavior, influenced by factors such as the mode of excitation, building height, number of stories, aspect ratio, mass eccentricity, and slenderness. Studies indicate that impulsive and surface wave translational motions produce the most substantial structural responses, with deformation increasing alongside column height and grid thickness. When rotational components are included, deformations can be significantly amplified—rotational displacements may even double compared to translational effects alone. Soil-structure interaction under rotational ground motion further intensifies structural responses, particularly in mid- rise buildings, with power amplification reaching up to 90%. Neglecting the multidimensional and non- uniform nature of seismic inputs can lead to underestimations in large-span spatial structures, where non-uniformity contributes more to response increases. Near-fault rotational effects can raise drift ratios by as much as 15%, accelerating lateral displacements and floor accelerations in lower stories, which affects both occupant comfort and structural design. Dual systems combining moment frames with bracing outperform moment frames alone in resisting progressive collapse, although rotational effects can hasten hinge formation and increase demand. Accounting for rotational motions results in structural responses that are 1.1 to 1.6 times higher in terms of displacement, acceleration, and base shear, and 1.3 to 1.85 times greater for internal forces. In arch dams, rotations significantly elevate tensile and compressive stresses and crest displacements, with effects depending on reservoir conditions and excitation types. Rotational ground motions can increase total acceleration and displacement by up to 35%, depending on the structure's natural period and the characteristics of the seismic event. Rocking excitations contribute more to story shear as the number of stories increases, and structures with higher aspect ratios and mass eccentricities experience more pronounced rotational effects—for instance, base shear and roof acceleration can rise by over 70% and 250%, respectively. This study highlights the critical role of rotational components in seismic analysis of multi-story steel buildings. Using ETABS, 30 distinct structural models were analyzed through linear time history simulations to assess the influence of rotational motions across various earthquake scenarios.

CHARACTERISTICS OF ROTATIONAL COMPONENTS

Earthquakes produce six types of ground motion—three translational and three rotational (including two rocking and one torsional)—originating from seismic waves such as Love, Rayleigh, and primary waves. Although rotational motions can greatly affect critical structures like tall buildings, bridges, dams, and nuclear facilities, they are frequently overlooked due to limitations in traditional measurement tools and the absence of code requirements. For a comprehensive seismic evaluation, it is essential to incorporate rotational acceleration spectra and all six motion components in response history analyses to accurately capture the full impact of earthquakes on structural performance [Figure 1].

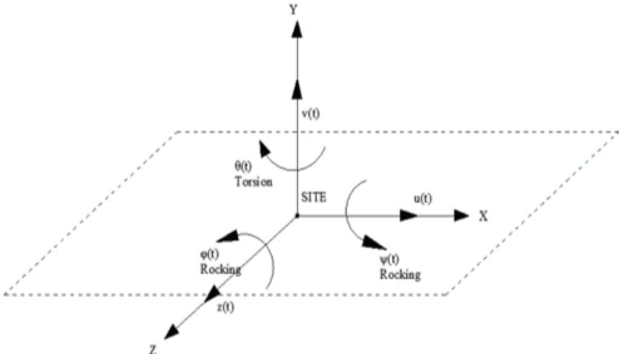

Fig. 1 Configuration of components of earthquake

The structure with lumped mass and stiffness at each level, as shown in Figure 2.2, is subject to ground motion with its six components. The equations that follow account for the horizontal degrees of freedom and do not take into account the rotation of the slabs. Let (M) be the mass matrix, (K) be stiffness, and (C) be damping. The structure's equation of motion is then determined by accounting for the translational ground acceleration in the horizontal direction x and the rotational ground acceleration in the vertical plane x-z, which is given by:

$$[M]\{\ddot{x}\} + [C]\{\dot{x}\} + [K]\{x\} =(\{m\}\ddot{x}+\{mh\}\ \theta\ \ddot{}) \quad (1)$$

$\{\ddot{x}\}$: vector made up of the degrees of freedom accelerations of the structure concerning the base,

$\{\dot{x}\}$: vector made up of the degrees of freedom of the structure's velocities,

$\{u\}$: vector that includes the degrees of freedom's displacements concerning the base,

$\{m\}$: vector that includes the translational masses in the translational excitation's horizontal direction. The main diagonal of the mass matrix (M) corresponds to the vector $\{x\}$ if it only contains the translational displacements in the horizontal direction of the excitation.

$\ddot{x}g(t)$: is the translational ground acceleration,

$\theta\ \ddot{g}(t)$: is the rotational acceleration at the base.

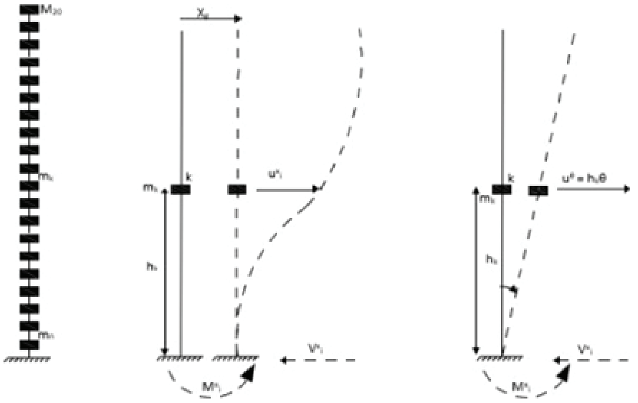

Fig. 2. Response of mass and stiffness model subjected to ground motion with translational and rotational components

The previous equation can be extended to three-dimensional scenarios, incorporating all six ground motion components: three translational and three rotational—specifically, one torsional (around the vertical axis) and two rocking (around the horizontal axes). A structure's response to these motions can be evaluated through time-history analysis by numerically solving Equation (1). Both linear and nonlinear analyses are applicable, with nonlinear behavior arising from material inelasticity or geometric changes that modify the stiffness matrix at each step of the analysis.

NUMERICAL MODELLING

This study focuses on a 20-story residential steel structure, approximately 60 meters in height, with floor plans aligned along the X, Y, and Z axes—where Z denotes the vertical direction. The building features 100 mm thick structural steel flat slabs arranged in a 12 m × 12 m square grid. It is constructed using S235 grade steel, with HEA300 beams and HEB500 columns. All section properties are sourced from the European steel section database.

Fig. 3 Plan of the simulated building

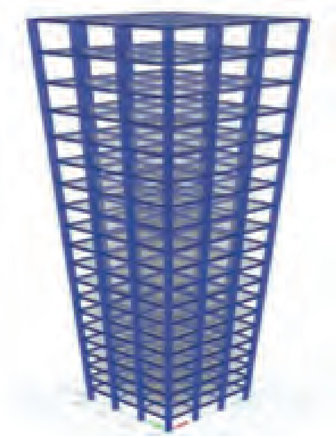

Fig. 4 3D view of the simulated building

The time-history data used in this study was sourced from the SINAPS@ post-seismic survey dataset, available through an open-access repository. This dataset originates from the ARGONET 3D accelerometric array located in Argostoli, Cephalonia (Greece), which was developed to enhance understanding of uncertainties in strong ground motion. It includes recordings from accelerometers, rotational sensors, and broadband seismometers installed across diverse soil conditions. For this analysis, data from the ROAN sensor—featuring collocated accelerometer measurements—was specifically utilized (Figures 5, 6, 7).

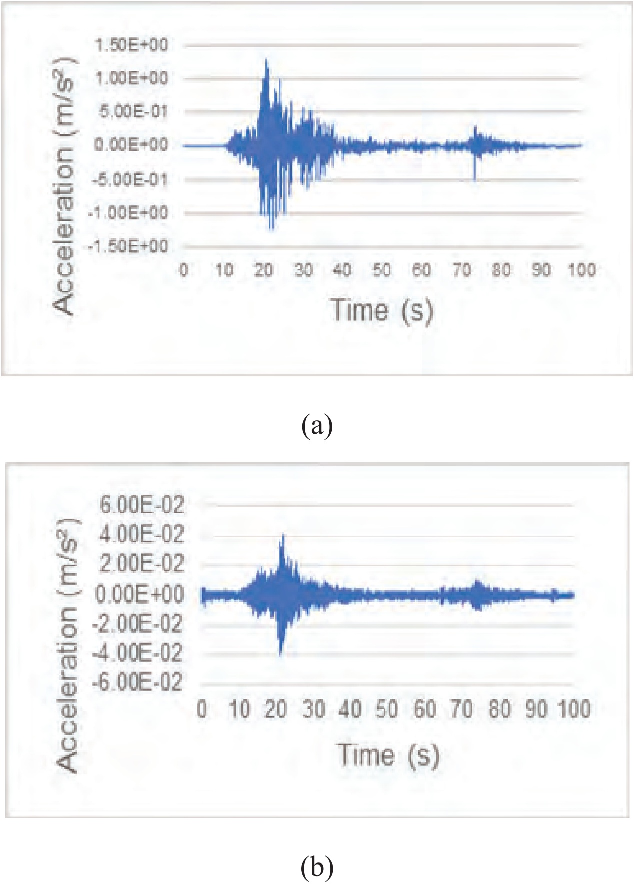

Fig. 5 Translation (a) & rotational(b) acceleration in East-West direction

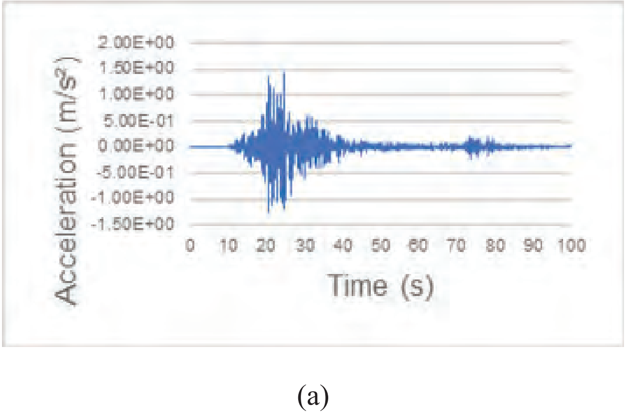

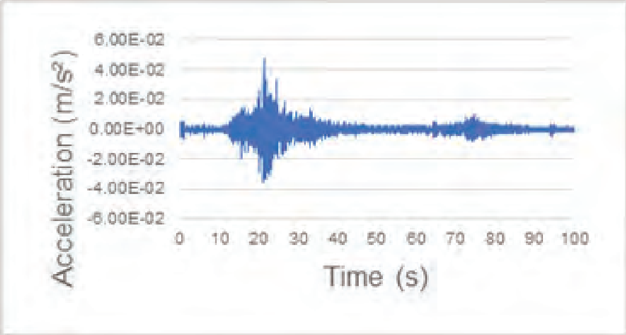

(b)

Fig. 6 Translation (a) & rotational (b) acceleration in North-South direction

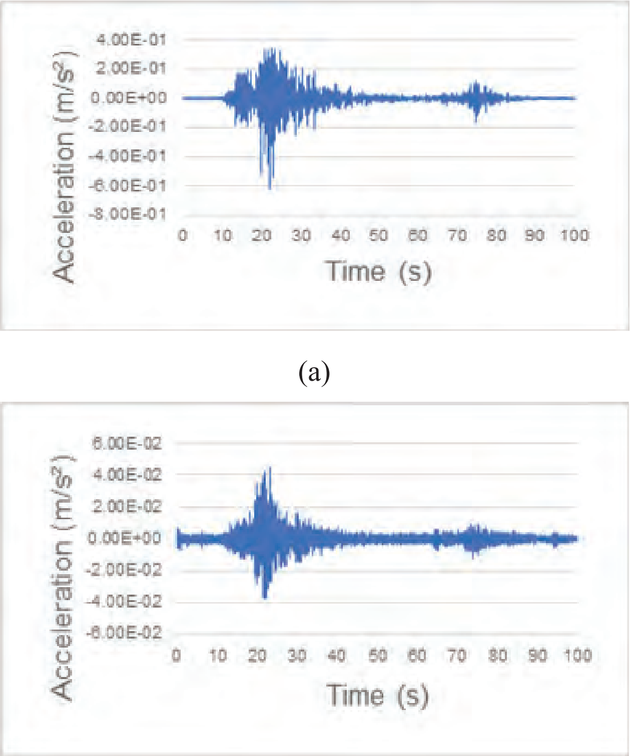

(a)

(b)

Fig. 7 Translation (a) & rotational acceleration in upward direction

RESULTS AND DISCUSSIONS

The analysis results for each group are shown in this section. The results of the seismic structural response in the X-direction will be presented first, and then the results will be described. The structural responses in the Y-direction will be described in a similar manner.

Group 1

In Group 1, the structural response of each model varies distinctly based on the direction and type of rotational excitation. Along the X-axis, Model 1 exhibits the lowest values for displacement, drift, base shear, and overturning moment, indicating minimal impact. Model 2, in contrast, significantly amplifies all these parameters, suggesting a stronger influence of its specific rotational input. Model 3 also contributes notably, especially to base shear and overturning moment, along with considerable displacement and drift. When all three rotational components are combined in Model 4, the structural responses increase markedly across all parameters, underscoring the cumulative effect of multi- directional rotations. In the Y-axis direction, Model 1 results in high displacement and overturning moment, with moderate drift and base shear. Model 2 shows minimal displacement and drift, low base shear, but an exceptionally high overturning moment. Model 3 has a strong influence on all response metrics, while Model 4 again produces the highest values overall, clearly demonstrating the additive impact of combined rotational excitations on structural performance (Figure 8).

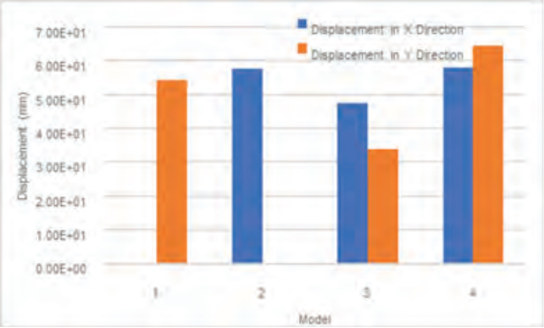

Fig. 8a Maximum displacements of Group 1

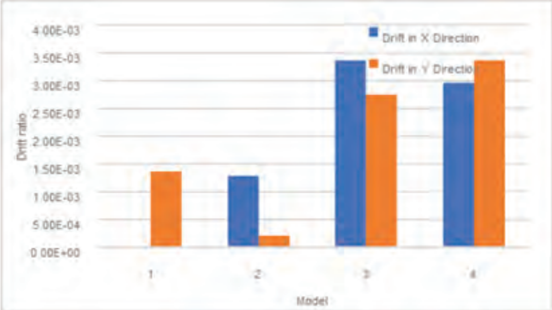

Fig. 8b Maximum drift ratio of Group 1

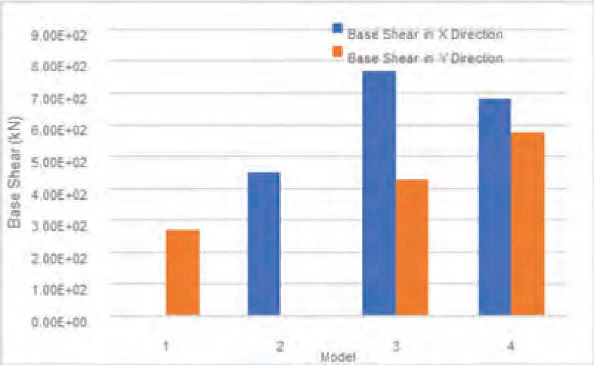

Fig. 8c Base shear of Group 1

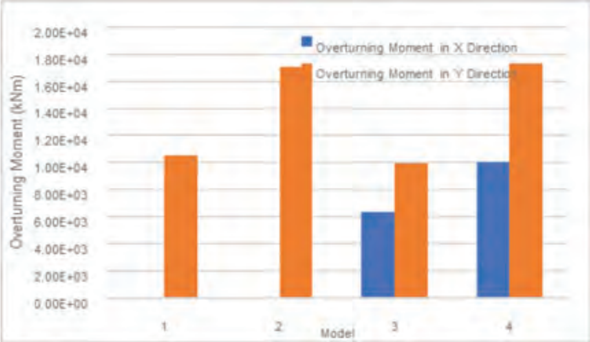

Fig. 8d Overturning moments of Group 1

Group 2

In the X direction, structural responses vary significantly across models due to different rotational inputs. Compared to Model 5, Model 6 shows no change in displacement or drift but experiences a dramatic 954% increase in overturning moment, while base shear remains constant—indicating a strong influence from the rotational component. Model 7 demonstrates a 39.6% rise in displacement, a 20.7% increase in drift, a substantial gain in base shear, and a sharp surge in overturning moment, highlighting the combined effect of North-South rotation with East-West translation. Model 8 results in a 15.4% increase in displacement and a 36.5% rise in drift, but a notable reduction in overturning moment, suggesting a mixed influence from vertical rotation. Model 9 shows significant increases across all parameters—33.4% in displacement, 32.7% in drift, 28.5% in base shear, and a dramatic rise in overturning moment—confirming that the combination of all rotational components with East-West translation greatly amplifies structural responses.

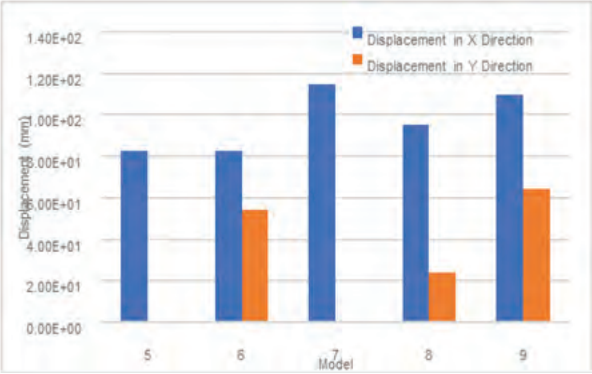

Fig. 9a Maximum displacements of Group 2

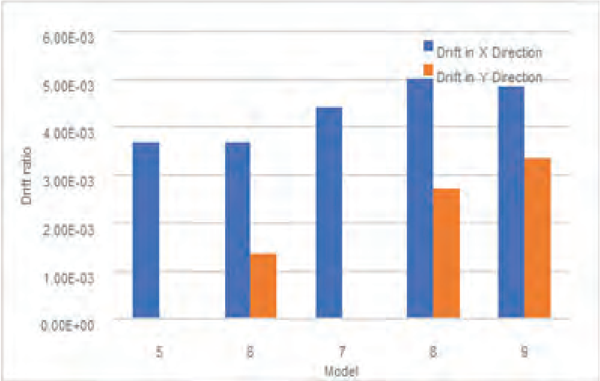

Fig. 9b Maximum drift ratio of group 2

In the Y direction, structural responses vary notably due to different rotational inputs. Compared to Model 5, Model 6 shows significant increases in displacement, drift, base shear, and an exceptionally large rise in overturning moment, demonstrating the strong influence of rotation in this direction. Model 7 results in minimal changes in displacement, drift, and base shear, but a noticeable increase in overturning moment, indicating a moderate rotational effect. Model 8 produces a substantial increase in displacement, a dramatic 273.6% rise in drift, and considerable gains in base shear and overturning moment, highlighting the pronounced impact of upward rotation. Model 9 exhibits marked increases across all parameters, confirming that the combination of all rotational components with East-West translation significantly intensifies structural responses. These pronounced increases are attributed to the added rotational forces, which amplify internal stresses, strains, and overall structural deformations (Fig 9).

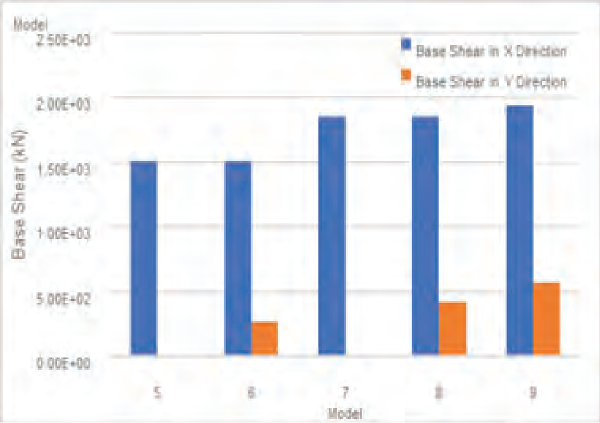

Fig. 9c Base shear of Group 2

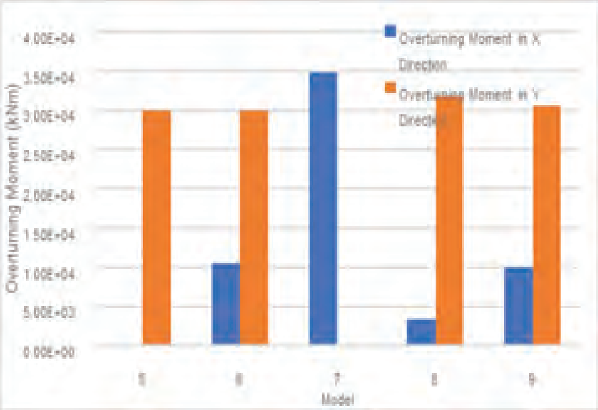

Fig. 9d Overturning moments of Group 2

Group 3

In the X direction, Models 11–14 show varying impacts compared to Model 10. Model 11 has minor increases in displacement and base shear, with negligible change in drift and overturning moment. Model 12 shows significant rises in displacement, drift, and base shear, driven by North-South rotation. Model 13 also increases most parameters but slightly reduces overturning moment, while Model 14 shows overall increases with a small drop in overturning moment, reflecting combined rotational effects. In the Y direction, Model 11 shows slight changes, Model 12 increases drift and overturning moment significantly, Model 13 has minimal impact, and Model 14 shows moderate increases across all parameters, confirming that combined rotations with North-South translation amplify structural responses. (Fig 10).

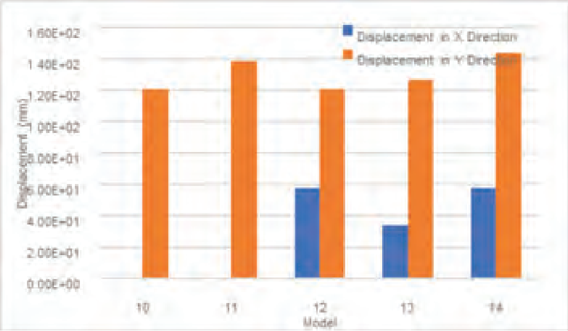

Fig. 10a Maximum displacements of Group 3

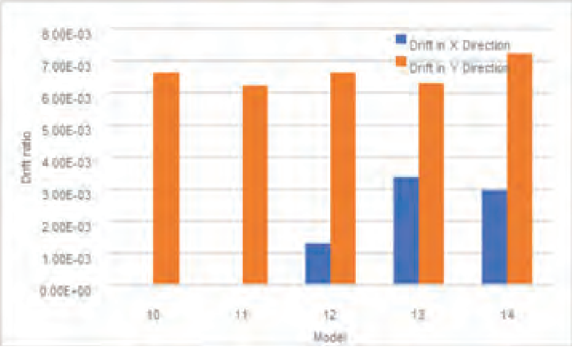

Fig. 10b Maximum drift ratio of Group 3

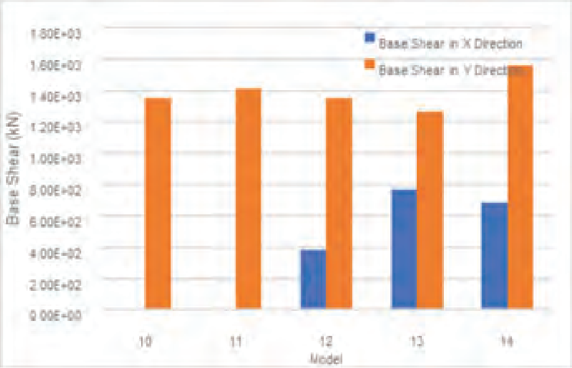

Fig. 10c Base shear of Group 3

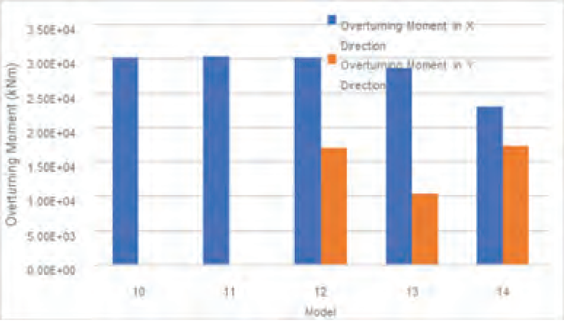

Fig. 10d Overturning moments of Group 3

Group 4

In the X direction, compared to Model 15, Model 16 shows minimal change except for a 3.1% drift increase and a 20.9% drop in overturning moment. Model 17 reflects strong North-South rotation effects with notable increases in displacement (39.6%), drift (18.8%), and base shear (23.2%), while overturning moment remains unchanged. Model 18 shows moderate increases in displacement, drift, and base shear, but a 5% decrease in overturning moment. Model 19 mirrors Model 17's increases but with a 6.9% drop in overturning moment. Models 20–22 show consistent displacement increases (~34.8%), drift (29.8–40.7%), base shear (22.5–28.5%), and a 5% reduction in overturning moment.

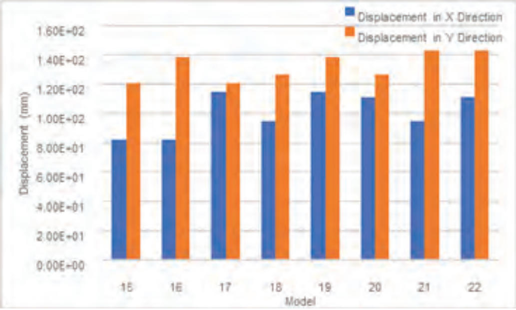

Fig. 11a Maximum displacements of Group 4

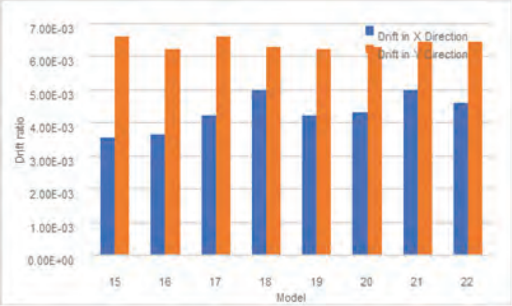

Fig. 11b Maximum drift ratio of Group 4

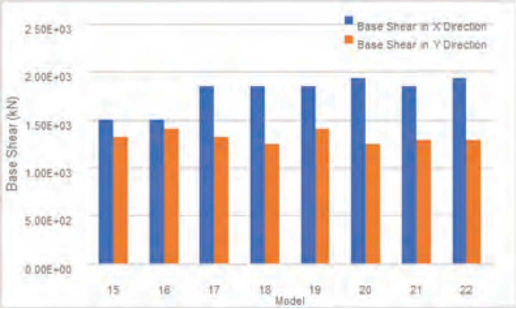

Fig. 11c Base shear of Group 4

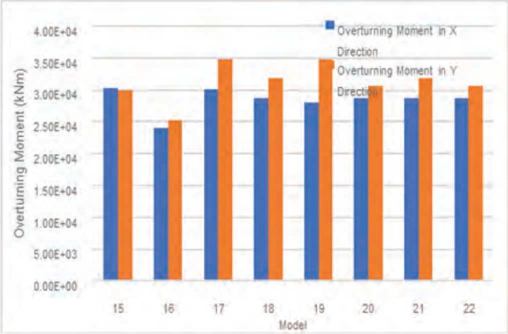

Fig. 11d Overturning moments of Group 4

In the Y direction, Model 16 records a 14% increase in displacement, 6% in base shear, 16% in overturning moment, and a slight 6% decrease in drift. Model 17 maintains displacement, drift, and base shear but experiences a significant rise in overturning moment. Model 18 shows small increases in displacement and drift (5%), a slight base shear decrease (0.3%), and a major drop in overturning moment. Model 19 presents increases of 14% in displacement, 8.6% in drift, and 15.6% in base shear, alongside a substantial overturning moment increase. Models 20 and 22 show no changes, while Model 21 only exhibits an increase in overturning moment (11).

Group 5

In the X direction, Model 24 (REW rotation) shows a small displacement increase (2.42%), large drift rise (70.27%), and moderate base shear increase (5.63%). Model 25 (RNS rotation) results in a large displacement increase (39.08%) and a notable overturning moment rise (129.80%), with other responses stable. Model 26 (RUP rotation) sees moderate displacement (15.28%) and base shear (16.12%) increases. Model 27 (REW + RNS) keeps displacement unchanged but matches Model 24's drift and base shear increases and Model 25's overturning moment rise. Model 28 (RNS + RUP) shows displacement (+26.63%), drift (+71.31%), and base shear (+16.12%) increases, but overturning moment decreases by 5.88%. Model 29 (REW + RUP) has no displacement change but increases drift (85.37%) and base shear (14.57%) while overturning moment drops by 11.39%. Model 30 (REW + RNS + RUP) results in increased displacement (26.63%), drift (85.37%), and base shear (14.57%), with a 6.11% reduction in overturning moment.

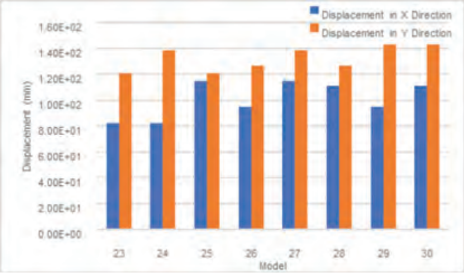

Fig. 12a Maximum displacements of Group 5

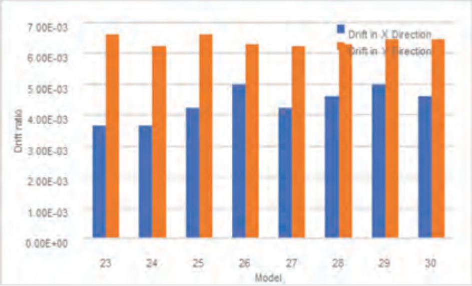

Fig. 12b Maximum drift ratio of Group 5

In the Y direction, Model 24 records a 21.49% displacement increase, a massive 455.37% rise in drift, base shear up by 15.29%, and overturning moment by 2.99%. Model 25 shows no displacement or base shear change but a 26.45% rise in overturning moment. Model 26 increases displacement (13.93%) and drift (88.43%). Model 27 mirrors Model 24's values for displacement, drift, and base shear, with overturning moment rising to 26.45%. Model 28 (RNS + RUP) has smaller increases: displacement (12.40%), drift (88.43%), base shear (4.48%), and overturning moment (4.40%). Model 29 (REW + RUP) shows displacement (+13.93%), drift (+98.35%), base shear (+7.14%), and overturning moment (+10.33%). Finally, Model 30 (REW + RNS + RUP) has displacement (12.40%), drift (98.35%), base shear (7.14%), and overturning moment (4.14%) increases (Fig 12).

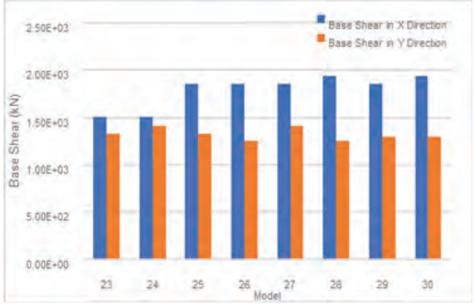

Fig. 12c Base shear of Group 5

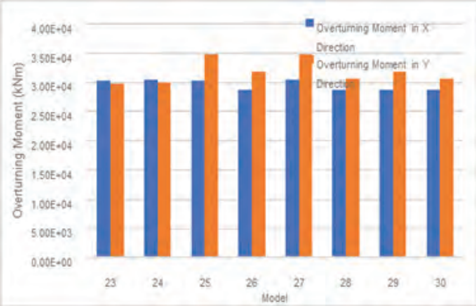

Fig. 12d Overturning moments of Group 5

CONCLUSIONS

This thorough investigation of the effects of earthquake rotational components on steel buildings has produced important new understandings of seismic response properties that are essential for improving structural resilience. After a thorough group-wise analysis, several trends have been identified that provide insight into the complex interactions between rotational and translational dynamics.

- In group 1, Model 4 (REW, RNS, RUP) exhibits a maximum overturning moment of 17.3 kNm, demonstrating the cumulative effect of rotations in all directions on lateral stability.
- In group 2, model 9 (TEW REW RNS RUP) in the X direction shows a maximum displacement of 259.03 mm, drift of 0.00968, base shear of 24.3 kN, and overturning moment of 477 kNm in the Y direction.
- In group 3, model 11 achieves the highest story displacement at 384.92 mm. Model 14 exhibits maximum story drift (0.00968) and base shear (23.8 kN), along with an overturning moment of 563 kNm in the X direction.
- In group 4, model 22 achieves maximum story displacement (416.56 mm) and story drift (0.00988) in the X direction. Model 19 records the highest base shear at 29.9 kN in the Y direction. Model 22 shows the maximum overturning moment of 749 kNm, also in the Y direction.
- In group 5, model 30 exhibits maximum story displacement (428.26 mm) and story drift (0.011) in the Y direction. Model 29 demonstrates the highest base shear of 31.3 kN in the X direction, along with

an overturning moment of 598 kNm, also in the X direction.

Considering rotational components of earthquakes in performance-based seismic analysis of tall buildings is crucial for achieving safer and more robust structural designs. Including these components significantly increases the seismic response, while omitting them can lead to inaccurate assessment of structural integrity during earthquakes. Incorporating rotational effects into seismic codes can improve structural resilience and safety. The study's limitations include simplifying modeling assumptions and potential uncertainties in the results, which should be acknowledged.

REFERENCES

1. Wei Wang, Guibo Nie , Wen Bai, Weidan Xu , Ke Du Wei Wang , Guibo Nie , Wen Bai, Weidan Xu , Ke Du 2023. Study on The Strong Earthquake Failure Mechanism of Space Grid Structure Considering Rotational Ground Motion. Structures (57).
2. Felipe Vicencio, Nicholas A. Alexander, 2022. Seismic Structure-Soil-Structure Interaction Between a Pair of Buildings with Consideration of Rotational Ground Motions Effects. Soil Dynamics and Earthquake Engineering (163)
3. Zhang Jie, Li Hongnan, Li Chao 2021. Seismic response of large-span spatial structures under multi-support and multidimensional excitations including rotational components. Earthquake Engineering and Engineering Vibration 20(1): 141-159
4. Afshin Khodaparast, HamidReza Tavakoli, Hor Khosravi, Hamid Rajabnejad 2021. Effect of Rotational Components of Strong Ground Motions on Behavior of High-Rise Buildings with Outrigger and Belt-Truss System, Asian Journal of Civil Engineering (22): 1639–1653
5. Siroos Gholampour, Reza Taghipour, Hamid Kazemei Felourdi, Saman Soleimani Kutanaei 2020. Investigating the Effect of Rotational Components on The Progressive Collapse of Steel Structures. Engineering Failure Analysis (121)
6. Nikos Pnevmatikos, Foteini Konstandakopoulou, George Papagiannopoulos, George Hatzigeorgiou, and Georgios Papavasileiou 2020, Influence of Earthquake Rotational Components on the Seismic Safety of Steel Structures, Vibration (3): 42-50.
7. Amir Javad Moradloo, and Abbas Naiji 2020. Effects of Rotational Components of Earthquake on Seismic Response of Arch Concrete Dams, Earthquake Engineering and Engineering Vibration 19(2): 349-362
8. Felipe Vicencio, Nicholas A. Alexander 2019. A Parametric Study on The Effect of Rotational Ground Motions on Building Structural Responses. Soil Dynamics and Earthquake Engineering (118): 191-206
9. Piotr Adam Bońkowski, Zbigniew Zembaty, Maciej Yan Minch 2019. Engineering Analysis of Strong Ground Rocking and Its Effect on Tall Structures. Soil Dynamics and Earthquake Engineering (116): 358–370
10. H. Tajammolian, F. Khoshnoudian, V. Loghman 2017. Rotational Components of Near- Fault Earthquakes Effects on Triple Concave Friction Pendulum Base-Isolated Asymmetric i. Structures. Engineering Structures (142)
11. Perron, V, Hollender, F.; Mariscal, A, Theodoulidis, N, Andreou, C, Bard, P, Cornou, C, Cottereau, R. Cushing, E.M, Frau, A 2018. Accelerometer, Velocimeter Dense-Array, and Rotation Sensor Datasets from the Sinaps@ Postseismic Survey (Cephalonia 2014–2015 Aftershock Sequence) (89), 678–687
12. Sbaa, S, Hollender, F, Perron, V, Imtiaz, A, Bard, P, Mariscal, A, Cochard, A, Dujardin 2017. Analysis of rotation sensor data from the SINAPS@ Kefalonia (Greece) post-seismic experiment—Link to surface geology and wavefield characteristics. Earth Planets Space (69): 124
13. EN 1993-1-1:2005, Eurocode 3: Design of steel structures - Part 1-1: General rules and rules for buildings
14. EN 1998-1:2004, Eurocode 8: Design of structures for earthquake resistance – Part 1: General rules, seismic actions and rules for buildings.

Seismic Performance of Hybrid Structural Systems over Steel Structure

Aswathi S
PG Scholar
Department of Civil Engineering
NSS College of Engineering
Palakkad, Kerala
✉ aswathysuresh210@gmail.com

Pooja Suresh
Assistant Professor
Department of Civil Engineering
NSS College of Engineering
Palakkad, Kerala
✉ poojasuresh@nssce.ac.in

ABSTRACT

A hybrid structure refers to a building or infrastructure that incorporates elements from different structural systems, different materials or construction techniques. This combination of approaches can enhance the overall performance, efficiency, and functionality of the structure. Thus hybrid structures provide civil engineers with versatile solutions for seismic resilience. This work involves modelling and analysis of a hybrid structure which uses a combination of concrete shear walls, steel beams, steel columns, concrete-filled steel tubular (CFST) columns and bracings. Different models are created to evaluate the performance of hybrid structural systems. The most hybrid model analyzed in this project utilizes shear wall, bracings, CFST columns forming strong outer frame, steel beams and steel columns. Proper analysis is carried out finding the optimum unsymmetrical placing of CFST columns. The seismic performance of such hybrid structural systems is analyzed by using various parameters like maximum storey displacement, storey drift and overturning moments. Analysing the parameters it has found that hybridizing the building has contributed to significant seismic performance. Using different material and structural systems improves the seismic performance because of the combined benefits of these materials that helps in promoting the energy dissipation, efficiency and flexibility of the building

KEYWORDS: *Hybrid structural system, Concrete filled steel tubular columns, Seismic analysis.*

INTRODUCTION

Seismic analysis is vital in earthquake-prone regions to ensure structural safety, reduce damage, and enhance resilience. It guides engineers in designing buildings that can withstand seismic forces, aiding in code enforcement, retrofitting, and preparedness. Hybrid buildings are particularly effective, combining materials like concrete and steel to reduce drift and damage while maintaining sustainability. This study uses ETABS software to analyze various hybrid systems—incorporating shear walls, bracings, and composite columns—for their seismic performance. Though initially costlier, these systems offer long-term benefits like improved safety, reduced repair costs, and better compliance with seismic standards.

BACKGROUND SUMMARY

Hybrid structural systems combine different construction materials and techniques to improve seismic performance. Tailored to meet structural and architectural needs, they enhance energy dissipation and reduce earthquake damage while ensuring code compliance. A typical system uses steel beams, columns, shear walls, CFST columns, and bracings. Steel offers strength and ductility, while CFST columns boost load capacity. Shear walls distribute lateral forces, and bracings control sway. Together, they improve safety, material efficiency, and design flexibility, making them ideal for resilient, modern construction in seismic zones.

METHOD OF ANALYSIS

To evaluate a structure's performance, both linear and nonlinear analyses are used. Linear analysis assumes elastic behavior and includes equivalent static and response spectrum (dynamic) methods. Nonlinear analysis accounts for material and geometric nonlinearity, using methods like nonlinear time history and pushover analysis (a nonlinear static method). Together, these approaches offer a comprehensive understanding of structural behavior under different loads.

Equivalent Static Method

The Equivalent Static Method (ESM) is widely used in structural engineering to evaluate seismic performance. It represents the dynamic earthquake response with an equivalent static lateral force applied to the structure. Assuming the building responds in its fundamental lateral mode, ESM calculates seismic forces in two horizontal directions along the building's main axes. The structure must withstand forces from both directions, but not at the same time.

METHODOLOGY

The seismic analysis of hybrid structural systems follows a clear methodology, starting with a literature review to build a strong foundation. Next, objectives are defined, followed by validating results against a reputable journal to ensure accuracy. Eight models are then developed, with the last two being highly hybrid, incorporating shear walls, bracings, CFST columns, steel beams, and columns. These models generate data for analysis, leading to well-documented conclusions that complete the study.

MODELLING AND ANALYSIS

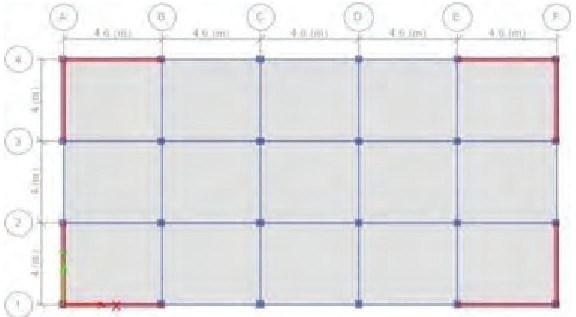

Fig. 1. Structural plan of G+9 storied building

A G+9 hybrid structural system was analyzed using models ranging from simple to highly hybridized. Different structural systems and materials were optimally placed to balance cost and performance. The building plan is 23m x 12m with 3m storey height. Seismic analysis used the Equivalent Lateral Load Method per IS 1893 (Part 1):2016. Results were evaluated based on maximum storey displacement, drift, and overturning moment. Figure 1 shows the building plan, while Tables 1 and 2 list seismic parameters and structural details.

Following Seismic parameters shown in Table 1 are considered for the analysis

Description	Specification
Response reduction factor, R	5
Importance factor, I	1.2
Zone factor, Z	0.36
Terrain category	2
Wind speed	44 m/s
Seismic zone	V
Soil condition	II

Following material properties shown in Table 2 are considered for the analysis:

Description	Specification
Number of stories	10
Building plan	23m x 12m
Height of each floor	3.2 m
Beam size	ISLB 250
Column size	ISMB 300
Thickness of CFST tube	13mm
Thickness of wall	150mm
Thickness of slab	100mm
Grade of concrete	M25
Grade of steel	Fe345

Loads Calculations

Calculating loads is an important step in the design of a structure. These forces include:

1. Dead load - 5 kN/m² (IS 875-2015)
2. Live load - 3 kN/m² (IS 875-2015)
3. Wind load - 44 m/s (IS 875-2015)
4. Seismic load (IS 1893-2016)

Building models

Eight models were created in ETABS to analyze the seismic performance of hybrid structural systems and compared with a conventional steel building. These range from simple to highly hybridized models using materials like shear walls, bracings, CFST columns, steel beams, and columns. Table 3 lists the models and their abbreviations used in the analysis.

Table 3 Abbreviations of the models

Sl. No.	Model	Abbreviation
1	Steel building	SB
2	Building with shear wall	B+SW
3	Building with CFST columns	B+C
4	Building with shear wall and CFST columns	B+SW+C
5	Building with shear wall and CFST columns (top half)	B+SW+C(t)
6	Building with shear wall and CFST columns (bottom half)	B+SW+C(b)
7	Building with shear wall, bracings and CFST columns(outer frame bottom 1-6 stories)	B+Br+SW+C (b(1-6))
8	Building with shear wall, bracings and CFST columns(outer frame top 1-6 stories)	B+Br+SW+C (t(1-6))

Analysis

Referring to Figure 2, conventional steel building (SB) modelled and the performance was evaluated. Steel buildings are common in high rise structures. Steel columns and beams are used as structural support in conventional steel buildings, which enable effective construction and design flexibility. Steel offers strength, flexibility, and durability.

Fig. 2. Conventional steel building

Referring to Figure 3, a 10-story building model includes concrete shear walls at all four corners. This placement enhances stability by evenly distributing lateral forces, reducing stress, and improving safety. It also limits deflections, increasing occupant comfort.

Fig. 3. Building with shear wall

Referring to Figure 4, a 10 storied building is modelled. The building is provided with concrete filled steel tubular columns, the columns are provided to the whole structure. CFST columns are a dependable option for guaranteeing structural integrity and safety in tall buildings because they offer enhanced load-bearing capacity, effective structural performance, less material consumption, and superior fire resistance.

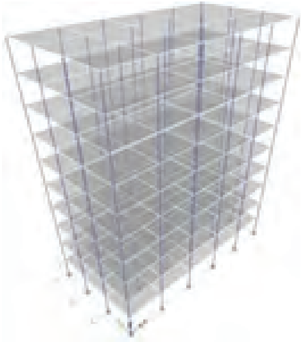

Fig. 4. Building with CFST columns

Referring to Figure 5.5, a 10 storied steel building is modelled. The building is provided with concrete filled steel tubular columns, shear wall at the 4 corners to the whole building. This hybrid structure perform better that the later models as it incorporates the benefits of both shear wall and CFST. All the columns utilized in this model are concrete filled steel tubular columns along with shear walls placing at the corners. This model thus enhances the seismic performance.

Fig. 5. Building with shear wall and CFST columns

Referring to Figure 6, a 10 storied steel building is modelled. The building is provided with concrete filled steel tubular columns only at the top half, shear wall at the 4 corners to the whole building. It would be uneconomical placing CFST columns to the whole building so utilizing the CFST columns on top half alone and shear wall at the corners to whole building shown significant seismic resistance.

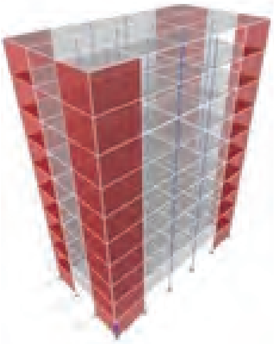

Fig. 6. Building with shear wall and CFST columns (top half)

Fig. 7. Building with shear wall and CFST columns (bottom half)

Referring to Figure 7, In this model, a 10 storied steel building is modelled. The building is provided with concrete filled steel tubular columns only at the bottom half, shear wall at the 4 corners to the whole building. The seismic evaluation is carried out by placing CFST columns at bottom half in order to find how this model's performance differ from the latter model.

Referring to Figure 8, In this model, a 10 storied steel building is modelled. The building is provided with shear wall, bracings and concrete filled steel tubular columns only at the outer cover from 4th to 10th. In this model bracings are introduced. In high-rise structures, bracing improves structural integrity and offers vital lateral stability by lessening sway during heavy winds or seismic activity. Bracings were introduced and the utilization of CFST columns were reduced.

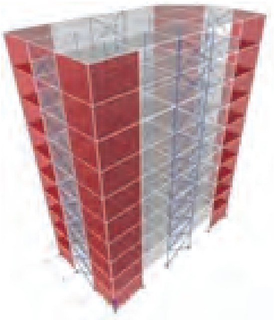

Fig. 8. Building with shear wall, bracings and CFST columns (outer frame bottom 1-6 stories)

Referring to Figure 9, a 10-story steel building is modeled with shear walls, bracings, and CFST columns placed only on the outer cover from the 1st to 6th stories. Bracing locations and CFST positions were varied for evaluation.

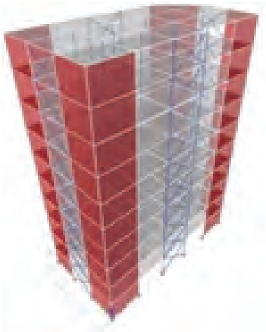

Fig. 9. Building with shear wall, bracings and CFST columns (outer frame top 1-6 stories)

RESULTS AND DISCUSSIONS

The seismic performance of a 10-storey hybrid structure was analyzed in ETABS using the Equivalent Lateral Load method. Key parameters such as maximum storey displacement, drift, and overturning moment were evaluated to assess structural stability and response under seismic loads.

Maximum story displacement

ETABS analysis showed all models had permissible displacement, with hybrid models performing better than the conventional steel building. The B+Br+SW+C(b1-6) model had the lowest displacement, showing a 56.45% reduction (Table 4, Figure 10), due to strategic placement of CFST columns at lower levels. This proves hybrid systems enhance seismic resilience and are ideal for high-rise buildings in seismic zones.

Table 4. shows the Percentage reduction of maximum values of storey displacement

Models	Maximum Displacement (mm)	Percentage Reduction (%)
SB	74.75	-
B+SW	48.5	35.11
B+C	71.22	4.72
B+SW+C	38.42	48.60
B+SW+C(t)	43.29	42.08
B+SW+C(b)	40.5	45.81
B+Br+SW+C(b (1-6))	32.55	56.45
B+Br+SW+C(t (1-6))	35.8	52.10

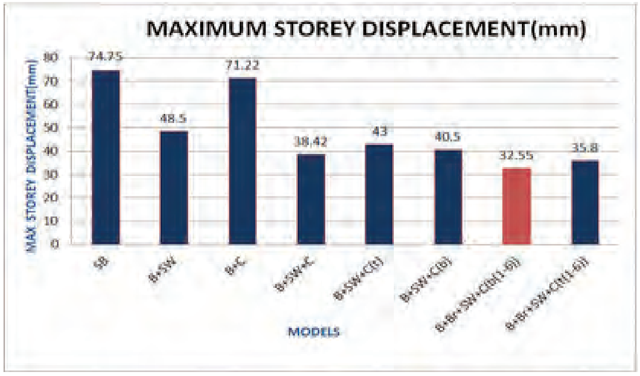

Fig. 10 Comparison of maximum displacement value.

Maximum story drift

The study evaluates maximum drift values of various models using ETABS, all within permissible limits. Compared to the steel building, all hybrid models exhibit lower drift, with the B+Br+SW+C(b(1-6)) model showing the least drift and best seismic performance (Figure 11). According to Table 5, this model achieves a 77.57% reduction, highlighting how integrating different structural systems and materials enhances performance, functionality, and sustainability.

Table 5. shows the Percentage reduction of maximum values of storey drift.

Models	Maximum Drift	Percentage Reduction (%)
SB	0.003567	-
B+SW	0.00156	56.26
B+C	0.00332	6.92
B+SW+C	0.00116	67.47
B+SW+C(t)	0.0019	46.73
B+SW+C(b)	0.00158	55.70
B+Br+SW+C(b (1-6))	0.0008	77.57
B+Br+SW+C(t (1-6))	0.00101	71.68

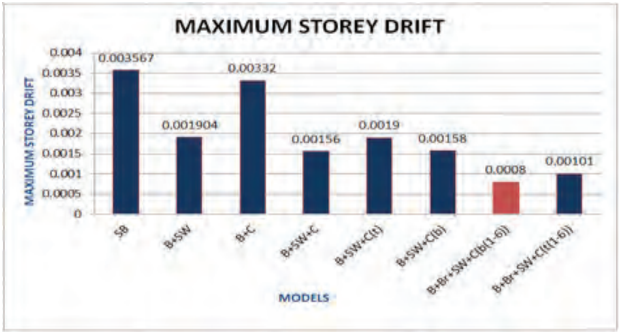

Fig. 11. Comparison of maximum drift values

Overturning moment

The study used ETABS to analyze overturning moments across models, as shown in Figure 12. The hybrid model B+Br+SW+C(b1–6), combining bracings, shear walls, and CFST columns, showed the lowest overturning moment, with a 60.93% reduction (Table 6) compared to steel structures. Strategic placement of CFST columns and hybrid systems led to improved seismic performance, optimizing structural efficiency, functionality, and sustainability.

Table 6 shows the Percentage reduction of maximum values of overturning moment.

Models	Overturning moment (kN – m)	Percentage reduction (%)
SB	89724	-
B+SW	77165	13.99
B+C	88712	1.12
B+SW+C	70303	21.60
B+SW+C(t)	74983	16.40
B+SW+C(b)	70966	20.90
B+Br+SW+C(b (1-6))	35047	60.93
B+Br+SW+C(t(1-6))	45408	49.39

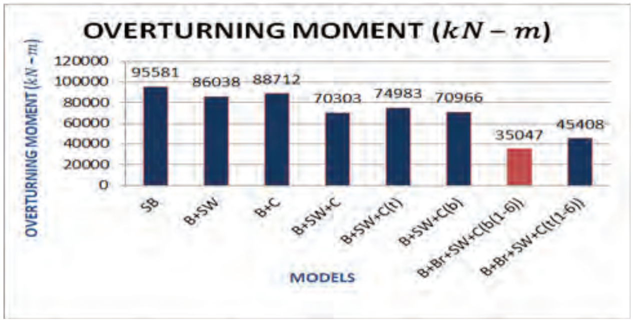

Fig. 12 Comparison of overturning moment values

Conclusions

A G+10 storied building was seismically analyzed using various materials and structural systems. Hybrid models, from simple to highly hybridized, were compared with conventional steel structures using ETABS, focusing on storey displacement, drift, and overturning moment.

- The B+SW model, with corner shear walls, outperforms steel buildings by resisting lateral loads and reducing deformation and drift.
- The B+C model uses CFST columns combining steel's strength and concrete's ductility to absorb seismic energy, reducing damage.
- The B+SW+C model combines shear walls and CFST columns, showing better performance than the first two models.
- The B+SW+C(t) and B+SW+C(b) differ by CFST column placement, with the bottom placement (B+SW+C(b)) improving lateral stability and load capacity.
- The B+Br+SW+C(b(1-6)) model performs best, combining bracings, shear walls, and CFST columns for superior seismic resistance.

Hybrid buildings are essential for modern construction, offering sustainability, efficiency, resilience, versatile design, and resource optimization—key for the future of architecture and engineering.

REFERENCES

1. Askouni, P.K., 2023. The Behavior of Hybrid Reinforced Concrete-Steel Buildings under Sequential Ground Excitations. Computation, 11(5), p.102.
2. Benny, B., Bazli, M., Rajabipour, A. and Arashpour, M., 2023. Durability of tubular sea water sea sand concrete and fibre-reinforced polymer hybrid structures: Mechanisms and effective parameters: Critical overview and discussion. Construction and Building Materials, 366, p.130206.
3. Bezabeh, M.A., Tesfamariam, S., Popovski, M., Goda, K. and Stiemer, S.F., 2017. Seismic base shear modification factors for timber-steel hybrid structure: collapse risk assessment approach Journal of Structural Engineering, 143(10), p.04017136.
4. Dakshata, B. and Sushma, C.K., PERFORMANCE ANALYSIS OF HYBRID STRUCTURE IN HIGH SEISMIC ZONE.
5. Li, Z., Dong, H., Wang, X. and He, M., 2017. Experimental and numerical investigations into seismic performance of timber-steel hybrid structure with supplemental dampers. Engineering Structures, 151, pp.33-43.
6. Moroni, F., Pirondi, A. and Kleiner, F., 2010. Experimental analysis and comparison of the strength of simple and hybrid structural joints. International Journal of Adhesion and Adhesives, 30(5), pp.367- 379.
7. Naseri, M.R. and Lallotra, B., 2021. A Review on Seismic Analysis of Hybrid Structures. International Research Journal of Engineering and Technology (IRJET), 8(4).
8. Pan, Y., Tannert, T., Kaushik, K., Xiong, H. and Ventura, C.E., 2021. Seismic performance of a proposed

wood-concrete hybrid system for high-rise buildings. Engineering Structures, 238, p.112194.

9. Sharma, S. and Tiwary, A.K., Analysis of multi-story buildings with hybrid shear wall: steel bracing structural system (2021) Innovative Infrastructure Solutions, 6 (3).

10. Ye, M., Jiang, J., Chen, H.M., Zhou, H.Y. and Song, D.D., 2021. Seismic behavior of an innovative hybrid beam-column connection for precast concrete structures. Engineering Structures, 227, p.111436.

Seismic Analysis of Multi-Storey Buildings with and Without Composite Columns

Nimisha Rajagopal
PG Scholar
Department of Civil Engineering
NSS College of Engineering
Palakkad, Kerala
✉ nimishaveerangath123@gmail.com

Bharati Raj. J
Assistant Professor
Department of Civil Engineering
NSS College of Engineering
Palakkad, Kerala
✉ bharatiraj@nssce.ac.in

ABSTRACT

It is now essential to design structures that are earthquake resistant due to a rapid rise in upward growth and rising probability of earthquakes. Composite columns are a great way to resist lateral forces and serve as a supporting framework in buildings that are constructed from composite materials. This study investigates the seismic performance of composite columns composed of composite materials such as Carbon Fibre Reinforced Polymers(CFRP) and Glass Fibre Reinforced Polymers(GFRP) with varying column cross sections using the finite element analysis software ETABS. In this study, the seismic behaviour of CFRP and GFRP columns is thoroughly investigated with different column cross sections. And found out the best composite material among these two then incoporated this into various kinds of plan configurations, including standard rectangular, L-shaped, H-shaped, and C-shaped structures. Response spectrum analysis is used in this study to assess a 16- story Reinforced Concrete structure with the goal of identifying the best composite materials with the best column cross sections. The focus of this study is on the effects of architectural arrangement and structural system selection on essential seismic characteristics, such as maximum storey displacement, maximum storey drift, and maximum storey shear. Remarkable results show that, in a variety of column cross sections, CFRP columns with circular column cross section consistently display higher storey shear resistance and help to lower maximum storey drift and maximum storey displacement. These findings highlight CFRP columns as a very advantageous option for building earthquake resistant structures since they provide better seismic performance when compared to conventional RC columns in regular buildings. Hence this advantage is utilized in plan irregular buildings to check how much those seismic parameters can be improved. The results underscore that there is significant improvement in those seismic parameters even in case of plan irregularity.

KEYWORDS: *Composite columns, Carbon Fiber Reinforced Polymer, Glass Fiber Reinforced Polymer, Maximum Storey Displacement, Maximum Storey Drift, and Maximum Storey Shear.*

INTRODUCTION

Seismic analysis is crucial to safeguard lives and communities from earthquake damage by understanding structural responses to seismic forces. Fiber Reinforced Polymers (FRP), reinforced with glass, carbon, or aramid fibers, enhance seismic performance due to their high strength, stiffness, and durability. FRP is valuable for new constructions and retrofitting existing buildings, improving resilience and reducing earthquake damage. Despite challenges like cost and material compatibility, ongoing research is advancing FRP technology for better earthquake resistance. This study compares the seismic behavior of multi-story buildings with traditional Reinforced Concrete Columns (RCC) versus those with Glass FRP (GFRP) and Carbon FRP (CFRP) columns, considering square and circular cross-sections across various plan shapes (rectangular, H-, L-, and C-shaped).

BACKGROUND SUMMARY

CFRP (Carbon Fibre Reinforced Polymer) and GFRP (Glass Fibre Reinforced Polymer) are increasingly used in high-rise buildings due to their lightweight, high strength, and resistance to fatigue and corrosion. Initially developed for aerospace and military use, CFRP later found applications in civil engineering, especially for retrofitting and constructing tall buildings due to its seismic efficiency and reduced dead weight. GFRP, known for corrosion resistance and low conductivity, is commonly used in facades and cladding but is also beneficial in reducing the overall building weight. Their use aligns with modern goals of performance optimization and sustainability, with ongoing research expected to enhance their properties further.

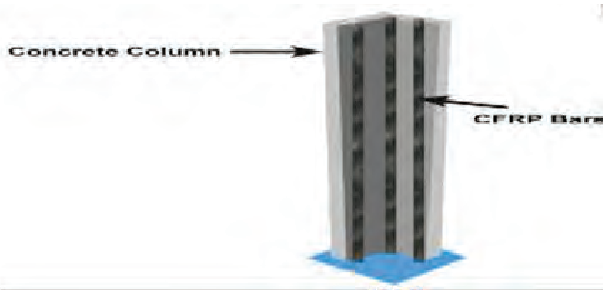

Fig. 1 CFRP Bars

Fig. 2 GFRP Bars

METHOD OF ANALYSIS

To evaluate structural performance, both linear (equivalent static, response spectrum) and nonlinear (time history, push-over) analyses are used. Among linear methods, response spectrum analysis evaluates seismic response using parameters like mass, stiffness, and damping by plotting the peak response of an idealized SDOF system across frequencies.

METHODOLOGY

The study involves literature review, model validation based on previous research, and building modeling with varying column shapes and materials. Seismic analysis is then performed to evaluate structural behavior, followed by comparison of response parameters to assess performance.

MODELLING AND ANALYSIS

A G+15 storey building (30 m × 20 m) is analyzed using conventional RCC, CFRP, and GFRP materials with circular and square columns. Irregular building plans (C, H, L shapes) are also modeled, as shown in Figures 3 to 4.

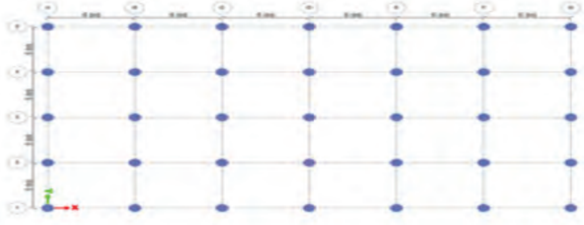

Fig. 3. Structural Plan of G+15 with circular columns

Fig. 4. Structural Plan of G+15 C-Shaped Structural Plan of G+15 C-Shaped Building with Regular Building Circular columns

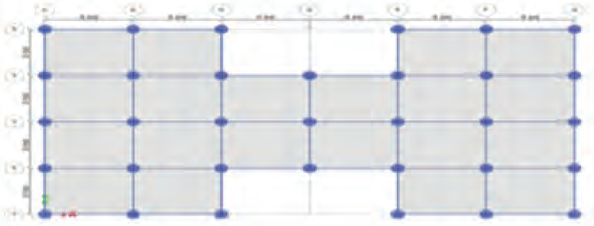

Fig. 5. Structural Plan of G+15 H-Shaped Building with Circular columns

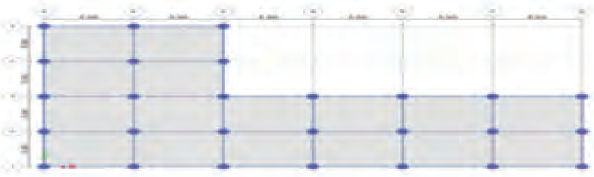

Fig. 6. Structural Plan of G+15 L-Shaped Building with Circular columns

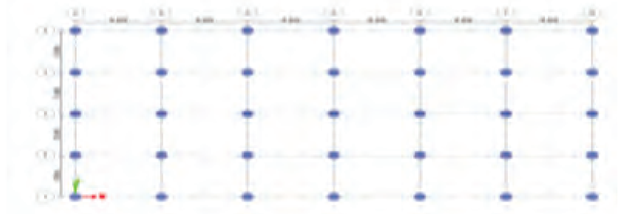

Fig. 7. Structural Plan of G+15 Regular Building with circular columns

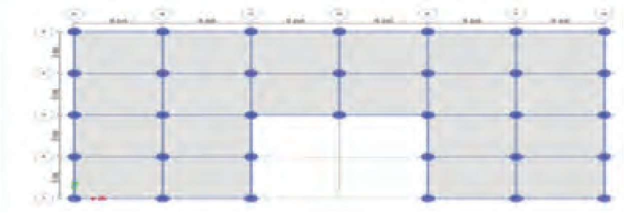

Fig. 8. Structural Plan of G+15 C-Shaped Building with Circular columns

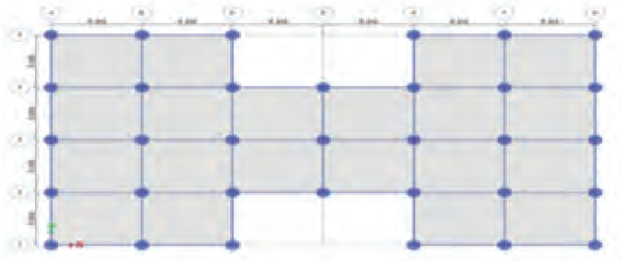

Fig. 9. Structural Plan of G+15 H-Shaped Building with Circular columns

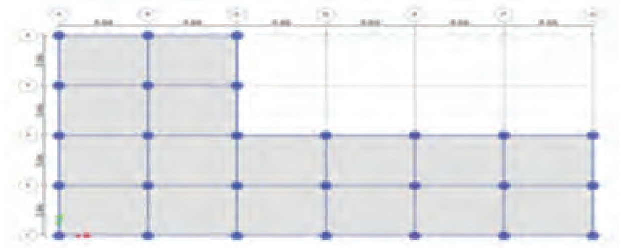

Fig. 10. Structural Plan of G+15 L-Shaped Building with Circular columns

Load calculation is a vital first step in structural design, involving accurate estimation of forces like:

i. Dead Load – 5 kN/m²,

ii. Live Load – 3 kN/m²,

iii. Wind Load – as per IS 875-2015 based on location and building features,

iv. Seismic Load – as per IS 1893-2016, considering seismic zone, soil, and building parameters,

v. SIDL – includes wall load (14.4 kN/m) and floor finish (1 kN/m²).

Table 1, Table 2 and Table 3 lists the Seismic Parameters,Structural Details and Material Properties respectively that are taken into consideration for the analysis

Table 1 Seismic Parameters

Seismic zone	III
Zone factor (Z)	0.16
Importance factor (I)	1
Response reduction factor (R)	5
Type of soil	Medium
Damping ratio	5 %

Table 2 Structural Details

Height of storey	3m
No of stories	16
Beam Size	600 X 250mm
Slab Thickness	150mm
Circular	Dia = 800 mm
Square	265 X 265mm

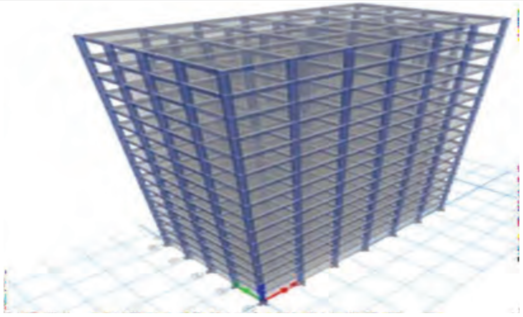

Fig. 11 3D Model of G+15 Regular Building with CFRP Circular Columns

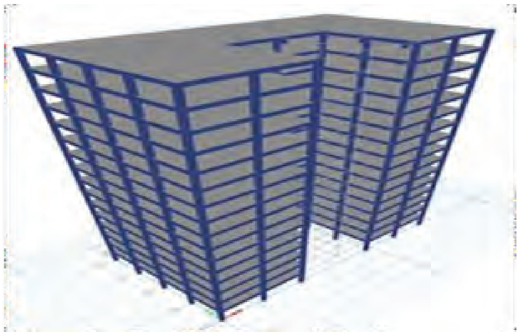

Fig. 12 3D Model of G+15 C-Shaped Building with CFRP Circular Columns

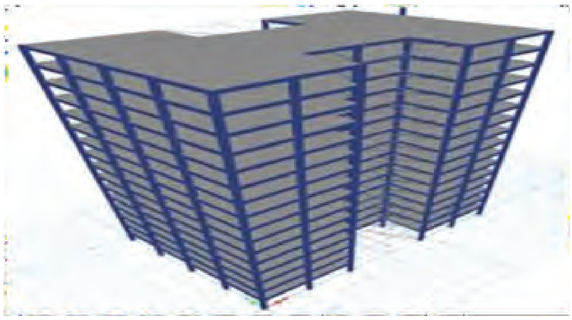

Fig. 13 3D Model of G+15 H-Shaped Building with CFRP Circular Columns

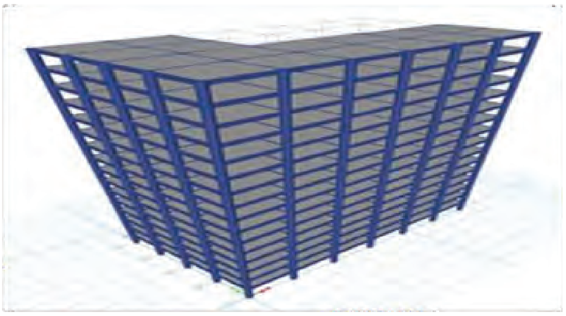

Fig. 14 3D Model of G+15 L-Shaped Building with CFRP Circular Columns

G+15 storey buildings are taken into account for modelling. ETABS is used to model various models for various column cross sections including circular and square each configuration has three unique models, one made of steel RC columns, second with CFRP columns and another with GFRP columns. Also For modelling, many plan configurations are taken into consideration, including rectangular, H- shaped, L-shaped, and C-shaped structures with the optimal column cross section and composite material

Table 2 Regular Buildings with Circular and Square columns

Models	Abbreviations	Models	Abbreviations
Regular Building Circular columns	RBCC	Regular Building Square Columns	RBSC
Regular Building Carbon Fiber Reinforced Polymer Circular columns	RBCFRPC	Regular Building Carbon Fiber Reinforced Polymer Square Columns	RBCFRPSC
Regular Building Glass Fiber Reinforced Polymer Circular columns	RBGFRPC	Regular Building Glass Fiber Reinforced Polymer Square Columns	RBGFRPSC

Table 3 shows abbrevations of irregular buildings with circular columns.

Fig. 15 Structural Plan of G+15 Regular Building with GFRP square columns

Table 3 Irregular Buildings with Circular columns

Models	Abbreviations	Models	Abbreviations	Models	Abbreviations
C-Shaped Building Circular columns	CBC	H-Shaped Building Circular columns	HBC	L-Shaped Building Circular columns	LBC
C-Shaped Building Carbon Fiber Reinforced Polymer Circular columns	CBCFRPC	H-Shaped Building Carbon Fiber Reinforced Polymer Circular columns	HBCFRPC	L-Shaped Building Carbon Fiber Reinforced Polymer Circular columns	LBCFRPC
C-Shaped Building Glass Fiber Reinforced Polymer Circular columns	CBGFRPC	H-Shaped Building Glass Fiber Reinforced Polymer Circular columns	HBGFRPC	L-Shaped Building Glass Fiber Reinforced Polymer Circular columns	LBGFRPC

Response Spectrum Analysis is a key seismic evaluation method that predicts a structure's response to earthquakes by considering mass, stiffness, and damping. It uses a response spectrum graphderived from real seismic data to show the peak response of a single degree of freedom system across different natural frequencies. Key response parameters include storey displacement (limited to H/500 as per IS 456:2000), storey drift (not exceeding 0.004 times the storey height per IS 1893:2016), and storey shear, which helps identify lateral force distribution. This analysis ensures buildings meet safety standards in earthquake-prone zones. The study showed that structures retrofitted with CFRP and GFRP composites had lower storey displacement, with detailed results in Table 4.

Table 4 Maximum Storey Displacement Values -Regular Buildings

Building Models	Maximum Displacement (mm)
RBCC	15.31265
RBCFRPC	13.61794
RBGFRPC	14.52863
RBSC	16.31885
RBCFRPSC	14.86765
RBGFRPSC	14.99758

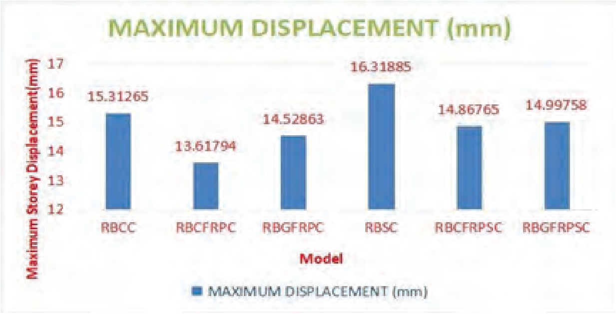

Fig. 16 Maximum Storey Displacement of Regular Building

For G+15 regular structures, lateral storey displacements for CFRP and GFRP circular and square columns are shown in Fig. 6.1. CFRP circular columns showed superior performance and were thus used in irregular buildings for further seismic analysis in ETABS. Displacement results for these irregular structures are presented in Table 5 and Fig. 17.

Table 5 Maximum Storey Displacement Values-Irregular Buildings

Building Models	Maximum Displacement (mm)
CBC	19.98632
CBCFRPC	19.74234
HBC	18.93495
HBCFRPC	18.87465
LBC	19.99931
LBCFRPC	19.87632

Fig. 17. Maximum Storey Displacement of irregular Buildings

Table 6 Maximum Storey Drift Values- Regular Buildings

Building Models	Maximum Drift
RBCC	0.000479
RBCFRPC	0.000432
RBGFRPC	0.000457
RBSC	0.000631
RBCFRPSC	0.000593
RBGFRPSC	0.000618

Fig. 18 . Maximum Storey Drift of regular Buildings

When it comes to G+15 regular rectangular structures, the maximum storey drift of those with CFRP,GFRP circular columns and Square columns are tabulated in Table 6 and graphically represented in Fig. 18. Based on the findings , CFRP circular columns performed well hence it is incooperated into irregular buildings and conducted seismic analysis using ETABS. When it comes to G+15 irregular structures, the Maximum storey drift of those with CFRP circular columns are tabulated in Table 7 and graphically represented in Fig. 19.

Table 7 Maximum Storey Drift Values – Irregular Buildings

Building Models	Maximum Drift
CBC	0.000716
CBCFRPC	0.000652
HBC	0.000693
HBCFRPC	0.000598
LBC	0.000763
LBCFRPC	0.000759

Fig. 19 Maximum Storey Drift of irregular Buildings

Table 8 Maximum Storey Shear Values

Building Models	Maximum Shear(kN)
RBCC	1965
RBCFRPC	2235
RBGFRPC	2059
RBSC	1680
RBCFRPSC	1997
RBGFRPSC	1896

Fig. 20. Maximum Storey Shear of regular Buildings

For G+15 regular structures, maximum storey shear for CFRP and GFRP columns is shown in Table 7 and Fig. 19. CFRP circular columns performed best and were used in irregular buildings for seismic analysis in ETABs.

Table 8 Maximum Storey Shear Values – Irregular Buildings

Building Models	Maximum Shear(kN)
CBC	1728
CBCFRPC	1798
HBC	1774
HBCFRPC	1852
LBC	1716
LBCFRPC	1788

Fig. 21. Maximum Storey Shear of irregular Buildings

When it comes to G+15 irregular structures, the Maximum storey drift of those with CFRP circular columns are tabulated in Table 8 and graphically represented in Fig. 21.

COST ANALYSIS

Cost is a key factor in material selection. CFRP is generally more expensive than steel due to its complex production and high-grade components, but its strength-to-weight ratio and durability can offset long-term costs. Steel is more affordable with simpler manufacturing but may require more maintenance due to rust and weight. GFRP, though costlier than steel, is less expensive than CFRP and involves specialized manufacturing, which raises its cost.

CONCLUSIONS

- The study on G+15 buildings showed that CFRP columns significantly enhance structural stability and earthquake resilience compared to GFRP and reinforced concrete (RC) columns.
- CFRP circular columns increased storey shear by about 12% over RCC columns and reduced maximum story drift by approximately 9%, indicating improved seismic performance.
- GFRP circular columns showed around a 4.5%

reduction in both storey shear and drift compared to normal RC circular columns.

- Lateral story displacement decreased by roughly 11% with CFRP circular columns and by about 5% with GFRP circular columns in regular rectangular buildings.
- Circular columns provide better seismic resistance due to uniform load distribution and fewer stress concentrations, while square columns are easier to construct but may have higher stress at sharp edges.
- CFRP columns offer exceptional fatigue resistance, strength, stiffness, ductility, and energy dissipation, making them highly effective during seismic events.
- GFRP columns have good strength and durability but lower stiffness and modulus, resulting in comparatively reduced seismic capabilities.
- RC columns, though economical and widely used, may require additional reinforcement and finishing to match the seismic resilience of composite materials.
- In irregular building plans (C, H, L shapes), CFRP circular columns reduced storey displacement by 12%, storey drift by 15%, and increased storey shear by about 4%, showing enhanced performance despite irregularities.
- Steel typically has a lower initial material cost per unit weight compared to CFRP and GFRP; however, total lifecycle costs depend on factors like installation complexity, maintenance, and design constraints.
- Selecting between CFRP, GFRP, and steel demands a comprehensive evaluation of cost, seismic performance, construction feasibility, and specific project requirements.

REFERENCES

1. Ali, M.A. and El-Salakawy (2016) “Seismic performance of GFRP-reinforced concrete rectangular columns’’. Journal of Composites for Construction, 20(3), p.04015074.
2. Gajendra (2015) “Seismic Evaluation Of Beam-Column Joints Using GFRP Bars In Multi- Storey Building using Etabs’’
3. Jun, Chenzhe, Wenbo, Xiangcheng and Yuping (2021), August “Experimental and numerical studies on seismic performance of rectangular concrete columns reinforced by CFRP bars with different ratios and positions’’. (Vol. 32, pp. 237- 253), Elsevier
4. Kumawat and Kalurkar, L. G. (2014) “Static & Dynamic Analysis Of Multistory Building Using Composite Structure.” International Journal of Research in Engineering and Technology, 3(7), 638-347.
5. Mincigrucci, Civera, Lenticchia, Ceravolo, Rosano and Russo,(2023) “Comparative Structural Analysis of GFRP, Reinforced Concrete, and Steel Frames under Seismic Loads”. Materials, 16(14), p.4908.
6. Ozcan, Binici, Ozcebe, (2008) “Improving seismic performance of deficient reinforced concrete columns using carbon fiber-reinforced polymers”. Engineering structures, 30(6), pp.1632-1646.
7. Purushothaman and Sukumaran (2017) “Comparative study on seismic analysis of multi storied buildings with composite columns”. International Journal of Engineering Research & Technology, ISSN, pp.2278-0181.
8. Shetty, Bhandary, Shetty (2020) “Comparative study on seismic performance of specially shaped RC columns with that of rectangular columns in high-rise structures”. International Journal of Structural Integrity, 11(2), pp.202-215.
9. Vedha and Pash (2019) “ Study of seismic and wind effects on multistorey RCC, steel and composite materials buildings using ETABS”. Int. J. Eng. Res. Tech., Special Issue, p.16.
10. Wang, Yang, Cheng, (2019) “Experimental study of seismic behavior of high- strength RC columns strengthened with CFRP subjected to cyclic loading”. Journal of Structural Engineering, 145(2), p.04018240.

Fluid Structure Interaction Analysis of Fabric Plate in Free Fall

Thamanna Iqbal
PG Scholar
Department of Civil Engineering
NSS College of Engineering
Palakkad, Kerala
✉ thammuiqbal69@gmail.com

Nisha A S
Assistant Professor
Department of Civil Engineering
NSS College of Engineering
Palakkad, Kerala
✉ asnisha@nssce.ac.in

ABSTRACT

This study conducts an in-depth fluid-structure interaction (FSI) analysis of a circular fabric plate moving downward in air with an initial velocity. The primary aim is to assess the fabric plate's dynamic response by examining displacement, velocity, stress, and pressure distributions. Utilizing the advanced capabilities of LS-DYNA software, the simulation captures the complex interaction between the air and the fabric structure. To ensure the FSI model's accuracy and reliability, results are systematically compared with those from a purely non FSI analysis, which ignores the effects of the surrounding air. This comparison offers a deeper understanding of how air-structure interactions influence the fabric plate's behavior. The findings reveal significant differences in the fabric plate's response under FSI conditions compared to structural-only conditions. The analysis shows that airflow around the fabric plate generates additional pressure forces and alters the overall stress distribution, effects not accounted for in the structural-only model. This research offers valuable insights into the dynamic behavior of fabric materials in fluid environments, relevant to applications such as parachutes, sails, and flexible aerospace structures. The use of LS-DYNA software demonstrates its effectiveness in addressing complex FSI challenges by accurately capturing the coupled behavior of fluid and structure.

KEYWORDS: *Fluid structure interaction (FSI), Fabric plate, LS DYNA.*

INTRODUCTION

Fluid-Structure Interaction (FSI) analysis is indispensable for understanding the behavior of membrane structures, which are inherently susceptible to dynamic interactions with surrounding fluids. By accurately representing these interactions, FSI analysis enables precise predictions of structural responses, pinpointing key parameters affecting integrity and facilitating design improvements. By exploring the intricate interplay between membrane structures and fluid dynamics, FSI analysis enhances insights into their performance under varied loading conditions, allowing engineers to refine designs and detect potential failure modes.

Membrane structures have captivated structural engineering due to their versatility, efficiency, and aesthetic appeal, driving extensive research and design exploration. Membrane constructions are vulnerable to a variety of environmental factors, including as wind, rain, and seismic activity, which can result in intricate fluid-structure interaction (FSI) phenomena, despite their widespread usage and structural inventiveness.

Fluid-Structure Interaction (FSI) analysis holds a crucial role in comprehending how fabric plates behave in scenarios involving free fall, where the interaction between flexible fabric structure and the surrounding air profoundly impacts their dynamics and effectiveness. Fabric plates are frequently encountered in various membrane structures such as parachutes, airbags, and inflatable structures, where their response to aerodynamic forces and fluid flow dynamics is fundamental for operational success and safety assurance. Therefore, grasping their reaction to aerodynamic forces and impact is pivotal for optimizing design enhancement. FSI analysis tackles these challenges by replicating the interactions between the deformable fabric structure and the airflow.

BACKGROUND SUMMARY

Garrec et al. examined simulations of parachute deployment utilizing strong Fluid-Structure Interaction (FSI) coupling methods and the LS-DYNA Implicit Computational Fluid Dynamics (ICFD) solver. The study attempted to precisely represent the complex interactions between the parachute and surrounding airflow during deployment by utilizing the sophisticated FSI coupling and ICFD solver of LS-DYNA [5]. Gao et al. created a novel coupling model to forecast the payload's trajectory and the parachute's opening phase during low-altitude airdrop operations. The work improved accuracy by introducing moving mesh technology to provide finite mass inflation modelling [3]. The difficult challenge of forecasting parachute inflation dynamics is tackled by Gao et al. through the integration of complex fluid- structure interaction (FSI) and flight mechanics behaviours within a limited mass context. The Navier-Stokes equations for incompressible flow are solved explicitly using the central difference approach in order to capture the complex dynamics [4]. Saeedi et al. used a two-way coupled fluid-structure interaction study to assess the aerodynamic performance because of the intricate relationship between aerodynamic load and membrane deformation [9]. Gao et al. modelled the FSI behaviour of parachutes using the LS-DYNA nonlinear finite element algorithm [16].

The objective of this project work is to assess the fluid – structure interaction of a membrane structure (fabric plate) moving downwards through air domain with an initial velocity.

FLUID STRUCTURE INTERACTION

The intricate, multidisciplinary discipline of fluid-structure interaction (FSI) examines the relationship that exists between solid structures and fluid movement. FSI is a multi-physics interaction between the principles of structural mechanics and fluid dynamics. It involves the interaction of an internal or external fluid flow with a moveable or deformable structure. Predicting fluid-structure interactions accurately is essential to guaranteeing the performance, safety, and dependability of engineering systems subjected to fluid forces. Fig 1 is a flow chart that illustrates the FSI Analysis procedure.

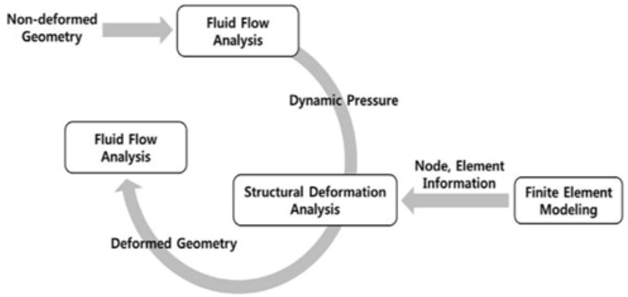

Fig. 1. Flow Chart of FSI Analysis [1]

The characteristics of fluids in motion are governed by the laws of fluid dynamics. Fluid flow may use buoyancy, lift, drag, and other mass effects to apply forces on adjacent structures. The behavior of solid structures under external loads, including stresses, strains, deformations, and vibrations, is described by the principles of structural mechanics. A structure's reaction to fluid forces is influenced by a number of variables, including the geometry, material qualities, boundary conditions, and structural damping. The coupling effects between fluid dynamics and structural mechanics are known as fluid-structure interaction, and they occur when fluid forces cause structural deformations and structural movements change the fluid flow field around them. The aerodynamic forces exerted by the surrounding fluid induce deformation resulting in alterations to its shape and orientation. Furthermore, the motion of the fabric influences the airflow around it, thereby modifying fluid dynamics and further impacting its behavior.

Arbitrary Lagrangian Eulerian (ALE) Mesh for FSI Analysis

The ALE method is highly relevant in FSI simulations because it accommodates materials undergoing significant deformation while ensuring computational stability. In FSI scenarios, like fluid flow interacting with flexible structures, ALE offers a versatile approach where the mesh can follow the fluid, the structure, or both. Employing an ALE mesh enables independent discretization of fluid and structure domains, enhancing the efficiency and accuracy of interactions between them. This technique addresses challenges such as mesh distortion and instability often encountered in purely Lagrangian or Eulerian methods. The adaptability results in more precise, stable, and efficient simulations, establishing ALE mesh as an essential tool in the analysis and application of fluid-structure interactions.

Mathematical Equations

The governing mathematical equations of FSI are based on the core principles of conservation laws, continuum mechanics, and thermodynamics. The Navier-Stokes equations describe the behavior of the fluid by expressing conservation laws as given in Eq. (1) and Eq. (2).

$$\frac{\partial \rho}{\partial t} + \nabla . (\rho u) = 0 \tag{1}$$

$$\rho \left(\frac{\partial u}{\partial t} + (u . \nabla)\, u\right) = -\nabla p + \mu \nabla^2 u + f \tag{2}$$

where, ρ is the fluid density, u is the fluid velocity vector, p is the pressure, µ is the dynamic viscosity and f represents the body forces like gravity.

The structural response is described by the equations of elasticity or dynamics of solids as expressed in Eq. (3).

$$\rho_s \frac{\partial^2 d}{\partial t^2} = \nabla . \sigma + f_s \tag{3}$$

where, ρ_s is the density of solid, d is the displacement vector, σ is the stress tensor and fs represent s the external forces.

FABRIC PLATE

A thin, flexible structure composed of fabric is commonly referred to as a fabric plate. It can take many different forms, including membranes, curved surfaces, and flat panels. Fabric plates find frequent application in engineering contexts where the benefits of lightweight and flexible materials are paramount. These constructions commonly depend on the characteristics of the fabric, such as its flexibility, robustness, and stretch ability, to fulfil particular roles such as generating aerodynamic lift.

Studying the movement of a fabric plate in air with an initial downward velocity is approached in two manners. Firstly, akin to structural analysis, the plate receives an initial velocity and experiences a load equivalent to atmospheric pressure. Secondly, in Fluid-Structure Interaction (FSI) analysis, the fabric plate is placed within the air, subjected to atmospheric pressure. The findings of stress, pressure, velocity, and displacement are compared for the two analysis situations.

Fabric Plate Model for Analysis

The fabric plate model adopted in the FSI analysis is of circular shape. The z-axis translation movement along the edge of the plate is unrestricted, while translations in other directions and rotations in all directions remain fixed. The initial velocity is provided along the edge of the plate. The plate is placed inside an air domain modelled with the size 800 x 800 x 2000 mm. Table 1 provides information on the model's geometry and materials.

Table 1. Fabric Plate Model Details

Parameters	Value
Diameter	150 mm
Initial Velocity	50 m/s
Mass Density	1.14e^{-7} tonne/mm^3
Modulus of Elasticity	270 MPa
Poisson's Ratio	0.39
Mass	0.5 kg

NON FSI ANALYSIS OF FABRIC PLATE

The fabric plate is subjected to an initial velocity and a pressure load of 0.1 MPa which is equivalent to the atmospheric pressure in order to perform the non FSI analysis. Fig 2 depicts the analysis model.

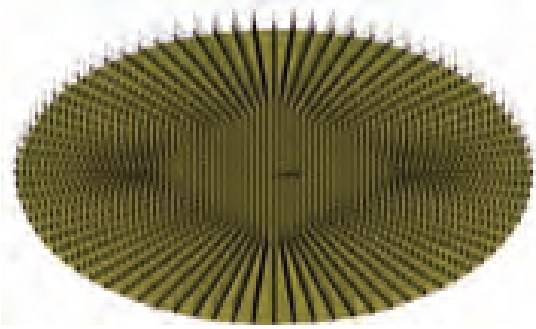

Fig. 2. Pressure Load applied on the Plate

Results of Non FSI Analysis

The results obtained for the non FSI analysis of plate is shown in Fig 3.

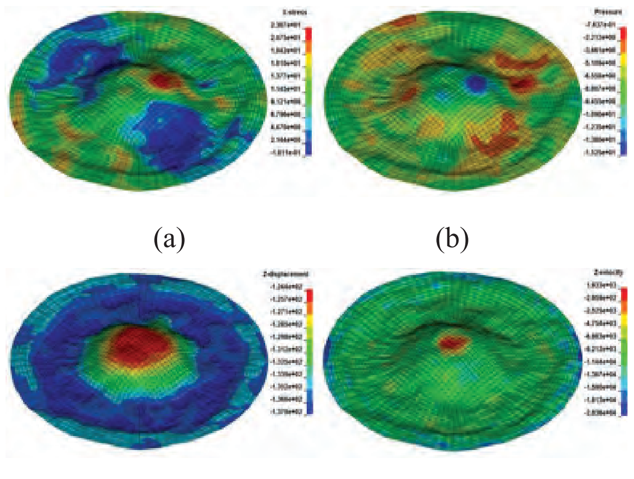

(a) (b)

(c) (d)

Fig 3. Contour Plots of Plate under Non FSI Analysis (a) Stress Results (b) Pressure Results (c) Displacement Results (d) Velocity Results

FSI ANALYSIS OF FABRIC PLATE

The FSI analysis is carried out for the fabric plate by placing the plate inside the air domain and utilizing the required LS DYNA keywords appropriately.

LS DYNA Keywords for FSI Analysis

Accurately defining keywords in LS DYNA is crucial for simulating the real behavior of both the structure and fluid in FSI analysis. To initiate atmospheric pressure in the simulation, *EOS_LINEAR_POLYNOMIAL is employed, setting the pressure to 1 atm. The coupling between the fabric plate and air is established using *CONSTRAINED_LAGRANGE_IN_SOLID. Within this keyword, the parameter CTYPE determines the coupling type, with penalty coupling being employed. The DIREC option specifies the coupling direction, with compression-only coupling in the normal direction selected for this analysis. The fabric plate serves as the slave part, while the air domain functions as the master part.

Validation of FSI Analysis of Fabric Plate

The FSI analysis involves placing the fabric plate within the air domain, where the drag force arises from the air surrounding the plate rather than directly applying force as a load in the simulation. The interaction between the fluid and solid components is defined using the available options within the software. Ensuring the correctness of the modelling strategy is crucial for the analysis to be valid. In general, when considering a fabric plate or any structure placed in the air and moving with an initial downward velocity, akin to free-fall conditions, the drag force is attributed to the motion of the structure by the surrounding air, as illustrated in Fig 4. The equations to calculate the terminal velocity of the plate is as shown in Eq. (4).

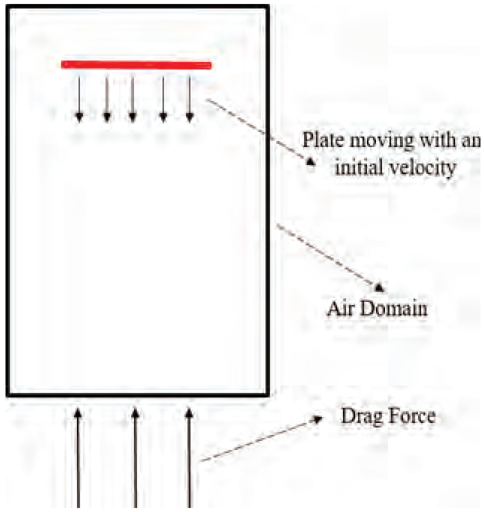

Fig. 4. Plate moving in Air domain

$$v_t = \frac{1}{\frac{1}{v_i} + \frac{C_D \rho S t}{2m}} \tag{4}$$

where, v_t and v_i is the terminal and initial velocity respectively, CD is the coefficient of drag, ρ is the density of air, S is the surface area of plate, m is the mass of plate and t is the time duration of analysis.

The initial rigid body velocity of the plate is set at 1530 mm/s, with a CD value specified as 0.8. Substituting values into Eq. (4) for a duration of 0.3 seconds yields a terminal velocity of 1520 mm/s. However, the terminal velocity obtained from the numerical analysis is 1480 mm/s. The difference in the values between both the methods gives an error percentage of 2.63 %, which is less than 5%. The terminal velocity vs. time graph is plotted for both the analysis for comparison as shown in Fig 5.

Given the relatively low percentage error observed between the two methods, it can be inferred that the approach of conducting numerical simulations for FSI analysis is acceptable. Consequently, it can be deduced that the outcomes derived from this study accurately replicate real-world conditions.

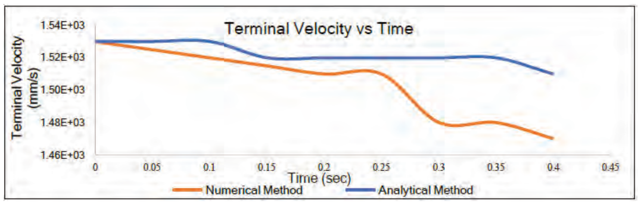

Fig. 5. Terminal Velocity vs. Time Graph

Results of FSI Analysis

The results obtained for the FSI analysis of fabric plate is shown in Fig 6.

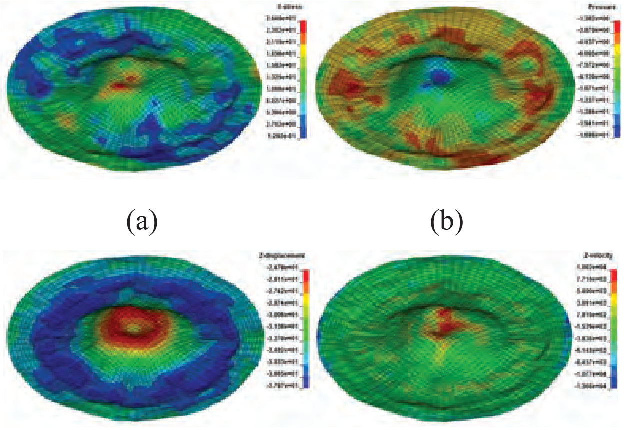

(a) (b)

(c) (d)

Fig 6. Contour Plots of Plate under FSI Analysis (a) Stress Results (b) Pressure Results (c) Displacement Results (d) Velocity Results

RESULTS AND INFERENCES

The fabric plate is studied under both FSI and non FSI analysis. Table 2 presents the results obtained for various parameters in both analyses.

Table 2. Comparison between FSI and Non FSI Analysis of Fabric Plate

Parameter	FSI Analysis	Non FSI Analysis
Stress	26.46 N/mm^2	23.07 N/mm^2
Pressure	15.25 N/mm^2	16.98 N/mm^2
Displacement	13.18 mm	13.50 mm
Velocity	13.08e^3 mm/s	20.36e^3 mm/s

The findings show that, in both scenarios, the stress value is almost same, suggesting consistent force application on the fabric plate across both methods. Similarly, the comparable pressure loads acting on the fabric plate demonstrate uniform conditions in both analyses. The differences in fabric plate displacement values highlight the significance of considering FSI interaction, as it leads to a more accurate estimation of membrane structure response. Furthermore, the greater reduction in velocity observed in FSI analysis compared to non FSI analysis reflects the presence of drag force, mirroring real-world conditions.

In free fall, objects experience drag force, proportional to the square of velocity, which rapidly diminishes their speed. Thus, when a fabric object starts with an initial velocity, it quickly encounters drag force, swiftly reducing its velocity. This mirrors the actual physics that underlies in a fabric plate's free fall state, which is precisely what the FSI analysis does. This underscores the importance of conducting FSI analysis for precise and realistic results, ensuring the faithful replication of real-world scenarios and highlighting its relevance in every study.

FSI analysis is essential for capturing the interaction between fluid and structure, which is vital for accurately predicting how structures behave when exposed to fluid forces. This analysis is crucial for both design and financial considerations, ensuring the structure performs as expected under fluid forces and preventing costly overdesign or potential structural failures. FSI analysis accounts for additional forces such as drag, which change the overall stress and pressure distribution on the structure, offering a more realistic understanding of its behavior in actual fluid environments, something structural-only analysis cannot provide. In summary, even if parameter variations appear insignificant in some cases, FSI analysis is crucial for accurately simulating and understanding the behavior of structures in fluid environments.

PRACTICAL IMPLICATIONS

The insights into the dynamic behavior of fabric materials in fluid environments are key to optimizing structural designs. By understanding stress and pressure distributions, engineers can select appropriate materials and design shapes that enhance both performance and safety. For tensile structures like fabric roofs, FSI analysis helps predict behavior under wind loads, enhancing both structural integrity and longevity. The study underscores the importance of selecting materials with the right flexibility, strength, and damping properties to withstand dynamic fluid forces. FSI analysis provides crucial data for safety features in applications like airbags and inflatable structures, ensuring reliable performance under sudden fluid impacts. Additionally, optimizing designs based on FSI results can lower material costs and improve structural efficiency, leading to significant cost savings over time.

FUTURE TRENDS

This research has greatly enhanced the comprehension of fluid-structure interactions in membrane structures, such as fabric plates. Ongoing exploration and application of these findings are expected to drive structural engineering forward, providing innovative solutions to intricate engineering problems. Future research should build on these foundational insights by investigating new materials and advanced modelling techniques to further expand the capabilities and applications of membrane structures across various engineering fields.

CONCLUSIONS

This comprehensive analysis has demonstrated the effectiveness of the methodologies and parameters used in LS-DYNA for solving Fluid-Structure Interaction (FSI) problems, highlighting their reliability in predicting the behavior of fabric plates. The main conclusions from the study are:

- The research highlights the complex dynamics of fluid-structure interactions in membrane structures, which are significantly influenced by environmental factors such as wind and pressure fluctuations, which can cause substantial deformations and stresses.
- The use of the ALE mesh in LS-DYNA has proven to be a powerful tool for capturing the intricate behavior of membrane structures and have enabled precise modelling.
- The investigation revealed that fabric plates undergo deformation under fluid loading, with the extent of deformation dependent on factors like fluid velocity, material properties, and boundary conditions.

REFERENCES

1. Bak, S., and Yoo, J. (2019). “FSI analysis on the sail performance of a yacht with rig deformation.” International Journal of Naval Architecture and Ocean Engineering, 11 (2): 648–661.
2. Coquet, Y., Bordenave, P., Capmas, G., and Espinosa, C. (2011). “Improvements in Fluid Structure Interaction Simulations of Parachutes Using LS-Dyna.” 21st AIAA Aerodynamic Decelerator Systems Technology Conference and Seminar, American Institute of Aeronautics and Astronautics, Reston, Virigina.
3. Gao, X., Zhang, Q., and Tang, Q. (2017). “Fluid–structure interaction and flight dynamics analysis of parachute–payload system during uncontrolled airdrop process.” Proceedings of the Institution of Mechanical Engineers, Part G: Journal of Aerospace Engineering, SAGE Publications, 232(13), 2499–2512.
4. Gao, X., Zhang, Q., and Tang, Q. (2016). “Fluid-Structure Interaction Analysis of Parachute Finite Mass Inflation.” International Journal of Aerospace Engineering, Hindawi Limited, 2016, 1–8.
5. Garrec, M. L., Poncet, A., and Lapoujade, V. (2019). “Parachute Deployment Simulations using LS- DYNA ICFD Solver and Strong FSI Coupling.” 12th European LS-DYNA Conference 2019.
6. Hadjioannou, M., Sammarco, E., and Barsotti, M. (2019). “Drag Force Simulation on Blast Loaded Fabric Roof.” 12th European LS-DYNA Conference 2019.
7. Janda, M. D., Roland, S. J., and Lowry, C. W. (2015). “Computational Analysis of Parachute Textile Seams and Joints.” 23rd AIAA Aerodynamic Decelerator Systems Technology Conference, American Institute of Aeronautics and Astronautics, Reston, Virginia.
8. Pruett, M., Accorsi, M., and Kandis, M. (2009). “Stress Analysis of the Parachute System for the Mars Science Laboratory Mission.” 20th AIAA Aerodynamic Decelerator Systems Technology Conference and Seminar, American Institute of Aeronautics and Astronautics, Reston, Virigina.

9. Saeedi, M., Wüchner, R., and Bletzinger, K.-U. (2016). "Fluid-Structure interaction analysis and performance evaluation of a membrane blade." Journal of Physics: Conference Series, IOP Publishing, 753, 102009.
10. Stein, K., Benney, R., Kalro, V., Tezduyar, T. E., Leonard, J., and Accorsi, M. (2000). "Parachute fluid–structure interactions: 3-D computation." Computer Methods in Applied Mechanics and Engineering, Elsevier BV, 190(3–4), 373–386.
11. Taylor, A.P. (2002). "Developments in the Application of LS DYNA to Fluid Structure Interaction Problems in Recovery System Design and Analysis." 7th International LS-SYNA Users Conference.
12. Tutt, B., Dave, P., Scott, R., and Ray, D. (2011). "Parachute Load Prediction using a Combination of Empirical Data and Fluid Structure Interaction Simulations." 21st AIAA Aerodynamic Decelerator Systems Technology Conference and Seminar.
13. Tutt, B. A. (2013). "Fluid Structure Interaction Parachute Benchmark Models in LS-DYNA." AIAA Aerodynamic Decelerator Systems (ADS) Conference, American Institute of Aeronautics and Astronautics, Reston, Virginia.
14. Tutt, B., Scott, R., Richard, C., and Noetscher, G. (2010). "Development of Parachute Simulation Techniques in LS-DYNA." 11th International LS-DYNA Conference.
15. Tutt, B. (2006). "The Application of a New Material Porosity Algorithm for Parachute Analysis." 9th International LS-DYNA Users Conference.
16. Xinglong, G., Qingbib, Z., Qiangang, T., and Tao, Y. (2013). "Fluid-Structure Interaction Simulation of Parachute in Low Speed Airdrop." Lecture Notes in Engineering and Computer Science.
17. Zhu, H., J. Tao, Q. Sun, H. Sun, F. Duan, Z. Chen, X. Zeng, and D. Soulat. (2023). "Effect of Shear Modulus on the Inflation Deformation of Parachutes Based on Fluid-Structure Interaction Simulation." Sustainability, 15 (6): 5396.

Parametric Studies on the Seismic Performance of Braced Corrugated Shear Panels

Junaid J
PG Scholar
Department of Civil Engineering
NSS College of Engineering
Palakkad, Kerala
✉ j.junaid353@gmail.com

Deepthy S Nair
Assistant Professor
Department of Civil Engineering
NSS College of Engineering
Palakkad, Kerala
✉ 91deepthy@gmail.com

ABSTRACT

This research examines the seismic performance of braced corrugated shear panels. It looks at how different thicknesses and depths of corrugations affect performance. The study used models with thicknesses between 6mm and 10mm and corrugation depths from 20mm to 100mm. Non-linear cyclic analyses were performed under cyclic loading conditions. The results show that thicker panels significantly improve performance. There is a 40% increase in energy dissipation capacity, a 20% improvement in ultimate load resisting capacity, and a doubling of the ductility ratio. However, by increasing the depth of the corrugations, it leads to increase in energy dissipation and ultimate load only up to a depth of 40mm. After that, energy dissipation capacity starts to decline. The study shows the need to optimize both thickness and depth. It reveals that raising both parameters at the same time can result in the panels becoming too stiff and reducing their energy dissipation capacity. Overall, these findings contribute to enhancing the earthquake resistance of braced corrugated shear panels.

KEYWORDS: *Corrugations, Ductility, Energy dissipation.*

INTRODUCTION

Braced Corrugated Ductile Shear Panels (BCDSP) offer a highly effective and modern solution for enhancing the seismic performance of structural systems. These panels incorporate corrugated steel profiles in combination with internal bracing mechanisms, creating a hybrid system that significantly improves a structure's ability to endure earthquake-induced stresses.

The corrugated geometry increases the panel's out-of-plane stiffness and allows it to undergo large deformations while still maintaining its load-bearing capacity. This deformation capacity is critical in seismic events, where energy dissipation and structural flexibility can prevent brittle failure.

The bracing elements within the panel act to restrain excessive lateral displacement, reducing inter-story drift and helping the building maintain its shape during dynamic loading. Unlike flat shear panels, the corrugated configuration allows for better distribution of stress and helps localize plastic deformation, which enhances ductility and energy absorption.

Additionally, this system can be tailored for use in both retrofitting older structures and in the seismic design of new buildings. In high-rise construction, where lateral loads are amplified due to building height, BCDSPs provide a reliable and adaptable solution that contributes to the overall durability and resilience of the structure during an earthquake.[4].

FINITE ELEMENT MODELLING OF BRACED CORRUGATED SHEAR PANEL

Model Details

Fifteen models with different thicknesses and depths of corrugations are examined to conduct a parametric study. This study aims to understand how changing various parameters impacts seismic performance. The parameters considered are the thickness of the corrugated panel and the depth of the corrugations. The thickness of the corrugated shear panels is 6mm, 8mm, and 10mm. The depths of the corrugations are 20mm, 40mm, 60mm, 80mm, and 100mm.

Material Properties

Table 1 shows the specifications of materials used in developing three different panel models having variations in thickness and corrugation depth.

Table 1. Material Specifications for models of variable parameters

PROPERTIES	VALUES
Bracing Steel Yield Strength	345N/mm2
Panel Steel Yield Strength	235N/mm2
Shear panel dimensions	450mmX450mm
Thickness of panel	6mm
Poisson ratio of steel	0.3
Total dimension	840mmx1400mm
Profile of corrugation	Trapezoidal
Angle of corrugation	450

Modelling

The analysis models are created with ANSYS software. The 20-node Solid186 element was chosen for building the models because it provides accurate results. Hexahedral elements were used for meshing to ensure proper representation of the geometry. The models vary in parameters like thickness and depth of corrugations. They are labeled asMTaDb, where the subscript T indicates the thickness value and the subscript D shows the depth of corrugations for each model. The basic model is shown in Fig 1.

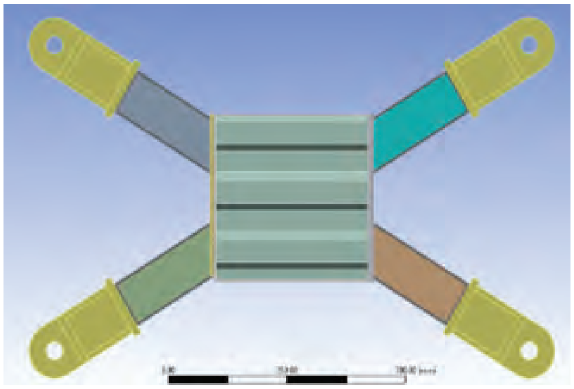

Fig. 1. Braced corrugated shear panel

Loading Protocol

The FEMA loading protocol is applied to every models. A displacement-controlled method based on the drift ratio (δ/H) was used, where δ represents lateral drift and H is the height between the top and bottom hinges. Displacement values are calculated from the drift ratios and applied as lateral displacements at the top node of the model. The bottom interface node was fixed to prevent both translation and rotation. The model analysis was primarily performed under cyclic loading conditions. The loading cycle is illustrated in Fig 2.

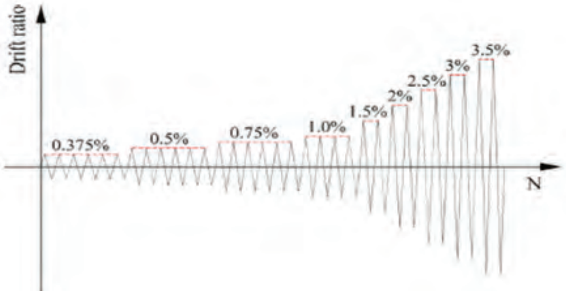

Fig. 2. Loading Protocol [11]

RESULTS

The output parameters for the analysis include Energy Dissipation Capacity, Ultimate Load, Maximum Displacement, and Ductility Ratio. The results from the ANSYS Software are hysteresis curves that display all the values of loads in every cycle at the respective drift values. The maximum loads from each cycle along with the related drift percentages are plotted to create envelope curves. The area under the hysteresis curves is found out using Origin Software to find the Energy Dissipation Capacity values. The results regarding maximum displacement, ultimate load, energy dissipation capacity, and ductility ratio for different models of braced corrugated shear panels with varying thicknesses at a constant depth of 20mm are shown in Table 2.

Table 2. Comparative Review of Results of Corrugated shear panel models of varying thickness at constant corrugation depth of 20mm

Models	Maximum Displace-ment (mm)	Maximum Load (kN)	EDC (kN mm)	Ductility Ratio
MT_6D_{20}	12.605	583.82	140.5377	4.01

MT_8D_{20}	16.8	753.02	199.13	5.34
$MT_{10}D_{20}$	25.205	915.91	247.870	8.02

The results of maximum displacement, ultimate load, energy dissipation capacity and ductility ratio for different models of braced corrugated shear panels of 6mm , 8mm and 10mm thickness at varying depths are given in Table 3, Table 4 and Table 5 respectively

Table 3. Comparative Review of Results of Corrugated shear panel models of 6mm thick panels of varying corrugation depths

Models	Maximum Displace-ment (mm)	Maximum Load (kN)	EDC (kN mm)	Ductility Ratio
MT_6D_{20}	12.60	583.82	140.53	4.01
MT_6D_{40}	25.21	623.23	164.28	8.01
MT_6D_{60}	25.21	627.06	163.23	8.01
MT_6D_{80}	25.21	628.85	160.77	8.01
MT_6D_{100}	25.21	618.8	157.96	8.01

Table 4. Comparative Review of Results of Corrugated shear panel models of 8mm thick panels of varying corrugation depths

Models	Maximum Displace-ment (mm)	Maximum Load (kN)	EDC (kN mm)	Ductility Ratio
MT_8D_{20}	16.8	753.02	199.13	5.34
MT_8D_{40}	25.20	773.32	205.7	8.02
MT_8D_{60}	25.20	778.7	204.69	8.01
MT_8D_{80}	25.20	779.23	202.68	8.01
MT_8D_{100}	25.21	781.22	200.16	8.01

Table 5. Comparative Review of Results of Corrugated shear panel models of 10mm thick panels of varying corrugation depths

Models	Maximum Displace-ment (mm)	Maximum Load (kN)	EDC (kN mm)	Ductility Ratio
$MT_{10}D_{20}$	25.20	915.91	247.87	8.02
$MT_{10}D_{40}$	25.20	916.24	245.31	8.02
$MT_{10}D_{60}$	25.20	919.92	244.1	8.02
$MT_{10}D_{80}$	25.20	920.29	241.73	8.02
$MT_{10}D_{100}$	25.20	923.04	238.74	8.02

The combined envelope curves for models of different thickness of corrugations at constant depth of 20mm is shown in Fig 3. The combined envelope curve showed that the maximum load values increased with increase in thickness of the shear panel.

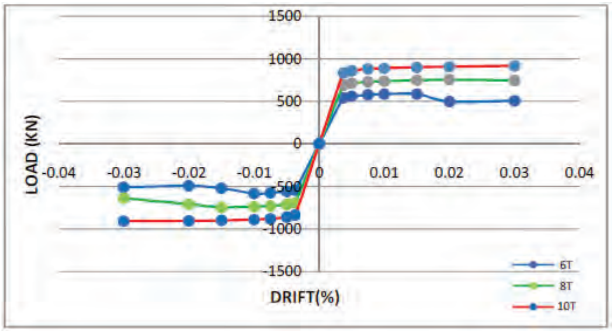

Fig. 3. Combined Envelope Curve for models of different thickness of panel at constant corrugation depth of 20mm

The bar graphsillustrating the variation of energy dissipating capacity, ultimate loads, and ductility ratios for models of different thickness of panels are given in Fig 4.

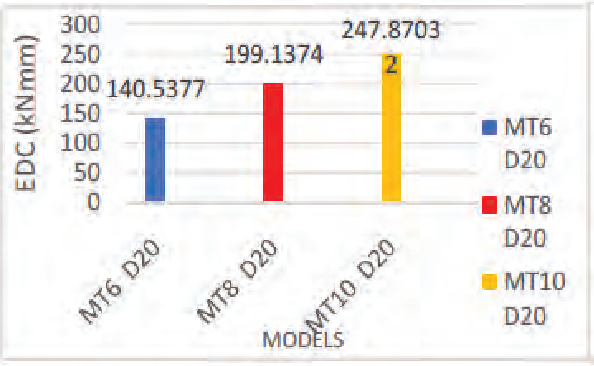

(a)

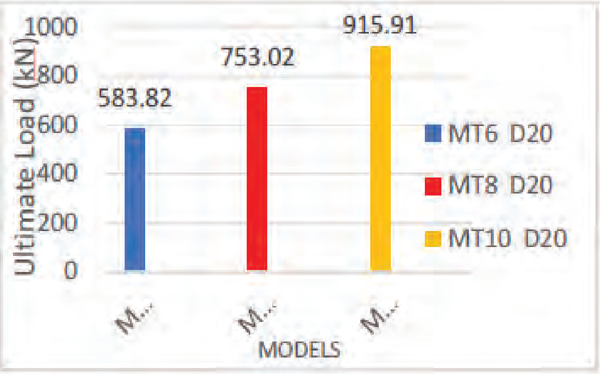

(b)

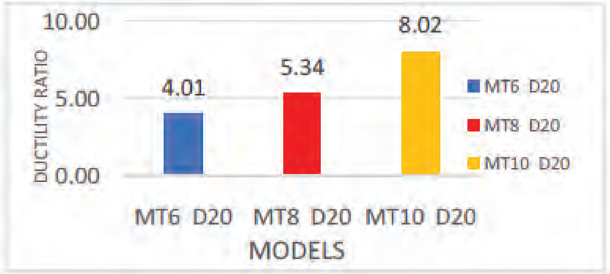

(c)

Fig 4: Comparison of results for models of varying thickness of panel (a) Energy Dissipation Capacity (b) Ultimate Load (c) Ductility Ratio

The comparison of output parameters for models with different panel thicknesses, as shown in Fig 4, revealed that increasing the thickness by 2mm at a constant depth resulted in an average increase of about 40% in energy dissipation capacity and a 20% increase in ultimate load carrying capacity. It was also noted that the ductility ratio nearly doubled when the panel thickness increased from 6mm to 10mm.The combined envelope curves for models of different depths of corrugations at shear panel thickness of 6mm is shown in Fig 5.

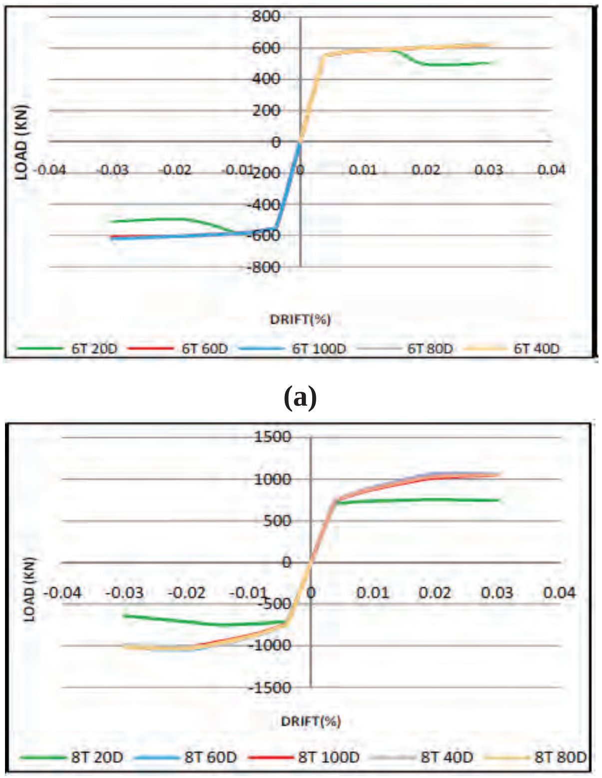

(a)

(b)

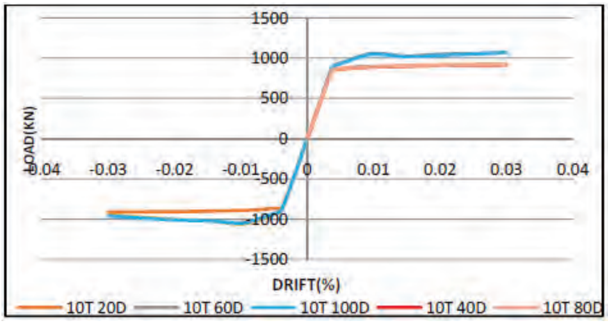

(c)

Fig 5: Combined Envelope Curves for (a)MT_6D_{20}, MT_6D_{40}, MT_6D_{60}, MT_6D_{80}, MT_6D_{100} models (b)MT_8D_{20}, $MT_8D_{40}$$MT_8D_{60}$, MT_8D_{80}, MT_8D_{100} models (c) $MT_{10}D_{20}$, $MT_{10}D_{40}$, $MT_{10}D_{60}$, $MT_{10}D_{80}$ $MT_{10}D_{100}$ models

The bar chart which represents the variation of energy dissipation capacity and ultimate load values of braced corrugated shear panel models of varying depth of corrugations at each panel thickness of 6mm, 8mm and 10mm are provided in Fig 6.

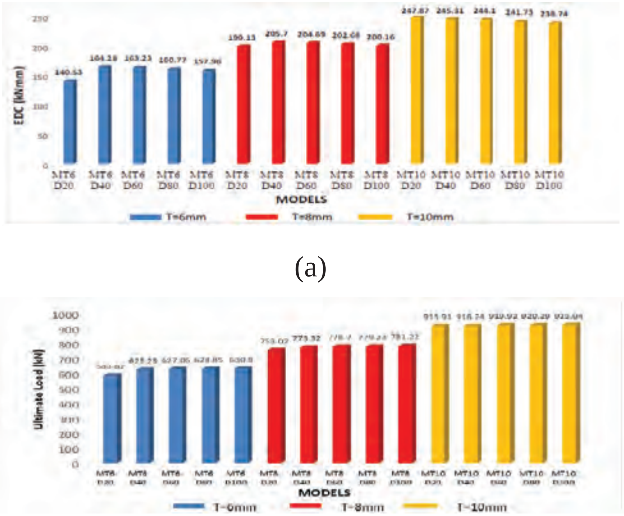

(a)

(b)

Fig 6: Comparative Review of Results (a) Energy Dissipating Capacity for varying depth of corrugations (b) Ultimate loads for models of varying depth of corrugations

From the analysis of energy dissipation capacity for shear panel models with varying depths, it was clear that panels with thicknesses of 6mm and 8mm showed higher energy dissipation as the depth of corrugation increased from 20mm to 40mm. However, further increases in depth caused energy dissipation to decrease. In contrast, for panels with a thickness of 10mm, the highest energy dissipation capacity occurred at a depth of 20mm, which fell with deeper corrugation. This decrease is due to over-stiffening caused by increasing both thickness and corrugation depth simultaneously. Similarly, when examining ultimate load values at varying depths of corrugation, significant differences were observed. For panels with thicknesses of 6mm and 8mm, ultimate load values increased noticeably as the depth of corrugation rose from 20mm to 40mm. However, beyond a depth of 40mm, the rise in ultimate load values became minor, indicating a limit beyond which further increases in corrugation depth do not significantly boost load-bearing capacity.

CONCLUSIONS

Increasing the thickness of shear panels at a constant depth leads to better seismic performance. Thicker panels increase the ability of structure to absorb and reduce seismic energy. This can make the structure more effective at handling seismic forces. Thicker panels can also support higher ultimate loads, which leads to rise in the overall load-bearing capability of the structure. With greater drift capacity, the structure can deform more without taking on severe damage. This improves its resilience during seismic events.

When the depth of the corrugations increases with each thickness, the results differ. For thicker panels, a shallower depth of corrugation is found to be better. This balance of stiffness and flexibility prevents early buckling while allowing energy dissipation. For thinner panels, a slightly deeper corrugation may be more suitable. This balance helps each panel achieve the best seismic performance.

Using both higher thickness and greater depth of corrugation at the same time can cause the shear panel to become too stiff. This extra stiffness reduces the panel's effectiveness in energy dissipation during seismic events since the increased rigidity hampers its ability to absorb and deform under stress. As a result, there is a noticeable drop in energy dissipation capacity and only slight improvements in ultimate load capacity. This outcome shows the need to optimize both thickness and corrugation depth to maintain the panel's overall performance.

REFERENCES

1. Akbari Hamed, A., &Mofid, M. (2015). On the experimental and numerical study of braced steel shear panels. The Structural Design of Tall and Special Buildings, 24(14), 853-872.
2. Brando, G., & De Matteis, G. (2011). Experimental and numerical analysis of a multi-stiffened pure aluminium shear panel. Thin-Walled Structures, 49(10), 1277-1287.
3. Chan, R. W., Albermani, F., & Williams, M. S. (2009). Evaluation of yielding shear panel device for passive energy dissipation. Journal of Constructional Steel Research, 65(2), 260-268.
4. Hareendran, A., & Beena, B. R. (2022, June). Seismic Performance of Braced Ductile Shear Panel. In International Conference on Structural Engineering and Construction Management (pp. 677-686). Cham: Springer International Publishing.
5. Kelly, J. M., Skinner, R. I., & Heine, A. J. (1972). Mechanisms of energy absorption in special devices for use in earthquake resistant structures. Bulletin of the New Zealand Society for Earthquake Engineering, 5(3), 63-88.
6. Li, Z., Albermani, F., Chan, R. W., &Kitipornchai, S. (2011). Pinching hysteretic response of yielding shear panel device. Engineering Structures, 33(3), 993-1000.
7. Mundada, A. P., & Modani, P. O. Effects of Various Bracing in Building with Rectangular Columns. International Journal of Advances in Engineering and Management (IJAEM), ISSN, 2395-5252.
8. Nakashima, M., Akazawa, T., & Tsuji, B. (1995). Strain-hardening behavior of shear panels made of low-yield steel. II: Model. Journal of structural Engineering, 121(12), 1750-1757.
9. Pourabdollah, O., Farahbod, F., &Rofooei, F. R. (2017). The seismic performance of K-braced cold-formed steel shear panels with improved connections. Journal of Constructional Steel Research, 135, 56-68.
10. Rahnavard, R., Hassanipour, A., Suleiman, M., & Mokhtari, A. (2017). Evaluation on eccentrically braced frame with single and double shear panels. Journal of Building Engineering, 10, 13-25.
11. Sun, Guohua, Cheng Bao, Wenyuan Liu, and Youzhen Fang. "Cyclic behavior of an innovative braced ductile thin shear panel." In Structures, vol. 32, pp. 973-986. Elsevier, 2021.

12. Sun, G., & Zhu, Y. (2021). Cyclic testing of an innovative self-centering X-braced ductile shear panel. Engineering Structures, 244, 112732.
13. Xiang, Y., Zhou, X., Shi, Y., Zhou, J., Ke, K., & Deng, F. (2023). Study on the seismic performance of cold-formed thin-walled steel frame with K-shaped braced shear panel. Thin-Walled Structures, 184, 110449.
14. Xu, L., Liu, J., & Li, Z. (2019). Cyclic behaviors of steel plate shear wall with self-centering energy dissipation braces. Journal of Constructional Steel Research, 153, 19-30.
15. Yu, Y., Hu, C., Zhao, F., & Jiang, L. (2022). Research on the specially-shaped corrugated steel plate shear walls with horizontal corrugation. Journal of Constructional Steel Research, 188, 107012.
16. Zhang, C., Aoki, T., Zhang, Q., & Wu, M. (2013). Experimental investigation on the low-yield-strength steel shear panel damper under different loading. Journal of Constructional Steel Research, 84, 105-113.
17. Zhang, C., Zhu, T., Wang, L., & Wu, M. (2017). Ultra-low cycle fatigue performance evaluation of the miniaturized low yield strength steel shear panel damper. Journal of Constructional Steel Research, 135, 277-284.

Shape Memory Alloy Integration in Exterior Beam-Column Joints: A Performance Analysis

Shahna Shirin M S
PG Scholar
Department of Civil Engineering
NSS College of Engineering
Palakkad, Kerala
✉ shahnashirinms@gmail.com

Deepthy S Nair
Assistant Professor
Department of Civil Engineering
NSS College of Engineering
Palakkad, Kerala
✉ 91deepthy@gmail.com

ABSTRACT

This study analyzes the behavior of Beam-Column Joints (BCJs) that are reinforced with Shape Memory Alloy (SMA) - Nickel-Titanium (Ni-Ti) when subjected to monotonic loads with varying percentages of SMA bars in the joint. Different models of BCJs are simulated in ABAQUS software with different percentages of SMA (25%, 50%, 75%, and 100%) as flexural reinforcement. The study also performs parametric studies to determine the Maximum Load, Energy dissipation, and Stiffness values. A performance comparison of the joint is performed between Ni-Ti SMAs in enhancing structural integrity versus conventional steel reinforcement. The results show that BCJs with 50% Ni-Ti SMA reinforcement exhibit superior performance. The SMA-reinforced BCJs show improvement in the performance of the parameters under study, emphasizing their potential for practical applications.

KEYWORDS: *Beam-Column Joints (BCJs), Shape memory alloys, Finite Element Modelling (FEM).*

INTRODUCTION

Beam-Column Joints (BCJs) in moment-resisting frames are typically the most vulnerable parts of a structure during seismic events. Earthquake-resistant design requires elastic behavior under moderate tremors and controlled inelastic behavior under stronger shaking. Conventional steel reinforcement, while effective in energy dissipation, leads to permanent deformations due to yielding. Shape Memory Alloys (SMAs), particularly Nickel-Titanium (Ni-Ti), offer a promising alternative due to their super- elasticity—allowing large inelastic deformations with full shape recovery upon unloading. SMAs exhibit high strength, excellent energy dissipation, strain recovery up to 8%, and resistance to corrosion and fatigue [17]. Their integration in BCJs reduces residual drifts, repair costs, and downtime, enhancing the ductility, durability, and seismic resilience of structures. The main objective is to to investigate the performance of BCJs reinforced with varying percentages of Ni-Ti SMAs under monotonic loads and compare them to conventional steel-reinforced joints.

BACKGROUND SUMMARY

Qian explored post-tensioned SMA strands in self-centering joints, improving seismic resilience, especially with thicker steel angles [13]. Sabbaghian and Kabir highlighted the ease of installation and reduced residual displacements with super-elastic SMA bars [16]. Elkafrawy studied Fe-SMA in prestressed RC beams, noting its effect on stiffness and behavior [5]. Qassim and Laftah investigated SMA-reinforced BCJs under static and cyclic loads, showing increased failure loads and displacements [12]. Rezapour applied Fe-SMA strips to masonry walls, enhancing stiffness and energy dissipation [15]. Muhammad Rahman emphasized the role of SMA shear reinforcement in improving crack recovery and load capacity [10]. Elbahy proposed SMA retrofitting for older RC frames to reduce residual deformations [4]. Youssef experimentally confirmed improved seismic performance of BCJs with super-elastic SMAs [18]. Ocel introduced SMA-based partially restrained connections with enhanced ductility and energy dissipation [11].

SHAPE MEMORY ALLOYS

Shape Memory Alloys (SMAs) are materials that regain their original shape after deformation through a reversible phase transformation process. These materials uniquely respond to external conditions like temperature, stress, or magnetic fields, enabling them to undergo shape changes. SMAs also possess remarkable elasticity, allowing them to recover their original shape even after significant deformation.The particular type of SMA used for the study is Nickel – Titanium SMA.

Ni-Ti Shape Memory Alloy (SMA)

The use of Nickel-Titanium (Ni-Ti) Shape Memory Alloy in seismic engineering becomes a promising area of exploration. Shape Memory Alloys (SMA) specifically take inverse deformations up to 8% strain (either by heating martensitic SMA or by unloading austenitic SMA) and dissipate moderate energy when subjected to repeated loading. Thus, they are considered a viable option for use as structural parts against seismic loading. Additionally, SMA (stainless steel equivalent) performs better in terms of aging and hardness due to its improved corrosion resistance. These properties make Ni-Ti SMAs useful in various applications, including medical devices, robotics, and structural engineering, where they can enhance the performance and resilience of structures like Beam Column Joints (BCJs).Tables 1 and 2 provide the properties of Ni-Ti SMAs, which have a composition of 55% Nickel and 45% Titanium.

Table 1 General Properties Of Ni-Ti SMA Bars [17]

Property	Description
Elastic Modulus	32000 MPa
Yield Strength (MPa)	450 MPa
Yield strain	0.014
Ultimate Strength (MPa)	500
Ultimate strain	0.035
Density (ton/mm3)	7.11 x 10^{-9}
Poisson's Ratio	0.33

Table 2 Super elastic properties of Ni-Ti SMA bars [17]

Transformation loading begins	450 MPa
Transformation loading ends	500 MPa
Transformation unloading begins	350 MPa
Transformation unloading ends	180 MPa
Transformation Strain	0.055

METHODOLOGY

The work methodology employs advanced numerical simulations using ABAQUS to comprehensively analyse BCJs reinforced with shape memory alloys (SMAs) under monotonic loads. Detailed 3D models, integrating concrete, steel, and SMAs, capture their nonlinear behaviours. Validation against experimental data ensures model accuracy. After the validation work, the same model is used for further analysis. A total of five models are modelled in ABAQUS. The results are plotted in graphical forms and finally compared. The methodology flowchart is as shown in Fig 1.

Fig. 1 Methodology flowchart

VALIDATION

The numerical model is validated in ABAQUS using experimental results from Youssef et al. [18], with the adopted model shown in Fig. 2.

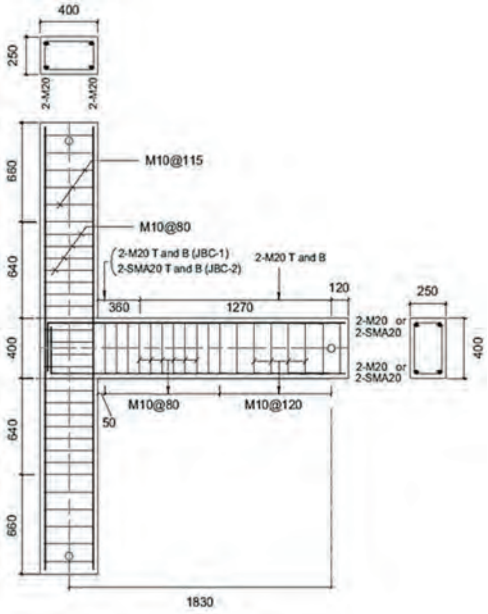

Fig. 2 Beam Column Joint for validation and analysis [17]

Finite Element Modelling

Beam and column profiles are initially modeled in ABAQUS based on the experimental setup, with reinforcements represented as truss elements. Material properties are defined, and components are assembled using embedded region interaction, assuming no slip between steel and concrete. The Concrete Damage Plasticity (CDP) model is used for concrete simulation. Two Joint Beam-Column (JBC) specimens are analyzed: JBC-1 with regular steel rebars and JBC-2 with Shape Memory Alloy (SMA) bars in the beam's plastic hinge zone. The SMA bars (20 mm diameter, 450 mm length) replace an equivalent steel segment and are connected via couplers, modeled using tie constraints. Boundary conditions include pinned and roller supports at column ends, with an axial load of 0.15 times the column capacity applied at the top [17]. A unit displacement is applied at the beam tip to determine maximum loads. Steps are defined for loading cases, and mesh sizes are assigned for each member. Finite element models are shown in Figs. 3 to 6 for validation.

(a) (b)

Fig. 3 (a) Beam and (b) Column Profiles

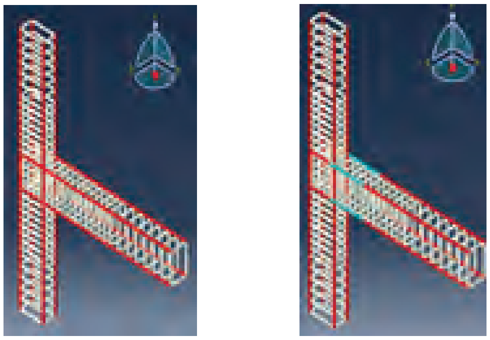

(a) (b)

Fig. 4 Reinforcement of BCJ with (a) steel and (b) SMA

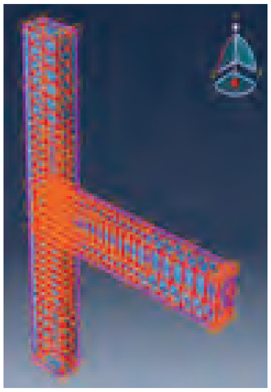

Fig. 5 RC-Rebar Embedded interaction

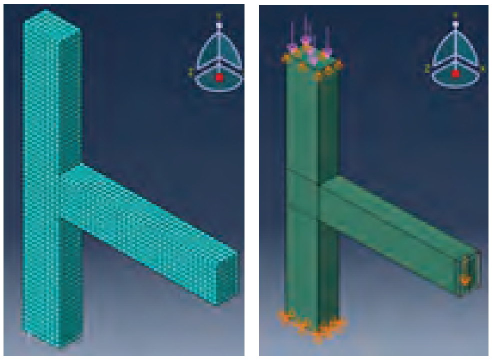

(a) (b)

Fig. 6 (a) Mesh discretization and (b) Boundary Conditions

Convergence Study

To begin with, a convergence study determines the ideal mesh size required to simulate BCJ performance. Numerical simulations use various mesh sizes from 50 to 20 mm. Fig 7 shows the convergence of mesh sizes to reach the ideal mesh size.

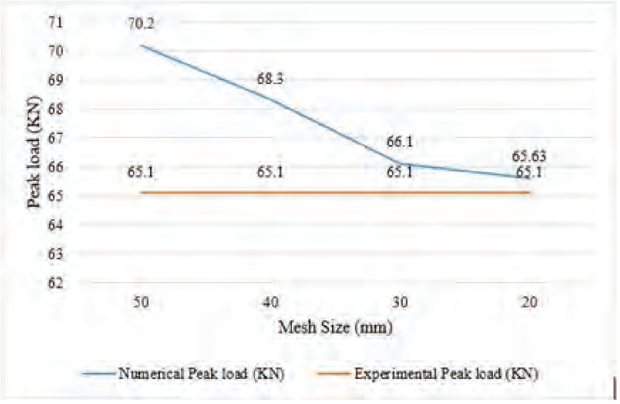

Fig. 7 Numerical Maximum load V/s Mesh Size Graph

Table 3 shows the convergence study results, including percentage error and the experimental and numerical maximum loads for different mesh sizes. The analysis identifies 30 mm as the optimal mesh size, balancing accuracy and computational efficiency. Beyond this, further mesh refinement has minimal impact. At 30 mm, the model contains 11,953 elements for both concrete and reinforcement.

Table 3 Results of the convergence study

Mesh Size (mm)	Experimental Peak Load (KN) [17]	Numerical Peak Load (KN)	No: of elements	Percentage error
50	70.2			
65.1		5372	7.83	
40		68.3	9142	4.91
30		66.1	11953	1.53
20		65.63	66523	0.81

Validation Results

Figs. 8 and 9 compare the numerical and experimental results [17] for BCJs reinforced with steel and SMA bars, showing a close agreement between the two.

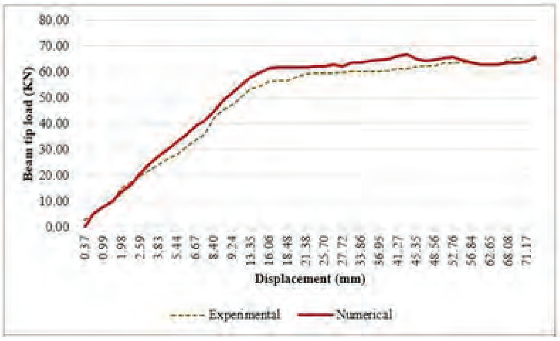

Fig. 8 Load V/s Displacement Graph for BCJ with steel

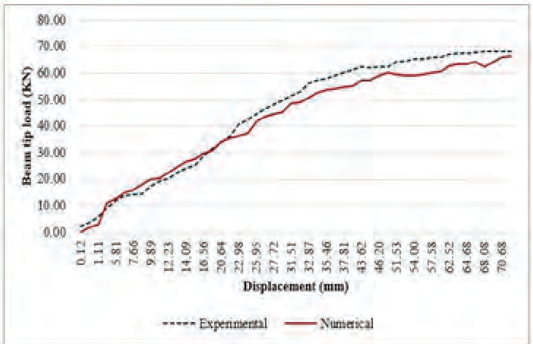

Fig. 9 Load V/s Displacement Graph for BCJ with SMA

Figures 10 to 11 show the comparison of key parameters for different samples. The numerical results closely align with experimental data [17], with errors ranging from 0.81% to 7.83%. The model effectively captures the overall response. Secant stiffness is determined from the slope of the load–displacement curve, while energy dissipation is calculated as the area under the curve.

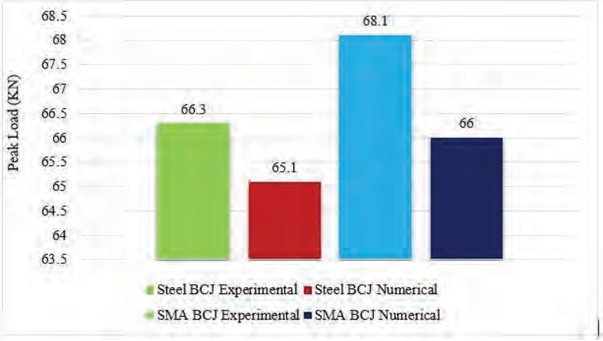

Fig 10 Numerical and Experimental Maximum [17] comparison between Steel and SMA

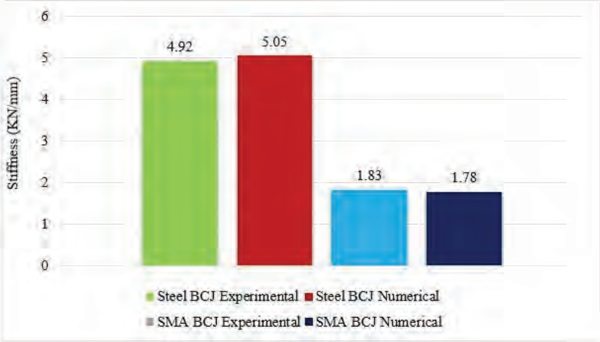

Fig 11 Numerical and Experimental Stiffness Load comparison between Steel and SMA

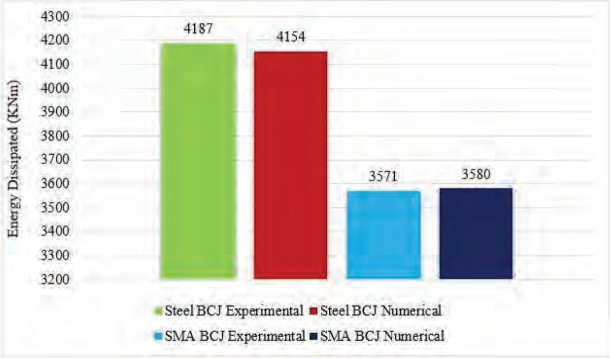

Fig. 12 Numerical and Experimental Energy dissipation comparison between Steel and SMA

NUMERICAL SIMULATION AND ANALYSIS

This section presents a numerical simulation to evaluate the performance of BCJs reinforced with varying ratios of steel to Ni-Ti SMA bars. The same validated model is used for analysis in ABAQUS. A total of five models are developed, as summarized in Table 6.1, where "NT" denotes Ni-Ti SMA.

Table 4 SMA reinforced BCJ models details

Sl No	Model	Steel to SMA ratio	No of Steel bars	No of SMA bars	Percent SMA reinforcement
1	Steel BCJ	-	4	0	0
2	NT25	3:1	3	1	25
3	NT50	2:2	2	2	50
4	NT75	1:3	1	3	75
5	NT100	-	0	4	100

RESULTS AND DISCUSSIONS

ABAQUS simulations were conducted for all five models. Load-displacement curves for four models—NT25, NT50, NT75, and NT100—are shown in Fig. 13. The maximum load, stiffness, and energy dissipation for each model are presented in Figures 14 to 15.

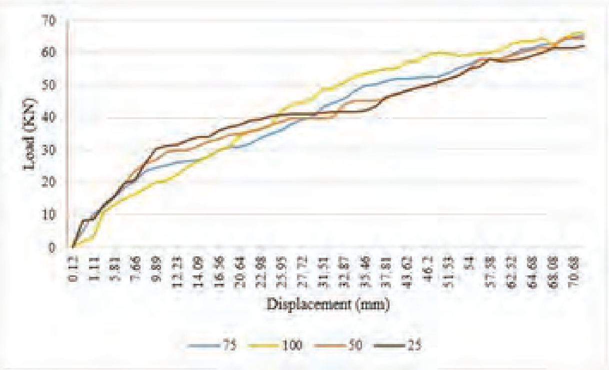

Fig. 13 Load-Displacement graph with varying percentages Ni-Ti SMA bars

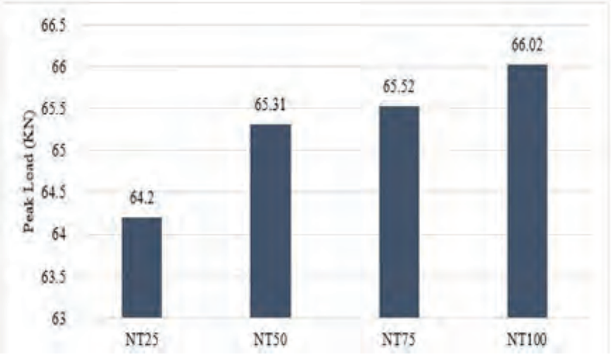

Fig. 14 Maximum Load of BCJ with varying percentages of Ni-Ti SMA bars.

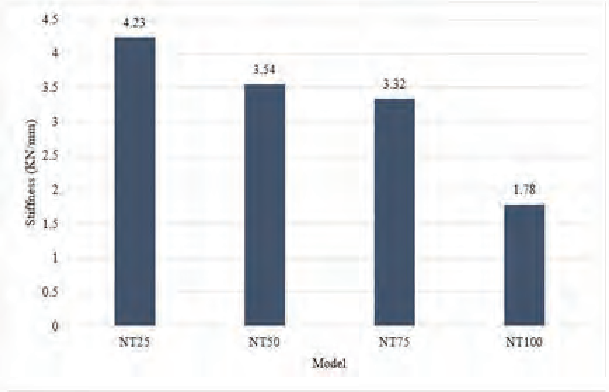

Fig. 15 Stiffness of BCJ with varying percentages Ni-Ti SMA bars

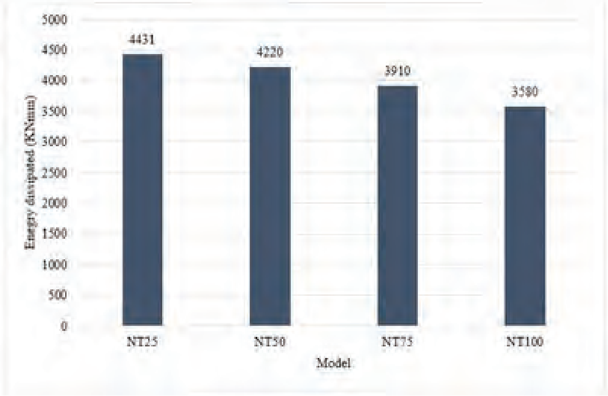

Fig. 16 Energy dissipation of BCJ with varying percentages Ni-Ti SMA bars

Result Comparison

The maximum loads, stiffness and energy dissipation for each percentage of reinforcement by Ni-Ti and steel bars are compared, as shown in Fig 16 to 18.

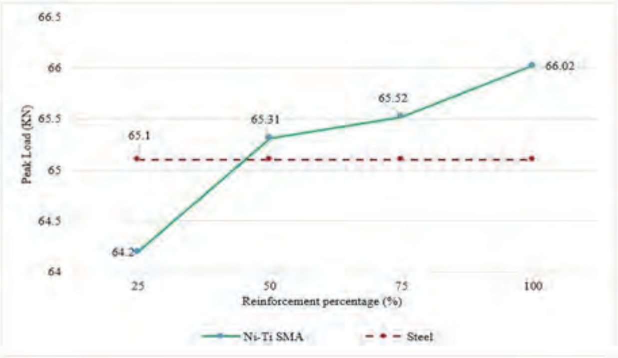

Fig. 16 Maximum load comparison of BCJ with varying percentages SMA bars

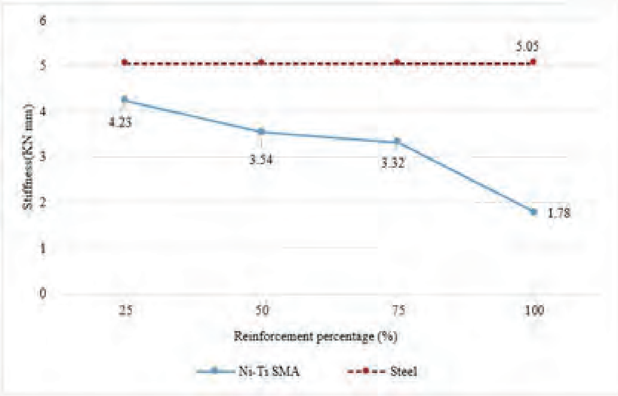

Fig. 17 Stiffness comparison of BCJ with varying percentages SMA bars

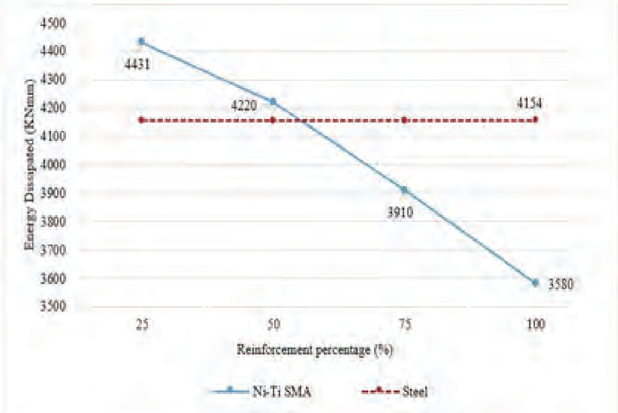

Fig. 18 Energy Dissipation comparison of BCJ with varying percentages SMA bars.

The validation models with only steel reinforcement treated as control specimens, and all other models are compared with them. The results of the comparison are shown in table 5.

Table 5 Result Comparison

Ni-Ti SMA %	25	50	75	100
Comparison with 100% steel				
Peak Load Capacity	-1.38	0.32	0.65	-1.41
Stiffness	-16.24	-29.9	-30.3	-183.7
Energy dissipation	6.67	1.59	-5.87	13.81

Discussions

In seismic zones, structures must withstand high loads, with energy dissipation playing a crucial role in reducing seismic damage. While higher stiffness limits deformation, excessive stiffness may cause brittle failure, making moderate stiffness preferable. Key findings from the results are:

- All models show similar maximum load capacities regardless of reinforcement ratio.
- The 25% SMA model is less suitable for seismic use, with a 1.38% drop in peak load and a significant 16.24% reduction in stiffness compared to 100% steel. Its 6.67% increase in energy dissipation is insufficient to offset these losses.
- The 50% SMA model outperforms 100% steel with a 0.32% higher peak load, 29.9% reduced stiffness, and 1.59% higher energy dissipation. This balance of moderate stiffness reduction and improved energy dissipation makes it ideal for seismic applications.
- The 75% SMA model has a 0.65% higher peak load, 30.3% lower stiffness, and 5.87% less energy dissipation than 100% steel. Despite slightly lower energy dissipation than the 50% SMA, it remains a viable seismic option due to its balanced performance.
- The 100% SMA model is unsuitable for seismic zones because its stiffness drops by 183.7%, compromising structural rigidity, despite good energy dissipation and acceptable peak load capacity.

Future Trends

While this study highlights 75% Ni-Ti SMA reinforcement as promising for BCJs, future research should focus on cyclic loading to better simulate earthquake conditions. Investigating combinations of Ni-Ti SMAs with advanced materials like high-performance concrete may further enhance performance. Optimizing joint design, conducting cost-benefit analyses, and assessing fire resistance are vital for practical implementation. Experimental validation remains essential, and integrating SMA-reinforced joints into smart, self-repairing or recentering structures offers exciting potential for next-generation seismic-resistant buildings.

CONCLUSIONS

This study evaluated Beam-Column Joints (BCJs) reinforced with varying percentages of Ni-Ti Shape Memory Alloys (SMA) under monotonic loading, compared to conventional steel. Validation included BCJs reinforced with both materials. Literature shows SMA bars shift the plastic hinge away from the joint face, enhancing structural resilience. Five models with different SMA-steel ratios were analyzed for stiffness, load capacity, and energy dissipation. The control used 100% steel. The 50% SMA model performed best, with the 75% SMA model also effective. Both showed notable plastic hinge relocation and improved resilience, demonstrating the potential of SMA-reinforced BCJs in practice.

REFERENCES

1. Alaneme, K. K., & Okotete, E. A. 2016. Reconciling viability and cost-effective shape memory alloy options – A review of copper and iron based shape memory metallic systems. Engineering Science and Technology, an International Journal 19(3): 1582–1592.
2. Alkateeb, T., & Sunny, A. 2022. Seismic Performance of Steel Frames with Shape Memory Alloy (SMA) Bracing System (839–846).
3. Choudhary, N., & Kaur, D. 2016. Shape memory alloy thin films and heterostructures for MEMS applications: A review. Sensors and Actuators A: Physical, 242, 162–181.
4. Elbahy, Y. I., Youssef, M. A., & Meshaly, M. Seismic performance of reinforced concrete frames retrofitted using external superelastic shape memory alloy bars. Bulletin of Earthquake Engineering 17(2): 781–802.
5. Elkafrawy, M. E., Mohsen Khalil, A., Abuzaid, W., Hawileh, R. A., & AlHamaydeh, M. 2022. Nonlinear Finite Element Analysis (NLFEA) of Pre-stressed RC Beams Reinforced with Iron-Based Shape Memory Alloy (Fe- SMA). Advances in Science and Engineering Technology International Conferences (ASET) 1.
6. Hafezolghorani, M., Hejazi, F., Vaghei, R., Jaafar, M. S. bin, & Karimzade, K. 2017. Simplified Damage Plasticity Model for Concrete. Structural Engineering International 27(1): 68–78.
7. Khalil, W., Saint-Sulpice, L., Arbab Chirani, S., Bouby, C., Mikolajczak, A., & ben Zineb, T. 2013. Experimental analysis of Fe-based shape memory alloy behavior under thermomechanical cyclic loading. Mechanics of Materials 63: 1–11.
8. Kumar R V, R., S, P., S H, A., & Kumara, P. C. A. 2022. A Review Article on FeMnAlNi Shape Memory Alloy.

Journal of Mines, Metals and Fuels 355–359.

9. Mohd Jani, J., Leary, M., Subic, A., & Gibson, M. A. (2014). A review of shape memory alloy research, applications and opportunities. Materials & Design (1980-2015) 56: 1078–1113.
10. Muhammad Rahman, Mohammed Al-Huri, Ali Al-gadhib, & Mohammed Alosta. 2019. Effectiveness of NiTi- SMA Bars at the Beam Column Joint Interface . SMAR -5th Conference on Smart Monitoring, Assessment and Rehabilitation of Civil Structures.
11. Ocel, J.,Des Roches, R., Leon, R. T.,Hess, W. G., Krumme, R., Hayes, J. R., & Sweeney, S. 2004. Steel Beam- Column Connections Using Shape Memory Alloys. Journal of Structural Engineering 130(5): 732–740.
12. Qassim Hameed, M., & Laftah Abbass, A. 2022. Behavior of Smart Reinforced Concrete Beam Column Joints by Using Shape Memory Alloy Reinforcement Under Repeated Loading. Diyala Journal of Engineering Sciences 117–126.
13. Qian, H., Ye, J., Gao, J., Cai, L., Zhou, J., & Zhang, H. 2023. Feasibility study of self-centring beam-to-column joints with posttensioned SMA strands. Structures 52: 205–219.
14. Rahmi, Y., Saputra, A., & Siswosukarto, S. 2017. Numerical Modelling of Interior RC Beam-Column Joints for Non-Engineered Buildings Strengthened Using Steel Plates. MATEC Web of Conferences, 138,

15. Rezapour, M., Ghassemieh, M., Motavalli, M., & Shahverdi, M. 2021. Numerical Modeling of Unreinforced Masonry Walls Strengthened with Fe-Based Shape Memory Alloy Strips. Materials 14(11): 2961.

16. Sabbaghian, M., & Kabir, M. 2023. Innovative use of shape memory alloys as reinforcements for concrete beam-column joints: an overview. Kufa Journal of Engineering 14(2) : 24–42.

17. Youssef, M. A., Alam, M. S., & Nehdi, M. 2008. Experimental Investigation on the Seismic Behavior of Beam- Column Joints Reinforced with Superelastic Shape Memory Alloys. Journal of Earthquake Engineering 12(7): 1205–1222.

Investigating the Effects of Fluid-Structure Interaction on the Modal Behaviour of Pipes and Shafts

Krishnanunni A. K
PG Scholar
Department of Civil Engineering
NSS College of Engineering
Palakkad, Kerala
🖂 kichan.ak@gmail.com

Jayalekshmi R
Professor
Department of Civil Engineering
NSS College of Engineering
Palakkad, Kerala
🖂 jayalekshmisankar@gmail.com

ABSTRACT

Fluid-Structure Interaction (FSI) is a critical area in engineering design, especially for structures like pipes and shafts that experience both fluid flow and vibrations. This study investigates the modal behavior (natural frequencies, shapes, and stability) of these structures in fully immersed and dry conditions. The research focuses on understanding FSI's impact on the dynamics of pipes and shafts commonly used in liquid propulsion engines, such as those found in Polar Satellite Launching Vehicles. By analyzing modal behavior, the aim is to gain valuable insights for fluid dynamics and vibration control. Ultimately, the successful implementation of damping mechanisms in fluid-filled pipes has the potential to significantly improve the reliability, efficiency, and sustainability of various engineering applications, particularly in liquid propulsion engines.

KEYWORDS: *Fluid-structure, Modal analysis, Shaft, Pipes.*

INTRODUCTION

The solid structures are always in contact with at least one fluid throughout their lifetime. As a result, the movement of the structure and that of the fluid are dependent to each other. Consequently, the structure and the fluid, act as a dynamically connected system when taken as a whole. The interplay between surrounding fluids and solid structures is a crucial aspect of structural and fluid dynamics, impacting the safety and functionality of diverse engineering systems. Fluid structure interaction (FSI) is an important topic in many engineering applications, particularly in passages like pipes, ducts, and channels where fluid flow and solid structures interact. This can have a big impact on system efficiency, safety, and performance. . The complex interaction between fluid forces and mechanical vibrations determines the dynamic behaviour of objects submerged in fluids. The presence of a surrounding fluid greatly affects the natural frequencies, mode shapes, and general stability of the structures, posing special issues due to fluid-structure interaction. Here an attempt is made undertaking a thorough modal study of pipes and shafts in both fully immersed and dry conditions.

The liquid propulsion engines play a pivotal role in aerospace and marine applications, where the efficiency and reliability of fluid transmission systems are critical for overall performance. In these engines circular shafts and tubular cylindrical pipes are commonly used as primary structural components. This paper addresses the dynamic characteristics of these structural elements. The outcomes of this research will contribute valuable insights to the field of fluid dynamics and vibration control. Ultimately, the successful implementation of effective damping mechanisms in fluid lines immersed in fluids has the potential to improve the reliability, efficiency, and sustainability of a wide range of engineering applications mainly in the liquid propulsion engines of Polar Satellite Launching Vehicles.

OBJECTIVE AND SCOPE OF WORK

The main objective of the study is to understand the dynamic characteristics of shafts and pipes immersed in water in the liquid propulsion engine of PSLV. The main scope of the work includes:

- To study the vibrational characteristics of a solid cylindrical shaft in dry and fully immersed conditions.

- To study the vibrational characteristics of fuel filled tubular section in dry and immersed conditions

Before the starting of the modal analysis of the shaft and the pipe, validation of a model created is done in order to ensure that the steps followed are correct. For the validation, a rod of 20mm diameter and 2m length made up of structural steel is adopted. The natural frequency of the rod is calculated both by the theoretical and analytical method by ANSYS software and the percentage error is determined to ensure the accuracy of the modelling. After the validation, the modal analysis of the shaft is done. The size of the shaft adopted is 50mm diameter and 1000mm length made up of structural steel. The structure is modelled in the ANSYS software, appropriate meshing is done and the modal analysis is performed to obtain the natural frequencies of different mode shapes. The modal analysis of the shaft is done for two cases, one in dry condition and the other in fully immersed in water condition. The next step is to do the modal analysis of the pipe. The size of the structural steel pipe adopted is 45mm internal diameter, 50mm external diameter and length of 1000mm. The structure is modelled in the ANSYS software, appropriate meshing is done and the modal analysis is performed to obtain the natural frequencies of different mode shapes. The modal analysis of the pipe is done for two cases, on in dry and empty condition and the other in fuel filled dry condition. All the results of the natural frequencies obtained from the different cases of the shaft and the pipe are analysed. The percentage change in the natural frequencies of the shaft and pipe are noted in this step. Based on the results and discussions proper conclusions are drawn. The effect of the water in the natural frequency of the vibrating structure is concluded.

MODAL ANALYSIS OF SHAFT

After the validation the modal analysis of the shaft is carried out in dry and immersed condition for the first three modes. In order to do the modal analysis of solid cylindrical shaft in dry condition, a shaft is modelled in the ANSYS software. Table 1 shows the dimensions and the properties of material which is used to model the solid cylindrical shaft. Fig. 1 shows the modelled solid cylindrical shaft in the ANSYS software.

Table 1. Properties of solid shaft

Material	Diameter	Length	Density
Structural Steel	50mm	1000mm	7850kg/m^3

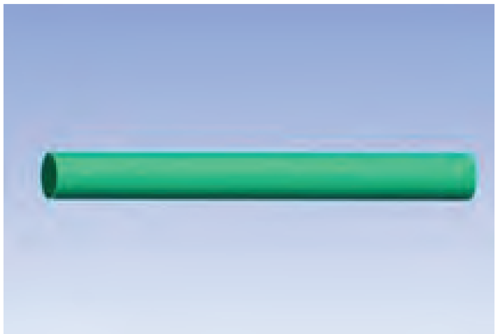

Fig. 1: Model of solid cylindrical shaft in ANSYS software

After the modelling of the solid cylindrical shaft, appropriate meshing is provided for the model. Simply supported boundary conditions are provided for the shaft and then the modal analysis is performed out. The natural frequencies are calculated for the first, second and third mode shapes of the shaft. Fig. 2. (a), (b) and (c) shows the natural frequencies obtained for the first, second and third mode shapes of the solid cylindrical shaft.

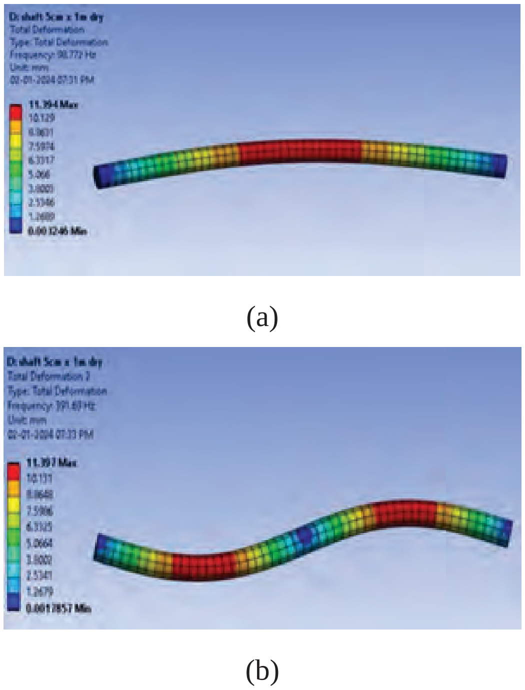

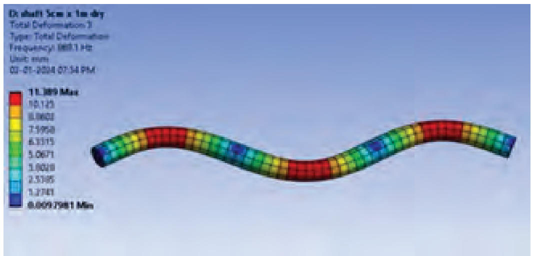

(c)

Fig.2 (a): First mode shape of dry solid cylindrical shaft (Natural frequency f1 = 98.772 Hz)

(b) : Second mode shape of dry solid cylindrical shaft (Natural frequency f2 = 391.69 Hz)

(c) : Third mode shape of dry solid cylindrical shaft (Natural frequency f3 = 869.10 Hz)

To understand the effect of water in the vibrational characteristics of the solid cylindrical shaft, the same cylindrical shaft is modelled with a layer of water cushion around it. The dimension of the water cushion is adopted as four times the diameter of the solid cylindrical shaft [7]. Table 2 shows the dimensions and the properties of material which is used to model the water cushion around the solid cylindrical shaft. Fig.3 shows the modelled solid cylindrical shaft with water cushion in the ANSYS software.

Table 2. Properties of water cushion

Material	Diameter	Length	Density
Water	200mm	1000mm	1000kg/m^3

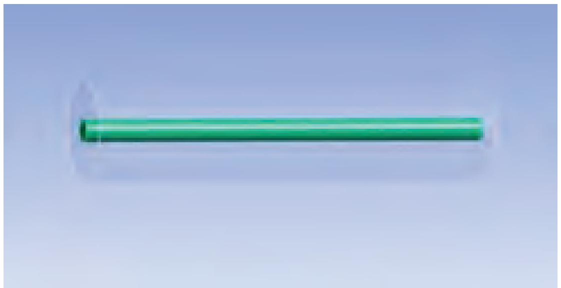

Fig. 3: Model of solid cylindrical shaft immersed in water

After the modelling of the solid cylindrical shaft with water cushion, appropriate meshing is provided for the model. Simply supported boundary conditions are provided for the shaft and then the modal analysis is carried out. The natural frequencies are calculated for the first, second and third mode shape of the shaft. The Fig.4. (a), (b) and (c) shows the natural frequencies obtained for the first, second and third mode shapes of the solid cylindrical shaft immersed in water.

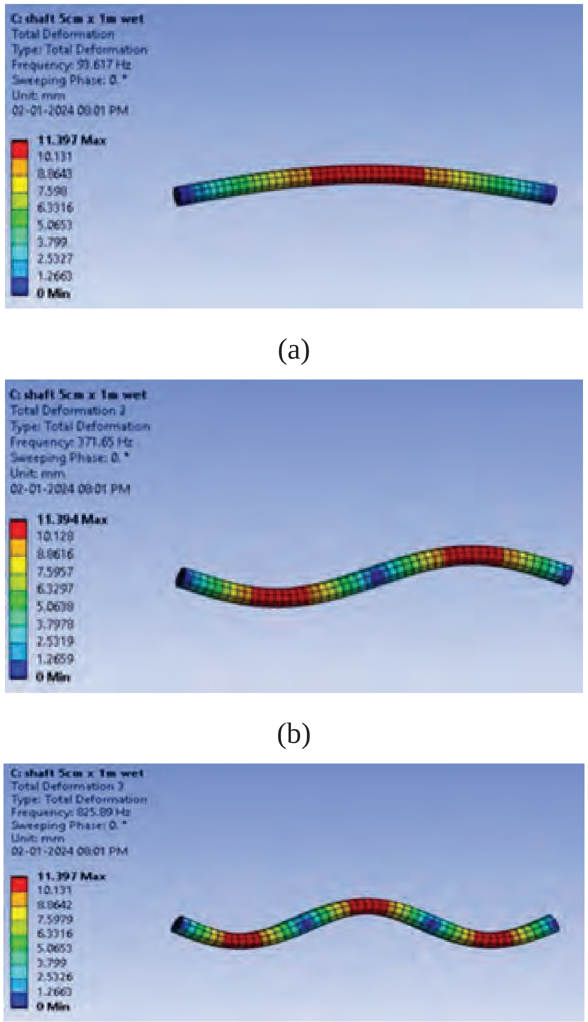

(a)

(b)

(c)

Fig. 4. (a): First mode shape of immersed solid shaft (Natural frequency f1= 93.617 Hz)

(b) : Second mode shape of immersed solid shaft (Natural frequency f2= 371.65 Hz)

(c) : Third mode shape of immersed solid shaft (Natural frequency f3= 825.89 Hz)

The natural frequencies of all three mode shapes of the dry solid cylindrical shaft and the solid cylindrical shaft immersed in the water cushion are tabulated. Table 3 shows these natural frequencies and the percentage reduction in natural frequencies.

Table 3. Natural frequencies of dry and immersed solid shaft

Conditions	First Mode	Second Mode	Third Mode
Dry Shaft	98.77 Hz	391.69 Hz	869.10 Hz
Immersed Shaft	93.62 Hz	371.65 Hz	825.89 Hz
Percentage Reduction	5.21%	5.39%	4.97%

So, the table shows that, there is a 5 to 6 percentage reduction in the natural frequencies of the solid cylindrical shaft when it is immersed in water. Thus, the damping effect of the water cushion brings change to the dynamic characteristics of the shaft which gets immersed in it.

MODAL ANALYSIS OF PIPE

In order to carry out the modal analysis of solid cylindrical pipe without fuel in dry condition, a pipe is modelled in the ANSYS software. Table 4 shows the dimensions and the properties of material which is used to model the solid cylindrical pipe. Fig.5 shows the modelled solid cylindrical shaft in the ANSYS software without fuel.

Table 4. Properties of solid cylinder pipe

Material	External Diameter	Internal Diameter	Length	Density
Structural Steel	50 mm	45 mm	1000mm	1000kg/m^3

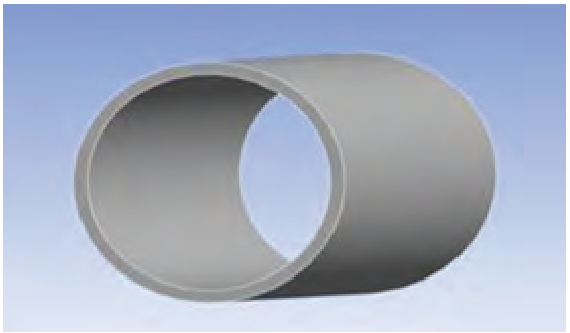

Fig. 5: Model of solid cylindrical pipe without fuel in ANSYS software

Simply supported boundary conditions are provided for the pipe and then the modal analysis is carried out. The natural frequencies are calculated for the first, second and third mode shape of the pipe. Fig. 6. (a), (b) and (c) shows the natural frequencies obtained for the first, second and third mode shapes of the solid cylindrical pipe without fuel in dry condition.

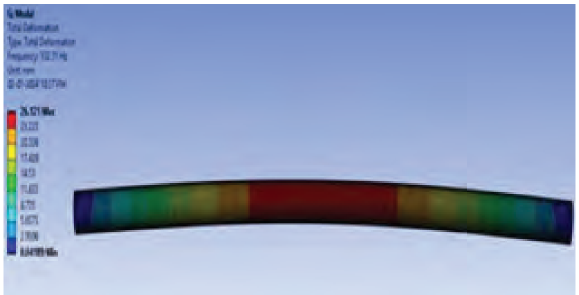

(a)

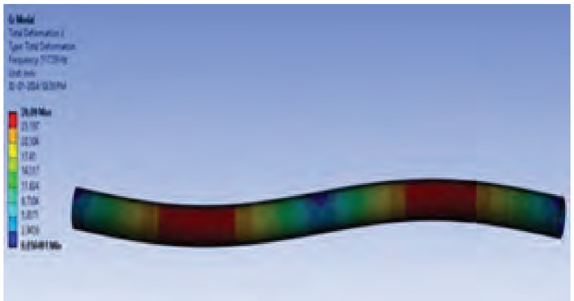

(b)

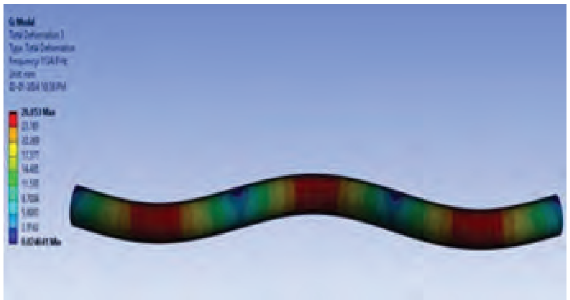

(c)

Fig. 6. (a): First mode shape of dry pipe without fuel (Natural frequency f1=132.31 Hz)

(b) : Second mode shape of dry pipe without fuel (Natural frequency f2=517.59 Hz)

(c) Third mode shape of dry pipe without fuel (Natural frequency f3=1124.90 Hz)

To understand the effect of fuel in the vibrational characteristics of the solid cylindrical pipe, the same cylindrical pipe is modelled with a layer of fuel cushion inside the pipe. Table 5 shows the dimensions and the properties of material which is used to model the fuel cushion inside the solid cylindrical pipe. The Fig. 7 shows the modelled solid cylindrical pipe with fuel cushion in the ANSYS software with fuel.

Table 5. Properties of fuel cushion

Material	Diameter	Length	Density	Pressure
N_2O_4 + UDMH	45 mm	1000 mm	795 kg/ m^3	65 bar

Fig. 7: Model of solid cylindrical pipe with fuel inside

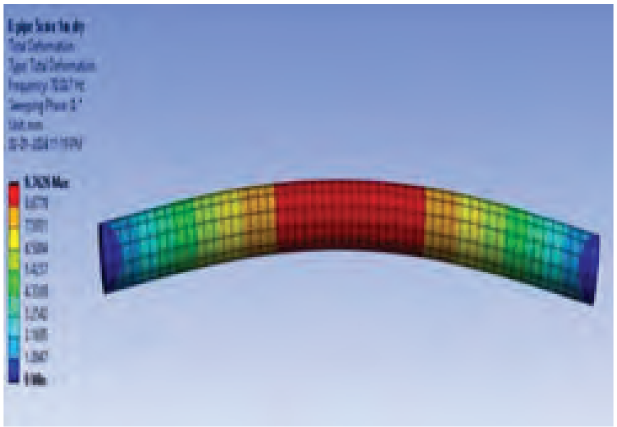

(a)

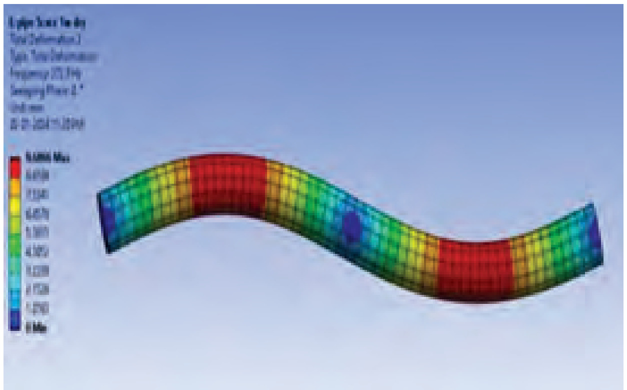

(b)

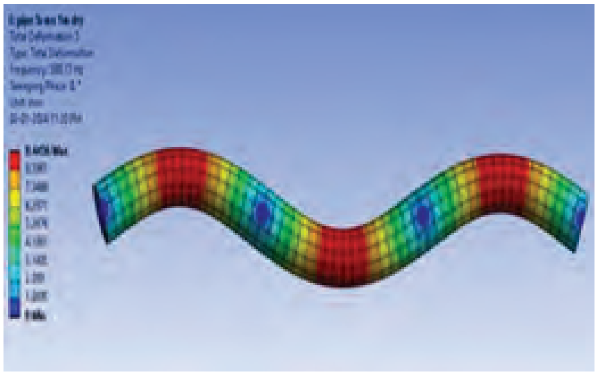

(c)

Fig. 8. (a): First mode shape of dry pipe with fuel (Natural frequency f1=70.027 Hz)

(b) : Second mode shape of dry pipe with fuel (Natural frequency f2=272.90 Hz)

(c) : Third mode shape of dry pipe with fuel (Natural frequency f3=589.13 Hz)

Table 6. Natural frequencies of various cases of pipe

Cases	First Mode (Hz)	Second Mode (Hz)	Third Mode (Hz)
Empty Pipe	132.31	517.59	1124.9
Fuel filled Pipe	70.027	272.9	589.13
Immersed Pipe	66.392	258.736	558.55

Simply supported boundary conditions are provided for the pipe and then the modal analysis is carried out. The natural frequencies are calculated for the first, second and third mode shapes of the pipe. Fig.8 (a), (b) and (c) shows the natural frequencies obtained for the first, second and third mode shapes of the solid cylindrical pipe with fuel

The natural frequencies of all three mode shapes of the dry solid cylindrical pipe without fuel and the solid cylindrical pipe with fuel are tabulated. Table 6 shows these natural frequencies and the natural frequency of immersed fuel filled pipe calculated based on the percentage change in the natural frequency of solid cylindrical shaft in dry and fully immersed condition.

The table shows that there is a 47 percentage reduction in the natural frequencies of the solid cylindrical pipe when it is filled with fuel. The natural frequency of the immersed pipe with fuel is greater than 60Hz which is the maximum resonance frequency of the PSLV rocket. The damping characteristics of the cylindrical pipe is changed due to damping effect of the outer water cushion.

RESULTS AND DISCUSSIONS

Table 7 shows the natural frequencies of the solid cylindrical shaft and the solid cylindrical pipe under dry and immersed conditions. It also gives the natural frequencies of the pipe with and without the inside fuel.

Table 7. Natural frequencies of various cases of shaft and pipe

Cases	First Mode (Hz)	Second Mode (Hz)	Third Mode (Hz)
Dry Shaft	98.77	391.69	869.10
Immersed Shaft	93.61	371.65	825.89
Empty Pipe	132.31	517.59	1124.90
Fuel filled Pipe	70.03	272.90	589.13
Immersed Pipe	66.39	258.73	558.55

It is observed that there is 5 to 6 percentage reduction the natural frequency of a structure when it is immersed in water. There is about 30 to 34 percentage increase in the natural frequency when a solid shaft is converted into hollow shaft and introduction of fuel in the pipe brings about a 47 percentage reduction in the natural frequency of the pipe.

CONCLUSIONS

From the project conducted, the following conclusions are obtained:

- Introduction of vibrating structures in fluid filled mediums have a direct effect on the dynamic characteristics of the structures as there is a reduction in the natural frequencies of the structures
- There is a 5 to 6 percent reduction in the natural frequencies of the structure when immersed in water
- The hollow pipe has higher natural frequency than the solid shaft
- Filling of hollow pipe with the fuel at 65 bar pressure induces 47 percentage reduction in the natural frequency of the pipe and may be attributed to the damping of the infilled fluid.
- After immersed, the pipe filled with fuel in the water, the natural frequency obtained for first mode shape is 66.392Hz which is greater than 60Hz which is the resonant frequency of rocket, which will prevent resonant vibration. Hence amplification of vibration is avoided and the model created is safe.

REFERENCES

1. Amabili M., (1996), "Free Vibration of Partially Filled Horizontal Cylindrical Shells", Journal of Sound and Vibration, 191 (5), 757–780
2. Chu, M. L. and Brown. S., (1981). "Experiments On The Dynamic Behavior of Fluid-Coupled Concentric Cylinders", Experimental Mechanics, 5, 129-137.
3. Cona. C., Osses. A., Planchard. J., (1997), "Added mass and damping in fluidstructure interaction", Computer methods in applied mechanics and engineering, Elsevier Ltd., pp- 387-405
4. Facci. A.L., Porfiri. M. (2013) "Analysis of three-dimensional effects in oscillating cantilevers immersed in viscous fluids. "Journal of Fluid and Structures, Elsevier Ltd. http://dx.doi.org/10.1016/j.jfluidstructs.2012.11.006
5. Fritz R.J. (1971), "The Effect of Liquids on the Dynamic Motions of Immersed Solids", Consulting Engineer, General Electric Co., Schenectady, N. Y. Mem. ASME, Journal of Engineering for Industry, http://manufacturingscience.asmedigitalcollection.asme.org
6. Iakovlev S., (2009). "Interaction between an external shock wave and a cylindrical shell filled with and submerged into different fluids", Journal of Sound and Vibration, 322, 401–437
7. Milkessa. D. (2012)," Bending Vibration Analysis of Pipes and Shafts Arranged in Fluid Filled Tubular Spaces Using FEM", Master Thesis Developed at University of Rostock, Germany
8. Nakamura. M., Hirota. K., Watanabe. Y., Mureithi. N. W., Takamatsu. H. (2002) " Dynamics of An In- line Tube Array Subjected To Steam water Cross-flow. Part

I: Two-phase Damping And Added Mass", Journal of Fluids and Structures, doi:10.1006/j#s.2001.0406 33

9. Sader. J.E.(1997), "Frequency response of cantilever beams immersed in viscous fluids with applications to the atomic force microscope", Journal of Applied Physics, Department of Mathematics and Statistics, University of Melbourne, Parkville, 3052, Victoria, Australia, doi: 10.1063/1.368002

10. Yu. K., Zijlstra. P., Sader. J. E., Xu. Q. H., Orrit. M.(2013) "Damping of Acoustic Vibrations of Immobilized Single Gold Nanorods in Different Environments" American Chemical Society, Department of Applied Physics, Eindhoven University of Technology, Eindhoven, Netherlands, dx.doi.org/10.1021/nl400876w

Finite Element Analysis of Buckling Behaviour in Asymmetrical Cruciform Steel Columns

Deepthi V
PG Scholar
Department of Civil Engineering
NSS College of Engineering
Palakkad, Kerala
✉ deepthiv659@gmail.com

Krishnachandran V N
Assistant Professor
Department of Civil Engineering
NSS College of Engineering
Palakkad, Kerala
✉ vnkrishnachandran@nssce.ac.in

ABSTRACT

The study investigates the structural response of unsymmetrical cruciform steel columns compared to standard I-sections, focusing specifically on buckling behavior. The research involves a comprehensive buckling analysis of cruciform columns with and without flanges, modelled using ABAQUS 2017 software. Key variables considered are column geometry and end support conditions, including fixed-hinged and fixed-free scenarios. The study reveals that cruciform columns with flanges demonstrate higher resistance to applied loads relative to cruciform column without flanges and standard I-sections, largely due to their geometric configuration which enhances stability and critical buckling load. This work provides valuable insights into optimizing steel column design for enhanced structural efficiency and suggests further avenues for experimental validation and refinement of design standards.

KEYWORDS: *Asymmetrical cruciform column, Threshold buckling load, Support conditions, FEM.*

INTRODUCTION

For buildings and other structures to be stable and intact, structural engineers must carefully consider how to construct their columns. Compressive action is the main method by which columns transfer loads, and several variables, including length, cross-sectional shape, material strength, and support conditions, affect how well they work [7]. I-sections have historically been used extensively in column design because of their easy fabrication and well-established structural characteristics. Alternative designs, including cruciform steel columns, may be more advantageous in terms of material efficiency and load-bearing capacity [1]. Cruciform columns have attracted attention because of their special geometric qualities, which can improve overall structural performance and buckling resistance. To create a composite built-up section, these columns are made by welding plates or I-sections in a cross-shaped pattern. To completely comprehend their buckling behaviour under varied loads and boundary conditions, a detailed analysis is required due to the intricacy of their design. The plain and flanged cruciform columns are shown in Figs 1 and 2 accordingly.

Fig. 1 Plain cruciform column

Fig. 2 Flanged cruciform column

The buckling response of standard I-sections and unsymmetrical cruciform steel columns is compared in this work. The study examines a variety of ISMB sections under fixed-free and fixed-hinged boundary conditions employing the finite element program ABAQUS 2017. The purpose of this study is to compare the outcomes to demonstrate the possible advantages of unsymmetrical cruciform columns over traditional I-sections, especially regarding load-bearing capability. By providing insights into more reliable and effective structural solutions for engineering applications, the research's conclusions aid in the optimization of column design.

MODELLING OF UNSYMMETRICAL CRUCIFORM STEEL COLUMNS THROUGH FEM

Geometric parameters

Different sections are welded along the principal axes to construct unsymmetrical cruciform columns, which have a cross-shaped design devoid of symmetry. Table 1 lists the material properties used for each model with a different boundary condition.

Table 1 Material properties of cruciform columns

Parameter	Value
Modulus of elasticity, E	200 GPa
Poisson's ratio	0.3
Yield strength, fy	250 MPa
Column length	10 m

All the column sections are selected as per IS808-1989. Dimensions of cruciform sections with and without flanges as per IS808-1989 can be found in Table 2 and Table 3 accordingly.

Table 2 Cross sectional dimensions of cruciform sections without flanges

Members	Overall Depth (Mm)	Thickness Of Section (Mm)
S1	100	4.7
S2	125	5
S3	225	6.5
S4	300	7.7
S5	400	8.9
S6	450	9.4
S7	500	10.2
S8	550	11.2
S9	600	12

Table 3. Cross sectional dimensions of cruciform sections with flanges

Mem-bers	Overall Depth (Mm)	Flange Width (Mm)	Thickness Of Web (Mm)	Thickness Of Flange (Mm)
S1	100	50	4.7	7
S2	125	70	5	8
S3	225	110	6.5	11.8
S4	300	140	7.7	13.1
S5	400	140	8.9	16
S6	450	150	9.4	17.4
S7	500	180	10.2	17.2
S8	550	190	11.2	19.3
S9	600	210	12	20.3

Finite element modelling

All models were created using ABAQUS 2017 software in compliance with IS808-1989. All pieces are presumed to be perfectly welded [4]. To find the critical buckling load, 62 analyses were performed on a total of 31 models. Illustrative 3D views of unsymmetrical cruciform columns with and without flanges with a length of 10 meters are presented in Fig. 3 and Fig. 4, accordingly.

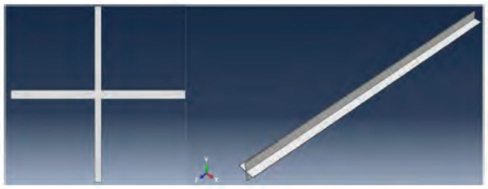

Fig. 3 3D representation of unsymmetrical cruciform steel columns without flanges using section225x6.5 at X-axis and section125x5 at Y-axis

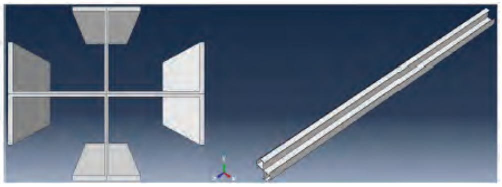

Fig. 4 3D representation of unsymmetrical cruciform steel columns with flanges using section300x140x7.7x13.1 at X-axis and section225x110x6.5x11.8 at Y-axis

All additional models were made in this manner. The section experiences axial compressive force along the longitudinal axis, causing the column to buckle before yielding. Boundary conditions are applied at both ends of the column to accurately replicate its support behavior and ensure a practical representation of how it responds to external loads.

FINITE ELEMENT-BASED SIMULATION OF STANDARD I-SECTIONS

A variety of ISMB sections are covered by the analysis, which has partially restrained and semi rigid end boundary requirements, per IS808-1989. The following material properties are applied to all models with different boundary conditions. Fig. 5 shows a cross-sectional view of a conventional I-section. Similar to this, other models were developed and examined. Table 4 lists the geometric properties of the standard I-sections.

Table 4 Geometrical properties of standard I-sections

Parameter	Value
Modulus of elasticity, E	200 GPa
Poisson’s ratio	0.3
Yield strength, fy	250 MPa
Column length	10 m

Fig. 5 Cross sectional view of standard I-section

RESULTS AND DISCUSSIONS

Tables 5 to 7 present the systematically obtained buckling response results for unsymmetrical cruciform columns, both with and without flanges, as analyzed using ABAQUS software, along with the corresponding results for typical I-sections.

Table 5. Threshold buckling load for unsymmetrical cruciform columns without flanges

Column Geometries	Threshold Buckling Load (Kn)	
	Partially - Restrained	Semi-Rigid
C1 - S1 x S2	9.09	25.43
C2 - S2 x S3	23.20	190.96
C3 - S3 x S4	65.13	534.63
C4 - S4 x S5	178.15	1456.95
C5 - S5 x S6	267.91	2184.51
C6 - S5 x S7	398.24	3239.71
C7 - S6 x S7	496.74	3737.17
C8 - S6 x S8	581.56	4715.09
C9 - S7 x S8	633.89	5133.62
C10 - S5 x S9	808.60	6533.89
C11 - S8 x S9	859.33	7537.68

Table 5. Threshold buckling load of unsymmetrical cruciform columns with flanges

Column Geometries	Threshold Buckling Load (Kn)	
	Partially - Restrained	Semi-Rigid
C1 - S10 x S11	65.20	521.61
C2 - S11 x S12	184.73	1482.69
C3 - S12 x S13	526.31	4218.75
C4 - S13 x S14	1255.66	10051.07
C5 - S14 x S15	1872.57	14992.60
C6 - S14 x S16	2236.84	20412.21
C7 -S15 x S16	2799.79	22408.39
C8 - S15 x S17	3841.67	30046.06
C9 - S16 x S17	4033.32	32289.23
C10 - S16 x S18	5112.24	32644.40
C11 - S17 x S18	5617.58	38959.36

Table 6 Threshold buckling load of standard I-sections

Column Geometries	Threshold Buckling Load (Kn)	
	Partially Restrained	Semi-Rigid
ISMB100	8.70	69.70
ISMB125	15.8	126.48
ISMB225	123.46	988.04
ISMB300	351.45	2812.50

ISMB400	837.43	6701.51
ISMB450	1248.99	9995.01
ISMB500	1866.83	14939.19
ISMB550	2689.96	21526.18
ISMB600	3745.02	29969.22

The threshold buckling loads of the columns are illustrated under the section below. From Fig. 6 to Fig. 8 display the comparison of threshold buckling loads of unsymmetrical columns under the respective end constraints.

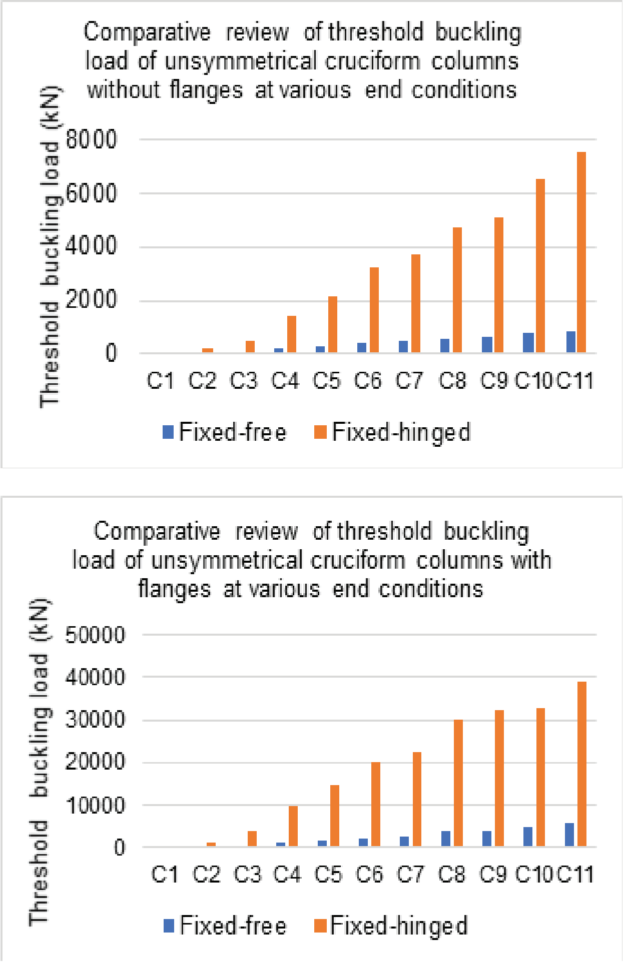

Fig. 6 Comparative review of threshold buckling load of unsymmetrical cruciform columns at various support conditions (a) without flanges (b) with flanges

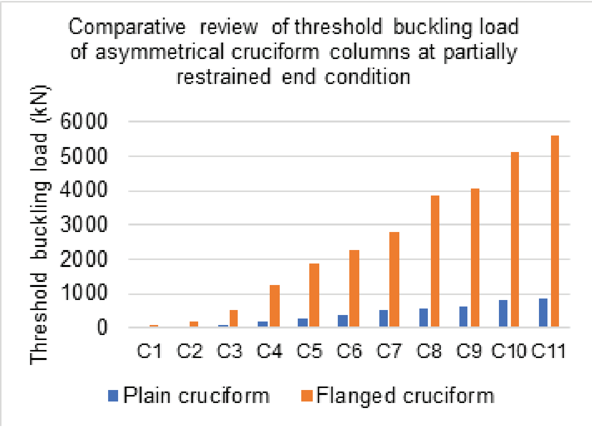

Figs 7 Comparative review of threshold buckling

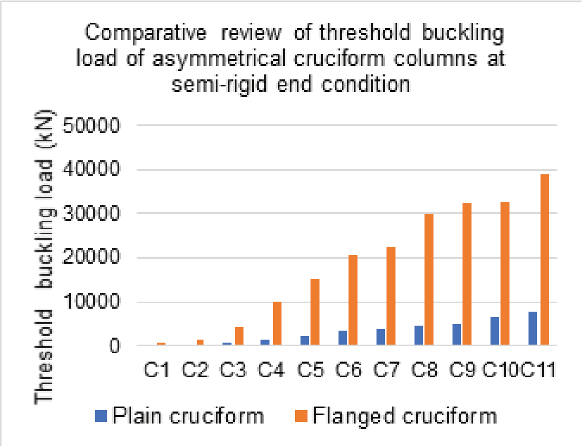

Fig 8 Comparative review of threshold buckling load at fixed free support condition load at fixed hinged support condition

CONCLUSIONS

Presented below are the conclusions of the research:

- The findings obtained are rely on a thorough examination of the buckling properties seen in unsymmetrical cruciform columns in comparison to standard I-sections. Relative to a standard I-section, examined units of cruciform columns with asymmetrical flanges may support more load.
- The structural instability response of all two unflanged and flanged unsymmetrical cruciform columns was carefully investigated in this study. In comparison to their plain equivalents, the results consistently showed that cruciform columns with flanges have superior resistance to load. Additional flanges aid in spreading the applied loads uniformly

throughout the column profile. The column's overall stability under axial compression is improved by this enhanced load spread, which also minimizes localized stress.

- Based on the threshold buckling load analysis, cruciform steel columns with semi-rigid support conditions exhibit superior buckling resistance relative to members having partially restrained end supports. This finding emphasizes the significance of support conditions in structural design.
- The structural member is better able to resist buckling because the fixed end entirely prevents transverse displacement. In addition, the hinged end allows for rotation, which helps redistribute certain compressive loads across the length of the structural unit. This efficiently increases the critical buckling load and reduces the overall bending moment.

Sections 600x210x12x20.3 and 550x190x11.2x19.3 of the unsymmetrical flanged cruciform demonstrate a greater load-bearing capacity in this investigation.

FUTURE TRENDS

To enhance the performance of cruciform columns, Further investigation is recommended in innovative materials namely composites and high-strength steel alloys. Additionally, it may be beneficial to study the behavior of cruciform columns under dynamic and seismic conditions, especially as the demand for resilient infrastructure grows. Understanding how these columns respond to various dynamic loads, including earthquakes, will be crucial for designing safer structures.

REFERENCES

1. Behzadi, B., Gardner, L., Wadee, M.A. (2022). "Behaviour, finite element modelling and design of cruciform section steel columns." Thin-Walled Structures, 182, 110124.
2. Cao, X., Chen, Y., Wang, W., Tao, Z., Wang, P., Kong, Z., Zhang, Y. (2023). "Local buckling of high strength steel welded cruciform-section columns under axial compression." Structures, 56, 104941
3. Cao, X., Shen, S., Wu, M., Tao, Z., Liu, S., Tao, Q., Kong, J., Zhang, H., Li, J., Zhang, Y., Cao, X., Kong, Z. (2022). "Residual stresses of 550 MPa high strength steel welded cruciform sections: Experimental and numerical study." Structures, 44, 579-593.
4. Cheng, Y., Nozawa, S., Hirohata, M. (2023). "High-accurate FE simulation on compressive behaviour of steel cruciform column with welding imperfection." Finite Elements in Analysis and Design, 221, 103960.
5. Chen, M., Lu, W., Shi, Y., Li, B. (2022). "Axial compression behaviour of cruciform cold-formed steel built-up columns: Shape optimization and experimental study." Journal of Building Engineering, 51, 104265
6. Guarracino, F., Simonelli, M.G. (2017). "The torsional instability of a cruciform column in the plastic range: Analysis of an old conundrum." Thin-Walled Structures, 113, 273-286.
7. Kumar, P.A., Anupriya, B. (2022). "Performance assessment of cruciform steel column: fem simulation." Materials Today: Proceedings, 64, 1043–1047.
8. Lu, W.-B., Chen, M., Shi, Y., Li, B.-S. (2023). "Numerical simulation and specification provisions for cruciform cold-formed steel built-up columns." Structures, 51, 484-497.
9. Naderiana, H., Sanchesa, R., Mercana, O., Kushnerb, P.J., Azharic, M., Ronagh, H. (2019). "Stability of stiffened cruciform steel columns under shear and compression by the complex finite strip method." Thin-Walled Structures, 136, 221-234.
10. Scherzinger, W.M. (2022). "Yield surface curvature and the stability of a cruciform column." International Journal of Solids and Structures, 257, 111542.

A Comprehensive Review on Metallic and Composite Pressure Vessels

Shabla K
PG Scholar
Department of Civil Engineering
NSS College of Engineering
Palakkad, Kerala
✉ shabla1999@gmail.com

Chitaranjan Pany
Structural Entity
VSSC
Thiruvananthapuram, Kerala
✉ c_pany@yahoo.com

Keerthy M. Simon
Assistant Professor
Department of Civil Engineering
NSS College of Engineering
Palakkad, Kerala
✉ keerthymsimon@nssce.ac.in

ABSTRACT

Pressure vessels play a vital role in various industrial applications, designed to safely contain and manage fluids under high pressure. Metallic pressure vessels, typically made from materials such as steel and aluminium, are explored in terms of their durability, fabrication methods, and established design standards. In contrast, COPVs, which consist of a metallic or plastic liner reinforced with a composite overwrap of high specific strength and high specific modulus in a resin matrix, are known for their lightweight properties and enhanced performance. This review offers an in-depth comparison between metallic pressure vessels and composite overwrapped pressure vessels (COPVs), focusing on their manufacturing processes, design criteria, and failure modes. This review aims to provide a thorough understanding of the strengths and limitations of metallic and composite overwrapped pressure vessels, which aids in the selection and design of pressure vessels for various applications.

KEYWORDS: *Pressure vessels, Metallic, Composite overwrapped.*

INTRODUCTION

Pressure vessels are containers used for the storage of fluids at a pressure different from ambient [1]. These kinds of vessels find applications in various fields: aerospace, nuclear, power generation, medical automobiles, and domestic applications [2-5]. Incorrect design or manufacturing of pressure vessels can result in leakage or explosion, leading to significant loss of life and property [3,6,7]. The purpose of a pressure vessel is to store or process a fluid at high pressure or temperature[8]. This necessitates the proper design and analysis of pressure vessels.

In applications requiring low pressure, pressure vessels can be manufactured by rolling metal sheets[9]. In high-pressure applications, the wall thickness of the pressure vessel becomes crucial as it directly relates to structural strength. While increasing wall thickness enhances structural performance, it also adds weight to the structure[9]. The increase in weight and corrosive nature are the major challenges with metallic pressure vessels [10]. Finding a trade-off between weight and strength is a crucial step in designing pressure vessels for lightweight applications. The excessive consumption of steel in various industries also necessitates the need of finding an alternative to steel[11]. Composite overwrapped pressure vessels (COPVs) serve as viable alternatives to metallic pressure vessels, particularly in applications requiring lightweight structures[12-15]. COPVs constructed with a titanium liner and epoxy carbon woven prepreg offer a substantial mass advantage of 66.33% over their metallic steel counterparts[16]. COPVs featuring HDPE liners and E-Glass epoxy composites exhibit a significant mass advantage of 61% compared to metallic pressure vessels[9] .COPV is about 70% lighter than steel pressure vessels and about 30 to 50% lighter than aluminium-lined tanks [17]. This is attributed to the high specific strength and specific modulus of fibers[18,19] .Appropriate selection of composite materials results in pressure vessels with comparable performance.

PRESSURE VESSEL

Pressure vessels come in various shapes, such as spheres, cylinders, cones, ellipsoids, and composites[20,21] . Among these, the cylindrical shape is the most common one[22]. Different parts of a pressure vessel include the shell, end domes, nozzles, and supports[23]. Shell is the primary structural component of the pressure vessel where fluid is contained. End domes (also known as heads or domes) are end closures provided as the closing end in a pressure vessel. This increases the strength, structural integrity and also provides sealing properties for the fluid contained inside. Different heads used in a pressure vessel include a flat head, a hemispherical head, an ellipsoidal head, a torispherical head, and a conical head[4,24-28]. Nozzles are openings used for attaching piping for flow into or out of the vessel, attaching connections, and providing access to the vessel interior at the manway. Manholes are access points used for the purposes of maintenance, cleaning, and inspection. Support is used to bear all the loads of pressure vessels, which are considered to be the non-pressurised part of the vessel. Saddles support the pressure vessel on the ground and increase the stability of the structure.

MATERIAL SELECTION

Key considerations for material selection include the material’s mechanical properties, thermal properties, corrosion, cost-effectiveness, and availability. These factors collectively guide the material selection process, ensuring the chosen material aligns with both the functional and economic demands of the project. Various factors are given in Table 1 [29,30].

Table 1. Various factors affecting material selection of pressure vessel

Factors	Description
Strength	Includes yield strength, tensile strength, creep, and rupture strength. Strength determines the thickness of the pressure vessel.
Fabric Ability	Ductility to roll into the required section and weldability to join sections
Corrosion Resistance	Corrosive action can deteriorate the metal.
Cost	Includes material costs, labour costs, overhead costs etc.
Fracture Toughness	Ability to resist brittle failure when subjected to low temperature, high stress,
Other Factors	Weight, thermal conductivity, electrical resistance, magnetic properties, etc.

TYPES OF PRESSURE VESSELS – METALLIC AND COMPOSITE

Depending on the materials, pressure vessel is mainly classified into metallic and composite.

Fig. 1: Metallic pressure vessels[5]

Fig. 2: Composite Overwrapped Pressure Vessel[31]

Metallic Pressure Vessels

Metallic pressure vessels are containers made of isotropic materials such as steel or aluminium as shown in Fig. 1. It exhibits excellent strength, durability, and resistance to high temperatures and pressure. It has low manufacturing costs, easy verification of fracture controls, and a more simple design [16]. The major disadvantage is that they add weight to the structure and its corrosive nature.

Composite Overwrapped Pressure Vessels (COPV)

A COPV consists of a metallic or plastic liner over which the composite material is overwrapped to contain fluid, as shown in Fig. 2. It consists of fibres and a matrix combined at a macroscopic level[32,33]. The liner serves as a gas barrier between the contained fluid[34] and composite layers and prevents leakage of fluid. The fibres bear the tensile stress, whereas the matrix acts as an adhesive that binds the fibre[16]. COPV is suitable for light-weight structures with a higher failure pressure capacity[9,16,33-37].

Several terms related to COPV are essential for understanding their structure and function. These include the liner, which holds and prevents the permeation of fluids, and the composite overwrap, which provides primary structural integrity and pressure resistance, as given in Table 2[38,39]

Table 2: Terms related to COPV

Terms	Description
Liner	An internal barrier that holds fluid and prevents its permeation.
Mandrel	Form around which resin impregnated fibers are wound.
Filaments	Individual fibers of indefinite length.
Prepeg	Ready-to-wind material in roving form that is impregnated with resin
Ply	A single prepeg is known as ply.
Lamina	A single ply in a laminate.
Strands	An assembly of continuous filaments
Tow	An untwisted bundle of continuous filaments.
Yarn	An assembly of twisted filaments forming a continuous length
Continuous filament	Individual rods of small diameter flexible fibers of indefinite length
Continuous filament yarn	Yarns formed by twisting two or re continuous filaments.
Bandwidth	Width of fibers applied to the mandrel
Band density	Quantity of fiber reinforcement per inch of band width

In a COPV, fibers are oriented along two principal stress directions. While fibers in the hoop direction can be easily laid along the cylindrical region, known as hoop layers[40] as shown in Fig. 3(a), applying them over the dome region is extremely challenging due to slippage. Therefore, fabrics are provided on the domes, known as doily layers which serve as hoop layers. It is also nearly impossible to position fibres in the longitudinal direction of the PV without slippage. So, fibers are wound at a low helix angle in the longitudinal direction, known as helical winding[40] as shown in Fig. 3 (b). Layers of fibers can be stacked in a specific pattern to form a laminate as shown in Fig. 4.

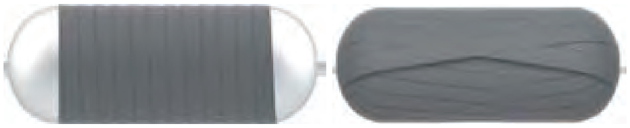

Fig. 3: (a) Hoop and (b) Helical windingl[37]

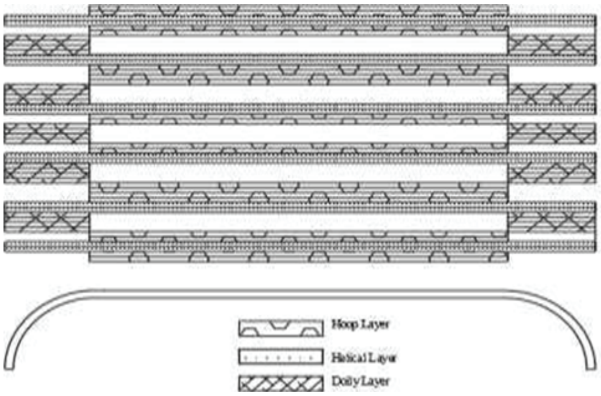

Fig. 4: Ply sequence [40]

It is preferable to lay the hoop layers as the outermost layers to get a proper consolidation effect[41]. The structure can be designed such that failure occurs in the cylindrical part due to hoop failure, which is primarily affected by membrane loading. On the other hand, helical failures are strongly affected by the bending loads due to the discontinuities. Therefore, design stresses for helical fibers are typically chosen to be lower than allowable stresses for hoop fibers. The preferred laminate sequence consists of helical layers wound alternately at ± the helical wind angle, followed by hoop windings to ensure adequate overall strength and stiffness[31,42]. The advantage of balanced symmetric laminate is that loading in one direction does not cause deformation in another plane[31].

COPVs are classified into I, II, III, IV, and V types based on construction[16,43-45], as shown in Fig. 5.

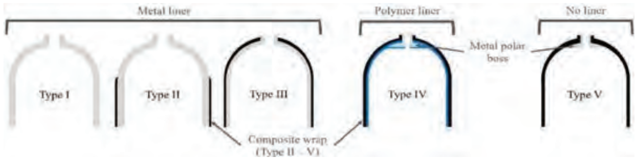

Fig. 5: Type 1, II, III, IV and V pressure vessel[46]

- Type I pressure vessel: PV, in which the whole structure is constructed from steel or aluminium, possesses substantial weight.
- Type II pressure vessel: PV with a metallic liner and an additional hoop-wrap of composites.
- Type III pressure vessel: PV with a metallic liner fully overwrapped with composites.
- Type IV pressure vessel: PV with a polymer liner and completely overwrapped composites.
- Type V pressure vessel : Type V pressure vessels are liner-less COPVs.

MANUFACTURING PROCESS

The manufacturing process of metallic PV and COPV is discussed below.:

Manufacturing Process of Metallic Pressure Vessels

The manufacturing process involves various steps[45].. Metal sheets are cut to size, with bevels and machining applied as necessary. Plates are then rolled into cylinders, utilising cold or hot rolling techniques. Longitudinal seam welds join metal edges parallel to the material's length, forming cylindrical shapes, while circumferential welds close loops or circles to extend cylinder lengths. Heads are cut, formed, and welded to the shell[47], potentially followed by heat treatment.

Manufacturing Process of Composite Overwrapped Pressure Vessels

The manufacturing process of COPV is carried out by the filament winding process[38,47]. Continuous fiber tows are passed through a resin material. The mandrel and the tow move relative to each other to wrap the fibers in a predetermined pattern over the liner. The resin is then dried at high temperatures to form prepreg tapes. After post-cure inspection, the vessel undergoes autofrettage. This involves pressurising the PV above the yield strength of the liner, leading to permanent deformation. As a result, it undergoes permanent deformation, leading to the formation of tensile strain in fiber composites and compressive strain in the liner.

DESIGN CRITERIA

Key factors affecting the design of pressure vessel is tabulated in Table 3.

Table 3: Design criteria of metallic pressure vessel and COPV.

DESIGN CRITERIA	METALLIC PV	COPV
Material Selection	• Include carbon steel, stainless steel, and alloy steels. • Resist internal and external pressure. • Should be corrosion-resistant. • Should be temperature-resistant.	• Metallic liner made of aluminium, stainless steel, or titanium. • Non-metallic liner made of polymers • Fibers are ofcarbon/glass/aramid • Epoxy as resins
Vessel Thickness	• Depends on internal pressure and material properties • Comply with standards such as the ASME boiler and pressure vessel code.	• Thickness and fiber layers are determined based on internal pressure and material properties. • Optimisation of fibers to maximise strength with minimum weight.
Stress Analysis	• Primary stress resulting from internal and external pressure • Secondary stress resulting from constraints like thermal expansion and contraction[50]. • Local stresses resulting from discontinuities or openings[51].	• Primary and secondary stresses from loadings, thermal effects, and interaction between liner and composite overwraps. • Interlaminar stresses in between composite layers.
Codes and standards	• Compliance with codes like ASME BPVC code API standards, PD5500, British Standards, European Codes.	• Compliance with the ASME BPVC code and others specific to COPVs. • Designed by using netting theory[52] classical laminate theory [54,55] etc.

FAILURES IN PRESSURE VESSEL

Failure in a pressure vessel occurs due to reasons relating to faults in materials and fabrication[30].

Failures in Metallic Pressure Vessel

Various types of failures in metallic pressure vessel is given in Table 4[14].

Table 4: Different types of failures in metallic pressure vessel.

Types	Description
Brittle Failure	Rapid crack propagation without significant deformation, often at low or intermediate temperatures. It occurs during a hydrostatic test with minor flaws.
Elastic buckling	Elastic buckling occurs when the structure becomes unstable under compressive stress and deforms significantly.
Plastic deformation	Excessive plastic deformation occurs when subjected to stresses significantly beyond its yield strength, leading to extensive and permanent distortion. To prevent excessive plastic deformation, ASME guidelines specify a stress limit.
Stress rupture	Creep deformation due to fatigue loading
Plastic instability	Cyclic deformation leads to significant, irreversible deformation due to the accumulation of plastic strain, ultimately leading to a loss of structural integrity.

Failures in Composite Overwrapped Pressure Vessel

Various types of failures in composite overwrapped pressure vessel are given in Table 5.

Table 5: Different types of failure in composite overwrapped pressure vessel

Types	Description
Burst from over pressurization	Bursting occurs when the vessel is operated beyond its design pressure
Fatigue failure of metallic liner	Repeated cyclic loading may result in failure of metallic liner
Burst resulting from liner	Progressive damage from matrix cracking, fiber breakage or other failures.
Stress rupture of composites	Time-dependent failure when subjected to a constant load over a period
Buckling of liner	Occurs when liner deforms under compressive stress.
Leak before burst	Failure mode where gas leaks through small cracks before a catastrophic rupture occurs. This gives an indication of how to detect the issue.

CONCLUSIONS

This review provides a detailed and comprehensive review of metallic and COPVs, focusing on their manufacturing processes, design criteria, and failure modes. Metallic pressure vessels, traditionally utilised for their robustness and established fabrication techniques, offer reliability and ease of manufacturing. However, they are susceptible to issues like corrosion, fatigue, brittle fractures, and heavier weight. On the other hand, COPVs, with their superior strength-to-weight ratio and stiffness-to- weight ratio, present a modern alternative to metallic pressure vessels. COPV is suitable for light-weight structure with high failure pressure capacity. The choice between metallic and COPVs should be guided by the specific requirements, operational conditions, and economic considerations. This review aims to serve as a comprehensive resource for the selection and design of PVs.

REFERENCES

1. Kumar, A.M., Manjunath, H.S. and Kumar, A.S.N. (2017). Design of pressure vessel using ASME codes and a comparative Analysis using FEA. International Research Journal of Engineering and Technology (IRJET), 4(11).
2. Yahya N. A., Daas, O. M., Alboum, N. O. F. and Khalile, A. H. (2018). Design of Vertical Pressure Vessel Using ASME Codes,pp.653-664. Modi, S., Modi, A. and Prajapati, R. Design and analysis of nozzle junction. (2018). International Journal of Science and Research, 7(1), pp. 1108-1111.
3. Sreelakshmi, M. G., & Pany, C. (2016). Stress analysis of metallic pressure vessels with circumferential mismatch using finite element method. International Journal of Scientific and Engineering Research, 7(4), pp. 479-484.

4. Kushwah, S., Parekh, S., Mistry, H. Darji, J. and Gandhi, R. (2021). Analysis of cylindrical pressure vessels with dissimilar ends and material comparison, Materials Today: Proceedings.

5. Sachidananda, H. K. and Durga, P. (2019). Design and analysis of pressure vessel. International Journal of Mechanical and Production Engineering Research and Development, 9(5), pp.125-136.

6. Mali, A., Bhosale, H. Bedi, D.S. and Modasara, A.(2017). A Review Paper on Study of Pressure Vessel, Design and Analysis. International Research Journal of Engineering and Technology, 4(5).

7. Yousaf, H. and Hamza, M., and Sattar, M.(2023). Design and analysis of a composite pressure vessel.

8. Mohanavel, S.V., Prasath, S., Arunkumar, M., Pradeep, G. M. and Babu, S.(2020).Modeling and stress analysis of aluminium alloy based composite pressure vessel through ANSYS software. Mater. Today Proc, 37(2), pp. 1911-1916.

9. A.R, Sreadha and Pany,C. (2020). Review on Fabrication of Bamboo Composite Materials Reinforced Concrete, pp. 258-279.

10. Sulaiman, S., Borazjani, S.,and Tang, S.H. (2013). Finite element analysis of filament-wound composite pressure vessel under internal pressure. IOP Conference Series Materials Science and Engineering, 50.

11. Yarrapragada, R., Kiran, B. V. and Krishnamohan, R. (2012). Composite Pressure Vessels.

12. Koushal, K., Manish, K. and Arun, K. (2022). Design and analysis of composite overwrapped pressure vessel with analysis of various overwrapping pattern. International Journal for Modern Trends in Science and Technology, 8(06), pp. 27-32.

13. Takalkar, A. S., Bhat, S. S., Chavan, S. S., Kamble, S.B., Kulkami, A.P. and Sangale, S.B. (2016). Finite element analysis of composite overwrapped pressure vessel for hydrogen storage, pp. 430-436.

14. Yu, B., Zhang, H., Ma, T.J. and Zhao, J.(2020) .Optimal Design of Composite Overwrapped Pressure Vessel for Space Application Based on Grid Theory Calculation and Numerical Simulation. 6th International Conference on Mechanical Engineering and Automation Science (ICMEAS). Moscow, Russia, pp. 93-99.

15. Gheshlaghi. R.M., Hojjati, M.H. and Daniali, H.R.M. (2018). Analysis of Composite Pressure Vessels.

16. Guo, K., Wen, L., Xiao, J., Lei, M. Wang, S., Zhang, C.and Hou, X. (2020). Design of winding pattern of filament-wound composite pressure vessel with unequal openings based on non-geodesics. Journal of Engineered Fibers and Fabrics, 15.

17. Liang, J., Wu, C., Zhao, Z., Tang, W. (2024). Forming Process and Simulation Analysis of Helical Carbon Fiber Reinforced Aluminum Matrix Composite. Metals, 11(12).

18. Pany, C. (2021). Cylindrical shell pressure vessel profile variation footprint in strain comparison of test data with numerical analysis. Liquid and Gaseous Energy Resources, 1.

19. Pany, C. (2022). Investigation of Circular, Elliptical and Obround Shaped Vessels by Finite Element Method(FEM) Analysis under Internal Pressure Loading. Journal of Scientific Technology and Engineering Research.

20. Hazizi, K. and Ghaleeh, M. (2023). Design and Analysis of a Typical Vertical Pressure Vessel Using ASME Code and FEA Technique. Design. 7(78).

21. Dhanaraj and Mallikarjuna, M.V. (2015).Design and Stress Analysis of a Cylinder with Closed ends using ANSYS.International Journal of Engineering Research and Applications, 5(4), pp. 32-38.

22. Bhinde, D. N. and Rajanarsimha, S.(2017). FEA analysis of pressure vessel with different type of end domes. Journal of Emerging Technologies and Innovative Research (JETIR), 4(2).

23. Lawate, S. and Deshmukh, B.B. (2015). Analysis of Heads of Pressure Vessel. International Journal of Innovative Research in Science, Engineering and Technology, 4(2), pp. 32-38.

24. Thattil, M.J. and Pany, C.,(2017). Design and analysis of pressure vessel with different end domes. International Journal of Science Engineering and Technology Research, 6(8), pp.1225-1233.

25. Digvijay, K. and Jewargi, S.S. (2015).Stress Analysis of Pressure Vessel with Different Type of End Connections by FEA. International Journal of Innovative Research in Science, Engineering and Technology, 4(5), pp. 2769-2775.

26. Patil, M.M. and Bajpai, L.(2014). Design, Analysis and Experimental Verification of Torispherical Head and Toriconical Bottom Pressure Vessel. International

Journal of Innovative Science, Engineering & Technology, 1(10), pp. 423-427.

27. Sadanandam, P., Ramesh, U., Samuel, T. (2017). Design and Analysis of Pressure Vessel Using Finite Element Method. International Journal of Latest Technology in Engineering, Management & Applied Science (IJLTEMAS),6(5).
28. Toudehdeghghan, A. and Hong, T.W. (2019). IOP Conf. Ser.: Mater. Sci. Eng. 469 012009
29. Nair, L., Arasu, Y. and Indu, V.S. (2013). Design of Laminated Pressure Vessel. International Journal of Science and Research (IJSR),6(14).
30. Ashok. T, HariKrishna. A. (2013). Analysis of LPG Cylinder Using Composite Materials, IOSR-JMCE, 9(2),pp. 33-42.
31. Mahdy, W., Ibrahim, H. and Soaly, E. (2013). Design Improvement of Composite Pressure Vessel Structure. International Conference on Aerospace Sciences and Aviation Technology,15,pp. 1-12.
32. Moskvichev, E. (2016). Numerical modeling of stress-strain behavior of composite overwrapped pressure vessel. Procedia Structural Integrity. 2
33. Alam, S. Yandek, G., Lee, R. and Mabry, J. (2020). Design and development of a filament wound composite overwrapped pressure vessel. Composites Part C: Open Access. 2.
34. Devaraju, A. and Pazhanivel, K., (2015). A study on stress analysis for design of pressure vessel. Int. J. Mech. Prod. Eng, 3(11), pp.98-101.
35. Kumar, G.C., Soundarya, N.R., Shobha, and Subashchandrabose. (2023). Analysis of a Composite Overwrapped Pressure Vessel by Analytical and Finite Elemental Approach. Journal of Mines, Metals and Fuels, 71(7), pp.1002–1007.
36. Greene, N., Yoder, T. and Saulsberry, R. (2019). Stress Rupture Testing and Analysis of the NASA WSTF-JPL Carbon Overwrapped Pressure Vessels. American Institute of Aeronautics and Astronautics. 5(2).
37. Peters, S.T. Composite Filament Winding. (2011). ASM International.
38. Madhavi, M.. “Design and Analysis of Filament Wound Composite Pressure Vessel with Integrated- end Domes.” Defence Science Journal 59 (2009): 73-81.ant in Sri Lanka.
39. Musthak, M., Valli, P.M. and Rao, S.N. (2016). Prediction of Transverse Directional Strains and Stresses of Filament Wound Composite Pressure Vessel by Using Higher Order Shear Deformation Theories, 6(3), pp. 79-87.
40. Ganesh, J., Kumar, K.S., and Kumar, B.A.(2018). Design and Analysis of Composite Pressure Vessel. International Journal of Science and Research (IJSR),7(8).
41. Rahul, B., Dharmahinder, S.C. and Dharani, J. (2022). A comprehensive review on the performance analysis of composite overwrapped pressure vessels. Engineering and Applied Science Research, 49(2), pp.272-287.
42. Regassa, Y., Jema, G., and Hirpa, G. L. (2022). Composite Overwrapped Pressure Vessel Design Optimization Using Numerical Method” Journal of Composites Science, 6(88).
43. Azeem, M., Ya, H., Alam, M., Kumar, M., Sajid, Z., Gohari, S., Maziz, A., Gemi, L., Abdullah, S. and Khan, S. (2023). Influence of winding angles on hoop stress in composite pressure vessels: Finite element analysis. Results in Engineering,10.
44. Moorthy, C. H. V. K. N. S. N. and Srinivas, V.(2018). Stress analysis of domestic composite LPG cylinder using Classical Lamination Theory. Int. J. Eng. Technol., 7(4), pp. 68–70.
45. Demir, K. U., Gokdag, I., Dagkolu, A. and Sahin, M. (2023). Shape and Size Optimization of an Aerospace Propellant Tank. 12th Ankara International Aerospace Conference (AIAC)
46. Pany, C. (2021). Structural Analysis of Metallic Pressure Vessels With Weld Sinkage in the Circumferential Joint . Journal of Scientific, Technology and Engineering Research , 2 (1) , pp.4-10 .
47. Mukund, K., Khatawate, V.H. and Patil, G.V.(2013). Weight Reduction of Pressure Vessel Using FRP Composite Material, pp. 300–310
48. Jois, K. C., Marcus, W., Thomas, G., and Johannes, S. (2021). Numerical Analysis of Filament Wound Cylindrical Composite Pressure Vessels Accounting for Variable Dome Contour. Journal of Composites Science,5(56).
49. Belardi, V. G., Ottaviano, M. and Vivio, F. (2023). Bending theory of composite pressure vessels: A closed-form analytical approach. Composite Structures, 329. 117799.

50. Daghia, F., Baranger, E., Tran, D.T. and Pichon, P. (2019). A hierarchy of models for the design of composite pressure vessels. Composite Structures. 235.

51. Padovec, Z., Vondracek, D. and Mares, T. (2023). The Analytical and Numerical Stress Analysis of Various Domes for Composite Pressure Vessels. Applied and Computational Mechanics, 16, pp.151- 166.

52. Sai, K.H.N., Rao, B.N., Pillai, T.P., Sajikumar, K.S. and Kumar K.P. (2023). Design and Analysis of a Metal Lined Composite Overwrapped Pressure Vessel. Journal of Polymer & Composites, 11(8).

53. Bhagyashri, U.B. and Mishra, H. (2015). A Review on Design and Analysis of Pressure Vessel. International Journal of Advance Research and Innovative Ideas in Education, 1(5).

54. William, G., Shoukry, S., Prucz, J., and Evans, T. (2013).Finite Element Analysis of Composite Overwrapped Pressure Vessels for Hydrogen Storage. SAE International Journal of Passenger Cars - Mechanical Systems, 6(3), pp.1499-1504.

Behaviour of Dissipative Embedded Column Base Connections Under Cyclic Loading

Revathykutty K M
PG Scholar
Department of Civil Engineering
NSS College of Engineering
Palakkad, Kerala
✉ revathykuttykm@gmail.com

Rohini G Nair
Assistant Professor
Department of Civil Engineering
NSS College of Engineering
Palakkad, Kerala
✉ rohinignair@nssce.ac.in

ABSTRACT

Dissipative embedded column base connections are aimed at redirecting inelastic energy dissipation. Unlike conventional methods that absorb this energy in steel columns, our focus is on controlled dissipation within the embedded section of these connections. Through detailed continuum finite element analysis, we investigate various loading and geometric factors using a highly accurate model validated against experimental data. The study examines how horizontal stiffeners in these bases can counter localized deformations and designs a specific dissipative zone within the steel column to limit inelastic deformations near the base. The ultimate aim is to enhance the resilience of first-story steel columns against local buckling. However, several factors influencing the behavior of these connections, such as steel column cross-sectional characteristics, axial load conditions, and history of lateral loadings, remain unexplored. Additionally, bidirectional effects stemming from three-dimensional earthquakes are yet to be studied. In this, we conduct analysis of Dissipative Embedded Column Base Connections (DECBs) with varying length-to-depth ratios. We also compare the performance of columns with Conventional Embedded Column Base Connections (CECBs) and DECBs, considering different cross-sections such as steel columns I-sections and rectangular hollow sections. Furthermore, we study oblique columns with varying angles of inclination.

KEYWORDS: *Dissipative embedded column base connections, Conventional embedded column base connection.*

INTRODUCTION

DECBs enhance seismic performance of steel column structures by incorporating energy-dissipating devices or materials into the connection design, which absorb and dissipate seismic energy, thereby improving ductility and reducing damage during earthquakes. In contrast, CECBs embed the column base directly into a concrete foundation without specific energy-dissipating mechanisms, relying on the inherent strength and rigidity of the concrete and steel interface to resist loads. While effective for general structural applications, CECBs do not provide the same level of energy dissipation and ductility under severe seismic loading as DECBs.

In seismic regions, fixed end column base connection in steel moment-resisting frames emphasize a strong base and weaker column approach, resulting in inelastic deformations near the column base during earthquakes. This can decrease flexural strength, torsional rigidity, and cause residual axial shortening in steel column. A proposed solution involves redirecting dissipation of energy in the column base, with studies showing success in using exposed column bases and ductile anchors to control yielding. While mid- and high-rise frames often use CECBs relying on the horizontal and vertical bearing of steel against concrete for resistance, DECBs incorporate a dissipative zone to enhance resilience and prevent local buckling. However, factors like steel column cross-sectional characteristics, axial loading condition, and bidirectional earthquake effects remain under explored. In order to solve these problems, this study simulates the hysteretic behavior of DECBs using a continuum finite element (CFE) model, validates the results against physical experiments, and examines how loading and geometrical parameters affect the cyclic performance of DECBs in comparison to CECBs.

PARAMETRIC STUDY

Column with varying length to depth ratio (Length of column above foundation – 1 m,1.5 m,2m and 2.5 m), Different cross sections (I section and Rectangular hollow cross section) and Oblique column (Selected angle of orientation with respect to major axis – 00,150,300,450,600,750 and 900) conditions are chosen for conducting parametric study in steel column with DECBs and CECBs connection.

Continuum Finite Element Analysis

The Finite Element Analysis (FEA) is a computational method for predicting response of structural components under various loading conditions by dividing structure into finite elements interconnected at nodes. The process includes pre-processing (model creation, material property definition, load application, and meshing), analysis (iterative calculations considering material behavior and loads), and post-processing (interpreting results to assess displacements, stresses, and strains). This method optimizes designs for safety, efficiency, and reliability across various industries. Model analysis is conducted by using Ansys workbench 2023 R2 software. The suggested CFE model analysis for CECBs and DECBs undergo cyclic loading analysis using real-world data from Inamasu et al. [9].

Material Properties

Tables 1 and 2 containing the dimensions and properties used for the analysis of I section and Rectangular hollow cross section column with CECBs and DECBs connection. Table 3. contains the Input Engineering [9] Data used for analysis in Ansys workbench 2023 R2 software.

Table 1. Dimensions of Test Specimens (I Section)

Specimens ID	d (mm)	bf (mm)	tw (mm)	tf (mm)	bf;r (mm)	Lc (mm)
C-N-0	400	180	8.6	13.5	-	1525
D-M1-1	400	180	8.6	13.5	88	1525

Table 2 Measured Dimensions of Test Specimens (Rectangular Hollow Section)

Specimen I.D	d (mm)	bf (mm)	t (mm)	Area of cross section (mm2)	bf;r (mm)	Lc (mm)
C-N-0	334	180	8	7980	-	1525
D-M1-1	334	180	8	7980	88	1525

Table 3. Input Engineering Data in Ansys workbench 2023 R2 [8-9]

Materials	Density (Kg/m^3)	Elastic Modulus (MPa)	Poisson's Ratio	Yield Strength (MPa)
Butyl Rubber	-	1.5	0.4	-
Styrofoam- xps	-	243	0.4	-
Concrete	-	9 x 104	0.15	-
Steel- Column	7850	2 x 105	0.3	-
Steel- Flange	-	2 x 105	0.3	377
Steel-Web	-	2 x105	0.3	407

The input engineering data for all materials used for modeling are summarized in Table 3. It containing Density, Young's modulus or Elastic modulus, Poisson's ratio and Yield strength for each materials.

Modelling

Model is developed by using ANSYS workbench software. A 20 Node solid 186 element type is employed in ANSYS software to develop the model. Hexahedral element are employed for meshing and element size is set at 40 mm.

The Fig 1. illustrate the model of I section column with DECBs and CECBs connections. Fig. 1(a) illustrates the model of the DECB connection in an I-section column. It is clearly observed that in the embedded portion of the flange section, it is cut with a radius, and the portion is filled with a dissipative element like Styrofoam. The embedded portion is fully covered with butyl rubber tape. Fig. 1 (b) illustrates the model of I sectional column with CECBs connection. In the model there is no dissipative elements are provided in the embedded portion of column and it is fully made with steel section.

(a) (b)

Fig. 1. (a) Model – DECBs I section, (b) Model – CECBs I section

The Fig. 2. illustrate the model of Rectangular hollow section column with DECBs and CECBs connections. Fig. 2.2 (a) illustrates the model of the DECB connection in a Rectangular hollow section column. It is clearly observed that in the embedded portion of column section, the two sides of rectangular column portion are cut with a radius, and the portion is filled with a dissipative element like Styrofoam. The embedded portion is fully covered with butyl rubber tape. Fig. 2.2 (b) illustrates the model of rectangular hollow sectional column with CECBs connection. In the model there is no dissipative elements provided in the embedded portion and it is fully made with steel section.

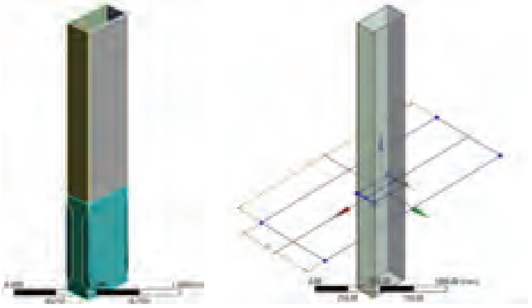

(a) (b)

Fig. 2. (a) Model – DECBs Rectangular hollow section, (b) Model – CECBs Rectangular hollow section

Boundary Conditions

Fig. 3 containing the boundary condition provided in DECBs and CECBs connection.

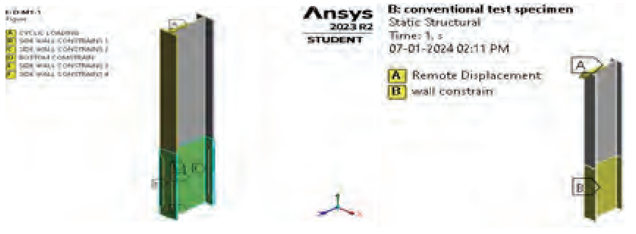

(a) (b)

Fig.3. (a) Boundary condition provided in DECBs connection, (b) Boundary condition provided in CECBs connection

Loading Protocol

Cyclic loading is the application of varying strains, stresses, or stress intensities to different sites on structural components. Fatigue degradation is the term to describe the possible degradation at the site. Fig. 4 and Table 4 [Example for validation model] Shows the FEMA loading protocol [1-2] is used for the cyclic loading analysis for the current study.

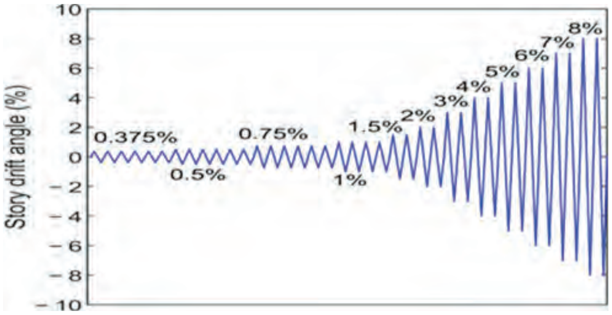

Fig. 4. FEMA Loading Protocol (Storey Drift Angle Vs Steps) [1-2]

Table. 4. Loading Protocol

AISC / FEMA Protocol			
Length (M)	**Drift Radian**	**Drift (% Rad)**	**Drift Displacement (Mm)**
1.525	0.00375	0.375	5.72
1.525	0.005	0.5	7.63
1.525	0.0075	0.75	11.44
1.525	0.01	1	15.26
1.525	0.015	1.5	22.89
1.525	0.02	2	30.52
1.525	0.03	3	45.79

1.525	0.04	4	61.06
1.525	0.05	5	76.35
1.525	0.06	6	91.66
1.525	0.07	7	106.98

RESULTS AND DISCUSSIONS

Analysed results and comparison of results are presented in the following sections.

Effects in Column with Varying Length to Depth Ratio

Table 5 containing the Peak load and maximum moment acting on the column with I section having DECBs connections corresponding to varying length of column above foundation (ie, 1m,1.5m,2m and 2.5m). These results show that the Peak load acting on column having 1-meter height above foundation is 461.46 kN and maximum moment acting on the column is 4.62×105kN-mm. For column having 1.525- m height above foundation having peak load of 310.29 kN and the maximum moment acting on column is 4.73×105 kN-mm. And in case of column having 2-meter height above foundation the peak load obtained is 237.23 kN and the maximum moment acting on column is 4.74×105 kN-mm. Column with 2.5-m height above foundation having peak load of 190.08 kN and the maximum moment acting on column is 4.75×105 kN-mm. Comparative analysis reveals that the height of the column increases, as that of the corresponding peak load decreases, while the maximum moment acting on the column gradually increases.

Table 5 Results Obtained from FEA Analysis

Length of the column above foundation (mm)	Peak load acting on column (kN)	D-M1-1 Mmax (10^5 kN-mm)
1000	461.46	4.62
1525	310.29	4.73
2000	237.23	4.74
2500	190.08	4.75

Effects in Column with Different Cross Section and Oblique Columns

Envelope Curve

The envelope curve is a fundamental measure employed to evaluate response of the structure subjected to lateral load, particularly in seismic events. It represent relationships between the applied load and corresponding lateral displacement or drift. Slope of the envelope curve in the inelastic range provides insights into the ductility of the structure. Higher slopes indicate greater ductility, allowing the structure to undergo larger deformations while maintaining a significant portion of its strength. Figs. 5 and 6 present the combination of envelope curves for all models of oblique columns with varying angles of orientation.

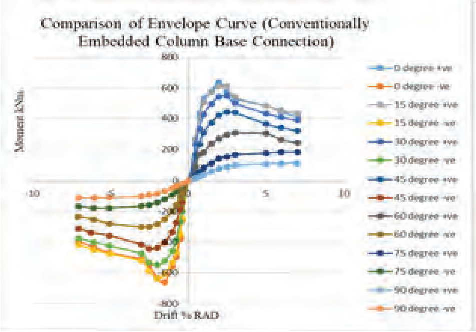

(a)

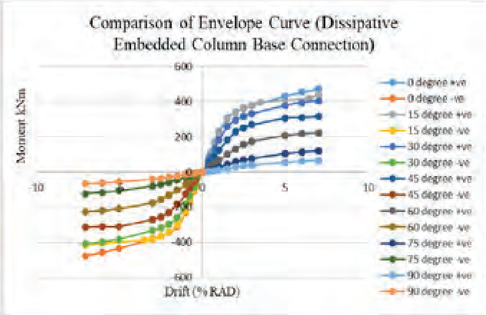

(b)

Fig. 5 Comparison of Envelope Curve for I Sectional (a) CECBs and (b) DECBs Oblique Columns

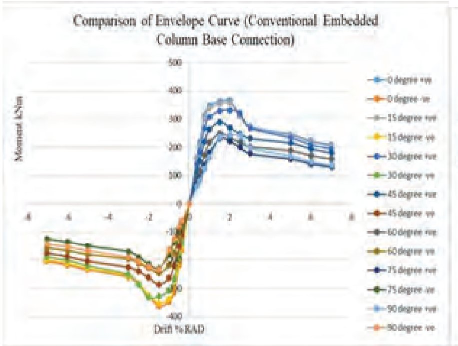

(a)

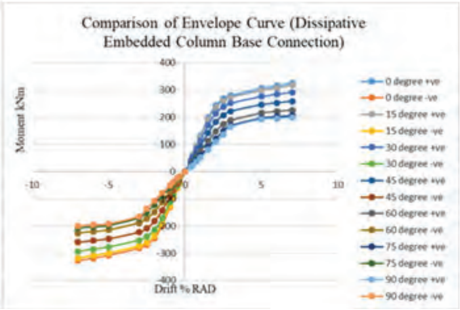

(b)

Fig. 6 Comparison of Envelope Curve for Rectangular Hollow Sectional (a) CECBs and (b) DECBs Oblique Columns

Table 6 and 7 illustrate the Ultimate moment and Yield moment obtained from analysis:

Table.6 Moment Capacities of I-Section Columns

Model	CECBs		DECBs	
	Ultimate Moment (kN-m)	Yield Moment (kN-m)	Ultimate Moment (kN-m)	Yield Moment (kN-m)
0^{0} Inclination	638.70	575.80	473.34	343.25
15^{0} Inclination	612.24	504.36	437.00	340.81
30^{0} Inclination	548.80	495.65	405.80	295.40
45^{0} Inclination	442.87	373.60	318.75	228.09
60^{0} Inclination	305.48	234.10	223.98	174.59
75^{0} Inclination	179.40	140.40	121.78	77.99
90^{0} Inclination	110.17	97.24	66.60	40.16

Table 7 Moment Capacities of Rectangular Hollow-Section Columns

Model	CECBs		DECBs	
	Ultimate Moment (kN-m)	Yield Moment (kN-m)	Ultimate Moment (kN-m)	Yield Moment (kN-m)
0^{0} Inclination	365.16	348.22	325.68	268.49
15^{0} Inclination	355.66	337.88	316.82	260.68
30^{0} Inclination	331.41	307.29	291.78	238.28
45^{0} Inclination	289.06	220.50	258.65	207.23
60^{0} Inclination	250.10	217.27	225.91	188.39
75^{0} Inclination	234.82	180.51	207.06	170.34
90^{0} Inclination	232.28	164.27	199.01	164.14

Energy Dissipation Capacity (EDC)

Table 8 indicates that DECBs connections demonstrate a higher energy dissipation capacity compared to CECBs connections for both I-section and Rectangular Hollow section cases. Specifically, columns oriented at 00 (major axis) exhibit greater ability to dissipate energy under cyclic loading conditions. In the case of I-section columns, the energy dissipation capacity (EDC) is measured at 201.88 kJ, while for Rectangular section columns, it is 130.01 kJ. Conversely, columns oriented at 900 (minor axis) display a lower capacity to dissipate energy. For I-section columns, the EDC is 11.01 kJ, whereas for Rectangular section columns, it is 51.96 kJ.

Table 8 Energy Dissipation Capacity Values

Energy Dissipation Capacity (EDC) (kNmm or kJ)			
Oblique Columns with I Sectional Cross section		Oblique Columns with Rectangular Hollow Cross section	
CECBs	DECBs	CECBs	DECBs
24.53	201.88	13.40	130.01
22.64	198.30	12.60	125.28
17.30	164.81	10.51	110.95
10.71	119.37	7.89	92.17
5.24	64.71	5.12	71.35
1.79	22.95	2.61	56.21
0.69	11.01	1.11	51.96

CONCLUSIONS

Major findings from the study are as follows:

- Columns with conventional bases experience axial shortening under 2% rad lateral drift, while DECBs experience less axial shortening regardless of loading history and drift amplitude due to their resilience against local buckling.
- Reduced flange width in the dissipative zones of the embedded column base connection is recommended and it validated to minimizing the local buckling in seismically compacted column cross sections.

- Use of Styrofoam and Butyl rubber tape in the reduced flange width area is recommended to minimize localized flange deformations under seismic or cyclic loads.
- Nonlinear continuum finite element simulations show that DECBs maintain stable hysteretic behavior even at 7% lateral drift because their primary energy dissipation mechanism does not rely on local buckling.
- DECBs have higher EDC than conventional bases, with I-section columns at 201.88 kJ and rectangular sections at 130.01 kJ along the major axis (i.e., angle of inclination 00) .
- Columns oriented along the minor axis (i.e., angle of inclination 900) show lower EDC, with 11.01 kJ for I-section and 51.96 kJ for rectangular sections.
- Transitioning from major to minor axis orientation results in a 94.55% reduction in EDC for I- section columns and a 60.03% reduction for rectangular columns.
- These findings highlight DECBs' superior performance in enhancing structural resilience and energy absorption, especially when aligned along the major axis (i.e., angle of inclination 00).

REFERENCES

1. Chi, B., & Uang, C. M. (2002). Cyclic response and design recommendations of reduced beam section moment connections with deep columns. Journal of Structural Engineering, 128(4), 464-473.
2. Elkady, A., & Lignos, D. G. (2018). Full-scale testing of deep wide-flange steel columns under multiaxis cyclic loading: Loading sequence, boundary effects, and lateral stability bracing force demands. Journal of Structural Engineering, 144(2), 04017189.
3. Elkady, A., & Lignos, D. G. (2018). Improved seismic design and nonlinear modeling recommendations for wide-flange steel columns. Journal of Structural Engineering, 144(9), 04018162.
4. Falborski, T., Torres-Rodas, P., Zareian, F., & Kanvinde, A. (2020). Effect of base- connection strength and ductility on the seismic performance of steel moment-resisting frames. Journal of Structural Engineering, 146(5), 04020054.
5. Falborski, T., Hassan, A. S., & Kanvinde, A. M. (2020). Column base fixity in steel moment frames: Observations from instrumented buildings. Journal of Constructional Steel Research, 168, 105993.
6. Freddi, F., Dimopoulos, C. A., & Karavasilis, T. L. (2020). Experimental evaluation of a rocking damage-free steel column base with friction devices. Journal of Structural Engineering, 146(10), 04020217.
7. Grilli, D. A., & Kanvinde, A. M. (2017). Embedded column base connections subjected to seismic loads: Strength model. Journal of Constructional Steel Research, 129, 240-249.
8. Inamasu, H., & Lignos, D. G. (2022). Finite element modeling and behavior of dissipative embedded column base connections under cyclic loading. Journal of Constructional Steel Research, 189, 107063.
9. Inamasu, H., de Castro e Sousa, A., & Lignos, D. G. (2022). Development and experimental validation of dissipative embedded column base connections for enhanced seismic performance of steel moment-resisting frames. Journal of Structural Engineering, 148(3), 04021280.
10. Inamasu, H., Kanvinde, A. M., & Lignos, D. G. (2021). Seismic design of non-dissipative embedded column base connections. Journal of Constructional Steel Research, 177, 106417.
11. Inamasu, H., Lignos, D., & Kanvinde, A. (2018). Influence of embedded steel column base strength on earthquake-induced residual deformations. In Proceedings of the 16th European conference on earthquake engineering.
12. Lignos, D. G., Hikino, T., Matsuoka, Y., & Nakashima, M. (2013). Collapse assessment of steel moment frames based on E-Defense full-scale shake table collapse tests. Journal of Structural Engineering, 139(1), 120-132.
13. Suzuki, Y., & Lignos, D. G. (2021). Experimental evaluation of steel columns under seismic hazard-consistent collapse loading protocols. Journal of Structural Engineering, 147(4), 04021020.
14. Trautner, C., Hutchinson, T., Grosser, P., Piccinin, R., & Silva, J. (2019). Shake table testing of a miniature steel building with ductile-anchor, uplifting-column base connections for improved seismic performance. Earthquake Engineering & Structural Dynamics, 48(2), 173- 187.

15. Trautner, C. A., Hutchinson, T., Grosser, P. R., & Silva, J. F. (2017). Investigation of steel column–baseplate connection details incorporating ductile anchors. Journal of Structural Engineering, 143(8), 04017074.

16. Trautner, C. A., Hutchinson, T., Grosser, P. R., & Silva, J. F. (2016). Effects of detailing on the cyclic behavior of steel baseplate connections designed to promote anchor yielding. Journal of Structural Engineering, 142(2), 04015117.

17. Zareian, F., & Kanvinde, A. (2013). Effect of column-base flexibility on the seismic response and safety of steel moment-resisting frames. Earthquake Spectra, 29(4), 1537- 1559.

18. Zhang, X., & Ricles, J. M. (2006). Experimental evaluation of reduced beam section connections to deep columns. Journal of Structural Engineering, 132(3), 346-357.Balakrishnan, S.; James, R. M. "Comparative Study of Tube in Tube Structures and Tubed Mega Frames". International Journal of Recent Trends in Engineering and Research 2019, 4(6), 18–26. https://doi.org/10.23883/ijrter.2018.4312.9

Seismic Analysis of Buckling Restrained Braced Frames

Sandra Mariya Martin
PG Scholar
Department of Civil Engineering
NSS College of Engineering
Palakkad, Kerala
✉ sandramariya48@gmail.com

Rohini G Nair
Assistant Professor
Department of Civil Engineering
NSS College of Engineering
Palakkad, Kerala
✉ rohinignair@nssce.ac.in

ABSTRACT

Building constructions in seismic zones frequently use buckling-restrained braced frames (BRBFs) as their lateral force-resisting systems. Using E-TAB software, this study examines the seismic performance of tall buildings with braced frames that are buckling constrained. The goal of the research is to assess the usefulness of different brace conformations in reducing the seismic response. In order to contrast the characteristics of storey displacement, storey drift, and storey shear, a building model is used to review the behaviour of the structure with and without BRB. For analysis of the structure three distinct configurations of bracings mainly, bare frame, inverted V and X-pattern are considered. The study provides a comprehensive assessment of how structures respond during seismic occurrences by considering a range of earthquake intensities and various configurations.

KEYWORDS: *Buckling-restrained braced frames, Seismic analysis, Braced frames, ETABS.*

INTRODUCTION

Due to the world's population growth, the construction industry finds it challenging to locate the land space needed for their projects. Therefore, instead of building their projects over a large area, the construction industry has begun to favour compact designs, which also helps to save money on materials and land. Hence, the vertical growth of buildings in the form of skyscrapers and high-rise buildings became the recent trends but these leads to an increased risk of seismic damage. Because of the collapse of structures, earthquakes mostly result in financial losses as well as fatalities. The seismic activity has a significant impact on the main structural components, such as beams and columns. As a result, the structural engineer is very concerned with creating an earthquake-resistant system that efficiently releases energy from the structure.

The preliminary aim of energy dissipation elements is to reduce the damage on the structural components caused due to seismic events. Bracing systems are evenly incorporated into the structure to withstand these lateral stresses without compromising its strength and stability. Nevertheless, the conventional bracings undergo buckling under compression when the lateral forces act on the structures. Hence, Buckling Restrained Braces (BRB) are the functional solution for this issue. Wakabayashi first proposed the concept of Buckling Restrained Braces (BRBs) in 1973. He created a system that consisted of two precast concrete plates placed between flat steel plates. BRBs are the new generation braced frame system mainly resist the lateral forces for instance seismic forces as well as wind force which is much more effective than conventional concentric braces. Buckling Restrained Braces (BRBs) has the ability to prevent the buckling under compression.

BACKGROUND SUMMARY

Buckling Restrained Braces (BRB) are the braces which attempts to inhibit buckling under compression. This allows the building to endure lateral loading mainly earthquake induced loading as well as wind force. BRBs are capable of yielding under compression and tension without the braces buckling. Fig. 2.1 depicts the composition of BRB. It mainly exhibits stable hysteretic behaviour and high energy dissipation capacity. Moreover, it can be easily connected to the structural members like beams and columns of the building. Also, these BRB elements can be replaced after a major seismic event if necessary. Compared to conventional braces,

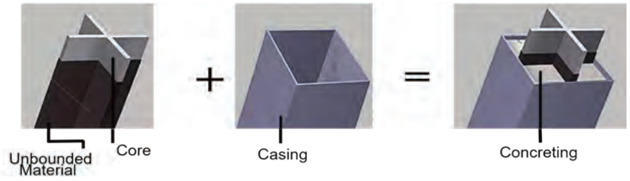

Fig. 1 Composition of BRB

BRBs provides cost effective solution in lateral load resisting system and easier to install as compared to other seismic-resistant systems. Buckling Restrained Braces uses its ductility of steel to afford system ductility. BRBs can be configured in various ways according to the building height, geometry, expected seismic forces the BRB configurations are selected.

BRBs are considered as the new generation braces which has a stable energy dissipation property. It has examined the base shear, storey displacement and various parameters and has emphasized the importance of the BRB. BRB is considered as the best lateral load resisting system and is provided to minimize the lateral displacement of the structure. BRB enhance building resilience by preventing buckling and allowing controlled yielding during seismic events. They contribute significantly to the safety and stability of structures.

- Single bracing configuration: single BRB is accommodated between two structural element and offer lateral load resistance in one direction.
- V- bracing configuration: BRB with V-shaped pattern which involves two BRBs oriented diagonally from the central point and extending downwards to both ends.
- X-bracing configuration: BRB are installed in X-shaped pattern and it is used in buildings with design or architectural preferences.
- Inverted-V bracing configuration: two BRBs are installed in inverted-V shaped pattern and it is effective in resisting lateral loads also providing architectural flexibility.

Different configuration BRBs accommodated in the buildings are illustrated in Fig. 2.

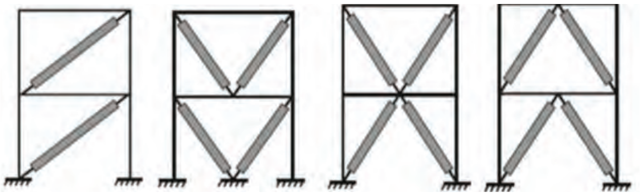

Fig. 2: Different configuration of BRBs

MODELLING OF STRUCTURE

A G+5 storeyed steel structural is taken for the analysis. The modelling is carried out in ETABS, with and without incorporating BRB. Different configurations of BRB like X-pattern as well as Inverted-V type are kept at the middle and corner of the steel structure. Structural details of the models are shown in Table 1.

Table 1: Structural details of the model

Description	Specifications	
Number of stories	G+5	
Height of each floor	4m	
Beam size	ISMB 350	
Column size	Interior Column ISHB 300	
	Exterior Column ISHB 450	
Type of BRB	X-pattern, Inverted V	
Seismic zone	V	
Soil condition	Medium soil	
Response reduction factor, R	5	
Importance factor, I	1.5	
Zone factor, Z	0.36	
Terrain category	4	
Wind speed	44 m/s	
Yield stress	Beam	240MPa
	Column	330MPa
	BRB	240MPa

A G+5 storeyed steel structure is considered for modelling. By using ETABS software steel structure with and without BRBs are modelled. Various models were created- bare frame, X-configuration at centre, X-configuration at corners, inverted-V configuration at centre, inverted-V configuration at corners. Structural plan of G+5 storey steel frame is illustrated in Fig. 3.

Fig. 3 Structural plan of G+5 storey building

Building Models

The following models are modelled in the ETABS software for finding the seismic performance of structures using response spectrum analysis.

MODEL 1: 3D model of G+5 storey building without BRBs

MODEL 2: 3D model of G+5 storey building with X-pattern BRBs at the centre of building

MODEL 3: 3D model of G+5 storey building with X-pattern BRBs at the corners of building

MODEL 4: 3D model of G+5 storey building with inverted-V pattern BRBs at the centre of building

MODEL 5: 3D model of G+5 storey building with inverted-V pattern BRBs at the corners of building 3D model of G+5 storey building with different configuration of BRBs are depicted. Fig 4 shows the bare frame, also Fig 5 picturises the G+5 storey building with X-pattern BRBs at the centre of building and 3D model of G+5 storey building having X-pattern BRBs accommodated at the corners of the building is depicted in Fig. 6.

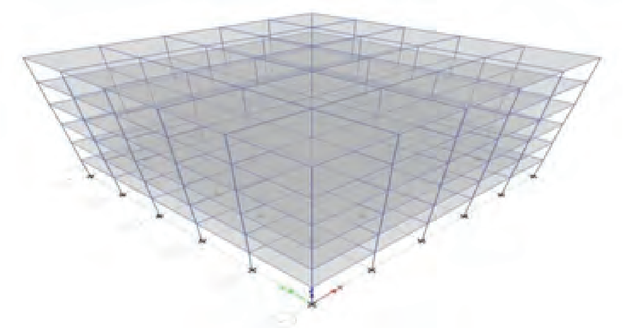

Fig. 4: 3D model of G+5 storey building without BRBs

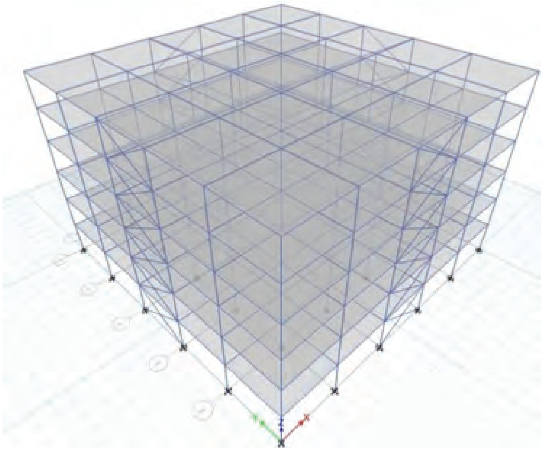

Fig. 5: 3D model of G+5 storey building with X-pattern BRBs at the centre of building

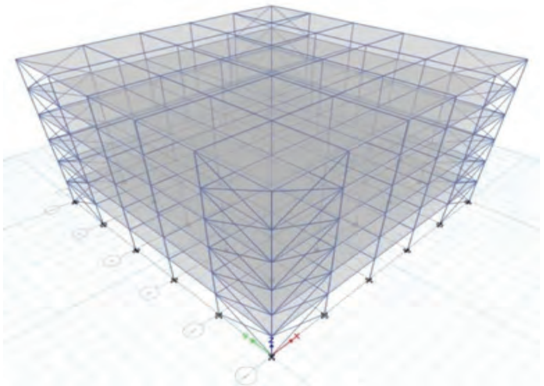

Fig 6: 3D model of G+5 storey building with X-pattern BRBs at the corners of building

Fig 7 shows the building with inverted-V BRBs given at the centre of the building and 3D model of G+5 storey building with inverted-V pattern BRBs at the corners of the building has been depicted in Fig. 7.

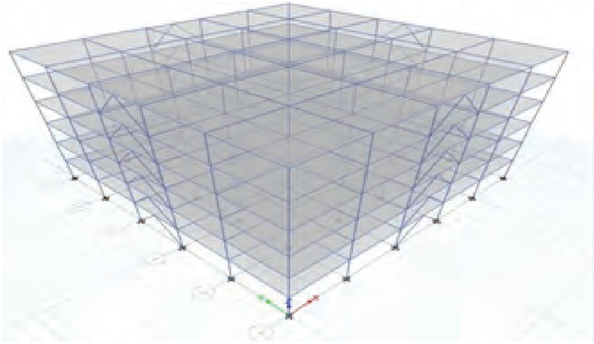

Fig. 7: 3D model of G+5 storey building with inverted-V pattern BRBs at the centre of building

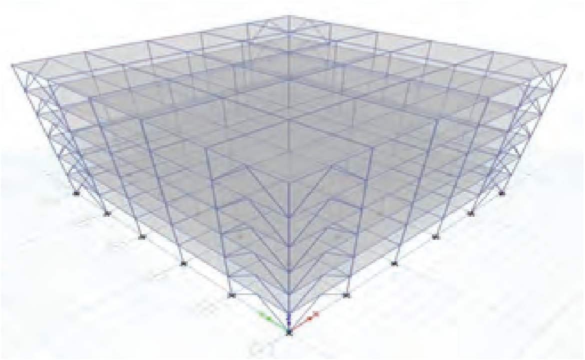

Fig. 8: 3D model of G+5 storey building with inverted-V pattern BRBs at the corners of building

RESULTS AND DISCUSSIONS

Maximum storey displacement, maximum storey drift and storey shear of the steel structure by accommodating BRB and by response spectrum analysis their performances was carried out in ETABS software. Thus, a comprehensive comparison is conducted among different configurations.

Maximum Storey Displacement

Maximum storey displacement of the steel structure having different configuration of BRB are illustrated in Fig 9. Compared to all the models inverted-V BRBs shows less displacement and hence it is more effective to resist the lateral forces.

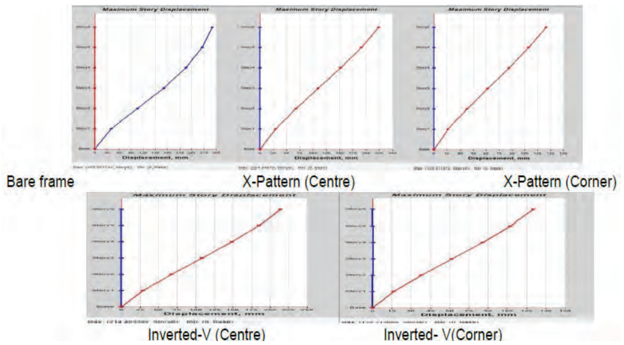

Bare frame X-Pattern (Centre) X-Pattern (Corner)

Inverted-V (Centre) Inverted- V(Corner)

Fig. 9: Maximum storey displacement for different configuration of BRB

Table 2 displays the comparison of maximum displacement of G+5 steel structure and Fig 4.2 depicts the bar graph of the maximum displacement of models with different configurations.

Table 2: Comparison of maximum storey displacement of G+5 steel structure

Configurations	Maximum Storey Displacement (mm)
Bare Frame	289.50773
X-Pattern (Centre)	224.04079
X-Pattern (Corner)	129.51197
Inverted-V (Centre)	214.40339
Inverted- V(Corner)	125.21568

Comparison of steel structure is done; that is with the model without BRB and with the structure by incorporating BRB at the centre and corner of the building. Table 3 displays the percentage decrease in the maximum storey displacement of BRBs with various configurations in comparison to bare frame. BRBs incorporated at corner position has the more percentage reduction in storey displacement, of which inverted-V configuration shows the greater value.

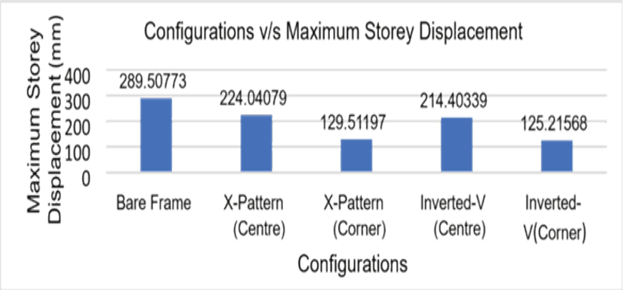

Fig. 10: Comparison of maximum displacement of G+5 steel structure

Table 3: Percentage reduction in maximum displacement of G+5 steel structure

Configurations	Percentage Reduction
X-Pattern (Centre)	22.6131
X-Pattern (Corner)	55.2647
Inverted-V (Centre)	24.1775
Inverted- V(Corner)	56.7487

Maximum Storey Drift

Maximum storey drift of the steel structure having different configuration of BRB are illustrated in Fig 11. Storey drift value should be less that is the structure which is seismic resistant will show less drift value.

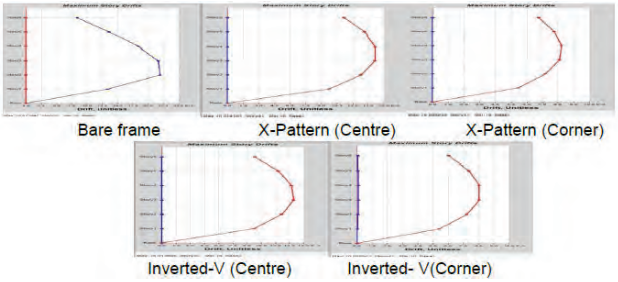

Fig. 11: Comparison of maximum storey drift of G+5 steel structure

Configurations	Maximum Storey Drift
Bare Frame	0.021947
X-Pattern (Centre)	0.014183
X-Pattern (Corner)	0.008234
Inverted-V (Centre)	0.013908
Inverted- V(Corner)	0.008062

Table 4 compares the storey drift of G+5 structure and obtained the value of 0.008062 for structure incorporated with inverted-V BRBs. Fig. 12 displays the bar graph of the maximum storey drift for each model.

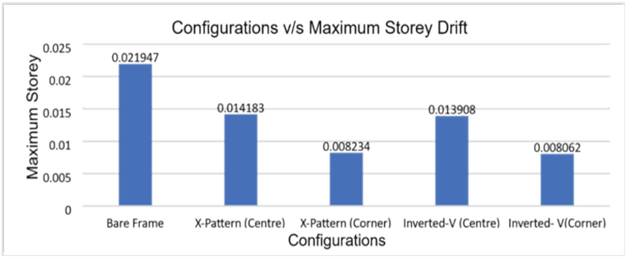

Fig. 12: Comparison of storey drift of G+5 steel structure

Percentage reduction of storey drift of steel structure with and without BRB is depicted in Table 5.

Table 5: Percentage reduction in storey drift of G+5 steel structure

Configurations	Percentage Reduction
X-Pattern (Centre)	35.3761
X-Pattern (Corner)	62.4823
Inverted-V (Centre)	36.6291
Inverted- V(Corner)	63.2661

Storey shear

Storey shear of the steel structure incorporated with different configuration of BRB are illustrated in Fig 13.

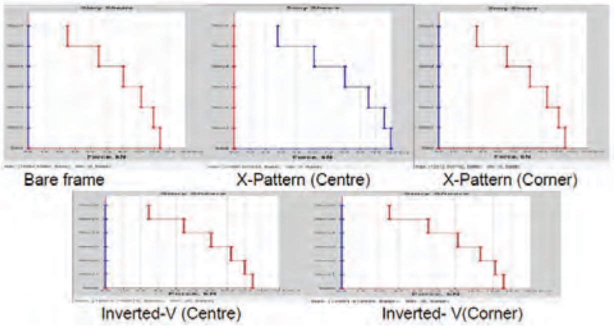

Fig 13: Storey shear for different configuration of BRB

Table 6: Comparison of storey shear of G+5 steel structure

Configurations	Storey Shear
Bare Frame	11966.90264
X-Pattern (Centre)	12594.53891
X-Pattern (Corner)	12812.00970
Inverted-V (Centre)	12677.70857
Inverted- V(Corner)	12881.41494

Table 6 compare the storey shear of the structure; the value of storey shear must increase that is its ability to resist the seismic forces increases.

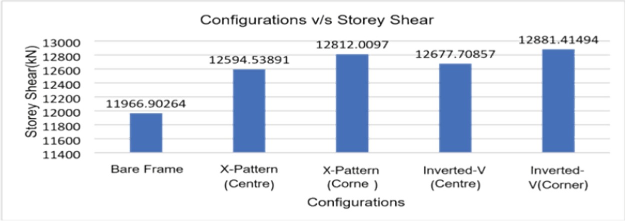

Fig 14: Comparison of storey shear of G+5 steel structure

When comparing the steel structure with and without BRB, the percentage increase in storey shear is shown in Table 7 and bar chart of the storey shear is depicted in Fig 15. By comparing with the structure with bare frame inverted-V BRBs shows percentage increase of 7.6336%.

Table 7: Percentage increase in storey shear of G+5 steel structure

Configurations	Percentage Reduction
X-Pattern (Centre)	5.2447
X-Pattern (Corner)	7.0620
Inverted-V (Centre)	5.9397
Inverted- V(Corner)	7.6336

CONCLUSIONS

G+5 storey steel structure with and without the different configurations such as X-pattern and inverted V pattern buckling restrained braces were analysed using ETABS software. The following closures were developed:

- From the analysis, the importance and effectiveness of BRB is studied from the comparison of model with and without the buckling restrained braced structure. Moreover, the maximum storey displacement, storey drift as well as storey shear is noted by response spectrum analysis.
- Additionally, from comparison of all the models it recorded that the inverted-V BRBs has greater ability to reduce displacement and drift, also increases the storey shear while seismic forces act on the structure.
- The optimal placement of BRBs at corners of the building frame is highlighted as a key factor in achieving favourable results.
- It is noteworthy that the inverted-V BRBs positioned at the corners reduced both drift and displacement by roughly 63.26% and 56.74%, respectively. Additionally, the storey shear of the G+5 structure under study increased by 7.63%.

REFERENCES

1. Hanieh Abedini, Seyed Rohollah Hoseini Vaez, Alireza Zarrineghbal, “Optimum design of bucklingrestrained braced frames”, Structures, Vol 25, pp 99-112 (March 2020)
2. Jinkoo Kim, Hyunhoon Choi, “Behavior and design of structures with buckling-restrained braces”, Engineering Structures Vol 26, pp 693-706 (September 2017)
3. Mahdi Eghbali, Esmaeil Asadian, Gholamreza Ghodrati Amiri, Seyed Ali Razavian Amrei, “Seismic performance of steel frames equipped with buckling-restrained braces (BRBs) using nonlinear static and dynamic analyses”, International ltd Journal of Vibroengineering, Vol 19, pp 1392-8716 (March 2017)
4. Muhamed Safeer Pandikkadavath and Dipti Ranjan Sahoo, “Mitigation of seismic drift response of braced frames using short yielding-core BRBs”, Steel and Composite Structures, Vol 23, pp 285302 (January 2017)
5. Nayana Surendran, Dr. K Subha, “Seismic Evaluation of Building with Buckling Restrained Braces”, International Journal of Scientific & Engineering Research Vol 8, pp 2229-5518 (November 2017)
6. Omid Souri, Massood Mofid, “Seismic evaluation of concentrically braced steel frames equipped with yielding elements and BRBs”, Results in Engineering, Vol 17 (December 2023)
7. Quan Gu, Alessandro Zona, Yi Peng, Andrea Dall’Asta, “Effect of buckling-restrained brace model parameters on seismic structural response”, Journal of Constructional Steel Research, Vol 98, pp 100-113 (March 2014)
8. Muhamed Safeer Pandikkadavath, Sujith Mangalathu, Romanbabu M Oinam, P C Ashwin Kumar, Dipti Ranjan Sahoo, N M Anoop Krishnan, “Drift Response Evaluation of Buckling-Restrained
9. Braced Frames (BRBFs) under Sequential Seismic Disturbances”, Materials Science and Engineering Vol 936 (October 2020)
10. R. Tremblay, M. Dehghani, L. Fahnestock, R. Herrera, M. Canales, C. Clifton, and Z. Hamid, “Comparison of Seismic Design Provisions for Buckling Restrained Braced Frames in Canada, United States, Chile, and New Zealand”
11. R. Tremblay, P. Bolduc, R. Neville, and R. DeVall,” Seismic testing and performance of buckling restrained bracing systems”, Canadian Journal of Civil Engineering, Vol 33, pp 183-198 (February 2006).

Influence of Flow Stress Curve and Other Damage Parameters on Ductile Failure Response

Meenu T R
PG Scholar
Department of Civil Engineering
NSS College of Engineering
Palakkad, Kerala
✉ meenutr2000@gmail.com

ABSTRACT

Ductile damage is observed in structural members undergoing large plastic deformation. Numerical prediction of damage/failure in any structure is very important for efficient design and optimization or residual life prediction. Generally, ductile damage occurs in three phases, namely void nucleation, void growth, and void coalescence, leading to total rupture. During the numerical prediction of the model, the failure process can be accomplished by simulating the plastic deformation beyond necking, using a void nucleation criterion, and finally providing a criterion for the evolution of void growth. Therefore, the input of the accurate stress-strain data, fracture strain, stress triaxiality conditions, and damage evolution law for element deletion are more important. This study aims to investigate the influence of different damage parameters on the ductile failure of the dog bone-shaped round bar specimens. The simulations are conducted using ABAQUS/CAE FE software, which implements ductile damage simulation using the conventional damage modeling technique. By conducting these studies, it aims to explore the significance of providing the full flow stress curves and the significance of choosing appropriate ductile damage parameters.

KEYWORDS: *Ductile damage parameters, Flow stress curve, ABAQUS/CAE*

INTRODUCTION

Ductile materials with remarkable mechanical capabilities have extensive applications in various engineering structures. High strength, ductility, toughness, and stiffness are some of their most remarkable characteristics. These qualities enable these materials to withstand enormous loads, deform plastically without sudden fracture or failure, and exhibit resilience to external forces. Because of these characteristics, metals play a pivotal role in structural applications. Despite their ductile characteristics, metals are susceptible to progressive damage accumulation during plastic deformation. Microstructural flaws, including voids, micro-cracks, and dislocations, arise within the material as the structure deforms. Over time, these flaws cause the material to become weaker and lose its ductility and ability to support loads, eventually leading to failure. Failure occurring with a specific level of measurable plastic deformation is a ductile fracture. From the micro-mechanisms perspective, ductile failure in metals is frequently associated with the emergence of ductile cracks, which are brought about by the nucleation, growth, and coalescence of micro voids and cracks.

Under loading conditions, the material behavior will initially be linear. However, upon loading beyond the yield strength, the material loses its elasticity, and plastic deformation is initiated, followed by the accumulation of damage within the materials. Fig. 1 depicts the different phases of ductile damage, which helps to better understand the growth and evolution of ductile damage within the specimens. From Fig. 1, it can be seen that initially, the deformation will be uniform within the material; as the deformation continues due to the localization of stress within the specimen, it leads to necking characterized by a considerable reduction in the cross-sectional area. The onset of the ductile damage is marked by the formation of micro-structural defects such as voids, and micro-cracks within the material. The damage growth phase is characterized by the expansion and propagation of the micro-structural flaws initiated during nucleation. With the accumulation of further damage, several flaws within the material may combine or coalesce, which is marked by the coalescence phase. Larger voids or cracks are created as a result of this process, accelerating the deterioration of material integrity and raising the possibility of the emergence of major flaws and finally leading to complete failure. [11] The following Fig. 2 depicts the ductile damaged specimens.

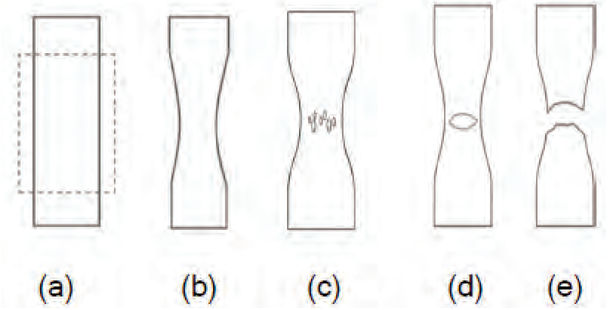

Fig. 1 Different phases of ductile damage [5]

Fig. 2 Ductile Damaged Specimens [15]

A damage model may be used to explain how a material's capacity to withstand loads or pressures tends to decrease over time due to internal cracks or faults. According to this model, a material undergoes a deterioration phase following the elastic and plastic phases, during which the initiation and expansion of internal voids affect the material's mechanical properties. The conventional method of damage modeling is investigated in this paper, which involves the incorporation of the stress-strain curves obtained from the experiments, which are actually the damaged stress-strain curves. Here, the damage stress-strain curves indicate that these input data can capture the material responses accurately. Thus, corresponding damage behavior under real-world conditions can be simulated, enhancing the accuracy in predicting the material behavior characteristics.

The accuracy of the ductile damage simulation depends on the precise input parameters given for the simulations, including the material properties, stress-strain curves, and ductile damage parameters. The implementation of ductile damage models can be clearly understood from the previous studies conducted; the process of void nucleation, growth, and coalescence leading to failure are well described.

Specification of failure mechanisms consists of four major parts, which are as follows: [6,9,10,14]

- Definition of effective (or undamaged) material response (as shown in the curve a-b-c-d' in Fig. 3)
- Failure initiation criteria (Point c in Fig. 3)
- Law of damage evolution (curve c-d section in Fig. 3)
- Option for element deletion, once the material stiffness is completely degraded, elements can be deleted from the calculation (Point d in Fig. 3).

These steps are followed to accurately simulate the ductile damage simulation using ABAQUS FE software. Materials such as steel, aluminum, and copper alloys, often used in industrial applications, are particularly susceptible to ductile damage. Thus, it is essential to comprehend the mechanics underlying ductile damage to forecast how materials will behave under different stress scenarios in engineering applications.

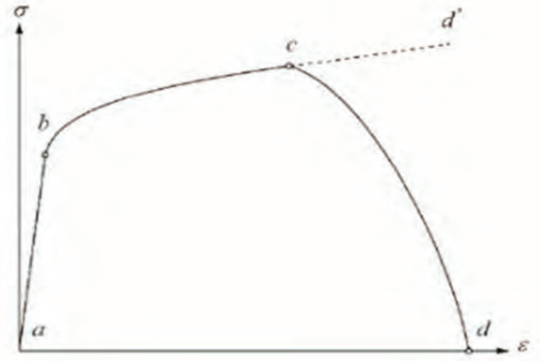

Fig. 3 Uniaxial tensile stress-strain curve of a standard material [6,9,14]

Even though many studies on ductile damage focus on the significance of ductile damage parameters, the importance of providing full stress-strain data for the simulations has to be studied properly. Moreover, the influence of other damage parameters in Abaqus in predicting the final failure must be understood for a better calibration of material data. Therefore, this paper will explore the sensitivity of the final failure to the input damage parameters in Abaqus.

FINITE ELEMENT MODEL

In this study, the ductile damage simulation of a smooth dog bone-shaped specimen without any initial imperfections is attempted. The geometry of the round dog bone specimen consists of a radius of 12mm at the shoulder part and 6mm at the gauge section, a gauge length of 80mm, and a total length of the specimen of 180mm. The FE simulation is carried out using the ABAQUS/CAE FE software. Due to the symmetry in geometry, the specimens were modeled as axisymmetric geometry discretized with four- node axisymmetric reduced integration elements (CAX4R) using transition meshing. The specimen was finely meshed at the central region to capture the damage behavior accurately, and the coarser mesh was given away from the center; this helped to save computational time. The bottom of the specimen was fixed, constraining all six degrees of freedom, and proper displacement was applied on the top in the axial direction by coupling all the nodes. The FE model of the smooth round bar thus modeled for the study is shown in Fig. 4.

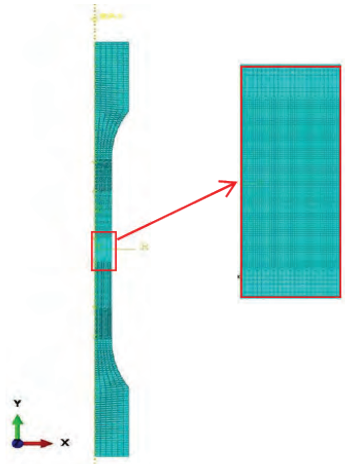

Fig. 4 FE Model of Smooth round bar used for the numerical study

For simulating large plastic deformation, the nonlinear geometry (NLGEOM) was kept on. Dynamic explicit analysis was conducted to accurately capture necking and the corresponding plastic deformations leading to failure.

INPUT PARAMETERS

Ductile damage simulation mainly depends on the accurate input parameters defined by the FEM software for accurately modeling the ductile damage within the materials. These parameters serve as the foundation for predicting the material behavior under plastic deformation. Thus, these input parameters should be selected and calibrated with at most care for effectively capturing the ductile damage behavior of the materials. The input parameters include the following:

- Mechanical properties, such as elastic modulus, yield strength, tensile strength, and elongation, are generally obtained through uniaxial tensile testing.
- The flow stress curve, which defines the material's stress-strain relations, is usually obtained from experiments of standard specimens.
- Damage parameters include the fracture strain, stress triaxiality, strain rate, and damage evolution law, which govern the relation between the applied stress and the damage evolution.

Hence, these parameters are to be precisely determined to ensure that accurate material damage responses can be obtained from the simulations.

Material Properties

Stainless steel round bar specimens are utilized to conduct these studies. From the experiments conducted, the initial yield stress of the specimen was found to be 235MPa and strain hardening exponent 0.1. Swift's power law determines the true flow stress, which may be given as per eq (1).[3]

$$\sigma = \square_0 \left(1 + \frac{s_p}{s_0}\right)^n \qquad (1)$$

where σ -True flow stress, $\square_0$ - Initial yield stress, s_0 - Initial yield strain,s0 - Plastic strain, n - Strain hardening exponent. Table 1 below depicts the material properties of the tensile specimen used for this study.

Table. 1 Material properties

SI No:	Material properties	Model input
1	Young's Modulus	210 GPa
2	Poisson's ratio	0.3
3	Mass density	7.8e-9 kg/mm^3

The above mentioned material properties are given as input to the software for the ductile damage simulation.

Stress-Strain Curves

Reliable predictions in ductile damage simulations using ABAQUS software may depend on proper material characterization. Often, design engineers tend to input the stress-strain available to them, which may be upto tensile strength limit, necking limit or ultimate strength limit, during the simulation of ductile damage. The full stress-strain curve's relevance in ductile failure must be brought out by understanding the response in displacement, true stress, and equivalent stress. Different boundaries of the stress- strain datasets are considered to examine the influence of the input flow stress curves. These different data limits are selected to fully comprehend how distinct segments of the stress-strain curve affect the output. The input stress-strain curves for studying the influence of stress-strain curves are as depicted in Fig. 5 below.

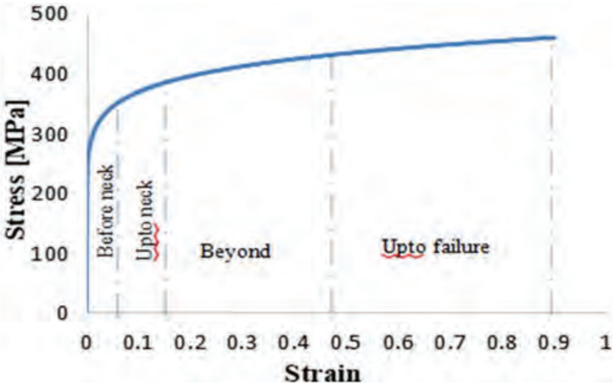

Fig. 5 Input flow stress curve

These boundaries pertain to particular parts of the stress-strain curve that are examined separately to evaluate their impact on the simulation outcomes, for example, flow stress data before the necking point, which represents the initial elastic and the plastic deformation, up to the necking point which covers the region until the onset of necking which will take into consideration the material behavior which marks the accumulation of plastic deformation, beyond necking point and up to failure point which provides the insights to ultimate strength and failure behavior of the material are considered for carrying out the study.

Ductile Damage Parameters

Accurate modeling of the ductile damage parameters is essential for effectively simulating the ductile damage behavior of the materials. The von Mises's damage model is utilized here for the damage simulation. Ductile damage, which ultimately leads to the failure of the material, can also be influenced by various factors, such as fracture strain, stress triaxiality, strain rate, damage evolution law, and element deletion criteria. The ductile damage may be inputted into two phases: the damage initiation and damage evolution criteria. Parameters governing the ductile damage initiation may include:

- Fracture strain - Fracture strain may be defined as the strain at which the material undergoes failure. It is a critical parameter governing the damage initiation because, beyond this value of strain, the damage initiates and eventually. For the current material, a fracture strain of 0.8 was considered.
- Stress triaxiality - Stress triaxiality may be defined as the ratio of the hydrostatic stress to the equivalent stress or the von Mises stress. It influences the onset of damage and characterizes the stress state within the material, which leads to failure. For a uniaxial tensile specimen, the triaxiality value may be chosen as 0.33.

Damage evolution describes the progressive degradation of the material once the conditions for damage initiation criteria are satisfied. It basically simulates the degradation in the material stiffness as the damage occurs within the material. The primary characteristics controlling this evolution law include the effective plastic displacement or the displacement at failure (Df) and the energy dissipation. [12] Here, displacement criteria is utilized for defining the damage evolution, and the expression for finding the effective plastic displacement or the displacement at failure is given in eq (2) .[4,6,13,14]

$$u_i^{pl} = L_{char} \cdot (\varepsilon_i^{pl} - \varepsilon_D^{pl}) \qquad (2)$$

Where, u_i^{pl} is the effective plastic displacement or displacement at failure, L_{char} is the element's characteristic length, εi^{pl} - Equivalent plastic strain at ultimate strength, εD^{pl} Equivalent plastic strain at damage initiation.

RESULTS AND DISCUSSION

For calibrating the damage evolution parameter, displacement at failure iterations was carried out to obtain a precise value. The influence of varying the parameter on the material response can be well understood from Table 2 depicted below.

Table 2 Calibration of displacement at failure parameter

Parameters	$D_f = 0.5$	$D_f = 0.1$	$D_f = 0.0125$
Logarithmic Fracture strain (LE22)	1.210	1.108	0.843

From Table 2, it can be observed that the material responses vary with the change in the displacement at the failure parameter. Here, the Df value of 0.0125 gives a more accurate value of the logarithmic fracture strain. It can be observed that lowering the displacement at failure (Df) tends to reduce the strain at fracture. The element deletion criteria are governed by the damage variable (Dcr). Traditionally, damage in Abaqus, the damage variable D is 0, representing undamaged material. Progression or accumulation of damage is indicated by the increase in the value of D to 1; on reaching 1, the material fails. However, in Abaqus, the element deletion criteria can be changed to accelerate damage initiation. The eq (3) below can relate the damage variable to stress response. [6,7,8,13,14]

$$\sigma = (1 - D)\bar{\sigma} \qquad (3)$$

Where σ - is the damage stress, $\bar{\sigma}$ -is the undamaged stress, D-is the damage variable The calibration of the damage variable is depicted in Table. 3.

Table 3. Calibration of damage variable

Parameters	$D_{cr} = 1$	$D_{cr} = 0.5$	$D_{cr} = 0.1$	$D_{cr} = 0.05$
Logarithmic Fracture strain (LE22)	0.8430	0.8285	0.8040	0.8020

From Table 3, it can be seen that a damage variable of 0.05 tends to give a more accurate response. Here, it can also be observed that lowering the damage variable value tends to reduce the logarithmic strain at fracture.

Fig. 6 shows the material's responses, which were obtained by calibrating the ductile damage parameters. Thus, the damage parameters were chosen from the iterations conducted, and the calibrated damage parameters are depicted in Table 4. These calibrated ductile damage parameters are given as input for conducting the ductile damage simulation. From the finite element analysis conducted the ductile damage was simulated within the specimen under study and the material responses of the same are plotted in Fig. 7.

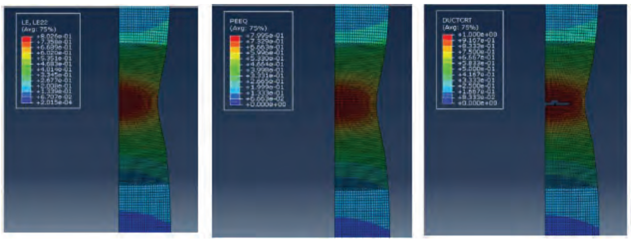

Fig. 6 Material Responses

Table. 4 Ductile damage parameters for numerical study

SI No:	Ductile damage parameter	Model input
1	Fracture Strain	0.8000
2	Stress Triaxiality	0.3300
3	Displacement at failure	0.0125 mm

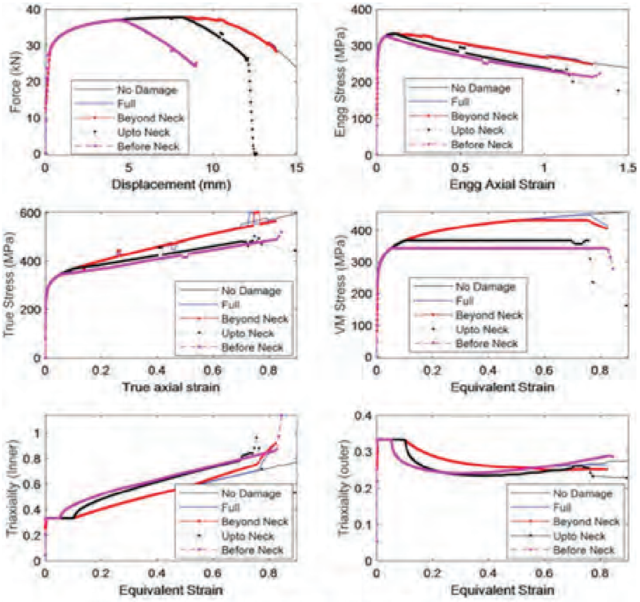

Fig. 7 Material responses with different input data points

From the finite element analysis conducted, it is evident that the input of flow stress before necking and up to necking does not simulate the actual material behaviour in all the output results, such as displacement, engineering stress, true stress as well, and von Mises stress. However, it is difficult to distinguish between the material response when flow stress curves beyond necking and up to failure are utilized, especially in force-displacement, engineering stress-strain, and true stress-strain curves. Notably, this discrepancy in the material response can be distinguished only when examining the equivalent stress or von Mises stress-strain response. Beyond the point up to which the input data are given, the software assumes it as a perfectly plastic material, thus failing to capture the post-necking material responses like the strain hardening and damage evolution. From the plots, it is evident that without inputting the full stress-strain curves, the simulation fails to capture the actual response of the material under loading conditions.

Understanding the correlation between triaxiality and equivalent stress strain further emphasizes the importance of accurate material characterization. From the material response curves, it can be seen that the triaxiality remains constant up to the point of necking; thereafter, it tends to increase on the inside and decrease on the outer side of the specimen.

Thus, from the study, it is evident that full stress-strain curves are necessary for accurately capturing the material response, ensuring a more reliable prediction of the material responses. Hence, engineers and researchers should prioritize including full stress-strain data for simulations. This enables them to predict the accurate material response under loading conditions providing insights to develop better designs of the structures with improved strength and durability, and preventive measures can also be implemented.

CONCLUSIONS

Studies on ductile damage play a crucial role in offering various insights into the material behaviour, structural performance, and failure mechanisms involved. Thus, the present study focused on minimizing the experimental efforts for the ductile damage analysis by using the FE software ABAQUS/CAE to simulate ductile damage within the specimens under study. The study underscores the influence of the flow stress curve on the material responses. Traditional studies conducted was carried out utilizing only the available data either upto tensile strength limit or necking or upto ultimate strength limit. Thus it is necessary that the sufficient studies regarding the inclusion of partial or full stress strain curves to be attempted. From the simulations conducted with partial and full data input curves, it was evident that inclusion of full stress-strain curves is necessary for accurately capturing the material responses, which will ensure more reliable predictions than partial input curves. To evaluate this, different boundaries of datasets were analyzed, and the findings revealed that the incorporation of whole stress-strain data is necessary for the accurate prediction of the material responses. It also signifies the importance of providing precise and appropriate ductile damage parameters to effectively simulate the ductile damage and obtain accurate material responses. These studies shed light on the material behaviour during deformations and failure under various loading conditions. Thus, ductile damage studies enable engineers to predict the material behaviour under practical circumstances, allowing for safer and more reliable engineering structures.

REFERENCES

1. Bao, Y. (2005) “Dependence of ductile crack formation in tensile tests on stress triaxiality, stress and strain ratios”, Engineering fracture mechanics, 72(4),505-522
2. Bai, Y., Teng, X., Wierzbicki, T., (2009) “On application of stress triaxiality formula for plane strain fracture testing, Journal of Engineering Material, 131(2).
3. Choung, J.M. and Cho, S.R., (2008), “Study on true stress correction from tensile tests”, Journal of Mechanical Science and Technology, 22, 1039-1051.
4. Dou, W., Xu, Z., Han, Y., Huang, F. (2023) “A ductile fracture model incorporating stress state effect”, International Journal of Mechanical Sciences, Elsevier, 241, 107965.
5. Kossakowski, P G.(2012) “Influence of Initial Porosity on Strength Properties of S235JR Steel at Low Stress Triaxiality”, Archives of Civil Engineering, 58(3), 293-308.
6. Li, F., Yuan, H., Liu, H. (2021) “Implementation of metal ductile damage criteria in Abaqus FEA” Journal

of physics: Conference series, IOP Publishing, 1906, 012058.

7. Mashayekhi, M., Ziaei-Rad, S (2006) "Identification and validation of a ductile damage model for A533 steel", Journal of Materials Processing Technology, 177, 291–295.
8. Mashayekhi, M., Ziaei-Rad, S., Parvizian, J., Niklewicz, J., Hadavinia, H. (2007) "Ductile crack growth based on damage criterion: Experimental and numerical studies" Mechanics of Materials, Elsevier, 39, 623–636.
9. Prantl, A., Ruzickal, J., Spaniel, M., Moravev, M., Dzugan, J., Konopik, A. (2013) "Identification of Ductile Damage Parameters", Metals, MDPI, 8(32), 89-92.
10. Ribeiro, J., Santiago, A., Rigueiro, C. (2016) "Damage model calibration and application for S355 steel", 21st European Conference on Fracture, 2, 656-663.
11. Tian, Z., Yang, Fei., Wang, S., Liu, Z., Chen, A. (2023) "Plasticity and Ductile Fracture of High- Strength Steel Center-Holed Plates under Tension", Metals, MDPI, 13(5), 994.
12. Xue, Z., Pontin, M.G., Zok, F.W., Hutchinson, J.W. (2010) "Calibration procedures for a computational model of ductile fracture", Engineering Fracture Mechanics, Elsevier, 77, 492–509.
13. Yang, F., Veljkovic, M., Liu, Y. (2020) "Ductile damage model calibration for high-strength structural steels" Construction and Building Materials, Elsevier, 263, 120632.
14. ABAQUS User's Manual.
15. https://www.linkedin.com/pulse/mechanical-properties-review-strength-stiffness-hardness-wang-wznmc/.

Seismic Response of Multi-Storied Buildings on Geomembrane Isolation Material

Shahana N K
PG Scholar
Department of Civil Engineering
NSS College of Engineering
Palakkad, Kerala
✉ shahanank94@gmail.com

Sreelekshmy Pillai G
Associate Professor
Department of Civil Engineering
NSS College of Engineering
Palakkad, Kerala
✉ sreelekshmypillai@gmail.com

Rekha Ambi
Associate Professor
Department of Civil Engineering
TKM College of Engineering
Kollam, Kerala
✉ rekha.ambi@tkmce.ac.in

ABSTRACT

Earthquakes are natural disasters capable of causing severe damage or even complete collapse of buildings. Therefore, to provide safe living conditions, structures must be constructed to withstand the effects of earthquake. By embedding isolation material in soil below the foundation, the buildings will experience reduced acceleration and displacement during seismic events. Seismic isolation material has the property of damping and thereby absorbs the seismic wave energy. Thus, the seismic isolation material in soil prevents excessive forces acting on the building. The effectiveness of geomembrane as a seismic isolation material was analysed in this study. ANSYS software was used to analyze seismic responses, including roof acceleration, displacement, and storey drift, of a G+4 building in order to assess the effectiveness of this seismic isolation material. The main goal of this work to suggest the optimum depth and effective thickness of geomembrane that decreases the transmission of seismic wave energy.

KEYWORDS: *Isolation material, Geomembrane, Roof acceleration, Storey drift.*

INTRODUCTION

One of the most frequent natural catastrophes that demolish buildings is an earthquake. shaking of the ground, liquefaction of the soil, collapse of buildings, destruction of property, death, etc. are all possible outcomes of earthquakes. Buildings undergo more acceleration and deflection during seismic events. Engineers utilise a range of methods, such as base isolators, damping devices, flexible materials, etc., to distribute incoming seismic energy. For many years, geotechnical and structural engineers have collaborated to provide innovative strategies for minimising the structural reaction to seismic occurrences. One of the methods utilized to solve this issue by building the structure over the soil with seismic isolation mat materials. Seismic isolation material can reduce the stresses delivered to the structure by absorbing and distributing seismic energy.

Compared to a natural rubber bearing isolator, the scrap tire rubber cushion has a substantially higher damping efficiency [2]. Vibration management for masonry structures by the use of geotextile to isolate the superstructure from the foundation [5]. When compared to a fixed foundation, the isolated structure's acceleration at roof level was reduced by 50%.[4] carried out a study using ABAQUS software to evaluate the effectiveness of non-woven geotextile in seismic isolation applications. In reinforced concrete (RC) structures, the geotextile acts as a lining material to enhance seismic isolation. The RC building's dynamic response was diminished as a result of the decreased seismic energy delivered to the structure. The horizontal acceleration was reduced by 40% as a result of the addition of isolation material. Rubber and sandy soil were used for isolation to reduce the seismic response of the structure.[3] used ABAQUS software to conduct the investigation. The goal of the investigation was to determine the optimum isolation material thickness for two- and four-story buildings. At a depth of two meters, the effectiveness of rubber-mixed soil was almost the same regardless of the number of floors considered. According to the results of numerical research on rubber isolation material for low- and mid-rise buildings, low-rise buildings are more successful in reducing floor acceleration [1]. The strength, and tensile strength of soil are all improved by the addition of coir fiber or mat. Additionally, coir fiber reduces soil settling and increases the soil's bearing capacity. [7] discovered that a significant decrease in roof acceleration, base shear, and bending moment occurs when coir mat is used as an isolation medium.[8] investigates the efficiency of coir mat-reinforced soil as a seismic isolation medium. ANSYS software was used to simulate a five-storey building with a raft foundation on both soft and rigid soil types, considering cases with and without isolation materials. The analysis identified 1000 mm as the most effective depth for placing the isolation layer beneath the foundation. [9] came up with a practical way to reduce the impact of earthquakes by using natural coir mat and rubber mat as isolation materials. The analysis revealed that coir mats are a more effective way to prevent roof deflection than rubber isolation material.

As seen above, one way to lessen a building's seismic response during an earthquake is to embedded isolation material in soil below the foundation. Several experimental and analytical studies were conducted to examine how buildings with isolating materials responded to earthquakes.

This study attempted to investigate the how the G+4 building response by using geomembrane as seismic isolation material. To determine the optimum depth and effective thickness, the inquiry was carried out by altering thicknesses and depth (position). Thereby this study provides effective thickness at the optimum depth, for the reduction in seismic response of G+4 buildings.

MODELLING AND ANALYSIS

The G+4 building was analyzed using ANSYS software both with and without isolation materials. Fig.1 (a) and (b) depict the perspective and side view of the G+4 building respectively. That was modeled by ANSYS software for this G+4 building on a raft foundation with soft soil. As illustrated in Fig.2., dashpots were installed along the boundaries of the soil model to prevent the reflection of seismic waves. The simulation applied ground motion data from the 1940 El Centro earthquake. Material properties and geometric details used for modeling were sourced from [8], with Table 1 presenting the relevant characteristics and Table 2 outlining the dimensions of both structural components and soil.

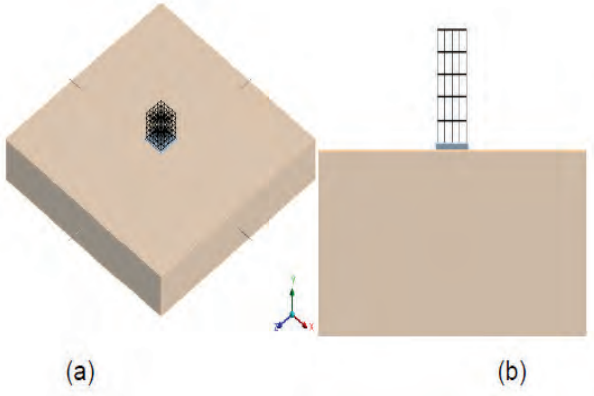

Fig. 1. Modelling and Analysis

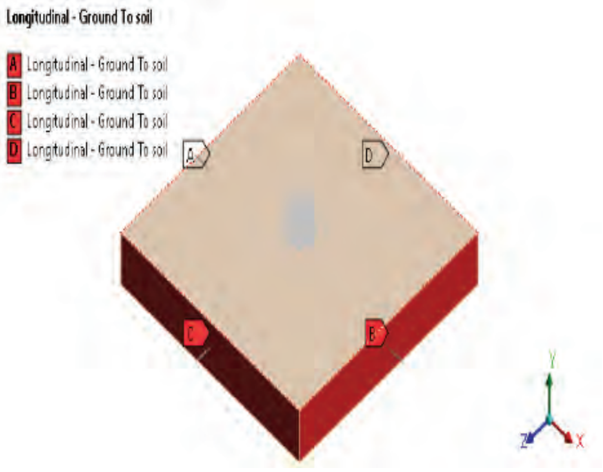

Fig. 2. Placement of dashpots along the boundaries of the soil in the simulation model.

Table 1. Material properties of the structural components and soil [8].

ELEMENT	ELEMENT CHARACTERISTICS		
	DENSITY (kN/m^3)	YOUNG'S MODULUS (MPa)	POISSON'S RATIO
RC beam, column and raft foundation.	25	25 x 10^3	0.15
Soil	16	65	0.4

Table 2. Dimension of structural elements, soil. [8]

ELEMENT	DIMENSION (L X B X D) m
RC beam	4 x 0.3 x 0.3
RC column	3 x 0.5 x 0.5
Raft foundation	18 x 18 x 1
Soil	170 x 170 x 30

The G+4 building's seismic study was conducted without the use of isolation materials. The G+4 building without base isolation had seismic responses of 31.7 m/s^2, 143.56 mm, and 18.4 mm for roof acceleration, maximum storey displacement, and drift, respectively. Buildings using soil and isolation materials were modelled and analysed.

The isolation material used in this investigation is geomembrane. Table 3 presents the properties of the geomembrane. Analysis was done on how well geomembrane reduced roof acceleration, displacement, and drift. In order to perform the study, several depths and geomembrane thicknesses were used.

Table 3. Characteristics of geomembrane [7]

Isolation Material	Density (kN/m^3)	Young's Modulus (MPa)	Poisson's Ratio
Geomembrane	930	780	0.3

To evaluate the performance of the G+4 building, the geomembrane layer was embedded at various depths—0 mm (foundation base), 500 mm, 600 mm, and 1000 mm. Table 4 lists the isolation material characteristics taken into consideration for the investigation. The analysis is carried out for these depths and found out the optimum depth. Variations in thickness (500 mm, 1000 mm, 1500 mm, and 2000 mm) allowed the study to be conducted at the optimum depth. Fig. 3. (a) and (b) show the building with 500 mm and 2000 mm thickness geomembrane respectively.

Table 4. Specifications of isolation materials

Isolation Material	Embedded Depth (mm)	Dimension (L X B X D) m
Geomembrane	0, 500, 600, 700 and 1000	20 x 20 x 0.5
	THICKNESS (mm)	DIMENSION (L X B) m
	500, 1000, 1500, and 2000	20 x 20

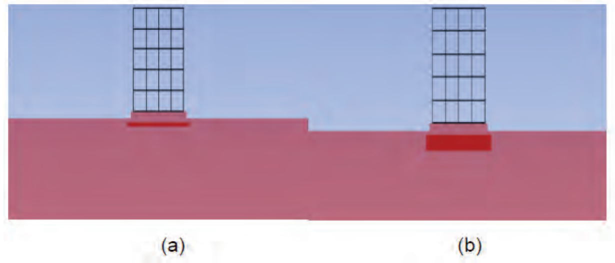

(a) (b)

Fig. 3. The building model incorporating geomembrane isolation material placed at a depth of 600 mm, with thicknesses of (a) 500 mm and (b) 2000 mm.

RESULTS AND DISCUSSIONS

The analysis revealed that placing isolation material beneath the foundation at different depths and thicknesses effectively minimized the seismic response. The differences in the seismic reactions of structures with geomembrane at various depths and thicknesses are covered in the following.

Influence of Different Embedment Depths of Isolation Material on Roof Acceleration, Maximum Storey Displacement, and Drift

Installation of geomembrane in the soil might absorb and disperse the seismic energy, It lessens vibration, and as a result, the structure's roof experiences less acceleration than a building without geomembrane. The fluctuation of roof acceleration at various depths is seen in Fig. 4. The roof acceleration first drops when the isolation material is embedded, and the graph thereafter exhibits nearly continuous fluctuation between 500 and 700 mm. And then again, the roof acceleration increased beyond 700mm depth. Implementation of isolation material could separate the building from earthquake vibration, and thus reducing the ability of propagation of seismic waves and thereby decreasing the roof acceleration.

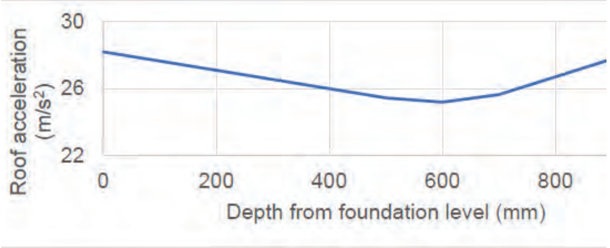

Fig. 4. Variation in roof acceleration for the building with geomembrane installed at different embedment depths.

Similar to how roof acceleration works, geomembrane might also aid in lowering storey displacement through the absorption and distribution of seismic energy, which lowers vibration amplitude. Fig. 5. displays the variation in the maximum storey displacement at different depths. The displacement of storeys increases at first, then decreases over time, and then increases once again as the embedment depth increases. The seismic response is observed to be reduced very much at depths between 600 and 1000 mm.

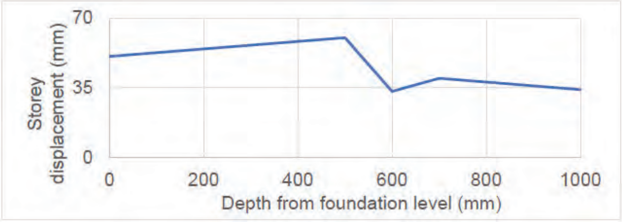

Fig. 5. Maximum storey displacement observed in the building for various geomembrane embedment depths.

It is discovered that the maximum storey drift was reduced by placing geomembrane at a different depth. Fig.6 illustrates how the maximum storey drift varies with embedment depth of geomembrane. Similar trends in storey displacement are shown by the variance in storey drift trend. Depth from 600 mm to 1000 mm shows the maximum reduction in storey drift. By altering the characteristics of the soil, isolation material can lessen the amount of ground motion that reaches the building. Isolation material can lessen the lateral pressures applied to the building by keeping seismic waves away from it, which reduces the maximum storey drift.

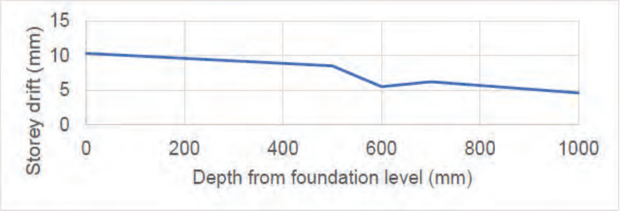

Fig. 6. Variation in maximum storey drift of the building corresponding to different depths of geomembrane embedment

When constructing on a geomembrane at a depth of 600 mm, the roof accelerates the least, and the minimal reaction for displacement and storey drift falls between 600 mm and 1000 mm. But for roof acceleration at depth 1000 mm shows a large value as compared to depth at 600 mm. So, overall consideration the optimum depth is found to be 600 mm.

Influence of Geomembrane Thickness on Roof Acceleration, Storey Displacement, and Drift

In order to determine the effective thickness, the geomembrane is positioned 600 mm below the surface, and its thickness is varied from 500 mm to 2000 mm. Fig.7. illustrates how the maximum roof acceleration of a structure changes depending on the thickness and optimal depth of the geomembrane (600 mm). The pattern indicates that up to 1500 mm of thickness, the roof acceleration is nearly constant. The roof acceleration decreases as the thickness increases above 1500 mm.

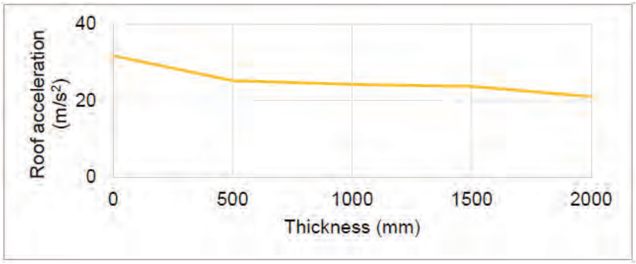

Fig. 7. Maximum roof acceleration of the building with geomembrane layers of different thicknesses

Fig.8. shows the maximum storey displacement of a structure with different geomembrane thicknesses positioned at an optimum depth of 600 mm. At 500 mm thickness, the storey displacement is first decreased;

at 1000 mm thickness, it is raised; and at 1500 mm thickness, it is decreased once again. The greatest storey displacement variation is almost constant beyond 1500 mm of thickness.

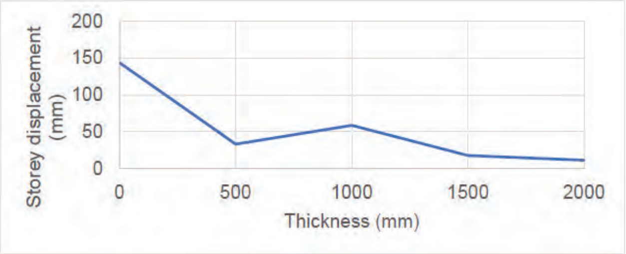

Fig. 8. Changes in maximum storey displacement for the building with varying geomembrane thicknesses.

The maximum storey drift of a structure with variable geomembrane thickness at an optimum depth of 600 mm is depicted in Fig. 9. The fluctuation of storey drift has a similar pattern to that of storey displacement. The storey drift was found to be almost consistent between thicknesses of 1500 mm and 2000 mm.

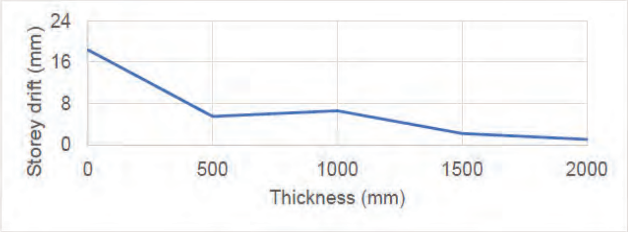

Fig. 9. Variation in maximum storey drift of the building corresponding to different geomembrane thicknesses.

Variations in earthquake responses (roof acceleration, maximum storey displacement, and storey drift) have been noted at optimum depth 600 mm on varying thickness, nearly constant values found for 1500 mm to 2000 mm. By considering the cost effectiveness the effective thickness is taken as 1500 mm. For 1500 mm thickness percentage of reduction for roof acceleration, maximum storey displacement and storey drift is 25.30 %, 87.67 %, and 88.04 % respectively. By introducing additional damping into the soil-structure interaction, the geomembrane helps absorb and dissipate seismic energy, which in turn lowers the amount of seismic force reaching the structure. The geomembrane with 1500 mm thickness at 600 mm depth of embedment introduced flexibility into the soil-structure interaction, allowing for controlled deformation and movement, which reduces the overall seismic response. By isolating the building from the underlying soil movements, the geomembrane helps in mitigating the direct impact of seismic waves on the structure.

CONCLUSIONS

This research involved a numerical simulation using ANSYS software to assess the seismic behavior of a G+4 structure incorporating geomembrane as a base isolation material. The analysis was performed by embedding geomembrane at various depths and thicknesses within the soil beneath the foundation. The goal of the study was to determine the geomembrane's effective thickness at the optimum depth. The findings showed that 600 mm is the optimum depth. Embedding the geomembrane led to a noticeable reduction in roof acceleration, storey displacement, and storey drift. Beyond a thickness of 1500 mm, the seismic response of the structure showed minimal variation, particularly at the optimal embedment depth of 600 mm. Based on the analysis, the most effective configuration was identified as a geomembrane thickness of 1500 mm placed at a 600 mm depth. Under this setup, the reductions observed were 25.30% in roof acceleration, 87.67% in storey displacement, and 88.04% in storey drift.

REFERENCES

1. Forcellini, D. (2020), 'Assessment of geotechnical seismic isolation (GSI) as a mitigation technique for seismic hazard events. Geosci 10: 1–14.
2. Mishra, H. K., Igarashi, A., Matsushima, H., and Furukawa, A. (2012), 'Experimental and analytical study of unbonded and bonded scrap tire rubber pad as base isolation device'. In 15th world conference on earthquake engineering, Lisbon, Portugal.
3. Nanda, R. P., Dutta, S., Khan, H. A., and Majumder, S. (2018), 'Seismic protection of buildings by rubber-soil mixture as foundation isolation'. International Journal of Geotechnical Earthquake Engineering (IJGEE), 9(1), 99-109.
4. Nanda, R. P., Dutta, S., Das, A., and Khan, H. A. (2017), 'Geosynthetic liner as foundation isolation for seismic protection'. International Journal of Geosynthetics and Ground Engineering, 3, 1-7.
5. Nanda, R. P., Agarwal, P., and Shrikhande, M. (2012), 'Base isolation by geosynthetic for brick masonry

buildings. Journal of Vibration and Control, 18(6), 903-910.

6. Satyanarayana, K. G., Sukumaran, K., Kulkarni, A. G., Pillai, S. G. K., & Rohatgi, P. K. (1986) Fabrication and properties of natural fibre-reinforced polyester composites. Composites, 17(4), 329-333.

7. Sreya, M. V., Jayalekshmi, B. R., and Venkataramana, K. (2021), 'A study on seismic response of buildings on coir mat reinforced sand bed'. In IOP Conference Series: Materials Science and Engineering (Vol. 1114, No. 1, p. 012018). IOP Publishing.

8. Sreya, Jayalekshmi, B. R., & Venkataramana, K. (2022). Effect of Coir Reinforced Soil on the Seismic Response of RC Framed Buildings. Indian Geotechnical Journal, 52(3), 568-589.

9. Sreya, Jayalekshmi, B. R., & Venkataramana, K. (2023), 'A Comparative Study on Dynamic Response of Buildings Resting on Coir and Rubber mat Reinforced Soil Bed'. In IOP Conference Series: Earth and Environmental Science (Vol. 1149, No. 1, p. 012012). IOP Publishing.

10. Whinnery, L. L., Neuschwanger, C. L., & GOODS, S. (1998), 'Mechanical properties of a structural polyurethane foam and the effect of particulate loading'. San Francisco: USDOE Office of Energy Research.

11. Xu, R., & Fatahi, B. (2018), Influence of geotextile arrangement on seismic performance of mid-rise buildings subjected to MCE shaking. Geotextiles and Geomembranes, 46(4), 511-528.

Analytical Study of Metamaterial Self-Sensing Concrete Blocks as A Structural Member

Aleena Mariyam Jacob
UG Scholar
Department of Civil Engineering
Saintgits College of Engineering
✉ akayaar33@gmail.com

Avinash Krishna R
UG Scholar
Department of Civil Engineering
Saintgits College of Engineering
✉ alenjoseph020502@gmail.com

Alen Joseph
UG Scholar
Department of Civil Engineering
Saintgits College of Engineering
✉ aleenamj249@gmail.com

Habby Philip Mathew
UG Scholar
Department of Civil Engineering
Saintgits College of Engineering
✉ habbyphilipmathew2003@gmail.com

ABSTRACT

Concrete is essential for durable infrastructure, and the development of advanced concrete materials with enhanced functionalities and mechanical tunability is critical for reimagining traditional infrastructure systems. This paper introduces a new lightweight composite metamaterial concrete with exceptional mechanical properties and sensing capabilities. The proposed self-sensing metamaterial concrete system combines mechanical metamaterials with carbon nanotube- enhanced concrete, featuring reinforcement auxetic polymer lattices fully embedded within a conductive cement matrix.

Three polymer lattice patterns are designed using SolidWorks software, ensuring the concrete and lattice remain bonded under various loading conditions. Different polymers for the lattice are analysed based on their material properties and 3D printability. The optimal design and material for the lattice are determined through an ANSYS-based validation process, and the finalized design is 3D printed to create the mould. The finalised Metamaterial block is then interlocked and studied as a structural member likely a beam.

The metamaterial-concrete block is formed by integrating self-sensing concrete enhanced with multi-walled carbon nanotubes (MWCNT) into the lattice. This integration induces contact electrification between the layers under mechanical excitations. Additionally, the sensing functionality of the concrete systems is explored for health monitoring of large-scale concrete structures. Potential applications for this system include building base isolators, machine vibration isolators, shock-absorbent bike lane pavements, and runway pavements for decelerating aircraft in short lengths. This metamaterial self-sensing concrete paradigm paves the way for designing smart infrastructure systems with advanced functionalities.

KEYWORDS: *MWCNT, Mechanical metamaterials, Self-sensing concrete.*

INTRODUCTION

Concrete, a crucial construction material, faces long-term issues due to its brittleness and limited tensile strength, necessitating structural health monitoring to ensure its safety and longevity in the construction industry. [1].

To overcome these limitations and improve concrete performance, extensive research has been conducted over the past few years. A primary emphasis has been on the formulation of new concrete types that feature enhanced mechanical properties achieved through traditional reinforcement methods [2][3][4]. Extensive studies has focused on creating cementitious composites with self- sensing abilities [5]. To achieve self-sensing properties, researchers have incorporated conductive elements like carbon black [6][7], fibres [8][9], nanotubes [10], and steel reinforcements [11] into cementitious systems, either independently or in combination [12].

Our project intends to explore and refine mechanical metamaterial multifunctional self-sensing concrete. This involves the amalgamation of mechanical metamaterials and structural health monitoring (SHM) ideas into a singular composite for concrete structures. The system is constructed with a polymer lattice integrated into a self-sensing concrete matrix, exhibiting adjustable buckling, self-recovery, and energy absorption functionalities. The study focuses on improving concrete's ductility for structural applications, particularly in smart civil infrastructure. The use of mechanical metamaterial concrete design can enhance its multifunctionality, attracting interest in engineering applications. The auxetic arrangement ensures stability and compressibility, while the residual geometry reinforces the concrete. Future developments include beam-form composites and metamaterial self-sensing concrete systems.

METHODOLOGY

Methodology

The research began with an extensive literature review to identify a viable and innovative topic within materials science, metamaterials, and concrete technology. This review aimed to understand current trends, gaps, and emerging concepts. The research focuses on a metamaterial concrete system, a concept that uses metamaterials to enhance the structural integrity of concrete. The design is validated using ANSYS software, a 3D model created using SolidWorks, and tested under various loading conditions. The model is then prepared for 3D printing using materials like PLA, PETG, or TPU. The mix design for self-sensing concrete is refined through experimentation, and metamaterial concrete blocks are cast and tested for compressive strength, ductility, and resistance properties. The research explores using these blocks as structural members, such as beams, incorporating the unique properties of metamaterial lattices. This methodology could potentially transform real-world construction practices.

Materials and Methods

Mechanical metamaterials are custom-designed materials featuring unique geometric structures, typically incorporating composites such as plastics and metals which are structured in repetitive designs at sizes smaller than the wavelengths that influence them. A review was conducted on materials such as Poly Lactic Acid (PLA), Thermoplastic Polyurethane (TPU) and Polyethylene Terephthalate Glycol (PETG) to identify appropriate alternatives, with a focus on water resistance, thermal expansion, and bonding performance with concrete. The combinations of Poly Lactic Acid- Thermoplastic Polyurethane and Polyethylene Terephthalate Glycol-Thermoplastic Polyurethane were selected for further examination.

Table 1 Specifications of materials

Specifications	PLA	PETG	TPU
Specific Gravity	1.25 g/cm^3	1.27 g/cm^3	1.10 g/cm^3
Young's Modulus	2350 MPa	1711 MPa	26 MPa
Compressive strength	30 MPa	55 MPa	23.7 MPa
Poisson's Ratio	0.30	0.38	0.45

Material Combination for Lattice and Mix Proportion

A pair of hybrid modelling approaches was employed to identify the most suitable material for metamaterial lattice structures, ensuring a balance between structural performance and material efficiency. PLA was initially used for Parts 1 and 3, due to its user-friendliness and eco-friendliness. TPU was chosen for its flexibility, durability, 3D printability, and resilience for Part 2. The model was redesigned in SolidWorks, replacing PLA with PETG for Parts 1 and 3, due to its superior heat and water resistance and thermal expansion. TPU continued to be used for Part 2.Also application of ABS was studied, but rejected due to inadequate layer adhesion during 3D printing and concerns about toxic fume emissions. Alternative materials with better printing characteristics and fewer emissions were considered more suitable for metamaterial lattice applications. applications.

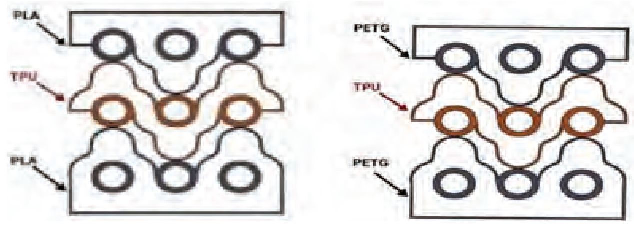

(a) (b)

Fig. 1. Sketch of TPU-PLA Combination and TPU-PETG Combination

The study applied Ordinary Portland Cement 53 and explored its characteristics for a mix design. In accordance with the IS 10262:2019 guidelines, a design mix for M25 concrete was devised with a w/c ratio of 0.475, aggregate within 6mm size, and 0.5% Multi-Walled Carbon Nanotubes to enhance self-sensing capabilities.

ANALYTICAL INVESTIGATION

Modelling in Solid Works

Solid Works software was used to create models of the polymer lattice for a proposed system. This software is crucial for converting 3D designs into physical products, providing detailed views, dimensions, annotations, and other information. Three distinct designs were created, each with unique variations to improve the functionality of this metamaterial concrete composite. The designs were carefully crafted to ensure the lattice and concrete remain bonded under loading conditions. Detailed drawings for all designs were developed in three separate parts, which collectively form the final models. 2 different models were created by making changes in unit cell.

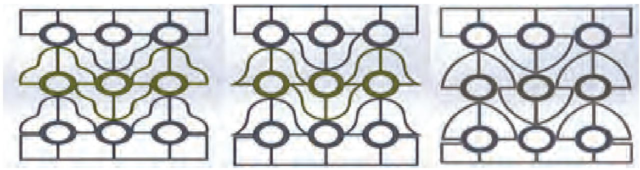

(a) (b) (c)

Fig. 2. (a) Model 1 (b) Model 2 (c) Model 3

Analysis of Metamaterial Blocks in ANSYS

The polymer lattice's design and material were confirmed through the use of ANSYS software. Experimental testing involved cubic dimensions, with the lattice size standardized to 15 cm × 15 cm × 15 cm. Two essential tests were conducted: ultimate and cyclic compression tests. The strain rate was 0.16 cm/min. Advanced analytical methods were utilized to examine the deformation behaviour and stress response, ensuring optimal performance and durability.

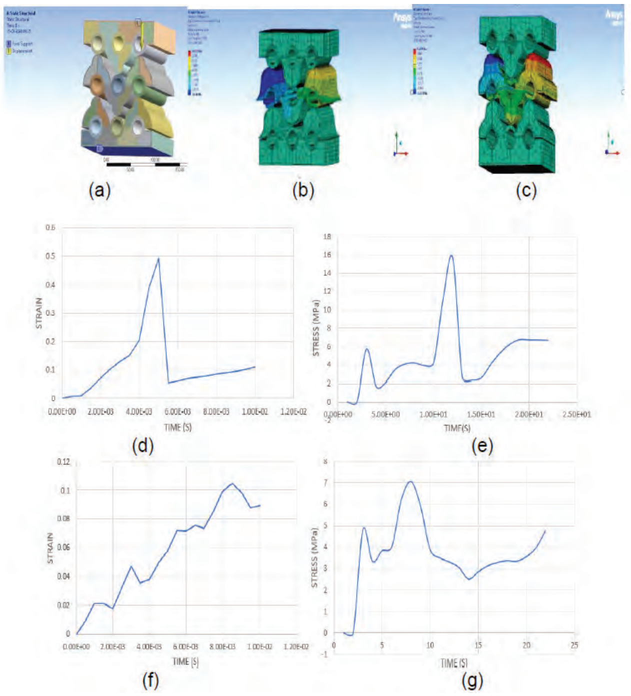

Fig. 3. Analysis results of PLA and TPU unit cell model. (a) Boundary conditions (b) Anisotropic deformation of first (c) Anisotropic deformation of second model (d) Time-dependent strain curve of second model (e) Time-dependent stress curve of second model (f) Time-dependent strain curve of first model (g) Time-dependent stress curve of first model.

Model 3 (Fig. 2c) was excluded from early evaluations due to circumstances surrounding Model 2 (Fig. 2b), where a sudden strain drops, shown in Fig 4(d), indicated localized failure, inconsistent load performance, and a design that could pose operational risks in dynamic environments. In contrast, Model 1 (Fig. 2a) exhibited negligible deflection under maximum stress, indicating a more favourable geometry. The evaluation of these two final models resulted in the choice of Model 1 as the primary combination. Furthermore, the other combination was evaluated using the primary model, as illustrated in Fig 4.

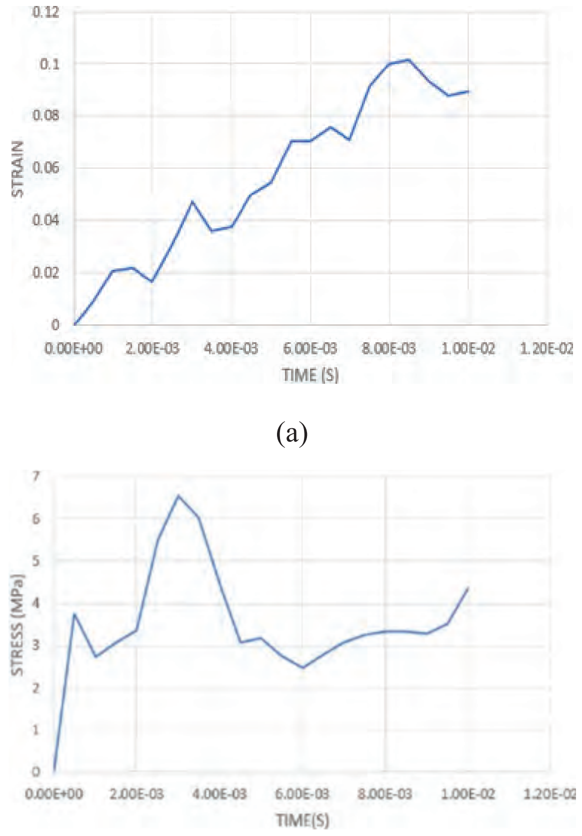

(a)

(b)

Fig. 4. Evaluation results of the finalized model (a) Time-dependent strain behaviour (b) Stress response

Development and Analysis of Structural Member

The designed composite block was employed as a unit part in the design of a beam in Solid Works, with the chosen model serving as the base module. The simply supported beam was analysed using a 512mm span, 150mm width, and 187mm depth, with a fixed support and displacement element as boundary conditions. A UDL of 100 kN was applied to the top surface for analysis.

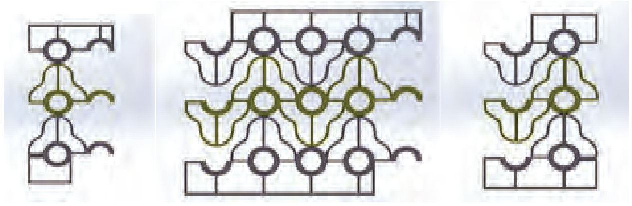

(a) (b) (c)

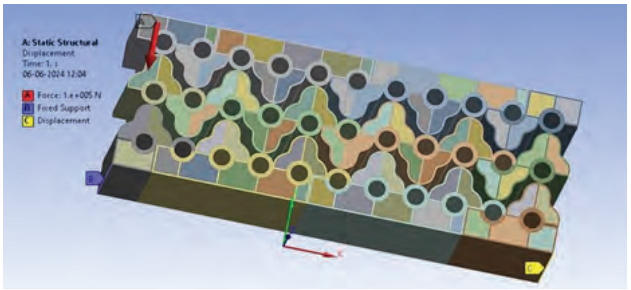

(d)

Fig. 5. Representations of the model: (a) Left part, (b) Intermediate part, (c) Right part, (d) Applied boundary conditions for the beam element

The beam model was analysed using the ‘static structural’ analysis system in ANSYS. The focus was exclusively on the behaviour of the model within the elastic region. This limitation was due to the composite nature of the materials involved—PETG, TPU, and concrete—and the unknown failure criteria for PETG and TPU. Consequently, the non-linear behaviour of the beam model was not examined.

During the analysis, the beam model, subjected to a load of 100 kN under simply-supported conditions, exhibited a total deformation of 10.554 mm, as illustrated in Figure 7. The stress-strain curve corresponding to this model is presented in Figure 8. This analysis provided critical insights into the elastic performance of the composite beam, revealing how the combined materials respond to applied loads within the elastic deformation range. This information is essential for understanding the initial structural performance and ensuring the design’s viability under typical loading conditions without reaching material failure.

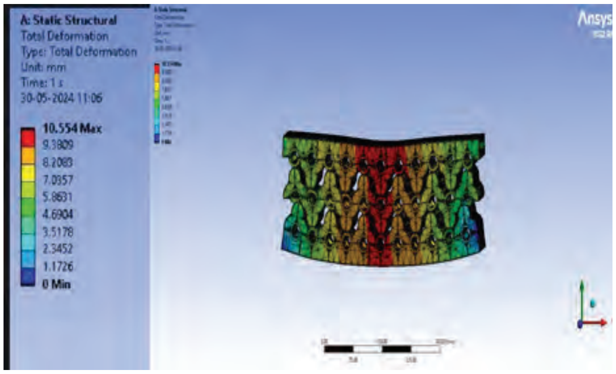

Fig. 6. Total deformation of beam model

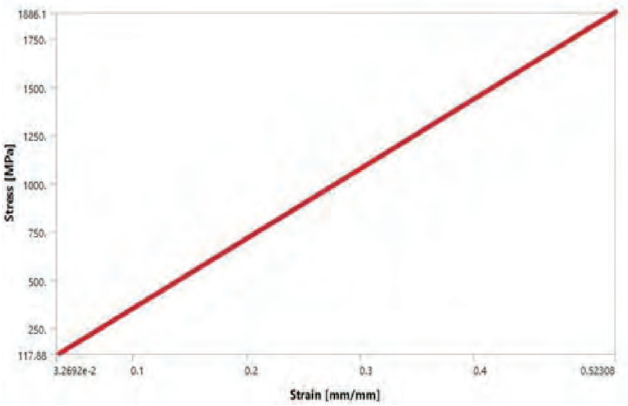

Fig. 7. Stress – strain curve for beam model

EXPERIMENTAL STUDY

The polymer part of the metamaterial composite (Fig.3a) is prepared for 3D printing, using TPU, PETG and PLA fibres as determined by the analysis results. This strategy is intended to generate a tangible prototype for additional assessment and practical demonstrations. The creation of auxetic lattices utilized 3D printing technology, particularly employing polyplex filaments. Initially, prototypes consisting of 3x3 unit cells were developed using two suggested combinations of PETG, TPU, and PLA filaments.

PLA was chosen for its rigidity and the ease with which it can be printed, while PETG was selected for its flexibility, structural integrity, impact resistance, and durability. TPU was incorporated into every lattice due to its reduced Young's modulus, rendering it appropriate for significant deformability and energy absorption.

The particular mechanical features of each material were strategically leveraged to furnish the auxetic lattice with the requisite qualities, including an auxetic behaviour and augmented mechanical strength. The concrete composition was designed with a maximum w/c ratio of 0.475, effectively avoiding any surplus water content to preserve the final properties. The pouring phase was executed with precision to maintain the integrity of the polymer lattice geometry, and the consolidation process was conducted to ensure complete compaction. After the curing process, compression tests and resistance measurements were carried out to assess the self-sensing capabilities.

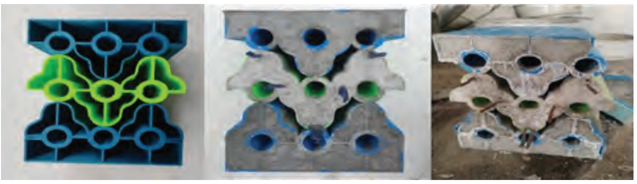

(a) (b) (c)

Fig. 8. (a) 3D printed prototype of 3x3 block (b) Composite filled with concrete (c) Damaged TPU- PLA model

The TPU-PLA model revealed notable chemical degradation, which can be linked to the natural biodegradability of PLA. As time progressed, interaction with water caused hydrolytic degradation, which contributed to the deterioration of PLA. This lack of resistance to water resulted in a weak compatibility between the concrete and PLA parts within the composite.

Compression Test and Resistance Measurement

Conversely, the PETG-TPU model exhibited structural stability. The load-displacement data was collected in real-time using a Universal Testing Machine (UTM), while resistance values were measured at the same time with a multimeter and plotted in relation to the applied load. To prepare for the testing, PETG-TPU composite specimens were created following standard dimensions and specifications. Each specimen was securely mounted in the UTM, and the load was applied in increments.

The machine recorded the load and displacement at each step, while resistance measurements were taken at three designated points during the compression test. The machine allowed live monitoring of load-displacement response, while resistance data were concurrently given by the multimeter. Measurements of resistance were performed at three locations on the model by linking multimeters during the loading phase, and these were plotted in relation to the applied load. The resulting load-deflection graph is displayed in Fig 9, while the load versus resistance graph can be found in Fig 10.

PETG takes the load initially, and as its ultimate strength approaches, PETG filaments begin to break, as shown by the first peak in Fig 9. As the load increases and the concrete begins to yield, TPU filaments will then become compressed. All of the metamaterial block's components, including PETG, TPU, and concrete, fail at the breakpoint.

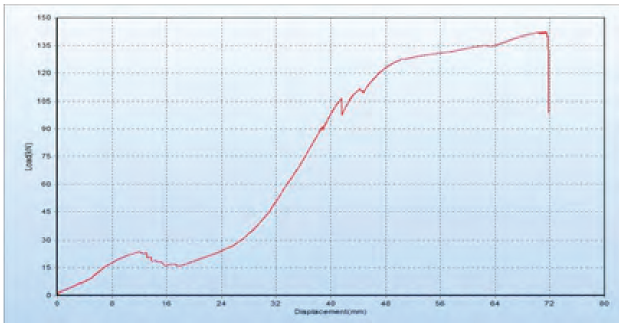

Fig. 9. Load vs displacement graph of PETG–TPU model obtained from UTM

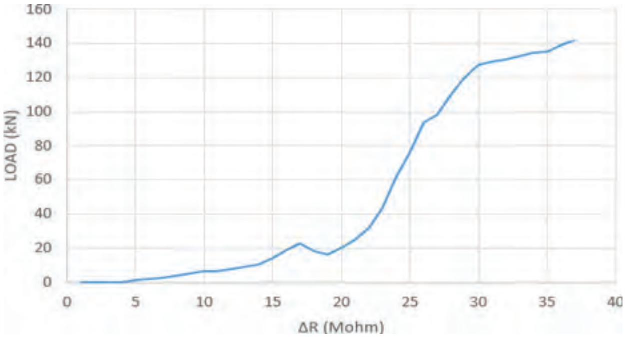

Fig. 10. Load vs Resistance graph

In areas where tension is evident, a steady response in resistance in relation to load was observed, with resistance escalating simultaneously from the initial crack point. This indicates the incorporation of self-sensing behaviour, represented in Fig 10 . The TPU-PETG model effectively utilizes the self- sensing capabilities of concrete to detect damage development and assess failure risk, providing essential real-time data for SHM. This comprehensive examination highlights the promise of the TPU-PETG combination as a dependable and responsive material for uses that necessitate both mechanical durability and self-monitoring features.

CONCLUSION

In addressing some drawbacks of concrete, like its lack of ductility and weakness under tensile loads, many studies have been conducted to improve its durability over time. Mechanical metamaterials, which are defined by their geometry, shows significant admirable properties. The study included a variety of metamaterial prototypes and materials, with lattices designed in SolidWorks and stimulated in ANSYS.

Upon thorough investigation the integrated metamaterial self-sensing concrete displays significant compressibility, mechanical versatility, and sensing features, an advancement in concrete materials. The compressibility of the concrete is primarily linked to the polymeric auxetic lattice design, bringing it into closer alignment with the idea of concrete reinforced with polymers.

Prospective initiatives may entail large-scale evaluations to substantiate the proposed model, along with further studies to investigate alternative materials and unit cell arrangements for the creation of varied models. The metamaterial blocks were converted into beams, which yielded favourable results in the analysis.

By establishing boundaries and criteria, this research intends to deliver important perspectives within the area of concrete technology. The innovative nature of the proposed idea necessitates additional investigation into various mechanical and structural health monitoring aspects to fully realize its potential.

REFERENCES

1. Karbhari, V.M., Ansari, F.: Structural health monitoring of civil infrastructure systems.UK: Woodhead Publishing Cambridge; (2009).
2. Asprone, D., Menna, C., Bos, F., Salet, T., Mata-Falcón, J., Kaufmann, W.: Rethinking reinforcement for digital fabrication with concrete. Cement and Concrete Research, vol. 112, pp. 111-121, (2018).
3. Wang, L., Ma, G., Liu, T., Buswell, R., Li, Z.: Interlayer reinforcement of 3D printed concrete by the in-process deposition of U-nails. Cement and Concrete Research, vol. 148, (2021).
4. Scerrato, D., Giorgio, I., Della, C., Madeo, A., Dowling, N.E., Darve, F. Towards the design of an enriched concrete with enhanced dissipation performances. Cement and Concrete Research, vol. 84, pp. 48-61, (2016).
5. Abedi, M., Fangueiro, R., Correia Antonio, G.: A review of intrinsic self-sensing cementitious composites and prospects for their application in transport infrastructures, Constr. Build. Mater. 310 (2021).

6. Monteiro, A.O., Loredo, A., Costa, P.M.F.J., Oeser, M., Cachim, P.B.: A pressure sensitive carbon black cement composite for traffic monitoring, Constr. Build. Mater. 154 1079–1086 (2017).

7. Ding, Y.N., Chen, Z.P., Han, Z.B., Zhang, Y.L., Pacheco-Torgal, F.: Nano-carbon black and carbon fiber as conductive materials for the diagnosing of the damage of concrete beam, Constr. Build. Mater. 43 233–241 (2013).

8. Wu, S.P., Mo, L.T., Shui, Z.H., Chen: Investigation of the conductivity of asphalt concrete containing conductive fillers, Carbon 43 (7) 1358–1363 (2005).

9. Chen, B., Wu, K., Yao, W.: Conductivity of carbon fiber reinforced cement-based composites, Cem. Concr. Compos. 26 (4) 291–327 (2004).

10. Naqi, A., Abbas, N., Zahra, N., Hussain, A., Shabbir, S.Q.: Effect of multi-walled carbon nanotubes (MWCNTs) on the strength development of cementitious materials, J. Mater. Res. Technol. 8 (1) 1203–1211 (2019).

11. Ding, Y.N., Liu, G.J., Hussain, A., Pacheco-Torgal, F., Zhang, Y.L.: Effect of steel fiber and carbon black on the self-sensing ability of concrete cracks under bending, Constr. Build. Mater. 207 (2019).

12. Konsta-Gdoutos, M.S., Aza, C.A.: Self-sensing carbon nanotube (CNT) and nanofiber (CNF) cementitious composites for real time damage assessment in smart structures, Cem. Concr. Compos. 53 162–219 (2014).

13. Barri, K., Jiao, P., Zhang, Q., Chen, J., Wang, Z. L., & Alavi, A. H.: Multifunctional meta- tribomaterial nanogenerators for energy harvesting and active sensing. Na0no Energy, 86, 106074 (2021).

Analysis of AFRP Strengthened Shear Deficient Beams with Varying Number of Layers

Arya J
Assistant Professor
Department of Civil Engineering
NSS College of Engineering
Palakkad, Kerala
✉ aryaj@nssce.ac.in

ABSTRACT

Due to factors such as aging, evolving design standards, or environmental challenges, structural components often need to be strengthened or retrofitted. In this study, Aramid Fiber Reinforced Polymer (AFRP) sheets are externally wrapped around beams to enhance their load-bearing capacity. The investigation involves finite element analysis of beam specimens measuring 1800 mm × 150 mm × 200 mm, with stirrup spacing of 75 mm. Strengthened reinforced concrete beams are modeled layer by layer using ANSYS software. Structural performance was examined for three categories: control beams, shear-deficient beams, and those retrofitted with AFRP. The loading condition is under two point loading. Additionally, the load–deflection characteristics of the specimens are analyzed through parametric studies.

KEYWORDS: *Finite element analysis, Aramid fiber reinforced polymer, ANSYS software.*

INTRODUCTION

In modern structural engineering, the need to reinforce shear deficient (SD) beams has become increasingly important, especially in regions vulnerable to seismic activity. Aramid Fiber Reinforced Polymer (AFRP) has emerged as a highly effective material offering high strength, resistance to adverse effects of environment, and its durability making it suitable for strengthening and retrofitting structural elements.

Fiber Reinforced Polymer (FRP) materials are widely recognized today as highly effective for reinforcing and rehabilitating reinforced concrete (RC) structural elements. Shear failure in RC elements is typically sudden and brittle, making it crucial to strengthen shear-deficient members, especially in regions prone to seismic activity. AFRP, when compared to other commercially available fibers, offers superior resistance to fire, impact, and fatigue. The brittle nature of shear failure in RC structures necessitates the strengthening of shear-deficient beams, for which AFRP provides a lightweight and efficient reinforcement solution.

Among various fiber-reinforced polymers, AFRP is particularly suitable for retrofitting shear-deficient beams, offering superior impact resistance and fatigue durability. Strengthening of shear-deficient (SD)beams using AFRP sheets wrapped externally has shown significant improvements in load carrying capacity. AFRP has become a preferred material for reinforcing shear-deficient concrete beams, especially in structures located in seismic regions.

MODELING AND VALIDATION OF CONTROL AND SHEAR DEFICIENT BEAM

Element types SOLID 186 and REINF 264 are used for modeling shear deficient beams and control beams, respectively. ANSYS 2022 R1 is utilized in modelling. Three stirrups, arranged with one in the middle and the other two at the ends, each 750 mm apart along the reinforcement., are present in the shear-deficient RC beam SD.

Validation of Control beam

The beam is designed with a rectangular cross section of 150 mm width and 200 mm depth and an overall length of 1800 mm. Stirrups are provided at a spacing of 160 mm, as illustrated in Fig. 1. The beam spans a clear distance of 1500 mm. The concrete material parameters and reinforcement information are provided by Nawal Kishor Banjara and K. Ramanjaneyulu [6]. Tables 1 provide the material parameters of concrete.

Table 1 Concrete properties

Properties	Value
Poisson's ratio	0.2
Grade of selected Concrete	40MPa
Uniaxial tensile strength	3.19 N/mm^2
28 days Compressive strength	44.69 N/mm^2
Modulus of Elasticity	31500 N/mm^2

Reinforcing steel exhibits a Poisson's ratio of 0.3, a yield stress of 500 N/mm², and a modulus of elasticity of 200,000 N/mm².

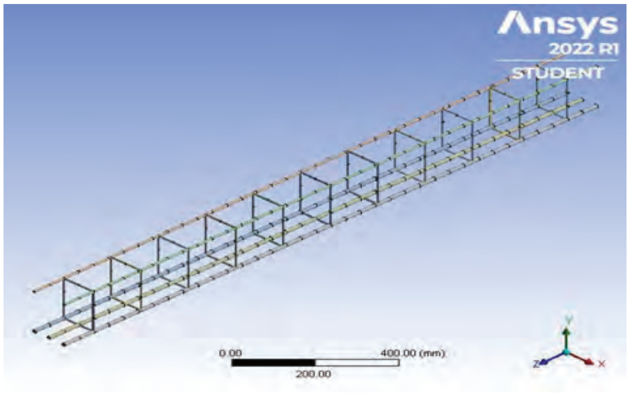

Fig. 1 Control specimen reinforcement details

The highest load the beam could carry was 94.61 kN, which resulted in a deformation of 7.6 mm. For analysis, the displacement control approach with a 100mm maximum displacement and 10mm increments is used. The support condition provided for the beam is simply supported.

Validation of SD beam

With an overall length of 1800 mm, the beam has a rectangular profile measuring 150 mm in width and 200 mm in depth. The SD beam has three stirrups, as illustrated in fig. 2, arranged with one in the middle and the other two at the ends, each 750 mm apart along the reinforcement. Material characteristics are same to those of the control beam.

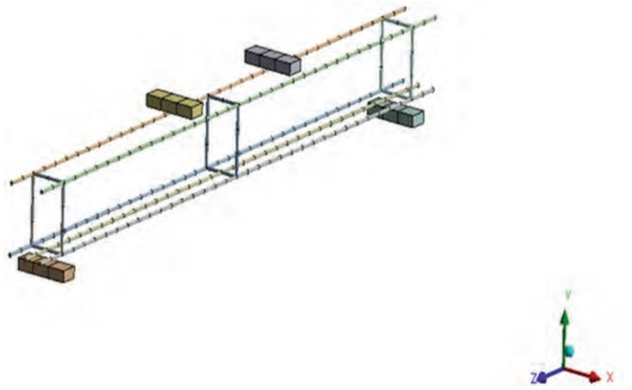

Fig. 2 Reinforcement details of the SD beam

Once the shear-deficient beam is modeled, the hexahedral mesh is created. For analysis, the displacement control approach with a 100mm maximum displacement and 10mm increments is used. The support condition provided for the beam is simply supported.

The SD beam reached a maximum load of 60.69 kN with 4.4 mm deformation, as per ANSYS results.

AFRP-STRENGTHENED SHEAR-DEFICIENT BEAMS WITH DIFFERENT THICKNESS LEVELS

Externally reinforced shear-deficient beams are modeled and analyzed. The strengthened RC beam is modeled layer by layer. The strengthened RC beam is reinforced with epoxy-impregnated AFRP fabric, which is applied as a fully wrapping strip and has two layers of AFRP strip with a 50mm width applied at the bottom.

Geometric Modelling of Externally Strengthened Shear Deficient Beams

The varying thicknesses of AFRP along the full span are 0.286 mm, 0.572mm, 0.858mm, 1.144mm and 1.43mm and a AFRP strip of 50mm width is placed along the underside of the SD beam.. The width of AFRP layer is taken as 85 mm, which is half of the beam's effective depth. The length of SD beam is 1800mm. An AFRP strip measuring 50 mm is placed at the bottom face, and the properties of Epoxy and AFRP materials are outlined in Table 2.

Table 2 Properties of epoxy resin and AFRP

Material	Modulus of Elasticity	Tensile Strength	Poisson's Ratio	Layer Thickness (mm)
Epoxy	3800 N/ mm2	45 MPa	0.21	1
AFRP	1310000 N/mm2	47.2 MPa	0.3	0.286

Five models of Shear deficient beams are created using ANSYS software as shown in fig 3.

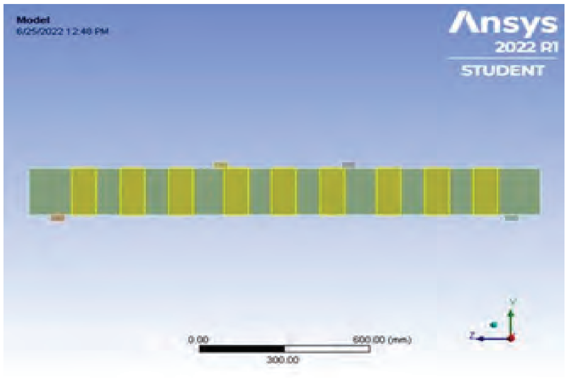

Fig. 3 Modelling of Strengthened SD by varying the number of layers or thickness of AFRP

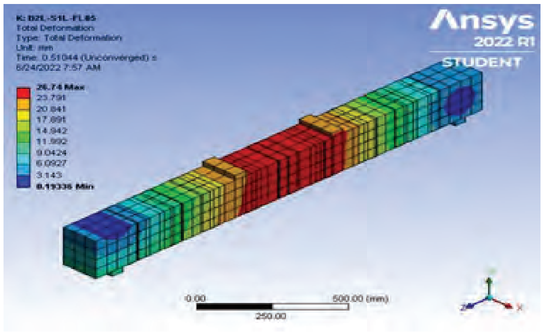

(a)

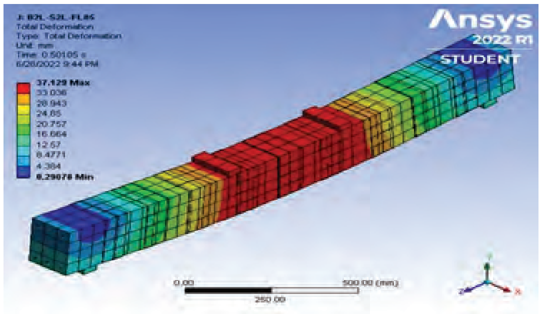

(b)

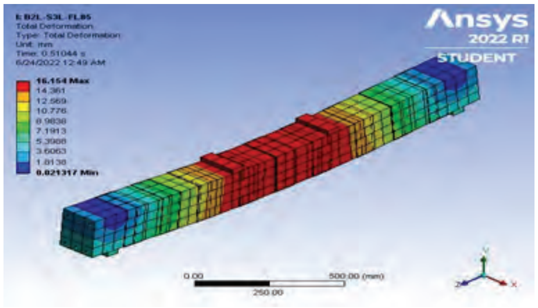

(c)

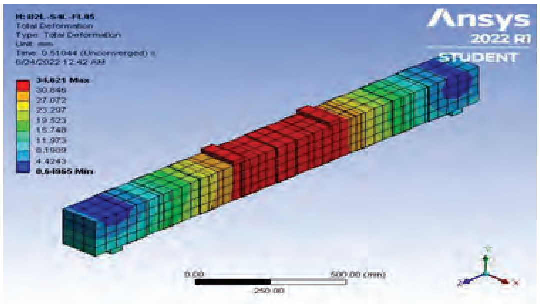

(d)

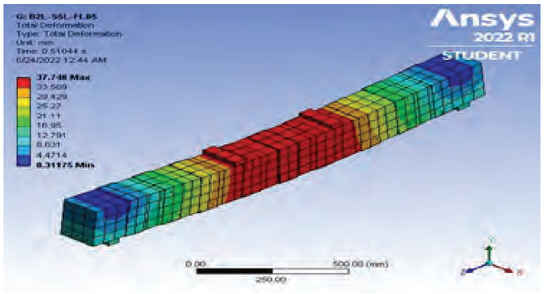

(e)

Fig. 4 Deformation Models of Strengthened SD by varying the number of layers or thickness of AFRP(a) one, (b) two, (c) three, (d) four, and (e) five AFRP layers

The performance of strengthened shear-deficient beams with different thicknesses along the full span is analyzed, as shown in Figure 4.

Comparison of results

In the case of single-layer AFRP strengthening, the beam achieved an ultimate load of 113.32 kN and experienced a deformation of 23.889 mm. When two layers were applied, the maximum deformation increased to 31.026 mm, corresponding to an ultimate load of 118.51 kN. With three layers, the deformation slightly rose to 31.729 mm, while the beam carried an ultimate load of 119.11 kN. With four layers, the deformation slightly reduced to 29.912mm, while the beam carried an ultimate load of 119.68 kN. Finally, the beam with five AFRP layers experienced a deformation of 29.467 mm and reached the highest load-bearing capacity of 120.11 kN. The load deflection comparison of Strengthened SD in full span is shown in figure 5.

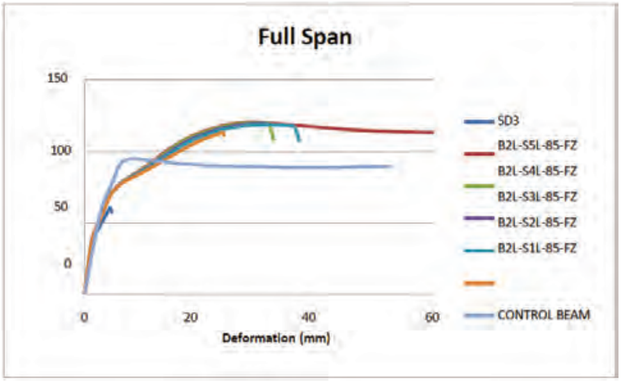

Fig. 5 Load deflection comparison Strengthened SD in full span

CONCLUSIONS

AFRP-externally strengthened shear-deficient beams with different layers are modeled and examined. Strengthened beams made of GFRP and AFRP are compared. The following findings are drawn:

- Only a slight increase in load-carrying capacity is noted with additional AFRP layers beyond five.
- The SD beam with single layer AFRP along the full span and double layer of AFRP at the bottom of the SD beam have ultimate load carrying capacity (113.22 KN) and corresponding deformation (23.889 mm) as compared to two, three, four or five layers which is greater than the ultimate load carrying capacity (94.612 KN) and corresponding deformation (7.6578 mm) of the Control beam.
- Therefore, the application of a single AFRP layer is considered sufficient to enhance the load-carrying capacity of SD beams.

REFERENCES

1. Abdul Saboor Karzad, Moussa Leblouba "Repair and strengthening of shear-deficient reinforced concrete beams using Carbon Fiber Reinforced Polymer" 2019 a. https://doi.org/10.1016/j.compstruct.2019.110963
2. Alan Saeed Abdulrahman , Mohamed Raouf Abdul Kadir "Behavior and flexural strength of fire- damaged high-strength reinforced rectangular concrete beams with tension or compression zones exposed to fire repaired with CFRP sheets" 2021
3. Chalachew B. Hunegnaw , Temesgen W. Aure "Effect of orientation of stirrups in combination with shear span to depth ratio on shear capacity of RC beams" 2021 https://doi.org/10.1016/j.heliyon.2021.e08193
4. Emine Aydın , Elif Boru, Ferhat Aydın "Effects of FRP bar type and fiber reinforced concrete on the flexural behavior of hybrid beams" 2021 https://doi.org/10.1016/j.conbuildmat.2021.122407
5. Md Abul Hasan, Mitsuyoshi Akiyama Flexural behaviour of reinforced concrete beams repaired using a hybrid scheme with stainless steel rebars and CFRP sheets" 2020 https://doi.org/10.1016/j.conbuildmat.2020.120296
6. Nawal Kishor Banjara, K. Ramanjaneyulu "Experimental and numerical investigations on the performance evaluation of shear deficient and GFRP strengthened reinforced concrete beams" 2017 http://dx.doi.org/10.1016/j.cdonbuilmat.2017.01.089
7. R.A. Hawileh, H.A. Musto , J.A. Abdalla, M.Z. Naser "Finite element modeling of reinforced concrete beams externally strengthened in flexure with side-bonded FRP laminates" 2019 https://doi.org/10.1016/j.compositesb.2019.106952
8. S. Syed Ibrahim, S. Kandasamy "Effect of discrete steel fibres on strength and ductility of FRP laminated RC beams" 2021 https://doi.org/10.1016/j.asej.2020.10.005
9. Swapnasarit Kar , K.C. Biswal "External shear strengthening of RC beams with basalt fiber sheets: an experimental study" 2021 https://doi.org/10.1016/j.istruc.2021.01.094
10. Xiangqing Kong , Xuejian Qi, Yihan Gu, Isah Abba Lawan, Yandong Qu"Numerical evaluation of blast resistance of RC slab strengthened with AFRP" 2018 https://doi.org/10.1016/j.conbuildmat.2018.05.081
11. Yassir M. Abbas, Ahmet Tuken "Improving the structural behavior of shear-deficient RC deep beams using steel fibers: Experimental, numerical and probabilistic approach" 2022 https://doi.org/10.1016/j.jobe.2021.103711

Incorporation of Fly Ash and Recycled Fine Aggregate in Photo-luminescent Concrete

Hannah Gibi
UG Scholar
Department of Civil Engineering
Mar Athanasius College of Engineering
Kothamangalam, Kerala
✉ hannahparappattu@gmail.com
Vidhya S
UG Scholars
Department of Civil Engineering
Mar Athanasius College of Engineering
Kothamangalam, Kerala
✉ vidhyasivada4@gmail.com

Haripriya Sasi
UG Scholars
Department of Civil Engineering
Mar Athanasius College of Engineering
Kothamangalam, Kerala
✉ abhinandana2002@gmail.com
Abhinandana T.S
UG Scholars
Department of Civil Engineering
Mar Athanasius College of Engineering
Kothamangalam, Kerala
✉ hari287ms@gmail.com

ABSTRACT

In this modern era where energy demand is increasing and material availability is declining, road lighting seems to be one among the major issue faced by the governments across the world. Hence a concrete dormant in daylight and producing luminescence at night-time along with providing a better strength with the reduced usage of raw aggregates proves to be efficient in managing daily energy consumption in an effective manner. In this research, two materials are taken, namely fly ash and recycled fine aggregate (RFA). These two materials are waste products and hence reduces carbon emission and cost for overall concrete construction. Cement replacement with fly ash is studied under varying percentages 15%, 20%, 25% and 30%. Fine aggregate replacement with recycled fine aggregate is studied under varying percentages as 50%, 60% and 70%. Compressive strength, split tensile strength and slump test properties are checked for both replacements. The percentage proportions of fly ash and RFA mixes that gives the maximum result values for these tests are taken as the optimum percentages of fly ash and RFA to be used as cement replacement and fine aggregate replacement respectively. Strontium aluminate is used as the light emitting pigment. It is scattered in the composition and the strength result is obtained within the safe limit.

KEYWORDS: *Fly ash, Recycled fine aggregate (RFA), Strontium aluminate.*

INTRODUCTION

The use of fly ash and recycled fine aggregate (RFA) in photoluminescent concrete demonstrates significant progress in sustainable construction techniques and material science. Photoluminescent concrete, capable of emitting light when charged by sunlight or artificial light sources, is renowned for its visual appeal and practical attributes in a variety of architectural and infrastructural settings. Furthermore, incorporating fly ash, a coal combustion by-product, and RFA from construction and demolition waste, plays a crucial role in addressing environmental concerns by decreasing waste production and reducing the carbon footprint associated with traditional concrete.

The primary objective of this research is to investigate how fly ash and recycled fine aggregate can work together to improve the properties of photoluminescent concrete, aiming to enhance sustainability and performance.

This study aims to uncover how different combinations of fly ash and RFA affect the properties of photoluminescent concrete through laboratory experiments and analysis. It seeks to evaluate factors such as compressive strength, split tensile strength, workability and durability when exposed to environmental conditions, to offer valuable insights into the practicality and effectiveness of using sustainable additives in the production of photoluminescent concrete.

The findings of this research have the potential to advance sustainable construction methods by providing a sustainable construction methods by providing a sustainable alternative to traditional concrete formulations. Additionally, by showcasing the potential of incorporating fly ash and RFA into photoluminescent concrete, the research contributes to the wider conservation on research efficiency, waste reduction and environmental responsibility in the construction industry.

LITERATURE REVIEW

Babu et al. [1] investigated the efficiency of fly ash in concrete under varying percentages, and the percent variations of replacement was conducted from 15 % to 25%. Karthik M et al. [3] studied the utilization of RFA as a sustainable material for characteristic strength in concrete. They found that RFA can be used as a fine aggregate replacement in concrete and this replacement material would improve workability and durability properties of the mix. Kou et al. [5] explored the utilization of RFA along with the incorporation of fly ash. They found that the application of fly ash and RFA improved the mechanical and durability properties of concrete mix. They also investigated the physical properties of fly ash that adds strength in concrete. Hence, from these two observations, the research takes the replacement materials as fly ash for cement replacement and RFA for fine aggregate replacement study. Strontium aluminate as a light emitting pigment was taken from the observations of a study conducted by E.R.RPK Prakash and Lijaz Ahmed. To evaluate the luminescence behavior of the concrete mix, they used U.V test. Ultimately, with all these findings the research was carried out.

OBJECTIVES

- To obtain the optimum proportion of fly ash as cement replacement in concrete mix.
- To obtain the optimum proportion of RFA as fine aggregate replacement in concrete mix.
- To study the mechanical properties of concrete mix with fly ash as cement replacement and RFA as fine aggregate replacement.
- To investigate the physical properties of fly ash and RFA that induce strength in concrete mix.
- To analyze the effect of strontium aluminate as a light emitting pigment in the concrete mix.
- To analyze the economic viability of incorporating fly ash and RFA as replacement materials in photo-luminescent concrete.
- To analyze the environmental feasibility of incorporating fly ash and RFA as replacement materials in photo-luminescent concrete.

MATERIALS USED

The raw aggregates utilized in the photoluminescent concrete are namely, fly ash, cement, fine aggregate, RFA, coarse aggregate-20mm and 12mm, water and strontium aluminate as the light emitting pigment.

1) Cement: Cement functions the role as a binding material. Ordinary Portland cement with grade 53 (Ultratech cement) having specific gravity 3.16, consistency 34% and initial setting time as 32 minutes, conforming to IS 4031 is used.
2) Fly ash: Fly ash is used as the replacement material for cement, in different proportion as 15%, 20%, 25% and 30%. Class F fly ash is taken with a specific gravity of 2.03. After coal combustion in the plant, fly ash is the finer particle that is obtained. The concrete's compressive strength and durability are significantly influenced by this compound. The C-S-H gel formed during the hydration process the alkali aggregate reactions in the mix. Additionally, fly ash acts as a pozzolan, improving the cementitious property and enhancing the material's resistance to chemical attack, thereby increasing the concrete's longevity.
3) Fine aggregate: M-sand is used as the fine aggregate, which falls under the zone II in the particle distribution curve, conforming to IS 383, 1971. They are granular materials usually made from natural sand or crushed stone particles that are usually less than 4.75 mm in size. They play a crucial role in strength, workability and overall performance of concrete.
4) Recycled fine aggregate: Recycling limits the need

for extracting and processing new aggregates, leading to conservation of natural resource and minimizing environmental impact.They also exhibit consistent properties if sourced from uniform materials. They are obtained by passing the crushed old concrete through sieve size 4.75 mm [3].

5) Light emitting pigment: Strontium aluminate is used as the light emitting pigment [2]. In this study it is usually termed as glow in dark powder. Chemically, strontium aluminate exhibits phosphorescent behavior, storing energy in the day time when exposed under sunlight and emitting light in the night throughout. This property imparts the characteristic glow to the concrete. This makes it suitable for various applications like bicycle pavement, pedestrian pavement, decorative and safety purposes.

6) Water: Pure portable water free from suspended particles, toxic contaminants and bacterial products is utilized for both preparing and curing concrete. High rise buildings are frequently chosen due to urbanization and the high cost of land. Using a lower water/cement mix is deemed optimal as it results in lower porosity and provides maximum strength and durability.

MIX DESIGN

The mix design is prepared as per IS 10262, 2019 with M20 as the grade and 0.42 as the w/c ratio (from table 5, IS 456) taken. The degree of workability is taken as 100 and the exposure type as severe. OPC 53 grade Ultratech cement is taken.

EXPERIMENTAL SET UP

The ultimate aim of this research is to obtain the percentage proportions of fly ash and RFA mixes in M20 mix, to be used as cement replacement and fine aggregate replacement respectively, without compromising the strength and durability properties as performed by the normal control mix, with strength test and slump test. The strength tests incorporated in this study are Compressive strength test and split tensile strength test. For compressive strength test, concrete cubes of 15cm x 15cm x 15 cm is used. And, or split tensile strength test, concrete cylinders of height 30 cm and diameter 15 cm is used.

Initially, two control specimens were prepared with 0% replacement for both, and the test studies were conducted on them. Then, concrete specimens with cement replaced by fly ash in varied proportions of 15%, 20%, 25% and 30% were prepared and the test studies were conducted on them. The percentage proportion of fly ash mix that gave maximum test values is taken as the optimum fly percentage for replacing cement in the mix. Then, concrete specimens with fine aggregates replaced by RFA by varied proportions of 50%, 60% and 70% were prepared and tests were conducted on them. The percentage proportion of RFA mix that gave maximum test values is taken as the optimum RFA proportion for replacing fine aggregates in the mix. Further, the tests were analyzed on the concrete mix having cement replacement by optimum fly ash percentage and fine aggregate replacement by varied proportions of 50%, 60% and 70%. The fly ash- RFA mix that gave maximum test values is analyzed, to check whether the combination of both would ultimately change the optimum proportion of RFA or not. All the above test results were compared with the respective tests on control specimen and the percentage proportions is finalized, meanwhile the deviations were analyzed to check whether the strength is reached, increased or not.

Material analysis

Control Specimen Analysis

Two control specimens (specimens with 0% replacement for cement and fine aggregate) were prepared, one for compressive strength test and the other for split tensile strength test and the study was carried out. Also, two more control specimens were prepared, with GID embedded on them. The test studies were further repeated on them.

Analysis on mix having Cement replacement with various proportions of Fly Ash

Initially, concrete mixes replacing cement by 15%, 20%, 25% and 30% fly ash proportions were prepared

[1] and was studied under the slump test and the 28th day compressive strength test.

Optimization Decision

Based on the compressive strength test and the slump test conducted on the concrete mix having cement replacement by 15%, 20%, 25% and 30% fly ash proportions, a decision is made to select a specific fly ash proportion as the optimum fly ash percentage, which shows maximum values for these test results. This proportion represents the optimum fly ash percentage to be used as cement replacement in concrete.

Analysis on mix having Fine Aggregate replacement by 50%, 60% and 70% Proportions

Initially, concrete mixes replacing fine aggregates by 50%, 60% and 70% RFA proportions were prepared [3] and was studied under the slump test and the 28th day compressive strength test.

Optimization Decision

Based on the compressive strength test and the slump test conducted on the concrete mix having fine aggregate replacement by 50%, 60% and 70% RFA proportions, a decision is made to select a specific RFA proportion as the optimum RFA percentage, which shows maximum values for these test results.

Workability analysis

Slump test was conducted on the specimens cast as above and the specimen in which the mix having fine aggregates replaced with 60% recycled fine aggregates shown a better slump value, while the mix with 50% RFA did not met the desired criteria and the one with 70% RFA showed reduced mechanical properties, in terms of durability, exposure properties etc. (Table 4)

Analysis On Mix Having Cement Replacement By 25% RFA And Fine Aggregate Replacement By 50%, 60% And 70% RFA

The study was further continued to develop a mix with the combination of both the replacements, using fly ash and RFA respectively [4]. Since cement is the main compound giving strength to the mix, the optimum fly ash percentage as obtained was chosen for cement replacement here. However, to check whether the behavior of RFA mixes will show difference in behavior when combined with fly ash composition, three mixes having cement replacement using 25% fly ash and fine aggregate replacement by 50% RFA, 60% RFA and 70% RFA were prepared and the test studies were further carried out. The test studies were conducted over the 28th day analysis [4,5].

Optimization Decision

Based on the results obtained from the strength test analysis done on the mixes, the RFA mix that gave maximum test results is taken as the optimum RFA proportion to be added to the 25% fly ash proportion.

In this research, the GID powder is just sprinkled over the surface, while it gave a better test result. However, this area gives the future scope of studying the effects of varying the quantities of GID powder sprinkled over the surface, to obtain a better result .

RESULTS AND DISCUSSIONS

Compressibility Strength Test

Ability of a material to resist axial loads pushing it together is measured by compressive strength, which is crucial in structural applications. In general, compressive strength of concrete improves with higher proportions of cementitious materials because of their superior bonding properties. Comparing compressive strength allows for evaluating different materials or variations of the same material, such as various concrete mixes. This comparison aids in optimizing material selection and design choices based on performance requirements, cost-effectiveness and environmental considerations. Usually, 28th day compressive strength test results are taken for calculations.

Table 1. Compressive strength test results

C_7	$C2_8$	C_{90}
22.09 MPa	28.05 MPa	31.94 MPa

Table 2. Compressive strength test results

C_7 GID	C_{28} GID	C_{90} GID
20.71 MPa	26.88 MPa	28.45 MPa

Table 3. Split Tensile test results

P_7	P_{28}
3.429 MPa	3.42 MPa

As per the 28th day compressive strength test conducted, from table 1 and 2, the control specimen without GID showed a compressive strength of 28.05 MPa while the one with GID showed a compressive strength of 26.88 MPa. A declination in compressive strength is observed when GID is embedded over them, this is because of the strontium aluminate content embedded over it. When they are sprinkled over the mix, they get mixed with the mix, weakening the bonding between the compounds in the mix, ultimately leading to a structurally disintegrated composition

Table 4. Compressive strength test results

Mixes with cement replacement using fly ash in various percentages	$(CF_{15}GID)_{28}$	$(CF_{20}GID)_{28}$	$(CF_{25}GID)_{28}$
Compressive strength obtained (MPa)	**26.64 MPa**	**28.88 MPa**	27.40 MPa

(CFxGID)28 – concrete mix at 28th day having cement replacement by x% fly ash proportion, for compressive strength test

From table 4, for cement replacement, by fly ash, higher compressive strength value is showed by the mix having 25% fly ash.

Table 5. Compressive strength test results

Mixes	$(CR_{50}GID)_{28}$	$(CR_{60}GID)_{28}$	$(CR_{70}GID)_{28}$
Compressive strength obtained	28.21 MPa	28.91 MPa	27.42 MPa

From table 5, it is observed that for fine aggregate replacement using RFA, higher values of compressive strength were shown by the mix having 60% RFA.

Table 6. Compressive strength test results

Mixes having cement relacement by 25% fly ash and fine aggregate replaceement by 50%, 60% and 70% RFA	$(CF_{25}R_{50}GID)_{28}$	$(CF_{25}R_{60}GID)_{28}$	$(CF_{25}R_{70}GID)_{28}$
Compressive strength obtained (MPa)	30.956	33.281	28.63

$(CFxRyGID)_{28}$ – concrete mix at 28th day having cement replacement by x% fly ash proportion and fine aggregate replacement by y% RFA proportion, for compressive strength test.

Since cement is the main component giving strength to the mix, 25% fly ash proportion is chosen for cement replacement in the combination. Then the behavior of this mix with RFA proportions analyzed that 60% RFA proportion with 25% fly ash mix gave high compressive strength value (table 6).

The compressive strength test study shows that, 25% fly ash proportion is chosen for cement replacement mix, 60% RFA is chosen for fine aggregate replacement mix and 25% flysh-60% RFA proportions is chosen for cement replacement-fine aggregate replacement mix.

And a detailed analysis showed that all the above mixes with GID sprinkled over the surface gave a strength value higher than that of the control specimen with GID. This proves that the incorporation of them into photoluminescent concrete would ultimately increase the cementitious properties even with the reduced usage of conventional material content, paving the path to sustainability in the construction sector.

Workability Test results

The easiness in mixing, transporting, placing and compacting concrete is what workability refers to. In this research, workability is studied with slump test. Generally, slump of degree 100 or nearer to 100 is taken for M20 grade concrete. It is normally considered as a highly workable concrete.

Table 7. Slump Test Results

Percentage proportions by which fly ash is used to replace cement in the mix	0%	15%	20%	25%	30%
Slump value (mm)	64	78	82	99	110

For control specimen, slump value is obtained as 64 mm. From, table 7, it is observed that the slump value nearer to 100 is given by the mix having cement replacement by 25% fly ash proportion.

Slump test conducted on fine aggregate replacement mix with 50%, 60% and 70% RFA proportions revealed that, the mix with 50% RFA mix did not met the desired criteria for strength and durability criteria and the other mix having 70% RFA mix have shown signs of reduced mechanical properties, meanwhile the one with 60% RFA shown better results in terms of durability, and mechanical properties.

Hence, from slump test on workability analysis, it is inferred that 25 % fly ash proportion is chosen for cement replacement mix and 60% RFA mix is chosen for fine aggregate replacement mix.

Split tensile strength test results.

The split tensile strength measure's the material's availability to resist tensile stress applied perpendicular to its axis. Higher values of split tensile strength indicate mix with higher proportions of cementitious properties.

Table 8. Split tensile strength test results

Mixes with 25% fly ash and 50%, 60% and 70% RFA	$(PF_{25}R_{50}GID)_{28}$	$(PF_{25}R_{60}GID)_{28}$	$(PF_{25}R_{70}GID)_{28}$
Split tensile strength test obtained (MPa)	3.7	5.56	4.10

(PFxRyGID)28 -concrete mix having cement replacement – fine aggregate replacement by x% fly ash- y% RFA proportions, for split tensile strength test

The result obtained from the compressive strength test when checked with split tensile strength test, also gave the same result as, 60% RFA proportion when added to 25% fly ash mix gave the higher split tensile value than the other mixes with 50% and 70% RFA.

Also, from table 8, a detailed analysis shows that the 25% fly ash- 60% RFA mix with GID shown a split tensile value higher than that of the control specimen with GID.

Hence, from split tensile strength test, the 25% fly ash-60% RFA mix is taken as the cement replacement - fine aggregate replacement mix.

The optimum proportions for the replacements are the percentage proportions of the replacement items that gives maximum result for the tests. In this study the proportions are inferred after conducting workability test, compressive strength test and split tensile strength test.

Finally, from the compressive strength test, workability slump test and the split tensile strength test, the result obtained is that, the optimum fly ash proportion for cement replacement is 25%, the optimum RFA proportion for fine aggregate replacement is 60%, and the optimum fly ash-RFA proportion for cement replacements and fine aggregate replacement is 25% fly ash-60% RFA.

When fly ash is included in the concrete mixture, it reacts with lime produced from the combination of water and cement to form a calcium-silicate-hydrate gel (C-S-H), which exhibits binding properties similar to that of cement. Additionally, the reactive glassy components of fly ash interact with calcium and alkali hydroxides released from the cement-fly ash-system, producing a cementitious gel that contributes to strength. The round shape of fly ash allows it to fill void spaces typically occupied by water, thus reducing the water-to-cement ratio and ultimately enhancing the strength of concrete. Hence, ultimately, fly ash concrete mix would yield more strength values as compared with that of the control mix with cement [5].The rougher surface texture of RFA can add binding property to the mix. The compound also consists of an adhered mortar from previous concrete, which could contribute to an overall cementitious matrix that adds strength in concrete. Hence RFA-concrete mix would add more strength in concrete as compared with that of the control mix with medium sand as fine aggregate [3,6]. Hence, these properties induce strength in the mixes where the addition of GID powder reduced the mechanical properties. Thus, RFA and fly ash seems to be the viable option for replacements.

To check whether the 25% fly ash and 60% RFA mix is economically viable and feasible, cost analysis study was conducted over them. Since 16.72 % reduction in cost is found with incorporation of 25% fly ash as cement replacement and 60% RFA as fine aggregate replacement, the research suggests that this concrete construction is viable and economically feasible.

The research was further continued to get the luminescent intensity behavior of the cement replacement- fine aggregate replacement mix. The final mix with 25% fly ash 60% RFA proportion, with GID embedded over them after curing period was taken from the ponded water and was placed in the sunlight for 6 hrs. The specimen when placed in darkness, at night showed a deep intense green color, which lasted throughout the night. It is also discerned that the product also glowed in day time when placed in darkness. And the comparison of this luminescence with that of the control specimen embedded with GID showed that the integration of fly ash and RFA into the mix as replacements won't limit the luminescence behavior, however an increase in luminescence intensity was observed.

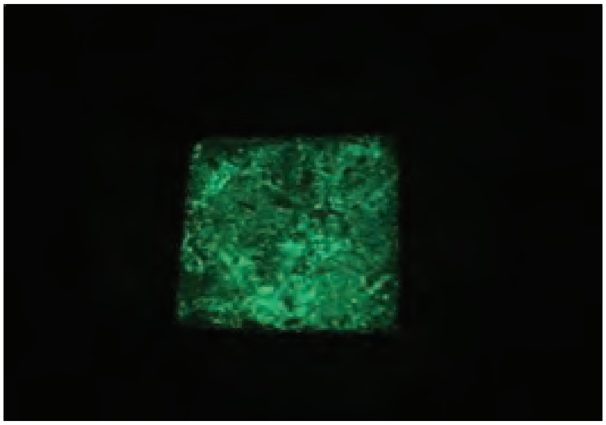

Fig. 1. Luminescence in Photo-luminescent Concrete kept in dark

Development of concrete with varied proportions of GID powder finds to be an area where future study could be done. On analysing the constraints as time, cost, easiness in construction etc the mix CF25R60GID proves to be more economically viable and productive. Construction of Bicycle pavement, walkways, road safety markings, pollution inhibition, road signalling, night lightning, aesthetic appealing, etc. marks the applications for this construction technology. This makes the concrete design much safer and more productive with every chance of future improvement. This ameliorates the construction practice to be much more sustainably green and innovative, providing scopes for future development, paving the path for a developed nation.

CONCLUSIONS

From this study we conclude that

- The optimum fly ash proportion for mix having cement replacement is 25% fly ash.
- The optimum RFA proportion for mix having fine aggregate replacement is 60% RFA.
- The optimum fly ash – RFA proportion for mix having cement replacement – fine aggregate replacement mix is 25% fly ash -60% RFA.
- Integration of GID over control mix would decrease the mechanical properties, however the incorporation of fly ash and RFA in a specific proportion would ultimately increase the mechanical properties of the photoluminescent concrete, hence better performance is reached.
- The profit earned by the construction of concrete mix with 25% fly ash and 60% RFA with GID embedded over the surface with that of the control mix is 8%. (for 1 m3 of concrete).
- The properties enhancing strength with the addition of fly ash are their round shape, pozzolanic action causing the formation of a 'C-S-H' gel, small size and glassy particle nature. The properties contributed by RFA inducing strength in concrete are their rougher surface texture and the presence of an adhered mortar creating an overall cementitious matrix.
- Construction of bicycle pavement, walkways, night lightning, pollution inhibition, road safety marking, aesthetic appealing, emergency signages in buildings, street lightning etc. include the applications of this construction practice.
- The mix with GID embedded over the surface proves out to be the perfect construction method for the photo-luminescent concrete design. This carves it out to be more productive, safer, faster, easier, economically viable and environmentally feasible. Making the design highly innovative with every scope for future development, this aids the design to be a much more sustainably green concrete construction practice.
- Quantity of GID powder required to be used as the surface coating to induce better results provides to be an area where research can be done.

REFERENCES

1. Babu, K. G., & Rao, G. S. N. (1996). Efficiency of fly ash in concrete with age. Cement and concrete research, 26(3), 465-474.

2. Dipika, G., Kaaviya, S., Kavitha, K. S., & Indhumathi, S. (2019). Exploratory study on photo luminescence induced concrete. Int J Civ Eng Technol, 10, 622-628.

3. Kaarthik, M., & Maruthachalam, D. (2021). A sustainable approach of characteristic strength of concrete using recycled fine aggregate. Materials Today: Proceedings, 45, 6377-6380.

4. Kou, S. C., Poon, C. S., & Chan, D. (2007). Influence of fly ash as cement replacement on the properties of recycled aggregate concrete. Journal of materials in civil engineering, 19(9), 709-717.

5. Kou, S. C., & Poon, C. S. (2013). Long-term mechanical and durability properties of recycled aggregate concrete prepared with the incorporation of fly ash. Cement and Concrete Composites, 37, 12-19.

6. Kurda, R., de Brito, J., & Silvestre, J. D. (2017). Combined influence of recycled concrete aggregates and high contents of fly ash on concrete properties. Construction and Building Materials, 157, 554- 572.

Comparative Study of Mechanical and Durability Properties of Foamed Concrete with Rice Husk Ash and Sugarcane Bagasse Ash

Karthika K S
UG students
Department of Civil Engineering
NSS College of Engineering
Palakkad, Kerala
✉ kskarthikasuresh13@gmail.com

Srihari S
UG students
Department of Civil Engineering
NSS College of Engineering
Palakkad, Kerala
✉ sriharithara@gmail.com

Nihala T N
UG students
Department of Civil Engineering
NSS College of Engineering
Palakkad, Kerala
✉ tnnihalanoushad@gmail.com

Praseeda K I
Assistant Professor
Department of Civil Engineering
NSS College of Engineering
Palakkad, Kerala
✉ praseedaki@nssce.ac.in

ABSTRACT

The rising construction costs have led to a search for sustainable alternatives, with foamed concrete (FC) being a versatile solution. This lightweight material, with 30% volume filled with air, offers a sustainable option for construction, especially in the form of blocks with densities below 1800 kg/m³. It addresses environmental concerns and provides thermal insulation properties, making it popular in the industry. The paper discusses about sustainable variations at replacement levels of 5%, 10%, and 15% that are attained by replacing cement with rice husk ash (RHA) and sugarcane bagasse ash (SCBA). Compressive strength, durability, water absorption, thermal conductivity, and wet and dry density are among the important factors being examined in order to determine the ideal replacement percentage for maximum performance.

Furthermore, the study evaluates production costs for eco-friendly options to promote sustainability and encourage the use of sustainable techniques in construction projects.

KEYWORDS: *Foamed concrete, Rice husk ash, Sugarcane bagasse ash.*

INTRODUCTION

Foamed concrete, also known as lightweight or cellular concrete, is a versatile building material with exceptional thermal and acoustic insulation properties. It is made of cement, water, foam, and fine aggregates, with a density ranging from 400 to 1800 kg/m³. Its self-flowing properties make it easy to pour and distribute, especially in tight spaces. Foamed concrete is also known for its environmental friendliness, as it can incorporate industrial waste like fly ash and recycled aggregates to reduce waste and environmental impact. It is commonly used in various construction applications, such as lightweight fill material, thermal insulation, and fire-resistant barriers. Producing high-quality foamed concrete requires careful consideration of factors like foam production method, ingredient selection, mix design, and water content control. Incorporating waste materials into the production process is recommended to improve durability and sustainability. Ongoing research and innovation in foam production technology and materials promise to enhance the efficiency and eco-friendliness of foamed concrete, paving the way for more environmentally conscious construction practices.

This study is intended (a) to investigate the properties of foamed concrete with cement replacement by Rice husk ash (RHA) and Sugarcane bagasse ash (SCBA) (b) To compare the mechanical and durability properties of foamed concrete using RHA and SCBA for different percentage of replacement (c) To compare production cost of conventional foamed concrete and foamed concrete using RHA and SCBA.

LITERATURE REVIEW

The studies looked at several areas of introducing alternative materials into concrete manufacturing to improve sustainability and reduce environmental impact. Ayyanar et al., 2023 employed a precise foaming agent-water ratio and high-grade cement to control and improve foam concrete properties. Jose et al., 2021 investigated the production of eco-friendly building blocks made from foamed concrete and ground granulated blast furnace slag, with the goal of promoting sustainable construction materials. Roslan et al., 2013 evaluated the effects of additives on the properties of lightweight foamed concrete, with the goal of improving its performance. Loganayagan et al., 2021 investigated the use of sugarcane bagasse ash as an ingredient in concrete mixtures, demonstrating its usefulness in increasing concrete strength qualities while lowering environmental impact. Berenguer et al., 2020 and Habeeb et al., 2010 both investigated the use of sugarcane bagasse ash and rice husk ash as partial replacements for Portland cement in mortar compositions, highlighting their potential as pozzolanic materials to improve concrete strength while reducing environmental impact. Overall, these studies provide important insights into the development and use of alternative materials in concrete manufacturing, emphasising their potential to improve sustainability and performance in construction projects.

EXPERIMENTAL INVESTIGATION OF MATERIALS

Materials

The materials used in the manufacture of foam concrete include OPC Chettinad M53 grade cement of specific gravity 3.05 as the binder, sand as fine aggregate of specific gravity 2.68 passed through a 300-micron mesh sieve, and potable water with a pH of 7. The synthetic Marjanol foaming agent, mixed with water at a 30:1 ratio, creates foam with a density of 78.50 kg/m³. Additionally, Rice Husk Ash (RHA) of specific gravity 2.43 and Sugar Cane Bagasse Ash (SCBA) of specific gravity 2.67 are used to enhance strength and durability, while Conplast SP430, a chloride-free superplasticizer, improves workability and reduces water demand.

Casting and Testing of Specimen

This research aims to make concrete production economical by replacing cement with Rice Husk Ash (RHA) and Sugar Cane Bagasse Ash (SCBA). The casting procedure for foamed concrete involves preparing cement, water, foaming agent, and fine aggregates, and determining the mix design for desired properties. Foam is generated and its stability and density are ensured. The concrete has a density of 1600 kg/m³ and a cement-to-fine aggregate ratio of 1:2. A water-to-cement ratio of 0.7 is used as RHA and SCBA are highly porous and requires more water to achieve workability. The dry and wet materials are mixed until homogeneous and poured into 100x100x100 mm moulds for testing. Due to the free-flowing nature of foamed concrete, no compaction is needed. After 24 hours, the specimens are demoulded and cured in water. Three cubes each are prepared for testing of 28-day compressive strength, dry density, water absorption, and thermal conductivity tests. Specimens are placed in a hot air oven at 110°C for 24 hours to measure dry density, water absorption, and thermal conductivity. In this study conducted, cement is partially replaced with RHA and SCBA at 5%, 10%, and 15%.

Fig. 1 Batching, Mixing, Placing of FC, Curing of FC

RESULTS AND OBSERVATIONS

Table 1 Test results after 7 and 28 days of mix proportion 1:2

Sl.No	Mix ID	Density (kg/m³)		Water absorption (%)	Compressive Strength (N/mm²)		Thermal Conductivity (W/mK)	Acid resistance test	
								Mass (%)	Compressive strength (N/mm²)
		7 days	28 days	28 days	7days	28 days	28 days	28 days	28 days
1	FC	1650	1640	11.95	6.25	11.65	0.6		
2	RHA5	1692	1699	12.53	10.07	14.41	0.9	2.24	14.22
3	RHA10	1674	1680	11.90	12.01	15.14	0.67	2.14	16.18
4	RHA15	1692	1660	12.04	6.84	9.58	0.6	2.37	11.98
5	SCBA5	1644	1671	14.40	9.32	12.08	0.96	1.57	13.53
6	SCBA10	1646	1643	15.52	10.01	13.79	0.68	1.76	15.01
7	SCBA15	1651	1651	15.48	6.12	9.24	0.61	1.96	11.77

Based on the observations, it was inferred that the dry density obtained was almost near to the fixed density of 1600 kg/m³, which was used for calculating the mix design.

The water absorption for conventional foamed concrete should not exceed 20 %. The observations indicate that both foamed concrete mixes containing RHA and SCBA replacements have water absorption values that fall within the 20% specified for conventional foamed concrete. This means that despite using alternative materials like RHA and SCBA, the foamed concrete blocks are absorbing water at rates that meet the required standards. Also, it was observed that FC using RHA show less water absorption compared to SCBA.

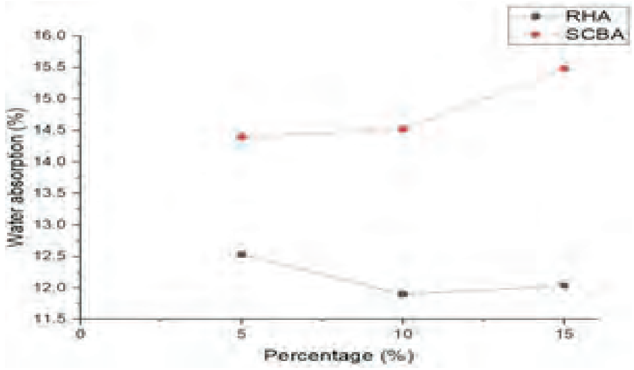

Fig. 2 Combined graph for 28-day water absorption of foamed concrete using RHA and SCBA

The observations indicate that adding RHA and SCBA gave more strength compared to conventional foamed concrete. And on comparing the compressive strength of foam concrete using rice husk ash (RHA) and sugarcane bagasse ash (SCBA) at different percentages of 5%, 10% and 15%, RHA consistently outperformed SCBA at all replacement percentages. Additionally, over the range of replacements tested, 10% RHA or SCBA replacement resulted in higher compressive strength than other replacement percentages. This suggests that the addition of RHA at a 10% replacement level resulted in the highest compressive strength of the tested varieties.

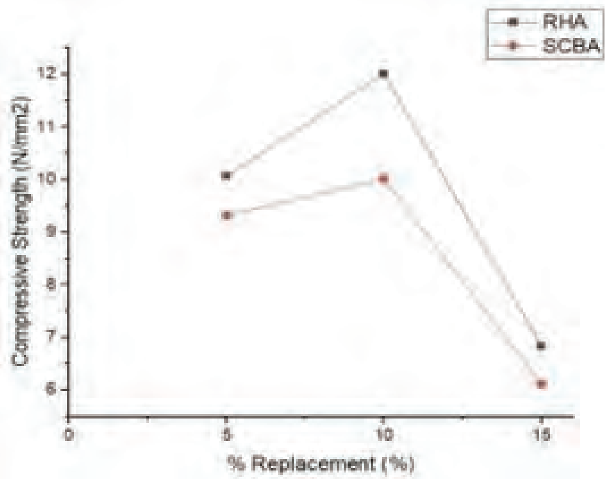

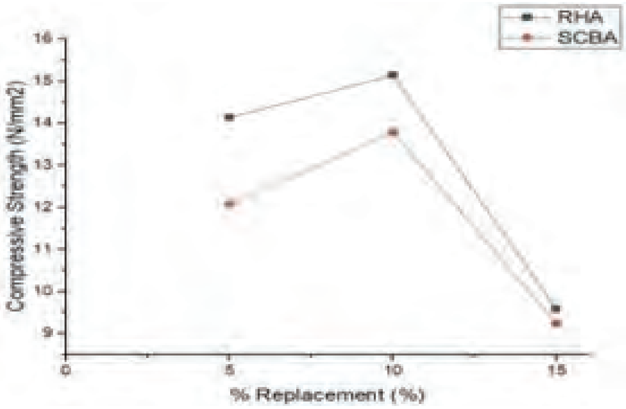

Fig. 3 Combined graph for 7 and 28 day compressive strength of foamed concrete using RHA And SCBA

Examining the thermal conductivity of foamed concrete (FC) using RHA and SCBA at different percentages of 5%, 10% and 15%, a consistent trend was observed in which RHA showed lower thermal conductivity value compared to SCBA at all replacement levels. This indicates that the addition of RHA improved the thermal insulation properties of foamed concrete mixtures. In addition, it was found that the thermal conductivity decreased as the percentage of ash replacement increased, suggesting that higher ash content improves the insulating properties. In particular, the findings showed that a decrease in cement content associated with the addition of RHA or SCBA resulted in a decrease in thermal conductivity, highlighting the role of cement content in influencing thermal properties. It should be noted that although the 15% replacement level showed the best overall results in terms of thermal conductivity, the differences between the 15% and 10% replacements were not found to be significant.

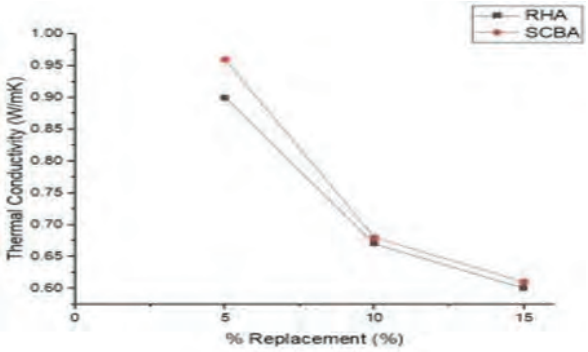

Fig. 4 Combined graphs for thermal conductivity of FC using RHA and SCBA

Evaluating the results of acid resistance test by the contribution of RHA and SCBA to foam concrete as partial cement replacements, it is particularly clear that SCBA performs better than RHA when analysing mass loss %. Although RHA tends to be stronger in compression testing, SCBA's lower mass loss indicates that it may be more resilient to environmental influences and maintain structural integrity over the long run. On the other hand, at a 10% replacement level, RHA has a higher compressive strength than SCBA. This suggests that using RHA in place of cement could improve the longevity and functionality of foam concrete.

COST ANALYSIS

An analysis was conducted to compare the cost of foamed concrete made from industrial byproducts (RHA and SCBA) and conventional foamed concrete used in construction. It is understood that the production cost of FC with waste materials is comparatively less than that of the existing foamed concrete. The detailed analysis is presented in the table 2.

Table 2 Cost analysis of 1 cube of FC and foamed concrete with RHA and SCBA

Sl. No	Description	Conventional foamed concrete			Foamed concrete with RHA			Foamed concrete with SCBA		
		Qty (kg)	Rate (Rs/kg)	Amount (Rs)	Qty (kg)	Rate (Rs/kg)	Amount (Rs)	Qty (kg)	Rate (Rs/kg)	Amount (Rs)
1	Cement	0.591	9.6	5.673	0.530	9.6	5.088	0.532	9.6	5.107
2	Fine aggregate	1.182	10.51	12.422	1.060	10.51	11.14	1.063	10.51	11.17
3	RHA	-	-	-	0.053	28.67	1.51	-	-	-
4	SCBA	-	-	-	-	-	-	0.053	-	-
5	Foaming agent	0.011	398	4.279	0.011	398	4.27	0.010	398	3.89
6	Total cost for 1cubes	Rs 22.371/-			Rs 22.017/-			Rs 20.16/-		

CONCLUSIONS

Foamed concrete mixes containing RHA and SCBA replacements have water absorption values that fall within the 20% specified for conventional foamed concrete. RHA has 2-3 % lower water absorption than SCBA due to its irregular structure, mainly composed of amorphous silica particles. Comparing the compressive strength of RHA and SCBA as cement substitutes, RHA outperforms SCBA at all replacement percentages. Specifically, the most promising results are at the 10% replacement level. Both RHA and SCBA can effectively replace up to 10% of cement, maintaining strong binding ability and workability, but exceeding this threshold reduces compressive strength by 4-6 %. In the case of thermal conductivity, it decreases when the cement proportion decreases by 5-15%. Cement has higher thermal conductivity compared to RHA and SCBA due to its composition of calcium silicates. As cement content decreases, the overall thermal conductivity of the concrete decreases, making it more insulating against temperature changes. The foamed concrete made with SCBA has 1- 2% lower mass loss in acidic environments than RHA, while RHA provides higher compressive strength compared to SCBA due to its pozzolanic properties.

Overall, RHA performs better than SCBA in terms of compressive strength and thermal conductivity, enhancing structural strength and thermal insulation. Using industrial by-products like SCBA and RHA lowers production costs and enhances sustainability in foamed concrete construction.

REFERENCES

1. Ayyanar, D., Puvaneshwaran, J. N., Vipurajan, E., Hameed, M. S., & Jeyaseela, J. (2023). Experimental Investigation on Strength Properties of Foam Concrete. East Asian Journal of Multidisciplinary Research, 2(4), 1517-1528.
2. Berenguera, R. A., Caprarob, A. P. B., de Medeirosb, M. H. F., Carneiroa, A. M. P., & De Oliveirac, R. A. (2020). Sugar cane bagasse ash as a partial substitute of Portland cement: Effect on mechanical properties and emission of carbon dioxide. Journal Name, 8(2), 103655
3. Habeeb, G. A., & Mahmud, H. B. (2010). Study on Properties of Rice Husk Ash and Its Use as Cement Replacement Material. Department of Civil Engineering, Faculty of Engineering, University of Malaya, Kuala Lumpur, Malaysia : 13(2): 185-190.
4. Jose, S. K., Soman, M., & Evangeline Y, S. (2021). Ecofriendly building blocks using foamed concrete with ground granulated blast furnace slag. International Journal of Sustainable Engineering, 14(4), 776-784. Jose, S. K., Soman, M., & Evangeline, Y. S. (2021). Influence of mixture composition on the properties of foamed concrete. Materials Today: Proceedings, 42, 399- 404.
5. Loganayagan, S., Mohan, N. C., & Dhivyabharathi, S. (2019). Sugarcane bagasse ash as alternate supplementary cementitious material in concrete. Civil Engineering Department, Bannari Amman Institute of Technology, Sathyamangalam 638 401, India.:45(2)1004 - 1007
6. Roslan, A. F., Awang, H., & Mydin, M. A. O. (2013). Effects of various additives on drying shrinkage, compressive and flexural strength of lightweight foamed concrete (LFC). Advanced Materials Research, 626, 594-604.
7. IS 2386 (Part 3) – 1963 – Specific gravity, density, voids, absorption and bulking IS 4031 (Part 1) – 1988 – Determination of fineness by dry sieving IS 4031 (Part 4) – 1988 – Determination of consistency of standard cement paste IS 4031 (Part 5) – 1988 – Determination of initial and final setting times IS 4031 (Part 11) – 1988 – Determination of density IS 2185 (Part 4) – 2008 – Preformed foam cellular concrete blocks Source of materials used: IndiaMART, online website Royal sand and gravels, Dhoni, Palakkad Veekay Traders - Cement Dealer in Palakkad Cement Wholesaler Cement Agencies Palakkad.

Sustainable and Energy Efficient Brick Production from Landfill Wastes

Liya Wilson C A
UG Scholars
Department of Civil Engineering
Muthoot Institute of Technology and Science
Varikoli, Kerala
✉ liawils2002@gmail.com

Joel Manoj
UG Scholars
Department of Civil Engineering
Muthoot Institute of Technology and Science
Varikoli, Kerala
✉ joelmanojpaul@gmail.com

Sana Jasmine K S
UG Scholars
Department of Civil Engineering
Muthoot Institute of Technology and Science
Varikoli, Kerala
✉ sanajasmine119@gmail.com

Tony Issac
UG Scholars
Department of Civil Engineering
Muthoot Institute of Technology and Science
Varikoli, Kerala
✉ tonyisaac224@gmail.com

ABSTRACT

The growing accumulation of landfill waste globally poses significant economic and environmental challenges, exacerbated by traditional brick firing methods that require temperatures above 900°C, leading to energy consumption and significant waste. Addressing this challenge requires innovative solutions, such as integrating landfilled organic and inorganic waste into brick production. By reducing the volume of waste sent to landfill and revolutionizing the brick firing process to operate at lower temperatures, around 200°C, this method offers a sustainable alternative to traditional brick production system. Experimental findings demonstrate promising compressive strength, reaching 9.2 N/mm^2 with a mix proportion of Clay: Sand: Red earth: Organic waste: Plastic waste = 5:3:1:0.5:0.5. These energy- efficient bricks help reduce waste and comply with sustainable building principles, marking an important step towards a cleaner, greener future.

KEYWORDS: *Energy efficient bricks, Sustainability, Casting.*

INTRODUCTION

The global increase in landfill waste, particularly plastic, poses significant environmental and economic challenges due to its longevity and lack of biodegradability. This strains waste management systems and impedes the implementation of effective solutions. Moreover, there is a propensity for easy seepage into the environment, prolonged persistence in the ecosystem, subsequent adverse effects on wildlife through entanglement, and ultimately inadvertent integration into the food chain as microplastics [1]. In 2012, the global waste generation amounted to 1.3 billion tons annually, with projections indicating an increase to 2.2 and 3.4 billion tons per year by 2025 and 2050, respectively [2]. With over million tons of plastic waste generated annually in India alone, the need for innovative solutions becomes increasingly urgent.

Clay-fired bricks remain prevalent in developing nations due to limited access to alternative construction materials, despite their associated social and environmental drawbacks. The environmental impacts related to the energy sources and resources necessary for brick manufacturing are substantial, as they result in direct and indirect consequences throughout supply chains, contributing to key environmental concerns in brick production such as carbon dioxide emissions, water usage, and land utilization [3]. In order to produce them, manufacturers must utilise a significant amount of firewood, which they do by firing old furnaces at temperatures over 900 ºC, which is the standard for developed nations [4]. Because of huge quantities of toxic emissions, brick kilns cause serious health issues [5].

Within this urgency, there is an emergence of creative and sustainable alternatives seeking to transform landfill waste into valuable resources. Among these innovative solutions, a promising one is the creation of bricks using a combination of organic and inorganic landfill waste. With our work, we are presenting an effective substitute for the expensive and rare natural resources clay and sand, which are used in the production of clay bricks, for the safe disposal of landfill wastes. Our objective is to find creative ways to produce energy-efficient brick that is also ecologically beneficial during the production process and for the final application of clay brick products.

LITERATURE REVIEW

The quest for sustainable and energy-efficient brick production has gained significant momentum in recent years, driven by the urgent need to address environmental concerns and reduce the construction industry’s reliance on traditional, resource-intensive materials. One innovative solution emerging from this research is the incorporation of landfill waste into brick production, which not only mitigates waste disposal issues but also enhances the properties of the bricks produced.

Recent advancements in sustainable construction materials have focused on the use of waste materials in unfired earth bricks. According to Mohamed Lachheb et al. (2023), the integration of agricultural and industrial waste materials has significantly improved the physical, mechanical, and thermal properties of unfired earth bricks. Notably, the inclusion of fibres at optimal content levels has resulted in substantial increases in compressive and flexural strength, ensuring the durability and robustness of these bricks. Moreover, these waste materials have reduced the thermal conductivity of unfired earth bricks, enhancing their thermal comfort in residential structures. The use of waste materials as substitutes for clay in brick manufacturing is another promising area of research. Kalaimani Ramakrishnan et al. (2023) investigated the feasibility of using waste materials such as fly ash, quarry dust, marble dust, eggshell powder, and rice husk ash in brick production. The study demonstrated that bricks made from these waste materials performed comparably to traditional clay bricks in terms of compressive strength and water absorption, while also being cost-effective to manufacture.

Prathik Kulkarni et al. (2022) explored the use of High-Density Polyethylene (HDPE) and Polypropylene (PP) in the production of plastic bricks. The study revealed that plastic bricks possess excellent water resistance, reduced weight, and impressive compressive strength, with HDPE bricks outperforming conventional clay bricks. These plastic bricks are suitable for constructing load-bearing walls and have potential applications in civil infrastructure and high-rise buildings due to their lightweight and sturdy characteristics. The improved temperature resistance observed during fire testing further underscores their suitability for diverse construction scenarios.

The transformation of HDPE plastic waste into construction materials, particularly plastic bricks have been investigated by Sabiha Sarwar et al. (2022). The research highlighted the significant environmental impact of plastic waste and the importance of sustainable, eco-friendly practices in the construction sector. The study found that plastic bricks with up to a 35% mixture of HDPE met recommended compressive strength standards, suggesting their potential as reliable load-bearing materials. However, it also identified a crucial threshold of 35% HDPE content, beyond which compressive strength and density decline, advising against their use in high-load situations. This research demonstrates the potential of plastic waste as a valuable resource for sustainable construction, provided that the material proportions are carefully managed.

MATERIALS USED

The materials used to produce bricks include organic waste, plastic waste, clay, sand and red earth as shown in fig. 1.

Plastic waste and organic waste are increasingly utilized to enhance sustainability and performance. Plastic waste, with its durable and non-degradable properties, serves as a significant binder when mixed with clay and water, strengthening the bricks during the heating process. This not only addresses plastic pollution but also contributes to the structural integrity of the bricks. Organic waste, composed of biodegradable materials, aligns with eco-friendly practices by recycling waste and reducing environmental impact. Its inclusion in brick production not only diverts waste from landfills but also reduces the need for conventional raw materials, thereby conserving natural resources. Additionally, the organic matter in the waste can improve the brick's thermal insulation properties, making buildings more energy-efficient. Clay, the primary binding agent, provides essential cohesion to the brick mixture, maintaining its shape during moulding and drying. Sand, particularly river sand, improves workability and plasticity, ensuring proper compaction and moulding. Red earth, rich in iron oxide, adds plasticity and strength, contributing to the overall durability of the bricks. Combined, these materials support the production of durable, sustainable bricks while promoting resource efficiency and reducing reliance on traditional materials.

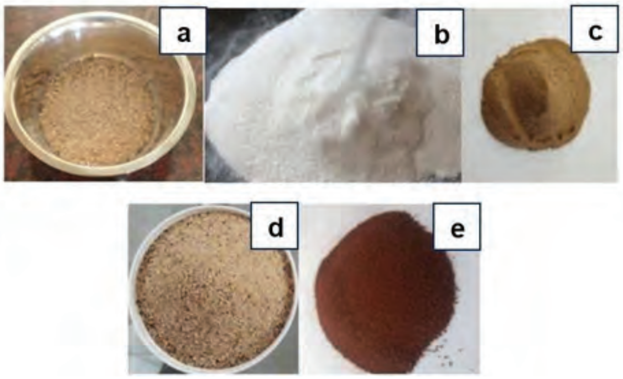

Fig. 1 (a) Organic waste (b) Plastic waste (c) Clay (d) Sand (e) Red earth

EXPERIMENTAL PROCEDURES

Initially, the main components like clay, sand, red earth, organic waste, and plastic waste needed for sample casting are gathered, made into fine powder and then sieve analysis is carried out. Only materials passing through a 600µ sieve are used. These components are then blended in dry form based on trial ratios, and the necessary amount of water is added to achieve the correct texture. Table moulding is utilized, with the mixture being placed into moulds sized 9.5cm × 4.5cm × 4.5cm and extruded after surface finishing. The samples undergo three stages of proper drying: first in the shade for 2 days, then under direct sunlight for 3 days, and finally baked in the oven for 24 hours. The brick specimens are subsequently assessed for compressive strength, and standard-sized bricks (19cm×9cm×9cm) are fabricated using hydraulic compression of 10 MPa for composition that attained increased strength. Ultimately, both compressive strength and water absorption tests are performed on the standard-sized bricks to assess their quality and designation, determining their suitability for various applications.

RESULTS AND DISCUSSIONS

Effect of temperature

The effect of temperature on the compressive strength properties of the bricks was examined by varying the temperatures from 160°C to 200°C, with an oven drying duration of 24 hours as shown in Table 5.1. This range was selected to determine how different heating conditions influence the structural integrity of the bricks. The experiment was conducted using a composition consisting of 90% clay, 5% plastic, and 5% organic waste of the total weight, combined with the required water content.

Table 1 Mix proportion 1

Sample	Temperature (ºc)	Compressive Strength (N/Mm²)
A	160	3.21
B	170	3.58
C	180	3.66
D	190	3.72
E	200	3.89

These results indicate that higher temperatures within the range tested improve the compressive strength of the bricks. This suggests that increasing the heating temperature enhances the bonding and cohesion within the brick material, leading to stronger and more durable bricks. The optimal temperature for achieving maximum compressive strength in this study was 200°C, where the highest strength of 3.89 N/mm² was observed.

Effect of sand

The effect of sand was studied by substituting a portion of the clay composition in the brick mixture. The mix proportion in Table 2 outlines various compositions of clay bricks, each denoted by a sample letter (A, B, C, D). The composition is represented as a percentage of different materials including clay, sand, red earth organic waste and plastic waste. As the clay content decreases from A to D, there's a corresponding increase in sand content, while other constituents remain relatively constant. All samples undergo firing at a temperature of 200 ºC, providing a standardized condition for comparison.

Table 2 Mix Proportion 2

Sample	Clay (%)	Sand (%)	Red Earth (%)	Organic Waste (%)	Plastic Waste (%)
A	70	10	10	5	5
B	60	20	10	5	5
C	50	30	10	5	5
D	40	40	10	5	5

Mix optimization

Compressive strength tests were conducted for all four mix proportions in accordance with IS 3495 (Part 1): 1992 to select the ideal mix proportion for casting standard sized bricks and the results of compressive strength test are shown in Table 3.

Table 3 Compressive strength results

Sample	Compressive Strength (N/Mm²)
A	3.9
B	4.2
C	4.52
D	3.78

The highest compressive strength among the four samples was achieved with Sample C, featuring a mix ratio of Clay: Sand: Red earth: Organic waste: Plastic waste = 5:3:1:0.5:0.5. The reason for increase in compressive strength along with increase in sand content up to 30% and decrease in compressive strength with further increase in sand content is due to a reduction in the cohesiveness of the mixture, resulting in weaker bonds between particles. Therefore, sample C has been selected as the ideal mix proportion for standard-sized bricks.

Casting of brick of standard size

After achieving a compressive strength of 4.52 N/mm^2 with a material mix that contains 30% sand and mix proportion of C: S: RE: OW: PW = 5:3:1:0.5:0.5, a standard brick of size 19 cm × 9 cm × 9cm was fabricated using the same composition and is shown in fig 2. This was accomplished by applying a compression force of 10 MPa using a hydraulic pressing machine to ensure thorough pressing eliminate voids and to increase the compressive strength. Additionally, a control brick was also casted for comparison purposes. Required amount of water was added for the correct mixing. The samples undergo three stages of proper drying: first in the shade for 2 days, then under direct sunlight for 3 days, and finally baked in the oven for 24 hours at 200 ºC.

Fig. 2 Standard sized brick

Compressive strength

Table 4 shows the compressive strength test results of standard sized bricks.

Table 4 Compressive strength results

Sample	Compressive Strength (N/Mm²)
Control brick	8.3
A	8.12

The results indicate that the compressive strength has increased to 8.12 N/mm², meeting the strength requirement for a second-class brick as per IS 1077:1992. This increase was observed when hydraulic compression of 10 Mpa was applied in combination with the addition of 30% sand, which was found to be the optimal percentage for enhancing strength.

Effect of air curing

Bricks were cast to standard brick size, with a hydraulic compression of 10 MPa applied during casting. Control bricks were also cast for comparison. After casting, the bricks were left to air dry for 7 days before undergoing 24 hours of oven drying at 200ºC. The composition, consisting C: S: RE: OW: PW = 5:3:1:0.5:0.5 remained consistent throughout the process. The compressive strength and water absorption tests were conducted further.

Compressive strength

Table 5 shows the compressive strength test results of standard sized bricks which were air cured for 7 days.

Table 5 Compressive strength results of air cured bricks

Sample	Compressive Strength (N/Mm²)
Control brick	8.48
A	9.2

The higher compressive strength of Brick A (9.2 N/mm²) compared to the control brick (8.48 N/mm²) can be attributed to several factors. Firstly, the application of hydraulic compression during casting likely contributed to denser packing of particles within the brick matrix, resulting in improved structural integrity. Air curing has enhanced bond formation due to the reaction of organic particles, further strengthening the brick. Additionally, the incorporation of plastic and organic components in Brick A's composition has enhanced its cohesion and strength properties, leading to the observed increase in compressive strength. Consequently, the combined effects of hydraulic compression during casting, air curing, and the modified composition result in Brick A exhibiting compressive strength characteristic of second-class bricks, surpassing that of the control brick.

Water absorption test results

In order to identify the class of the brick samples, water absorption test for this proportion was checked. Three samples corresponding to the proportion that yielded the maximum compressive strength were hours of immersion in water. Table 6 represents the results of water absorption test.

Table 6 Water Absorption Test Results

Sl. No.	Initial Weight (gm)	Final Weight (gm)	Water Absorption (%)
1	1533	1815	18.4
2	1531	1808.1	18.1
3	1534	1815.18	18.33

The obtained value of water absorption for the sample is 18.22%.

RECOMMENDATIONS FOR FUTURE RESEARCH

Future research should explore a wider variety of waste materials, including different plastics and industrial by-products, to find optimal combinations for brick production. Long-term durability and real- world performance tests are essential to ensure structural integrity and weather resistance. Optimizing hydraulic compression methods and investigating various curing techniques can enhance brick strength. Comprehensive life cycle assessments will evaluate the environmental impact compared to traditional methods. Economic viability studies are needed to compare costs and benefits. Additionally, research on thermal performance and structural applications will highlight the potential for energy-efficient construction. Developing standardized guidelines and understanding the environmental impact of waste collection will support broader adoption in the construction industry.

CONCLUSIONS

Proposed method for the manufacturing of energy efficient bricks using landfill waste introduce an effective means for waste disposal. This work is an attempt to introduce an innovative production method for the manufacturing of clay brick so as to reduce the firing temperature required in the brick kiln from 1000 ºC to about 200 ºC. It is done in order to reduce the amount of fuel required to be burned in the kiln thereby reducing the harmful effects of air pollution on the environment and also to adopt an alternative for the efficient disposal of landfill waste. In this work, partial replacement of natural resources like clay and sand by landfill wastes such as organic and plastic waste with varying proportions were done. The maximum value of compressive strength results was obtained as 9.2 N/mm^2 for the air cured brick of proportion C: S: RE: OW: PW = 5:3:1:0.5:0.5 by casting standard size bricks with the application of hydraulic compression of 10 Mpa.

The test for water absorption of the sample conducted as per IS: 3495-part 2-1992 also showed positive results. The value of water absorption value was found to be 18.22 % which is falling under second brick category. These results show that the samples comply with the specification of second-class bricks category and can be used in boundary walls and load bearing and non-load bearing structures. The long-term strength and fire resistance of the brick are beyond the scope of this work. Additionally, the cost of these bricks will be less compared to conventional bricks, making them a more economical option.

Thus, this work features on the production of cost effective, energy efficient and environmentally friendly brick units which will be a new aspect to reduce landfill volume and revolutionize the clay brick manufacturing sector in India. Additionally, greater variations in the types of materials used, hydraulic compression given, curing time, raw material ratios and temperature are recommended in further research.

ACKNOWLEDGEMENT

The authors would like to express their sincere gratitude to Dr. Mary Lissy P. N., Professor and Head, Department of Civil Engineering, Muthoot Institute of Technology and Science, Varikoli, for her valuable guidance, encouragement, and constant support throughout the course of this research work.

REFERENCES

1. A.M. Ragossnig and P. Agamuthu, 2021. Plastic waste: Challenges and opportunities. Waste Management and Research 39(5): 629-630
2. T. Kumari and A.S. Raghubanshi, 2023. Waste management practices in the developing nations: Challenges and opportunities. Waste management and Resource Recycling in the Developing World: 773-797
3. K. Islam, M. Motoshita, and S. Murakami, 2023. Environmental sustainability of bricks in an emerging economy: current environmental hotspots and mitigation potentials for the future. a. Sustainability 15(6):5228
4. L. Mbumbia, A.M. De Wilmars, and J. Tirlocq, 2000. Performance characteristics of lateritic soil bricks fired at low temperatures: a case study of Cameroon. Construction and Building Materials 14(3): 121-131
5. P.N. Mary Lissy, Carolin Peter, Kavya Mohan, Shone Greens and Sneha George, 2018. Energy efficient production of clay bricks using industrial waste. Heliyon 4(10)
6. Mohamed Lachheb, Nicolas Youssef and Zohir Younsi, 2023. A Comprehensive Review of the Improvement of the Thermal and Mechanical Properties of Unfired Clay Bricks by Incorporating Waste Materials. Buildings 13: 2314
7. K. Ramakrishnan, V. Chellappa, and S. Chandrasekarabarath, 2023. Manufacturing of Low-Cost Bricks Using Waste Materials. Materials Proceedings 13(1): 25
8. Prathik Kulkarni, Vikas Ravekar, P. Rama Rao, Sahil Waigokar, Sanket Hingankar, 2022. Recycling of waste HDPE and PP plastic in preparation of plastic brick and its mechanical properties. Cleaner Materials 5: 100-113
9. Sabiha Sarwar, Molla Rahman Shaibur, M.S. Hossain, M.R. Hossain, Ishtiaque Ahmmed, F. F Ahmed, A.H. Sarker, A.H. Shamim, 2022. Preparation of environmental friendly plastic brick from high-density polyethylene waste. Case Studies in Chemical and Environmental Engineering 7: 100-291

Fatigue Life Prediction of Concrete Using Artificial Neural Network

Shafiya A
PG Scholar
Department of Civil Engineering
NSS College of Engineering
Palakkad, Kerala
✉ ashafiya2001@gmail.com

Keerthy M Simon
Assistant Professor
Department of Civil Engineering
NSS College of Engineering
Palakkad, Kerala
✉ keerthymsimon@nssce.ac.in

ABSTRACT

Most concrete structures such as airfield pavements and highway, bridge slabs , marine support structures, and machinery foundations undergo fatigue loading throughout their service life. The cyclic load can decrease the life of these structural members immensely. While concrete is a naturally heterogeneous material, it can be approximated as homogeneous for analysis. But its material heterogeneity influences greatly its fatigue life for which it is hard to predict exactly using the conventional deterministic approaches. Hence, Artificial Neural Networks (ANNs) provide a suitable alternative for the fatigue life prediction of quasi- brittle materials such as concrete. This research aims at creating a predictive model based on ANN to precise assess the fatigue life of concrete.

INTRODUCTION

General Background

Upon exposure of materials to cyclic or repeated loading, fatigue is brought about where there is a steady and irreversible change in internal material structures that eventually result in crack formation and fracture. This is most relevant to most infrastructures subjected to intense cyclic loading, e.g., airport pavements, bridge decks, railway sleepers, roads, and offshore windmill support structures. Their life can be significantly reduced by fatigue cracks, and thus the importance of watching for crack growth in structures exposed to fatigue loading has to be emphasized. Depending upon how they fail in fracture, the materials can be classified into three categories: brittle, quasi-brittle, and ductile. Because of the homogeneous state, a brittle material like ceramics and a ductile material like metals exhibit failure in a more uniform way.

Fatigue behaviour of concrete

While the materials are subjected to under repeated loading, fatigue is a process that induces gradual and irreversible changes in materials, ultimately leading to cracking and failure. The phenomenon is most applicable to the majority of infrastructures exposed to severe cyclic loading, such as airport pavements, bridge decks, railway sleepers, roads, and offshore windmill foundation structures. Their life can be greatly reduced by fatigue cracks, and thus the need to take crack growth into account in structures under fatigue loading has to be highlighted. Depending on the manner in which they break, materials are defined as brittle, quasi-brittle, and ductile. As they are homogeneous, brittle materials like ceramics and ductile materials like metals break more predictably.

- Cement
- Aggregate
- Aggregate–Cement Paste Interface

The non-homogeneity of concrete resulted in formation of a very high number of internal defects which leads to the formation of cracks even before loading. Concrete fatigue crack propagation can be classified into three different zones.

- Microcrack formation zone
- Progressive cracking zone
- Sudden fracture zone

Fracture spreads through the weakest zones of the cementitious matrix.

Figure 1 indicates the growth of a crack in three types of materials where the representative growth of the crack in concrete is indicated.

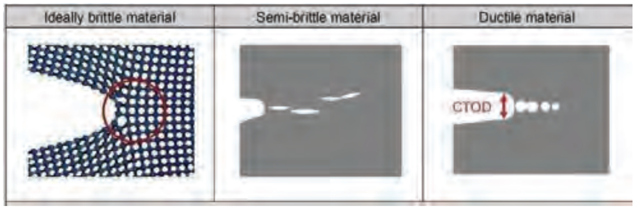

Fig. 1 Crack propagation in three different type of materials (Pippan et al, 2018)

Fig. 2 Fatigue crack on (a) structural component (b) bridge deck pavement (Suryavanshi 2010)

Need for fatigue analysis

Fatigue analysis is imperative for beams due to several reasons:

1. Assurance of Safety: Beams, say in bridges or buildings, are subjected to cyclic loading over their entire lifespan. Fatigue analysis ensures that such beams can sustain constant stressing, which ensures structural safety.
2. Extent of Life Analysis: Fatigue analysis calculates the life of the beam by studying how
3. cyclic loading influences structure strength over time, enabling maintenance and longevity assurance to be planned.
4. Economic Efficiency: Favorable fatigue behavior allows for effective design and choice of suitable materials with maximum efficiency, thereby leading to cost-effective construction and maintenance. Predictive reliability of fatigue life can prevent excessive repairs and replacements, reducing lifecycle costs.
5. Failure Prevention: Fatigue failures would cause failure like bridge collapse. Fatigue analysis avoids such failures by examining potential failure locations so design can be modified or structural components strengthened to avoid such failures.
6. Regulatory Compliance: Many engineering codes mandate fatigue analysis for cyclically loaded structures. Such compliance ensures structures conform to the regulatory code and withstand intended loading conditions throughout their life.
7. Fatigue analysis of beams in real life is extremely essential towards the provision of assurance on safety, durability, cost, and compliance to regulation in structural engineering practice.

Objectives

✓ To develop a prediction system to determine the fatigue life of concrete using ANN

Methodology

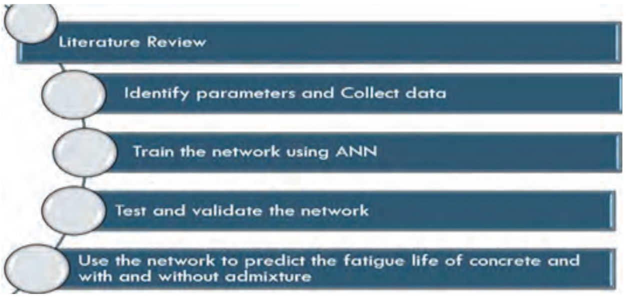

Fig 3 Steps involved in Methodology

- Design a literature overview of concrete fatigue failure mechanisms based on various approaches and the use of artificial neural networks (ANN) to solve complex problems.
- Investigate and supply training and model validation data based on material and fracture mechanics

concrete properties.

- Identify the best neural network configuration using MATLAB 2021a.
- Perform test for model consistency of the model using ANOVA.
- Develop the analytical model based on the rules of extraction of the obtained ANN model.
- Cross-verify the result obtained from ANN architecture and analytical model with existing experimental results.

Artificial Neural Network

A significant computing method utilized for numerous applications such as pattern recognition, statistical modeling, and classification is the artificial neural network (ANN). A key characteristic of artificial intelligence (AI), artificial neural networks (ANNs) seek to replicate human intelligence in robots by simulating the operations of neurons and learning patterns of the human brain to enable machines to learn and develop.

One of the powerful computing techniques applied for various objectives, including the perception of patterns, statistical modeling, and classification, is the artificial neural network (ANN). It is one of the core tools of artificial intelligence (AI), whose objective is to replicate human intelligence in robots. Artificial neural networks (ANNs) replicate the operations of neurons and learning processes of the human brain and allow computers to learn and acquire.

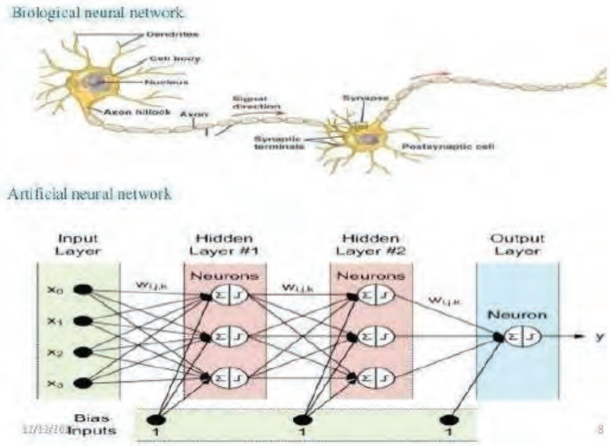

Fig. 4 ANN vs. Biological neural network (Hagan et al 1996)

ANN vs. biological neural network (Fig. 4) (Hagan et al., 1996) Although complex, a biological neural network inherently has three steps: first, it receives, subsequently processes or comprehends the information and feeds back or utilizes feed-forward to make decisions accordingly. An ANN architecture also comprises three stages: input, hidden, and output. The input layer receives the data. the hidden layer sense and process the information and lastly the output layer yields the output. Figure 4 shows the utilization of biological nervous system with ANN. The peculiarity of neural network is that it is not programmed according to task rules so that it is adaptable to solve different types of complicated problems. With ANN, the intricate relationship between inputs and outputs can be represented and can learn the patterns of data. ANN can learn from the provided samples without any prior knowledge to the complex equation. Depending on the problem to be solved, the architecture of ANN can be.

Single Layer Neural Network

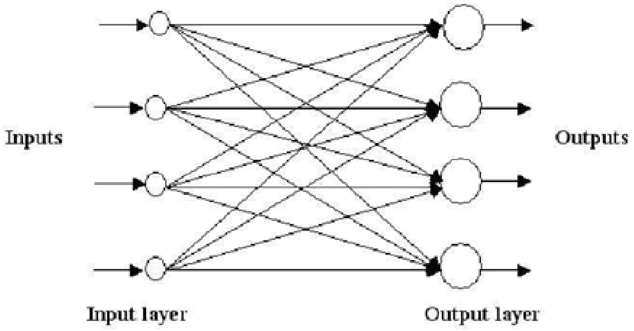

Fig 5 Single-layer perceptron perceptron (Hajela et al 1991)

A single-layer perceptron represents the simplest neural network architecture (SLP). In this, data travels only in one direction, i.e., input to output via an array of weights. This means there will not be any hidden layer. It is also called a single-layer network because there remains a single layer of connections between input and output.

Where d is the difference between the desired output and the predicted output. η is the learning rate (generally < 1), and x is the input vector. In scenarios where the classes are not linearly separable, the training of a single-layer perceptron fails to converge, as it is limited to linear decision boundaries. Where d is desired output - predicted output. η is learning rate typically less than 1 and x is input data. If cases are not linearly separable then learning process will never reach to a point in SLP as it's a linear classifier.

Multilayer Neural Network

A multilayer neural network is built from a single-layer perceptron with one or a few hidden layers. It is the most common network structure to date. In this type of network, every unit is implemented in a layered feedforward structure.

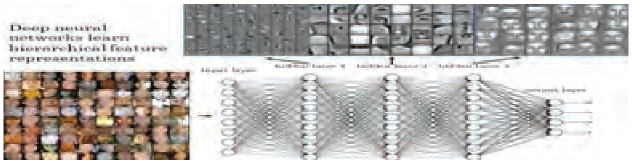

Fig. 6: Deep neural network representation (Hagan et al 1996)

ANN MODELLING

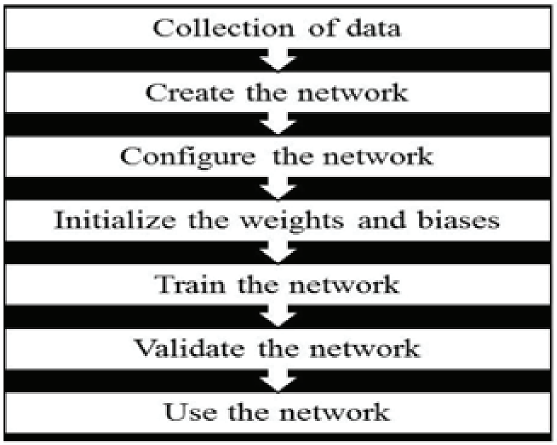

Fig. 7 Steps Involved in Ann Modelling

Table 1: Properties of specimen

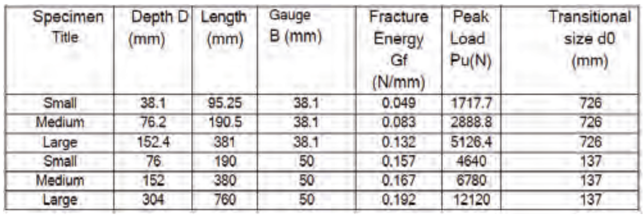

Specimen Title	Depth D (mm)	Length (mm)	Gauge B (mm)	Fracture Energy Gf (N/mm)	Peak Load Pu(N)	Transitional size d0 (mm)
Small	38.1	95.25	38.1	0.049	1717.7	726
Medium	76.2	190.5	38.1	0.083	2888.8	726
Large	152.4	381	38.1	0.132	5126.4	726
Small	76	190	50	0.157	4640	137
Medium	152	380	50	0.167	6780	137
Large	304	760	50	0.192	12120	137

Table 2: Parameters considered for SCC and PCC validation

Input Neuron No	Input Parameter
1	Span (L)
2	Maximum load (Pu max)
3	Thickness (b)
4	Depth (D)
5	Fracture Load
6	No of load cycles (N)
7	Nominal strength
8	Transitional size
9	Brittleness number
10	Tensile strength
11	% of superplasticizer
12	% of Admixture

VALIDATION RESULTS

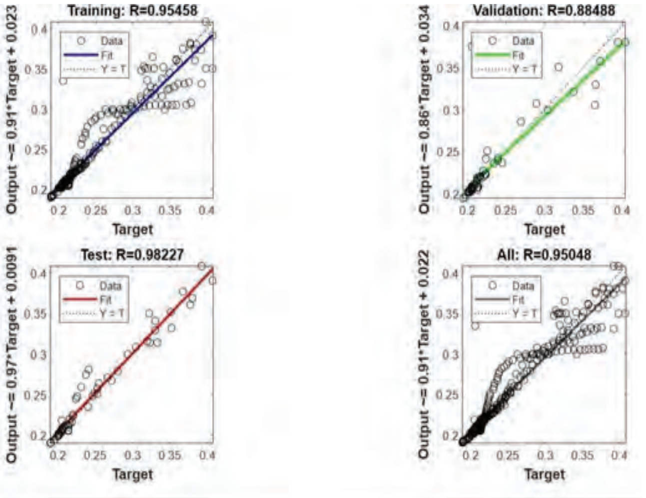

Fig. 8 Regression plots for training, validation, testing, and overall data in MATLAB R2017a

Table 3 All models are assessed using R and MSE values

Size of the hidden layer	Regression value	MSE
1	0.934	0.00044
2	0.935	0.00042
3	0.92	0.0010
4	0.94	0.00045
5	0.93	0.00038
6	0.927	0.009
7	0.89	0.00044
8	0.935	0.00074
9	0.937	0.00055
10	0.89	0.00067
11	0.935	0.0014
12	0.938	0.000209
13	0.938	0.000317
14	0.934	0.00028
15	0.0939	0.00023

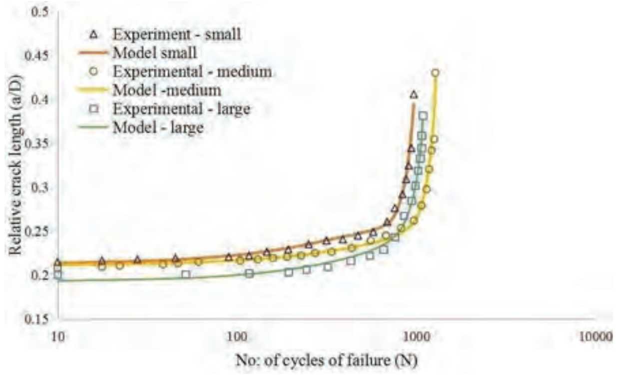

Fig. 9 Evaluation of relative crack length versus cycle count using the analytical model in comparison with Bazant et al.'s experimental findings

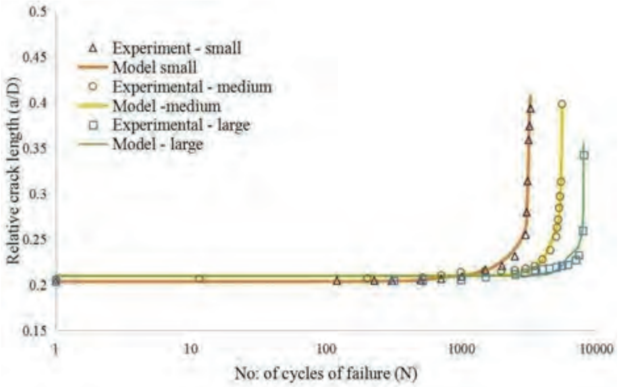

Fig. 10 Evaluation of crack growth behavior over cycles: analytical model predictions compared with Santosh et al.'s experimental data

The experimental research study of Santosh on plain concrete is employed once more in training the ANN model for estimation of the crack length for the model improvement and model calibration for every input parameter. The failure cycles with relative crack length as derived from the neural network model are comparable to the ones derived experimentally as shown in figure 10. In the improved model of the neural network, all the output predictions are all correct with an error that's less than 1%.

ANN Model For Self Compacting Concrete

Self Compacting Concrete (SCC) is a high performance concrete material applied in civil engineering that has the special quality to compact itself through gravity alone, do away with the use of external vibration on placing. It was originally created by Okamura, a Japanese scientist. Unlike normal concrete, SCC has greater fluidity, homogeneity, and stability, so that formwork could be filled up fully even for very dense reinforcement.

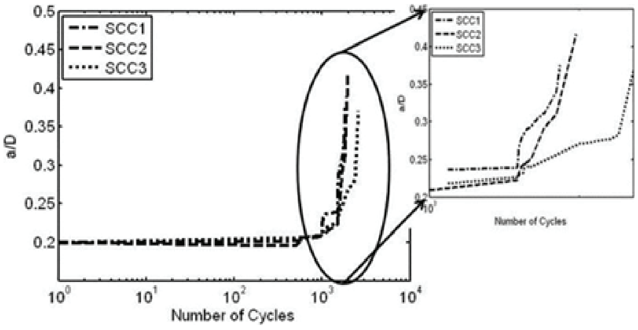

Fig. 11 : Data from SCC Curve

RESULTS AND DISCUSSION

In order to verify the validation of thus derived empirical formula, the same experimental data of self compacting concrete used to verify the validation of Hemalatha's network model [4] is used. There is good agreement between the calculation using empirical formula and experimental data.

Table 4 Results of combined data consist of Bazant-small,large curve, Santhosh-small, large curve,Scc1 and Scc2

Number of hidden nodes	Regression value	MSE
1	0.85	0.00076
2	0.77	0.0008
3	0.92	0.00015
4	0.928	0.0014
5	0.982	0.0000171
6	0.92	0.0026
7	0.926	0.00017
8	0.923	0.000087
9	0.932	0.000021
10	0.93	0.00026
11	0.9192	0.0004
12	0.918	0.0005
13	0.9313	0.00045
14	0.77	0.00012
15	0.92	0.000243

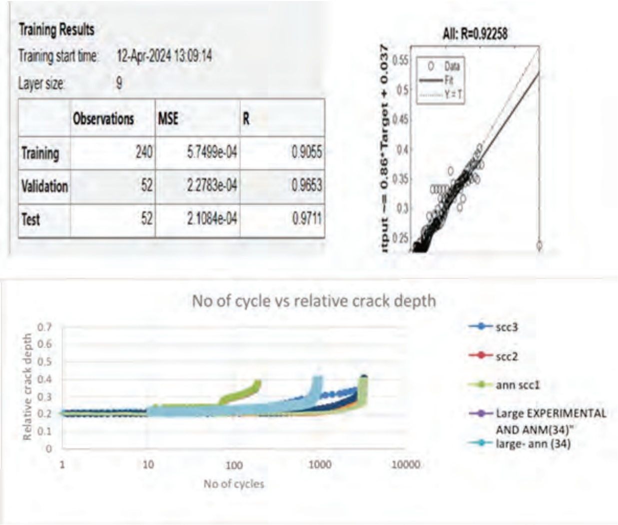
Training Results
Training start time: 12-Apr-2024 13:09:14
Layer size: 9

	Observations	MSE	R
Training	240	5.7499e-04	0.9055
Validation	52	2.2783e-04	0.9653
Test	52	2.1084e-04	0.9711

Fig. 11 combination 1 result

Results of combined data consist of Bazant-small,large curve,Santhosh-small, large curve, Scc1, Scc3-combination 1 Results of combined data consist of Bazant-Medium curve,Santhosh-Medium curve Scc2-combination 2.

Table : 4 Results of combined data consist of Bazant-small,large curve, Santhosh-small, large curve, Scc1.

Number of neurons in hidden layer	Regression value	MSE
1	0.85	0.00076
2	0.77	0.0008
3	0.92	0.00015
4	0.928	0.0014
5	0.982	0.0000171
6	0.92	0.0026
7	0.926	0.00017
8	0.923	0.000087
9	0.932	0.000021
10	0.92	0.00026
11	0.919	0.0004
12	0.918	0.0005
13	0.9313	0.00045
14	0.77	0.00012
15	0.92	0.000243

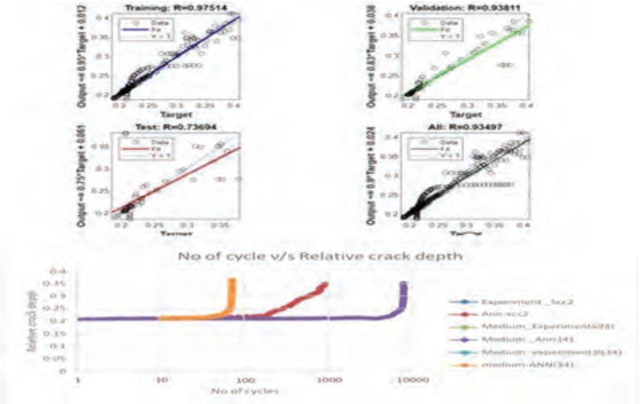

Fig. 12 combination 2 result

CHALLENGES AND LIMITATIONS

- Need for large and high-quality datasets
- Risk of overfitting or underfitting
- Interpretability of ANN results
- Generalizability to unseen conditions

ADVANTAGES OF USING ANN

- High accuracy with nonlinear behavior
- Time-saving compared to experimental fatigue tests
- Adaptive and self-learning capabilities
- Reduced experimental cost

CONCLUSIONS

In this study, the main conclusions are:

- ✓ Developed an ANN model to predict the fatigue life of cementitious material with MSE=0.00021 and R= 0.953 making the model viable
- ✓ Developed an Analytical model to predict the fatigue life of concrete (PCC)
- ✓ Validation is carried out for pcc & Draw a/d vs n graph for experimental & trialdatas similar plots are attained
- ✓ Trained scc datas and obtain the optimum value
- ✓ Because admixture content value added the obtained R^2 Value is 0.999 with minimum MS
- ✓ The fatigue loading behavior is not only a function

of the compressive strength but also of the microstructure of the concrete.

- ✓ Both the combinations gave the same results.
- ✓ Fatigue life to failure increases in SCC3 followed by SCC2 and SCC1 even though all the concretes were loaded with the same pattern. It is because of greater content of powder in SCC3 that results in low porosity and better microstructure
- ✓ Approximately 6000 datas were trained and employed as parameters

REFERENCES

1. A H Rahman, Al-gadhib, M H Baluch, A Shaalan and A R Khan 2000, Damage model for monotonic and fatigue response of high strength concrete, International Journal of Damage mechanics, 9., 57-78.
2. Abhijeet Dey, Ghanashyam Miyani, Arjun Sil 2019, Application of artificial neural network (ANN) for estimating reliable service life of reinforced concrete (RC) structure bookkeeping factors responsible for deterioration mechanism, Soft Computing 13(2)., 1-15.
3. Baluch M, Qureshy A and Azad A 1989, Fatigue crack propagation in plain concrete, Springer New York 16., 80-87.
4. Bazant Z P and Kazemi M T 1991, Size dependence of concrete fracture energy determined by RILEM work-of-fracture method International Journal of Fracture, 51(2)., 121-138.
5. Byung Hwan Oh 1986, Fatigue analysis of plain concrete in flexure, Journal of Structural Engineering, 112., 273-288.
6. C.S.Suryawanshi 2010, Fatigue in concrete concerns security and stability of flyovers,NBMCW, https://www.nbmcw.com/tech-articles/concrete/18265
7. Chandra Kishen J M and Rao P S 2007, Fracture of cold jointed concrete interfaces, Engineering fracture mechanics 74(1)., 122-131.
8. Dong Lei, Pei Zhang, Jintao He, Pengxiang Bai, and Feiping Zhu 2017, Fatigue life prediction method of concrete based on energy dissipation, Construction and Building Materials, 145., 419-425.
9. Hajela P, Berke L 1991, Neurobiological computational modes in structural analysis and design, Computers and Structures, 41., 657–667.
10. Hagan, M.T., Demuth, H.B., and Beale, M., Boston, MA, Neural networkdesign, PWS Publishing Company, 1996.

Analysis of Earthquake Response on Pile Group and Piled Raft Foundation

Meenu M R
PG Scholar
Department of Civil Engineering
NSS College of Engineering
Palakkad, Kerala
🖂 meenumohan1935@gmail.com

Sreelekshmy Pillai G
Associate Professor
Department of Civil Engineering
NSS College of Engineering
Palakkad, Kerala
🖂 sreelekshmypillai@gmail.com

ABSTRACT

The objective of this paper is to analyse and compare the response time history of pile group and piled raft foundation when subjected to earthquake excitation. This analysis aims to investigate the impact of raft interaction with soil on seismic response. Finite element modelling was conducted using ABAQUS software, incorporating appropriate soil properties and dimensional criteria. The models were analysed using the acceleration time history of the El-Centro earthquake. In conclusion, the seismic performance of the piled raft foundation was found to be better than that of pile group foundation based on acceleration response. This suggests that piled raft foundation may offer superior seismic resilience and stability compared to conventional pile foundation under similar seismic forces. Additionally, the study highlights the importance of considering soil- raft interaction effects in seismic analysis, as it significantly influences the overall response of the foundation systems. Furthermore, the findings underscore the potential benefits of using piled raft foundation in seismic-prone regions to enhance overall structural safety and mitigate potential damage.

KEYWORDS: *Seismic response, Pile group foundation, Piled raft foundation, Earthquake excitation.*

INTRODUCTION

Every engineered structure supported by the ground requires a foundation, which serves as an interface element between the structure and the earth. The foundation is a structural system that supports the superstructure of a building and transfers its load directly to the ground. Deep foundations are preferred over shallow ones for transferring large building loads to stable soil. The most commonly adopted deep foundations are pile foundations (Fig. 1), which support massive superstructures like bridges, multi-storied buildings, towers, and dams, particularly when the foundation soil has low bearing capacity.

A pile group is a type of deep foundation, consists of slender columns that transfer the load to a desired depth through either end bearing or skin friction. Piles are typically installed in clusters rather than individually, with the driving of nearby piles affecting the load-bearing capacity of each one. Soil compaction between adjacent piles increases contact stresses and enhances the shaft capacities of piles. The overall load-bearing capacity of a pile group is not merely the sum of the individual capacities of each pile. Instead, it is influenced by factors such as the installation method, ground conditions, pile group arrangement, and the type of cap used.

There are numerous instances where pile foundations suffered either total collapse or severe damage during earthquakes. At the time of earthquake, liquefaction can reduce the confining pressure exerted by surrounding soil on pile foundations, which leads to pile buckling. In such cases, piled raft foundations (PRF) are preferable because they are widely accepted as rational and economical foundations for tall buildings due to their improved load distribution through both the raft and pile components. The peak acceleration levels of PRFs vary depending on site conditions. i.e., buildings with PRF sin side annex cavation may experience higher peak accelerations compared to those with other configurations such as buildings with PRF at ground level. In case of liquefiable soil, vertical peak acceleration gradually increases with decrease in buried depth [5].

A combined system of piles and a raft, where both components share the loads of the superstructure, is termed a piled raft foundation (Fig. 2). By incorporating piles, a raft foundation expands the effective area of support and enhances its ability to withstand lateral forces, thereby improving the foundation's overall performance by increasing its ultimate load capacity and minimizing both settlement and differential settlement. Such foundations are commonly employed for large structures and in scenarios where the soil alone cannot adequately prevent excessive settlement. Piled raft foundations are increasingly favored for tall buildings. In instances where some piles are ineffective, a raft foundation allows for the redistribution of loads to the remaining piles, mitigating the impact of weaker piles on the foundation's overall performance. Typically, the piles primarily contribute to stiffness, while the raft provides additional capacity during ultimate loading conditions. The behavior of PRFs when subjected to lateral and real earthquake loading conditions has not been well understood due to the complexities arising from the interplay among the pile, soil, and raft under various loading conditions. The study aims the comparison of the behavior of pile group and PRF models under El Centro earthquake loading using ABAQUS software.

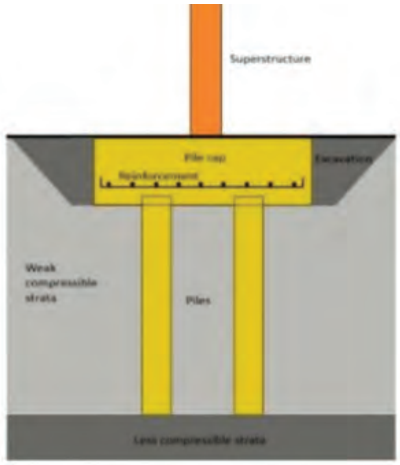

Fig. 1. Pile Foundation

The study aims the analyse of seismic response of pile groups by varying pile diameters and length, the influence of raft thickness on the seismic response of piled raft foundations, and the comparison of piled raft foundations over pile groups through response time history under earthquake excitation. An explicit solver is used in ABAQUS analysis.

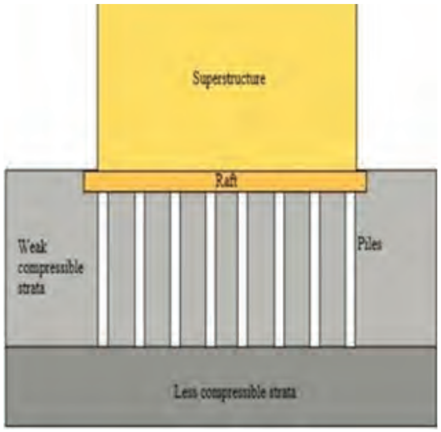

Fig. 2. Piled Raft Foundation

BACKGROUND SUMMARY

The earthquake response analysis on foundation systems, such as pile groups and piled raft foundations, is critical for ensuring the stability and safety of structures subjected to seismic activity. Pile groups consist of multiple piles driven into the ground, typically connected by a pile cap, while piled raft foundations combine piles with a raft (a solid slab) to distribute loads more efficiently. Both systems are widely used in engineering practice to support heavy structures, particularly in seismically active regions.

Understanding how these foundation systems behave under seismic loading is essential for several reasons such as ensuring the integrity of buildings and infrastructure during earthquakes, enhancing design methods to make foundations more cost-effective and resilient, meeting regulatory requirements and improving construction standards. Structures with piled raft foundation will be offering more superior seismic resilience and stability compared to conventional pile foundation under similar seismic forces. The load distribution mechanism between the pile and raft for a high-rise building during an earthquake was analysed, revealing that the kinematic effect is not significantly increase the axial force carried by the combined piled raft foundation (CPRF).However, enhancing the stiffness of the CPRF, significantly affects its ability to absorb more power applied by the earthquake[1] .The behavior of CPRF in seismically active regions is not fully understood because of the complex dynamic soil-pile- interaction. The maximum bending moment occurs at the pile head in homogeneous soil at shallow depths is due to kinematic interaction at the soil interface. The dynamic response of structure, in terms of Peak Ground Acceleration (PGA), is larger than that of the soil and raft [2]. Considering vertical settlement of CPRF, connection rigidity has only a minor influence, but it significantly affects the loads haring by the foundation components [3]. Studies on seismic responses of oblique pile group-soil-structure with different pile caps revealed that the maximum horizontal displacement occurred at the pile top [4]. Under bidirectional coupling earthquake excitations, gradual increase of vertical peak acceleration of liquefiable soil with decrease in depth was reported. It was also reported that for horizontal earthquake excitation the peak strain in the central and bottom of the pile group foundation is larger under bidirectional coupling [5].While analysing the performance of piled raft foundations for a 20-storey building, peak acceleration levels varied depending on the site conditions. Buildings with piled raft foundations inside an excavation experienced higher peak accelerations compared to configurations such as buildings with PRF at ground level. In the case of liquefiable soil, vertical peak acceleration gradually increases with a decrease in depth [6].In shaking table tests, peak acceleration at pile bottom was smaller than the peak acceleration at pile top [7]. At sites with coral sand and Fujian sand, acceleration amplification coefficient increased with a decrease in pile depth. The dynamic bending moment of columns in a coral sand was smaller than in a Fujian sand [8]. Vertical dynamic load sharing decreases with increase in seismic intensity, leading to differential settlement. Compared to a 12m pile, a 20m pile shows greater load sharing capacity and less settlement [9]. Key parameters like pile number, length, diameter, and thickness of raft play a crucial role in the performance of raft foundation. Numerical simulations of a piled-raft Foundation in cohesionless soil using ABAQUS software indicated that increasing pile diameter and length enhances the pile capacity [10].

MODELLING OF THE STRUCTURE

The modelling characteristics are described in this section. The study involves creating models in ABAQUS, assessing the earth quake response of pile and piled raft foundations. Modelling of pile group and piled raft foundation in ABAQUS involves creating 3D representation of the foundation with piles. The depth of soil as well as raft thickness is represented by extruding the sketch to desired depth. Large soil model with 28m depth was used. The piles are placed at the desired locations on the pile cap in case of pile group and on the raft for piled raft foundation. Corresponding material properties such as density, Young’s modulus, poisons ratio, etc. are then applied to the respective foundation types. Fixed boundary conditions are provided. After creating the model, seismic analysis has been performed using ABAQUS software in order to obtain acceleration, displacement and bending moment. The input data used for analysis purpose are shown in Table 1.

Table 1 Unit of Youngs modulus N/m^2

Properties	**Soil**	**Pile**	**Pile Cap**
Mass Density	1529 kg /m^3	2700 kg /m^3	2400 kg /m^3
Youngs Modulus	80×10^{12} N ⁄m^c	70×10^{15} N ⁄m^c	200×10^{15} N ⁄m^c
Poisson’s Ratio	0.3	0.2	0.2

To determine the optimum pile diameter, 3D models of pile groups with varying diameters were generated using ABAQUS software. These models included various pile dimensions, specifically focusing on pile length and diameter. A three-dimensional view of the pile foundation with a fixed pile length of 9 m and varying pile diameters of 0.5 m, 0.6 m, and 0.7 m are shown in Fig. 3, Fig. 4, and Fig. 5, respectively.

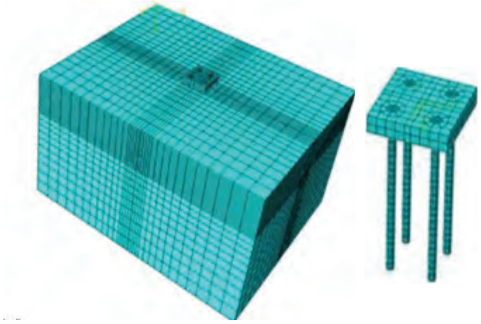

Fig. 3 3D view of pile group modelled with pile length = 9m, pile diameter = 0.5m

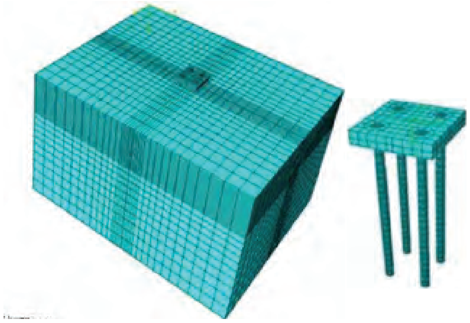

Fig. 4. 3D view of pile group modelled with pile length = 9m, pile diameter = 0.6m

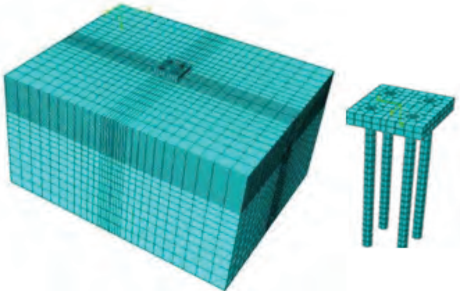

Fig. 5. 3D view of Pile group modelled with pile length = 9m, pile diameter = 0.7m

After analysing the pile group with varying pile diameters, it was observed that, an increase in pile diameter initially, resulted in a decrease in the seismic response experienced by pile group. Hence, pile diameter 0.7m was selected as the most suitable one. In order to find out the most suitable pile length, 3D models of pile group with varying pile length, were generated using ABAQUS software. The analysis has been carried out by modeling pile groups with varying pile length(i.e.,9m,12m,15m) and fixed pile diameter of 0.7m, which was found as the most suitable one in the above procedure. Determining the most suitable length was one of the crucial steps for ensuring the structural stability and performance of the pile group under various conditions, such as loading or environmental factors. By fixing the diameter, the analysis focused especially on the effect of varying pile length on the performance of the pile group. The analysis involved creating three dimensional models of pile groups with different length and then evaluating their performance against fixed criteria or objectives. Three-dimensional view of pile foundation with a fixed pile diameter of 0.7m and varying pile length of 9m, 12m and 15m are represented in Fig 6 through Fig.8.

Fig. 6. 3D view of pile group modelled with pile diameter=0.7m, pile length = 9m

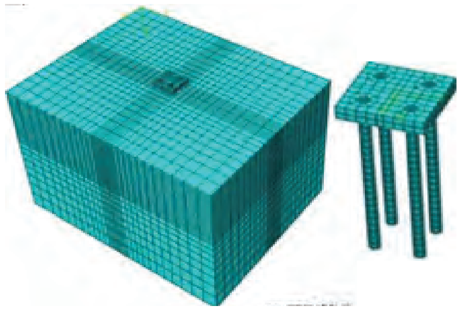

Fig. 7. 3D vew of pile group modelled with pile diameter=0.7m, pile length=12m

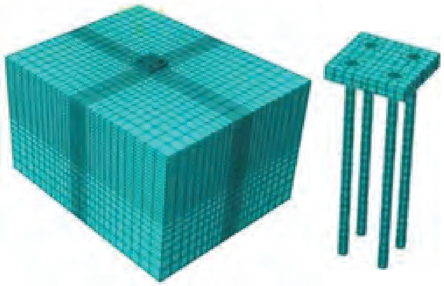

Fig. 8. 3D view of pile group modelled with pile diameter=0.7m, pile length=15m

The seismic response was found to decrease with increase in pile length when the diameter was maintained at 0.7m during the analysis of pile group. So, it can be concluded that, increasing the pile length to 15m, accompanied by pile diameter of 0.7m, seismic response such as peak acceleration, horizontal displacement and maximum bending moment of the pile group reduces. For finding most suitable thickness of raft (Rt), 3D models of piled raft foundation with varying raft thickness were made using ABAQUS software. The most suitable raft thickness was obtained by creating three dimensional models of piled raft foundations by fixing the above derived parameters such as length and diameter of pile, which plays a impactful role in the overall behavior of piled raft system. The length of pile was set to15m and diameter as 0.7m. The three-dimensional modelling of piled raft foundation with varying raft thickness 0.9m, 1.2m, 1.5m are shown in Fig. 9.

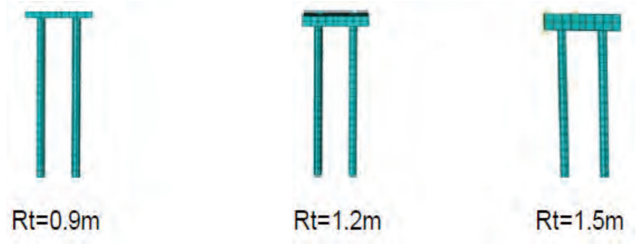

Fig. 9. Piled raft with varying raft thickness

After conducting analysis of piled raft foundations with different raft thickness, while maintaining fixed parameters for pile length and pile diameter (Lp=15m,Dp=0.7m), it was observed that increase in the thickness of the raft resulted in a marginal decrease in seismic response. i.e. Increasing raft thickness from 0.9m to 1.5m made reduction in seismic response of piled raft foundation. This suggest that thicker rafts provide better seismic performance than thinner one, by increases the stiffness and improves the load carrying capacity.

RESULTS AND DISCUSSION

The study focused on the seismic analysis of pile groups and piled raft foundations modelled using ABAQUS software. Initially, pile groups with varying diameters and lengths were analysed. From this analysis, the most suitable pile diameter and length were determined. These optimal dimensions were then used for the analysis of piled raft foundations, with varying raft thickness. The analysis identified the most suitable raft thickness.

Results of seismic analysis of pile groups and piled raft foundation systems are graphically represented.

Earthquake response for varying pile diameter

The results include ea tabulation, shown in Table 2, detailing the earthquake response of pile groups with varying diameters. The analysis illustrates how pile acceleration, displacement, and bending moment change with variations in pile diameter. The variations in seismic response due to changes in pile diameter are plotted in Figure 10.

Table2: Earthquake Response at Top of Pile Cap in Pile Group with Varying Pile Diameter

PARAMETERS		SEISMIC RESPONSE		
Pile length (m)	Pile diameter (m)	Acceleration (m/s^2)	Displacement (cm)	Bending moment (kNm)
9	0.5	21.05	66.07	586.07
9	0.6	19.46	60.7	484.77
9	0.7	17.89	57.33	469.6

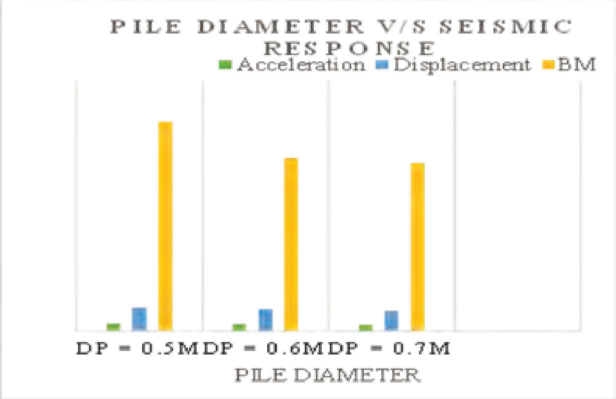

Fig.10.Variation of earthquake response of pile group with varying pile diameter

Decrease in the seismic response of pile group was observed when the pile diameter increases from 0.5 to 0.6 meters. This suggests that larger diameter piles may contribute to reduced vulnerability and improved stability of the pile group during earthquakes. Based on the data presented in Table 2, the most suitable diameter for the piles was determined to be 0.7 meters. This diameter yielded the best seismic response among the range of diameters tested, with peak acceleration, horizontal displacement, and maximum bending moment values of 17.89 m/s², 57.33 cm, and 469.6 kNm, respectively. Therefore, the most suitable pile diameter was determined to be 0.7 meters.

Earthquake response for varying pile length

Understanding the variation in earthquake response with changes in pile length is important. The results, tabulated in Table 3, shows the earthquake response of the pile group with varying pile lengths. The analysis demonstrated how peak acceleration, displacement, and bending moment change with variations in pile diameter. The graphical representation of the seismic response variations due to changes in pile length are shown in Fig. 11.

Table 3: Earthquake Response at Top of Pile Cap in Pile Group with Varying Pile Length

PARAMETERS		SEISMIC RESPONSE		
Pile diameter (m)	Pile length (m)	Acceleration (m/s^2)	Displacement (cm)	Bending moment (kNm)
0.7	9	17.89	57.33	469.6
0.7	12	16.05	50.21	415
0.7	15	14.2	44.25	399

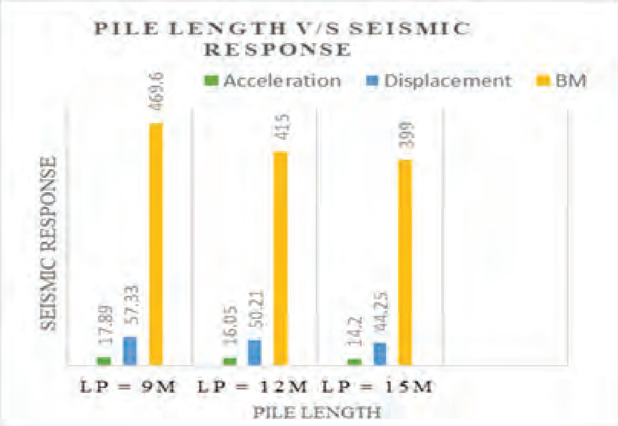

Fig. 11. Variation of earthquake response of pile group with varying pile length

When pile group was analysed, it was observed that increasing pile length to 15m, when diameter was maintained to be 0.7m showed a decrease in seismic response. Based on the analysis of earthquake response data, it can be concluded that increasing the pile length to 15 meters leads to a reduction in the seismic response of the pile group, which means that these parameters contribute in improving the stability and seismic performance of the pile group.

Earthquake response for varying raft thickness

Raft thickness is a critical parameter in the design and performance of piled raft foundations particularly in seismic loading conditions. The thickness of raft influences various aspects of the foundation behaviour, including load distribution, stiffness, and dynamic response during an earthquake. The results include a tabulation as shown in Table 4, showing the earthquake response of piled raft foundation with varying raft thickness. The analysis was done to show how the acceleration, displacement and bending moment changes with variation in raft thickness. The variation in seismic response due to change in raft thickness are plotted on Fig. 12.

Table 4: Earthquake Response at Top of Piled Raft Foundation with Varying Raft Thickness

PARAMETER			SEISMICRESPONSE		
Lp (m)	Dp (m)	Rt (m)	Acceleration (m/s^2)	Displacement (cm)	Bending Moment (kN m)
15	0.7	0.9	12.87	43.62	410
15	0.7	1.2	10.9	41.8	392.01
15	0.7	1.5	9.44	40.51	338

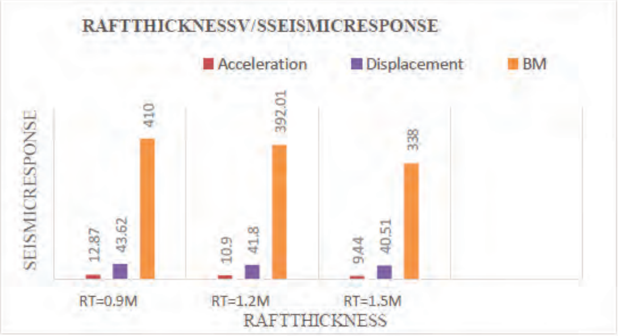

Fig.12.Variation of earthquake response of piled raft foundation with varying raft thickness

After conducting analysis on piled raft foundations with different raft thickness while maintaining fixed parameters such as pile length and diameter (Lp = 15m, Dp = 0.7m), it was observed that increasing the thickness of the raft resulted in a marginal decrease in seismic response. i.e. Increasing raft thickness from 0.9m to 1.5m made reduction in seismic response of piled raft foundation.

CONCLUSIONS

The pile group and piled raft foundations were analyzed by varying pile length, pile diameter, and raft thickness using ABAQUS. The conclusions from the analysis are given below.

- While analysing pile group foundation, it was observed that the seismic response values decreased with increase in pile diameter. When diameter of the pile increased from 0.5 m to 0.7m, the following percentage reductions were obtained from the seismic response. i.e., Peak acceleration, horizontal displacement, maximum bending moment reduced by 15%, 13.2%, 19.8% respectively.
- Similarly, while analysing pile group foundations with different pile length, it was observed that the seismic response decreased. When the pile length was increased from 9m to 15m, the following reductions in seismic response were occurred. i.e. Peak acceleration, horizontal displacement, maximum bending moment reduced to about 20.6%, 22.8%, 15% respectively.
- The analysis thus came into a conclusion that increase in pile length as well as pile diameter reduced the seismic response of pile group.
- When the piled raft foundation was analysed for varying raft thickness say, 0.9m, 1.2m, & 1.5m, there was a slight variation in seismic response of pile draft foundation. There occurs a slight decrease in the seismic response, as the raft thickness was reduced from 0.9m to 1.5m. The percentage reduction in seismic response such as peak acceleration, horizontal displacement, maximum bending moment were 26.65%, 7.13%,17.56%, respectively. Thus, from the selected thickness of raft, the most suitable raft thickness was found to be 1.5m.
- The lateral displacement of the piled raft foundation system was 9% less than that of the pile group.
- The maximum bending moment was reduced to about 15% for piled raft foundation than pile group.
- The seismic performance assessment revealed that the piled raft foundation exhibited better performance compared to the pile group foundation, with an acceleration response of approximately 36% lower than that of the pile group.

REFERENCES

1. AhmedEl-Attar.(2021).Dynamic Analysis of combined pile draft system. A in Shams Engineering Journal, 12(3), 2533-2547.
2. Ahmed M .Ali, Mahdi O.Karkush, and Ala N .Al-Jorany.(2023).Numerical Modelling of connected piled raft foundation under seismic loading in layered soils. Journal of Mechanical Behaviour of Materials, 32(1).
3. Ashutosh Kumar and Deepankar Choudhury.(2017). Loads haring mechanism of combined pile- raft foundation(CPRF) under seismic loads. Geotechnical Engineering journal of the SEAGS & AGSSE, 48(3).
4. Desen Kong, Yifei Bai,Yongpo Chen, and Meixu Deng. (2019).A Study on the Seismic Response Characteristics of an Oblique Pile Group-Soil-Structure with Different Pile Caps. Shock and Vibration.
5. Heng - yuan, De-ling, Chao, and Qi - quan. (2020). Experimental investigation on the dynamic response of pile group foundation on liquefiable ground subjected to horizontal and vertical earthquake excitations. Rock and Soil Mechanics, 41(3), 905-914.
6. Hamid Reza Bolouri Bazaz, Ali Akhtarpour, and Abbas Karamodin.(2021).A Study on the effects of piled-raft foundations on the seismic response of a high-rise building resting on clayey soil. Soil Dynamics and Earthquake Engineering, Vol 145.
7. Jing-bin, Zhong- ju, Yun- xiu, Chuang, Sui- zhu, Cong, Zhen. (2020). Dynamic response of pile foundation under pile-soil-fault coupling effect in meizoseismal area. Rock and soil mechanics, 41(7),2389-2400.
8. Qi Wu, Xuanming Ding, Yanling Zhang, and Zhixiong Chen. (2020). Comparative study on seismic response of pile group foundation in corals and and Fujian sand. Journal of Marine Science and Engineering, 8(3), 189.
9. Shahad Kh. Elias and Moataz A. Al- Obaydi. (2024). Effect of asymmetry piles length on piled raft foundation system under earthquake load. Journal of Engineering and Applied Science, 7(8).
10. ZehraKhan,and Abhishek Sharma.(2023).Numerical simulation of pile draft foundation in cohesionless soil using ABAQUS. Journal of Mining and Environment, 14(4), 1183-1203.

Study on the Suitability of Aluminium Based Water Treatment Sludge for Partial Replacement and Improvement of Subgrade Soil

Akshaya P
B Tech Student
Department of Civil Engineering
NSS College of Engineering
Palakkad, Kerala
✉ akshayasunil212@gmail.com

Amisha Sunil
B Tech Student
Department of Civil Engineering
NSS College of Engineering
Palakkad, Kerala
✉ amishasunilalakkal@gmail.com

Anupriya P C
B Tech Student
Department of Civil Engineering
NSS College of Engineering
Palakkad, Kerala
✉ anupriyapc22@gmail.com

Rejani V U
Professor
Department of Civil Engineering
NSS College of Engineering
Palakkad, Kerala
✉ rejanivu@nssce.ac.in

ABSTRACT

Aluminum-based water treatment sludge (WTS), a residual by-product generated during the purification of drinking water, has long been treated as waste by water management agencies globally. This material is commonly discarded into landfills or aquatic environments without adequate treatment, leading to environmental concerns. Despite the large volumes produced annually, comprehensive studies on its reuse and sustainable management remain limited. The present study evaluates the potential application of aluminum-rich WTS as a partial substitute for natural subgrade soil in road construction. To investigate the suitability of WTS, different proportions of sludge-soil blends were prepared and tested using the California Bearing Ratio (CBR) method. The findings were analyzed to determine the optimal percentage of sludge that enhances the strength characteristics of the subgrade, offering an environmentally responsible alternative to conventional materials.

KEYWORDS: *Water treatment sludge, Subgrade, California bearing ratio.*

INTRODUCTION

With the global population surpassing 8 billion, the demand for clean and safe drinking water has increased significantly. To meet health and safety standards, various water treatment processes are employed, many of which involve the use of chemical coagulants. A major by-product of these processes is water treatment sludge (WTS), which is generally treated as waste and routinely disposed of in the environment. Its global annual production reaches several million tons, posing serious challenges in terms of waste management and economic burden on the water treatment industry.

Currently, landfilling remains the most widely adopted method for WTS disposal. However, this approach is increasingly unsustainable due to high costs, limited landfill availability, and stricter environmental regulations imposed by governments and regulatory authorities. Consequently, there is a growing need to adopt more sustainable and eco-friendly sludge management strategies, such as recycling, reuse, and resource recovery.

Amid growing emphasis on zero-waste practices, the water industry is exploring alternative applications for WTS, particularly alum and iron-based sludges. One promising avenue is the utilization of WTS as a partial substitution for natural soil in geotechnical applications. This not only helps reduce environmental discharge but also contributes to circular economy goals by repurposing waste materials. Incorporating WTS with soil has shown potential to enhance soil index properties and California Bearing Ratio (CBR), indicating its viability in road construction and other civil engineering applications.

This study explores the feasibility of repurposing aluminum-based water treatment sludge in road construction, with an emphasis on performance and sustainability. This involves evaluating the potential of alum sludge, containing aluminium hydroxide, to enhance subgrade soil strength as determined by the California Bearing Ratio (CBR) test.

LITERATURE REVIEW

Several studies have investigated using water treatment residuals and waste materials in road construction to enhance sustainability and waste management. Water Treatment Residue (WTRs) has been found effective in reducing soil porosity and enhancing stability without compromising California Bearing Ratio (CBR) values, potentially reducing road construction costs by 10% and collapse potential by 24.7% (Nazir et al.,2020). Lime sludge and cement have shown promise in stabilizing expansive clay through chemical agents (Phanikumar et al.,2020), while water-treatment plant sludge mixed with lateritic soil remained within suitable geotechnical parameters for construction (Aline et al.,2022). Alum sludge demonstrated significant enhancements in soil strength with a 15% replacement, suggesting its potential as a low-cost soil stabilizer (Samarth et al.,2014). Similarly, aluminium-based water treatment sludge improved geotechnical properties, emphasizing circular economy benefits in road development. These findings collectively highlight the potential of water treatment waste materials for sustainable road construction and waste management. Previous research examined the use of aluminium and ferric sludge in clayey sandy soil and sandy soil for road pavement construction (Fiore et al.,2022), and also explored adding Alum Sludge to black cotton soil to reduce swelling and shrinkage (Samarth et al.,2014) . The present study focus on using locally sourced Red soil and Alum-based sludge from the Thycattussery Water Treatment plant.

METHODOLOGY

The methodology followed throughout the project involved a series of systematic steps beginning with a comprehensive literature review to understand previous research and establish a foundational knowledge base. This was followed by the collection of materials required for the study, including soil and sludge samples. The next step was the determination of solids present in the sludge to assess its suitability for use in soil stabilization. Theindex properties of the natural soil were evaluated and subsequently, tests were carried on soil containing varying percentages of sludge to observe changes in index properties.

The load carrying capacity was assessed through the CBR test on both untreated and sludge-treated soil samples. The strength of the subgrade was further evaluated by conducting CBR tests with different percentages of sludge. Finally, the results were analyzed in detail to establish the optimum sludge content that yields the best improvement in subgrade strength and overall soil performance.

Material Collection

Fig. 1 Water Treatment Plant

Fig. 2 Aluminium Based Sludge

The required amount of locally available soil was oven-dried for 24 hours before the tests were conducted. Aluminium-based sludge was obtained from Thycattussery Water Treatment Plant, Alappuzha (Fig 1). The obtained sludge was in dry pat form(Fig 2) and was subjected to air drying followed by oven drying for 24 hours.

Determination of Solids in Sludge

Solids in water or wastewater refers to the residue left after evaporation and drying at a specific temperature. Total solids are composed of total dissolved solids (TDS) that pass through a filter and persist as non-volatile residue upon evaporation, and total suspended solids (TSS), which are captured on the filter and represent the particulate fraction. Fixed solids are the residue remaining after ignition at 550 degrees Celsius, while volatile solids represent the organic material that vaporizes during this process. TDS encompasses all materials, liquid or solid, in solution or not, that pass through the filter. To determine TSS, the difference between total solids and total dissolved solids is calculated. This involves filtering a sample, evaporating the filtrate in a weighed dish on a steam bath, and then drying the residue until a constant weight is achieved.

Tests on Physical Properties of Soil

Tests were conducted to assess the engineering behavior of soil. Dry sieve analysis, was conducted as per IS: 2720 (Part 4)-1985, to determine particle size distribution. For sludge containing significant fines, wet sieve analysis is used, where the material is washed and sieved through a 75 μm sieve, and the retained gravel fraction is oven-dried and further analyzed. Atterberg's limits are determined as per IS 2720 (Part V and VI) to assess soil consistency based on varying moisture content. The optimum moisture content (OMC), found out using the Proctor compaction test, identifies the water content at which maximum dry density (MDD) is achieved. Additionally, the CBR test was performed on both untreated and sludge-treated soil in soaked conditions to evaluate the load-bearing capacity, providing critical data for pavement design and material selection under various environmental conditions.

RESULTS

Results and discussion focus on Biochemical tests involving the determination of solids in sludge to assess its organic matter content, Wet sieve analysis on Alum sludge, tests for Index properties and Proctor Compaction Testto observe soil behavior with varying percentages of added sludge. Furthermore, CBR test was carried out on soil-sludge mixtures at different dosages to evaluate subgrade strength and identify the optimum sludge content for maximum performance.

Determination of Solids in Sludge

Test for determining the Solids in Sludge was conducted for two samples, Sample 1 which is fresh sludge and Sample 2 which is an oven-dried sludge sample. Results from Table 1 indicated that organic matter is present in the sludge.

Table 1 Results of Solid test for Sludge samples

Parameter	Value(Mg/L)	
	Sample 1	Sample 2
Total Solids	4700	28500
Total Fixed Solids	300	20900
Total Dissolved solids	3350	1100
Total Suspended solids	1350	27400
Total Volatile solids	4400	7600
Fixed Dissolved Solids	0	0
Volatile Dissolved Solids	3350	1100
Fixed Suspended Solids	300	209000
Volatile Suspended Solids	1050	6500

In general, it is advisable to keep organic matter content in soil used for road construction as low as possible to ensure stability, compaction, and durability of the road. Thermal Treatment or heating the subgrade soil can accelerate the decomposition of organic matter and reduce its content. This process is typically used for remediation purposes to improve soil quality for construction or engineering projects.

Test on Index Properties of Soil

The behavior of the subgrade soil was assessed through various laboratory tests.

Dry Sieve Analysis

Sieve analysis is performed and the grain size distribution curve (Fig. 3) is plotted on a semi-logarithmic graph, with sieve sizes represented on the logarithmic scale and the percentage finer on the arithmetic scale. This curve provides a visual representation of the soil's gradation characteristics and helps in classifying the soil based on grain size distribution.

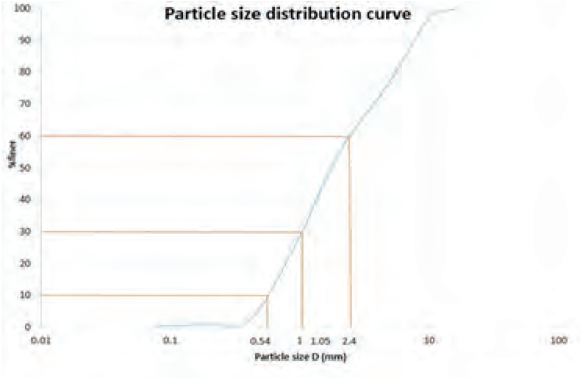

Fig. 3 Particle Size Distribution curve by Dry Sieve analysis

From the grain size distribution curve, the effective particle size (D10) is determined to be 0.54 mm. The particle sizes corresponding to 10% and 30% finer are identified as 1.05 mm and 2.4 mm, respectively. Using the results, the Uniformity Coefficient (Cu) and the Coefficient of Curvature (Cc) are determined as 4.137 and 0.792. Since the Uniformity Coefficient (Cu ≥ 4), the soil is classified as well-graded gravel, indicating a good range of particle sizes conducive to desirable engineering properties.

Wet Sieve Analysis

The Table 2 shows the Particle size (D) in mm and the percentage passing through each of the sieves.

Table 2 Particle Size Distribution Chart (Wet Sieve Analysis)

Particle size D(mm)	%Finer
10	100
4.75	99.72
2	96.7
1	92.4
0.425	86.59
0.212	83.19
0.150	82.19

As shown in Table 3, a significant portion of the material passes through the 75 µm sieve, indicating the presence of fine particles. Therefore, a hydrometer analysis is required to accurately determine the particle size distribution within the finer fraction of the soil.

Atterberg's Limits

Figure 4 illustrates the variation in the liquid limit of red soil with different percentages of added sludge. Correspondingly, Table 3 presents the variation in index properties of red soil with sludge content.

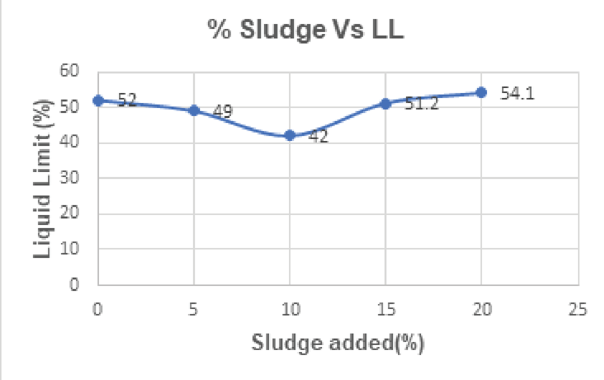

Fig. 4 Sludge added Vs Liquid Limit

It is observed from the graph that the liquid limit initially decreases, then reaches a downward peak, and then increases.

Table 3 Variation in Index properties

Material	LL (%)	PL (%)	PI (%)
Red Soil	52	25	27
Red Soil + 5% Sludge	49	22.86	26.14
Red Soil + 10% Sludge	42	21.26	20.74
Red Soil + 15% Sludge	51.2	30.3	20.9
Red Soil + 20% Sludge	54.1	31.75	22.35

It is observed from Table 3 that the LL, PL, and PI initially decrease, then reach a downward peak, and then increase.

Optimum Moisture Content Determination

A Standard Proctor Compaction Test was conducted to examine the relationship between dry density and water content for both untreated red soil and red soil mixed with varying percentages of sludge. The results, summarized in Table 4, highlight the compaction characteristics for each mix. As illustrated in Figure 5, the optimum moisture content increases progressively with the addition of sludge, indicating the material's higher water-holding capacity and its influence on compaction behavior.

Table 4 Results of compaction test

Sample	OMC (%)	MDD (g/cc)
Red Soil + 0% Sludge	18	1.56
Red Soil + 5% Sludge	20	1.64
Red Soil + 10% Sludge	22	1.6
Red Soil + 15% Sludge	25	1.52

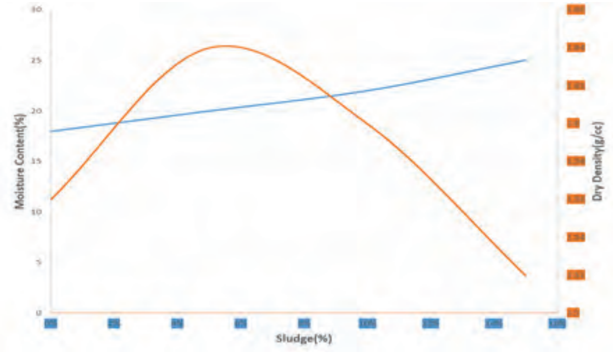

Fig. 5 Optimum Moisture Content and Dry Density Vs % Sludge added

The results indicate that the MDD and OMC for untreated red soil are 1.56 g/cc and 18%, respectively. In comparison, red soil mixed with 10% sludge achieves an MDD of 1.60 g/cc and an OMC of 22%, representing an improvement in compaction characteristics. Among all tested mixes, red soil with 10% sludge exhibits the highest MDD and OMC. As illustrated in the compaction curve, the dry density increases with the increase in sludge content up to 10%, after which it begins to decline. This trend suggests that moderate sludge content enhances compaction behavior, while excessive amounts may adversely affect soil structure and density.

California Bearing Ratio Test

The CBR value was determined for red soil with varying dosages of sludge, and the results are detailed in Table 5 and illustrated in Fig 6.

Table 5 Results of CBR for different samples.

Sample	CBR Value
Red soil	9.37
Red soil + sludge (5%)	11.6
Red soil + sludge (10%)	17.45
Red soil + sludge (15%)	14.8

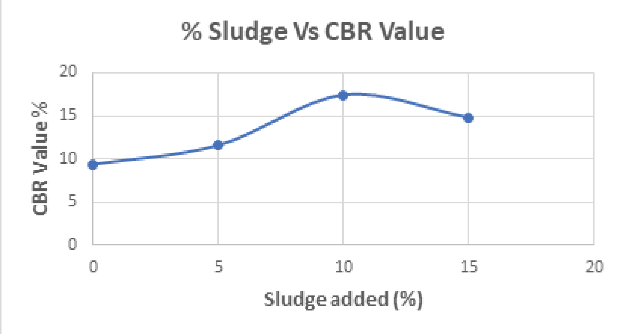

Fig. 6 Sludge added Vs CBR value

According to the findings, red soil mixed with 10% sludge exhibits the greatest resistance to penetration, indicating enhanced strength. The CBR test further confirms that the addition of 10% sludge significantly enhances the soil's load carrying capacity. Specifically, the CBR value increased from 9.37% for untreated red soil to 17.45% with the inclusion of 10% sludge, demonstrating a substantial improvement in strength and performance.

CONCLUSIONS

Currently, sludge generated from water treatment processes is primarily stockpiled or disposed of in landfills, presenting a significant opportunity for resource upcycling. The utilization of this material can contribute to emission reduction, cost savings, and support the water sector in advancing its sustainability goals. In this study, alum sludge samples obtained from the Thycattussery water treatment plant were characterized, and subjected to laboratory tests to assess their potential for use in subgrade layers

- The index properties of soil mixed with sludge—including plastic limit (PL), liquid limit (LL), and plasticity index (PI)—initially decrease, reaching a minimum before gradually increasing with higher sludge content. The trend was confirmed using the Cone Penetration Test.

- Compared to untreated red soil, samples with varying percentages of sludge exhibited higher optimum moisture content and maximum dry density.
- California Bearing Ratio (CBR) tests indicated that adding 10% sludge yielded the best performance, improving the CBR from 9.37% in untreated soil to 17.85% in the treated mix.
- Additionally, pre-treatment methods such as surface drying or oven-drying of sludge were effective in reducing organic matter, thereby enhancing soil durability.

The combination of red soil and aluminium-based sludge provides a viable solution for improving soil strength and its index properties. This approach supports sustainable and cost-effective practices in road construction by aligning with circular economy principles and contributing to net-zero emission targets. The enhanced strength and CBR values achieved through sludge addition make it a promising material for durable and environmentally responsible subgrade applications.

REFERENCES

1. Aline, R., Tejeda, M. E. L., & Gimenez, B. M. E., “Reuse of water treatment plant sludge mixed with lateritic soil in geotechnical works”, Environmental Challenges, 2022, vol. 7, 100465.
2. Fiore, F. A., Rodgher, S., Ito, C. Y. K., dos Santos Bardini, V. S., & Klinsky, L. M. G., “Water sludge reuse as a geotechnical component in road construction: Experimental study”, Cleaner Engineering and Technology, 2022, vol. 9, 100512.
3. Bureau of Indian Standards, “IS 2720 (Part 6): Methods of test for soils – Part 6: Determination of shrinkage factors”, Indian Standards, 1972.
4. Bureau of Indian Standards, “IS 2720 (Part 5): Methods of test for soils – Part 5: Determination of Liquid Limit and Plastic Limit”, Indian Standards, 1985.
5. MoRTH, “Specifications for Road and Bridge Works (5th revision)”, Ministry of Road Transport and Highways, Government of India, New Delhi, 2013.
6. Nazir, A. K., Mahmoud, E., Ali, M., & Ali, N., “Safe and economic disposal of water treatment residuals by reusing it as a substitution layer in roads construction (spectroscopic and geotechnical study)”, Environmental Science and Pollution Research, 2020, vol. 27, 30490–30501.
7. Phanikumar, B. R., & Raju, E. R., “Compaction and strength characteristics of an expansive clay stabilized with lime sludge and cement”, Soils and Foundations, 2020, vol. 60(1), 129–138.
8. Kalburgi, S., Gaidhane, K., Kshirsagar, D., Kasar, P., & Vishwakarma, R., “Soil stabilization by using alum sludge”, Journal of Emerging Technologies and Innovative Research (JETIR), 2014, 1–8.

Experimental Study on Human Hair as A Sorbent for the Removal of Oil From Domestic Waste Water

Farhana Ruby K
UG Student
Department of Civil Engineering
NSS College of Engineering
Palakkad, Kerala
✉ fruby911@gmail.com

Aswin Raj P
UG Student
Department of Civil Engineering
NSS College of Engineering
Palakkad, Kerala
✉ arpalliyath@gmail.com

Ashmil
UG Student
Department of Civil Engineering
NSS College of Engineering
Palakkad, Kerala
✉ ashmilas7994@gmail.com

Praseeda KI
Assistant Professor
Department of Civil Engineering
NSS College of Engineering
Palakkad, Kerala
✉ praseedaki@nssce.ac.in

ABSTRACT

The primary objective of this study is to evaluate the efficacy of human hair in purifying oil-contaminated water, addressing the challenge of excessive human hair disposal in landfills. Human hair emerges as a promising sorbent for treating oily wastewater due to its natural affinity for oils. The research involves systematic collection, cleansing, and thorough drying of human hair samples, along with the artificial preparation of wastewater to simulate real-world scenarios. Through meticulously designed equipment and experiments, the effectiveness of hair in extracting oil from wastewater is investigated, analyzing variations in different parameters to assess their impact on the process. The findings demonstrate that human hair achieves an adsorption efficiency greater than 80-90%. This innovative approach offers a cost-effective and sustainable means to mitigate oil spills, distinguishing itself from prevailing techniques due to its affordability, efficacy, and environment friendly attributes.

INTRODUCTION

The rapid expansion of industries and domestic sewage has led to increased oil- based waste, causing environmental pollution in aquatic ecosystems. Traditional oil removal methods are impractical due to limitations and high costs. Human hair, a prevalent component of municipal waste, can act as a bio-sorbent to extract oil from wastewater due to its natural properties and hydrophobic nature. Studies have shown that human hair outperforms other materials in oil adsorption capacity, making it a cost-effective and sustainable solution.

This paper investigates the adsorbing character of human hair for removing oil from domestic wastewater, examining efficiency, adsorption capacity, and reusability. The study's limitations include its focus on domestic oils, controlled laboratory conditions, and potential variations in human hair samples.

The findings suggest that human hair is a promising solution for oil removal from wastewater, but further research is needed to address the study's limitations and explore its applicability in real-world scenarios.

LITERATURE REVIEW

Understanding the nature of pollutants and their respective treatment requirements is crucial for effective wastewater management and environmental protection. Distinguishing between biodegradable and non-biodegradable pollutants is essential, as they require different biological and physical treatment approaches. The presence of oil and grease in wastewater poses additional challenges, including health hazards and adverse effects on treatability. High concentrations of oil and grease within sewer systems pose a significant risk of clogging and can contaminate water in both emulsified and free forms. This contamination renders the water toxic to aquatic life upon discharge into natural environments.

P. Sasirekha (2018) [1] conducted a study on using natural resources as alternative adsorbents for oil and grease removal. Hamizah Mokhtar et al. (2015)

[3] proposed the use of natural adsorbents for removing oil and grease from wastewater. By utilizing natural materials as adsorbents, this approach offers a potentially cost-effective and environmentally friendly solution to mitigate the impacts of oily wastewater discharge. Wastewater treatment, focusing on the removal of organic matter, inorganic matter, and heavy metals, has emerged as a crucial research area due to the environmental risks associated with the disposal of wastewater into oceans and other water reservoirs. Particularly, wastewater from petroleum-based industries and refineries contains diverse forms of organic matter. Sunil Jayant Kulkarni (2016) [2] highlighted that the ratio of Chemical Oxygen Demand (COD) to Biochemical Oxygen Demand (BOD) serves as a primary determinant in selecting treatment methods.

Human hair exhibits significant promise in mitigating hazardous oil spills across terrestrial and aquatic environments, including motor oils, heating oil, and crude oils. Researchers have investigated the adsorption properties of hair pigments across different colors such as brown, blond, and black. Additionally, studies have been conducted to assess the efficacy of hair in adsorbing oil in affected areas, highlighting its potential as a versatile and effective tool in environmental cleanup effort.

Gautam Kaushik et al. (2004) [4] conducted comprehensive experiments, both at macro and micro levels, to investigate the efficacy of human hair as an adsorbing medium for separating oil from water and observed that the efficiency of oil-water separation increased with higher oil concentrations and narrower bed widths, highlighting the intricate relationship between these parameters and the effectiveness of human hair as an absorbent.

Augustine Osamor et al. (2015) [5] explored the potential of human hair as a natural biosorbent for oil spills, investigating samples from diverse ethnic backgrounds including Asian, European, and African origins. The results revealed intriguing insights into the adsorption performance influenced by factors such as contact time, hair type, particle size, and adsorbent dose. Notably, hair of African origin exhibited remarkable effectiveness, particularly in adsorbing vegetable oil, showcasing its potential as a superior biosorbent for environmental cleanup efforts.

Naniwadekar et al. (2015) [6] proposed a groundbreaking solution utilizing human hair, typically discarded as waste, for the effective remediation of hazardous oil spills. They delved into the intricate science behind the interaction of molecules and atoms with solid surfaces, distinguishing between chemical bonding (chemisorption) and physical bonding (physisorption).

Ankush Gupta (2014) [7] leveraged the high oil affinity of human hair for oil- water separation, particularly in coastal cleanup efforts in America. Booms and mats made from human hair effectively recover spilled oil, with the recovered oil reaching up to 98%. This method offers sustainability as the oil-soaked hair can be reused numerous times. Moreover, human hair's ability to separate emulsified oil in water, a costly process using other methods, further highlights its efficacy in removing oil-containing effluents from waste water.

Nitin W. Ingole et al. (2014) [8] conducted a study on the removal of oil from wastewater using human hairs, both from men and women, through batch and column experiments. They investigated the adsorption behavior by analyzing the effects of pH, contact time, and adsorbent doses. Interestingly, they observed that the oil removal rate increased as the pH decreased, with maximum removal achieved at pH=1.0 and a temperature of 30 degrees Celsius.

The conventional methods for removing oil from water are not only costly but also time-consuming. However, utilizing human hair for this purpose presents a sustainable alternative. In a study by Akpevwe Kelvin Idogun et al. (2016) [9] hair samples were collected from diverse geographical regions - African, Asian, and European - and tested for their adsorption capacity against three types of oils: vegetable oil, crude oil, and diesel. The research revealed that African hair exhibited the highest adsorption capacity, followed by Asian and

European hair. The study also evaluated the reusability of human hair for oil sorption, demonstrating promising results.

METHODOLOGY

Materials required for the experimental study include human hair (minimum size of 2-3 inches), various oils (coconut oil, sunflower oil, palm oil), and mosquito net. Samples of human hair were collected from nearby saloons periodically. The collected human hair samples underwent a cleaning process where they were washed with boiled water mixed with washing powder and then thoroughly dried for sorbent preparation.

For the sorbent medium, approximately 50 grams of cleaned human hair samples were packed inside a cover made of black mosquito net with a diameter of over 90 mm. The net was cut into a circular shape, and the ends were stitched with black thread before being inverted to pack the hair inside the net. (Figure 1).

Domestic wastewater with an oil content ratio of 1:10 was prepared by mixing 250 milliliters of water with 25 milliliters of domestic oil. Major domestic oils such as coconut oil, sunflower oil, and palmolein oil were used for sample preparation.

To facilitate the study's objectives, a complete experimental equipment setup was required and prepared for conducting column tests of adsorption over batch tests.

For determining the amount of oil adsorbed on the sorbent bed, two methods were employed: the Density Method and the Oven Dry Method.

Fig. 1: Prepared sorbent medium for experiments

The Density Method involves measuring the density of the water sample to assess its purity or contamination levels. By comparing the density of the influent and effluent samples, the quality change in the water sample can be analyzed.

The Oven Dry Method utilized to determine the moisture content. The water content present after passing the influent through the sorbent medium can be eliminated by oven drying the sorbent bed for about 10-12 hours at a temperature of 100-150 degrees Celsius.

EXPERIMENTS

Distilled water was initially used to check the feasibility of the experimental idea, resulting in blank observations and results, indicating that human hair can efficiently serve as a sorbent medium for removing oil from domestic wastewater.

Fig. 2: Developed experimental setup

The efficiency of three different domestic oils (coconut oil, sunflower oil, palmolein oil) in adsorbing to human hair was studied. The results presented in this study identify the type of oil that can be removed using human hair as a sorbent and to what extent.

The adsorbing character of human hair with varying amounts of sorbent dosage was analyzed. This analysis involved conducting experiments with a single sorbent bed in the first stage and then introducing dual and triple beds in subsequent stages to observe variations in adsorption efficiency.

The pH level of domestic wastewater can vary, so it's essential to study the characteristics of human hair as a sorbent medium for both acidic and basic water samples. Two wastewater samples were prepared with NaOH and H2SO4 solutions to create basic and acidic samples, maintaining pH values of 8 and 4, respectively.

The reusability of the sorbent medium was evaluated to enhance its efficacy and sustainability. Sorbent beds used in previous efficiency tests were subjected to washing and non-washing methods to assess their reusability over multiple cycles of experiments. The sorbent beds were cleaned, dried, and reused for subsequent cycles to evaluate their performance without cleaning between cycles.

RESULTS AND OBSERVATIONS

The experimental study on the feasibility of using human hair as a sorbent medium for removing oils from domestic wastewater yielded significant findings. The study confirmed the feasibility of using human hair as a sorbent medium, with human hair showing greater adsorption characteristics towards sunflower oil compared to coconut oil but less than palmolein oil. In a 1:10 ratio of water to domestic oil, human hair exhibited varying efficiencies in removing different oils from wastewater. Sunflower oil showed the highest efficiency (90.78%), followed by palmolein oil (85.248%), while coconut oil exhibited the least efficiency. (Figure 3)

Increasing the number of sorbent beds resulted in enhanced adsorption, with maximum efficiency (97.88% in sunflower oil) achieved through maximum three number of sorbent beds. (Figure 4)

pH variations in wastewater promoted favorable conditions for adsorption, with human hair showing higher efficiency towards basic solutions (81.84%) compared to acidic solution (79.4%). (Figure 5)

The study revealed that palmolein oil demonstrated better efficiency up to 88.124% towards reusability compared to other oils, with efficiency increasing when reused without further cleaning. Conversely, coconut oil exhibited decreasing efficiency upon reuse. (Figure 6)

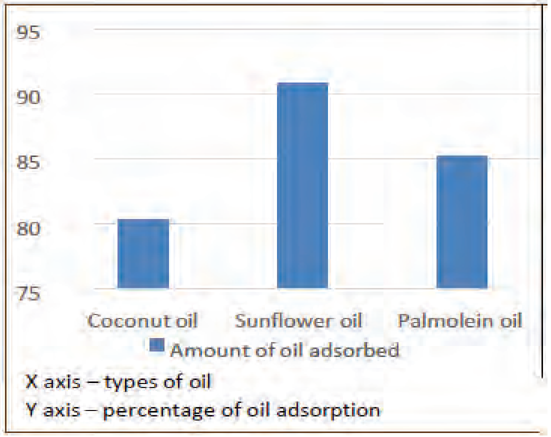

Fig. 3 Percentage of oil adsorbed for different types of oils

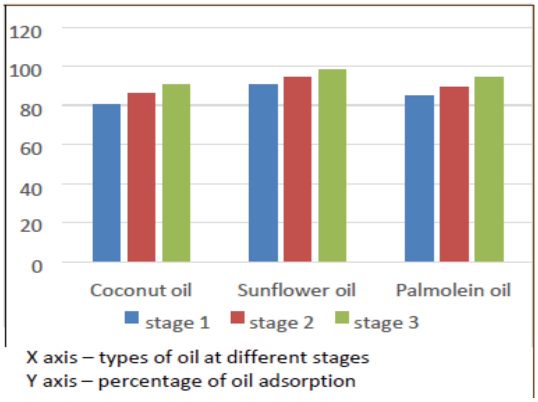

Fig. 4 Percentage of oil adsorbed for increasing number of sorbent beds

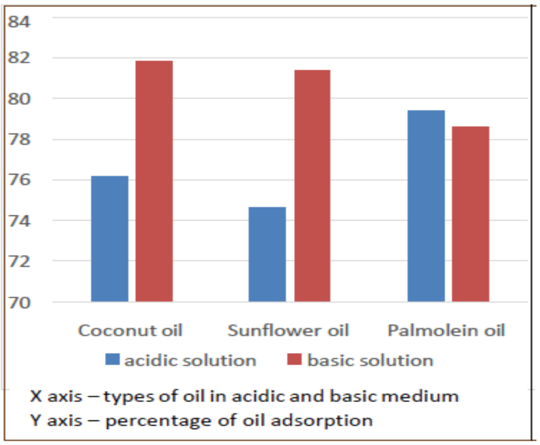

Fig. 5 Percentage of oil adsorbed for variation in pH of waste water

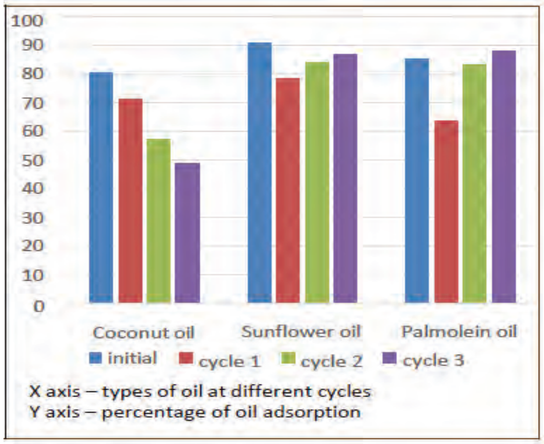

Fig. 6 – Percentage of oil adsorbed for reuse of sorbent beds

In summary, the experiments underscored the potential of human hair as a sustainable and effective sorbent medium for oil removal from domestic wastewater. The findings not only validate the feasibility of this method but also highlight the importance of sorbent dosage, adsorption characteristics, and reusability considerations for practical applications in wastewater treatment. Further research and innovation efforts are warranted to fully realize the potential of this eco-friendly approach in addressing the challenges of wastewater treatment and environmental conservation.

RESULT ANALYSIS

Sunflower oil showed better adsorption results compared to other oils, possibly due to its higher polarity and unsaturated fatty acid content, which increase its affinity for water molecules and enhance adsorption. In contrast, coconut oil's hydrophobicity and high saturated fatty acid content may reduce its adsorption in water. The variation in adsorption between sunflower oil and coconut oil may also be attributed to surface tension and fatty acid chain length. Sunflower oil's lower surface tension and longer chain length of unsaturated fatty acids may enhance its adsorption.

Additionally, the type of water used (distilled vs. normal) can impact adsorption, with palmolein oil showing better adsorption in distilled water, possibly due to the absence of impurities and minerals.

From the second experiment of varying sorbent dosage while conducting the experiments, it is clear that more oil can get adsorbed on to the sorbent surface when more amount of sorbent was used.

While analyzing with acidic and basic mediums of water samples, the formation of negatively charged ions in basic medium make a better bond with hair components. And the lower surface tension and interfacial tension between oil and water makes it easier for oil molecules to spread through water and make favourable adsorption. Also, oils are more soluble in acidic medium and this affect the density variation.

While conducting the reusability test, that difference in adsorption between cleaned and uncleaned human hair in three different cycles can be attributed to several factors, for cleaned hair in first cycle, the denaturation of proteins on hair surface leads to loss of their natural structural functions. This can affect the behaviour of oil to hair.

For uncleaned hair, already adsorbed oil can provide a hydrophobic environment that attracts oil molecules again. And they also has a more rough and irregular surface, which provide more sites for oil molecules to interact and adsorb. Reusing uncleaned hair again in the last cycle lead to more increased surface roughness and enhance more adsorption.

FUTURE EXPANSIONS

To further develop the use of human hair for oil-contaminated water purification, future research should focus on:

1. Broader contaminant scope: Include industrial oils, heavy metals, pharmaceuticals, and microplastics.
2. Field trials: Validate laboratory findings in diverse environmental conditions.
3. Hair type variations: Investigate different hair types and their impact on absorption capacity.
4. Scalability and hybrid sorbents: Develop equipment for large-scale application and explore combining human hair with other materials.
5. Molecular mechanisms and regeneration: Study oil absorption mechanisms and sorbent reusability.
6. Environmental impact and economic analysis: Evaluate biodegradability, secondary pollution, and costs compared to traditional methods.

7. External factors: Understand the influence of temperature, humidity, and other environmental factors.

Interdisciplinary collaboration and consideration of circular economy principles will be crucial for advancing practical applications and regulatory acceptance.

CONCLUSION

The experimental study conducted on the feasibility of using human hair as a sorbent medium for removing oils from domestic wastewater yielded promising results. The research demonstrated that this method is indeed feasible, supported by the developed sorbent bed and equipment. Moreover, the study revealed that human hair exhibits greater adsorption characteristics towards sunflower oil compared to coconut oil, albeit less than palmolein oil. In terms of efficiency, the experiments revealed compelling findings. In a 1:10 ratio of water to domestic oil, human hair displayed an impressive 90.78% efficiency in removing sunflower oil from wastewater, surpassing its efficiency for coconut oil (80.324%) and palmolein oil (85.248%). Notably, coconut oil exhibited the least efficiency among the tested oils. Further analysis elucidated the relationship between sorbent dosage and adsorption efficiency. It was observed that increasing the amount of sorbent directly correlated with enhanced adsorption, with maximum efficiency achievable through maximum sorbent dosage (three sorbent beds).

Consistently, sunflower oil exhibited higher adsorption rates compared to the other oils tested. Density measurements indicated significant variations in both basic and acidic solutions due to the presence of adsorbed oil contents. While the density method yielded satisfactory results, the oven dry method showed slight decrements in percentage adsorption, particularly in basic and acidic solutions. Assessing the reusability of the prepared sorbent unveiled some more insights. Palmolein oil demonstrated better reusability results compared to other oils, with efficiency increasing when reused without further cleaning. Conversely, coconut oil exhibited decreasing efficiency upon reuse, suggesting limitations in its removal using the prepared sorbent bed.

In conclusion, the findings not only validate the feasibility of this method but also highlight the importance of sorbent dosage, adsorption characteristics, and reusability considerations for practical applications in wastewater treatment. The comprehensive evaluation of human hair as a sorbent medium for oil removal from domestic wastewater underscores its multifaceted potential as a sustainable and effective solution to mitigate oil pollution. Beyond the laboratory setting, the project's insights pave the way for further research, innovation, and implementation efforts aimed at realizing the full potential of this ecofriendly approach in addressing the complex challenges of wastewater treatment and environmental conservation.

REFERENCES

1. P.Sasirekha (2018), Removal of Oil And Grease From Wastewater By Using Natural Adsorbent, International Journal of Applied Engineering Research, Volume 13.
2. Sunil Jayant Kulkarni (2016), An Insight Into Oil And Grease Removal From Wastewater From Petroleum And Refinery Industries, International Journal of Petroleum And Petrochemical Engineering, volume 2, issue 1.
3. Hamizah Mokhtar (2015), Removal of Oil And Grease From Wastewater Using Natural Adsorbents , Journal Teknologi.
4. Gautam Kaushik (2004), Treatment of Oil Water With Human Hair: A Preliminary Study, International Journal of Chemical Technology, Volume11.
5. Augustine Osamor (2015), Liquid Phase Sorption Characteristics of Human Hair As A Natural Oil Spill Sorbent, Journal of Environmental Chemical Engineering,volume 3, Issue 2
6. Naniwadekar, N.H. Shinde, S.V. Anekar (2015), Study of Adsorption of Oil On Human Hair, International Journal of Advanced Engineering Technology, Volume II, Issue II.
7. Ankush Gupta (2014), Human Hair Waste And Its Utilities: Gaps & Possibilities, Journal of Waste Management , Volume 2014.
8. Nitin W. Ingole (2014), Adsorption of Oil From Wastewater By Using Animal Fur, Journal of Environmental Science, Computer Science And Engineering & Technology ,Volume 3.
9. Akpevwe Kelvin Idogun (2016), A Novel Method For Adsorption Using Human Hair As A Natural Oil Spill Sorbent, International Journal of Scientific Engineering And Research, Volume 7, Issue 8.

Performance Analysis of Sewage Treatment Plant at Men's Hostel, M.A College of Engineering

Anna Rekha Simon
UG Student
Department of Civil Engineering
M.A College of Engineering
Kothamangalam, Kerala
✉ annarekhasimon2002@gmail.com

Jamsheer Abdul Majeed
UG student
Department of Civil Engineering
M.A College of Engineering
Kothamangalam, Kerala
✉ pajamsheer335@gmail.com

Akshara Johnson
UG Student
Department of Civil Engineering
M.A College of Engineering
Kothamangalam, Kerala
✉ aksharajohnson14@gmail.com

Niveditha K S
UG Student
Department of Civil Engineering
M.A College of Engineering
Kothamangalam, Kerala
✉ liyasitharausman@gmail.com

ABSTRACT

Sewage management is critical for maintaining public health and preserving the environment. Sewage Treatment Plants (STPs) are sewage management facilities designed to receive, treat, and dispose of sewage and wastewater. This study focuses on the optimization and analysis of STP at Men's hostel, MACE to enhance its overall efficiency and performance. The study employs a comprehensive approach, combining technologies and process modifications to address challenges and improve treatment outcomes. Through this interdisciplinary approach, the study aims to contribute valuable insights and practical recommendations for the advancement of STPs promoting a more efficient and sustainable framework for wastewater management.

KEYWORDS: *Sewage Treatment Plant (STP), Efficiency, Wastewater management.*

INTRODUCTION

Sewage treatment, often overlooked yet vital, plays a crucial role in maintaining public health and preserving environmental integrity. As populations grow and urbanisation intensifies, the management of sewage becomes increasingly challenging. Sewage typically contains organic materials such as human waste, food scraps, fats, oils, and greases These organic compounds contribute to the biochemical oxygen demand (BOD) of wastewater. The volume of wastewater generated continues to rise, posing significant challenges to water resources and ecosystems. Efficient sewage treatment methods are essential for the preservation of water quality. These pathogens pose significant risks to public health if wastewater is not adequately treated before discharge or reuse. Historically, sewage disposal was a simple affair, which consisted of dumping waste directly into nearby waterways. Human societies struggled with the disposal of waste, often resorting to crude methods that posed grave health risks. However, as societies evolved and became more aware of the detrimental effects of untreated sewage, the need for proper sanitation practices emerged. Despite these advancements, challenges remain in sewage management.

Ageing infrastructure, population growth, urban sprawl, and industrial expansion strain existing sewage systems, leading to overflows, leaks, and pollution incidents. Moreover, emerging contaminants such as pharmaceuticals, microplastics, and personal care products pose new challenges for wastewater treatment. Today, sustainable sewage management is a global priority. Addressing these challenges requires a comprehensive and integrated approach to sewage management, incorporating technological innovation, infrastructure investment, regulatory measures, public education, and stakeholder collaboration. By prioritising sustainable and resilient sewage management practices, communities can mitigate the adverse impacts of sewage on public health, the environment, and socioeconomic well-being. By treating sewage to remove pollutants and pathogens before discharge, sustainable solutions mitigate the adverse impacts of sewage pollution on aquatic habitats, soil health, and air quality. Additionally, sustainable approaches such as wetland restoration, green infrastructure, and natural treatment systems help to enhance ecosystem resilience, carbon sequestration, and climate change adaptation. The main objectives of this study are to analyse and improve the efficiency of STP of Men's Hostel, MACE and also to suggest possible solutions for challenges occurring during working of STP.

BACKGROUND SUMMARY

Analysis of sewage treatment plants are crucial in order to maintain their efficiency. Before and during the initial weeks of analysis of the selected STP, following steps were taken to know about the working condition of the plant.

- Literature Survey: Journals were referred for the purpose of the study. Knowledge was inferred and gained from these journals.
- Site Visit: A visit was scheduled and conducted to the Sewage treatment plant on the Men's hostel premises of MACE, Kothamangalam (fig.1)
- Identification of Problem: When the site was visited, smell was one of the major indicators that led us to believe that the sewage treatment plant was not working properly. Later COD tests were conducted on the samples from the clarifier, which gave a result of 589 mg/l. The COD value was very high, which indicated a huge organic content in the clarifier. This indicated the absence of biological processes at the aeration tank, which was due to the deficiency of aerobic microorganisms.
- Closing of STP for Microorganism breeding: Due to the deficiency in microorganisms, there was a need to culture them. The STP was closed for microorganism breeding, such that sewage was not passed through the plant. This was done when the hostels were producing very less sewage. A large amount of microorganism was supplied to the aeration tank through cow dung slurry.
- Supply of Micronutrients: As sewage was not passing through the aeration tank, there was need for micronutrients for the microorganisms. This was supplied to the aeration tank daily till the MLSS(Mixed Liquor Suspended Solids) test showed a satisfactory result.
- Observation of Microorganism development by MLSS test: MLSS test indicates the microorganism concentration. It is generally taken as the index of the mass of microorganisms in the aeration tank. The sufficient amount of microorganisms is necessary for biological degradation.
- Checking of COD at Clarifier until desirable values are obtained: COD is a critical parameter in determining water quality which represents the degree of organic contamination in water bodies. It is the amount of oxidant consumed during oxidation of organic substances present in water samples. The desirable limit of COD of a water sample that is being released to an inland water source is 250 mg/l.

Fig. 1: Selected STP

DETAILED WORK PROCEDURE

On August 22, 2023, Sewage Treatment Plant was temporarily closed for the purpose of microorganism breeding. 2000 kg of cow dung was purchased on the following day. It was then made into a slurry, sieved and fed into the aeration tank. In the presence of oxygen, facultative bacteria contained in cow dung acts like aerobic bacteria. These aerobic microorganisms will then break down the sewage collected in the aeration tank. On August 25,2023, 1 kg of peanut copra was mixed in 200 litres of water and supplied to the aeration tank at morning 8.00 am. It was done at a slow rate such that the mix was fed into the aeration tank in 12 hours. The same procedure was repeated at 8.00 pm in the evening. Supply of peanut copra was continued for a week in the above mentioned manner (fig. 2).

Fig. 2: Supply of micronutrients

In order to ensure that the desired amount of microorganisms are present in the aeration tank, MLSS test is conducted daily. MLSS stands for Mixed Liquor Suspended Solids. Results of this test give a microorganism index. As per the design criteria, desirable limit of MLSS is 4000 mg/L. In addition to this, 1 litre of sample is taken from the aeration tank in a graduated cylinder and observed for 30 minutes. Floc characteristics are observed and photos and videos of the same are also recorded (fig. 3). After 30 minutes, sludge volume is noted down.

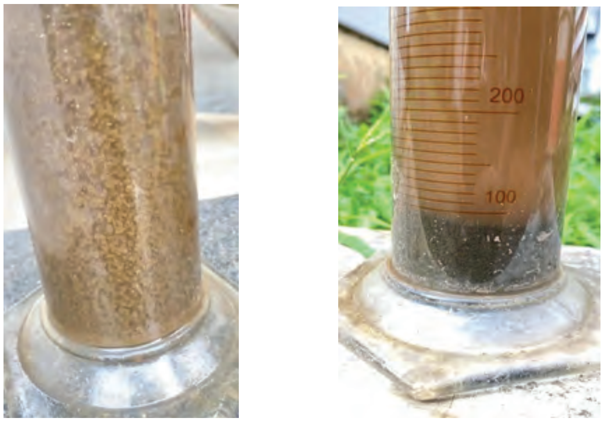

Fig. 3: a) Floc formation **b) Sludge settlement**

On September 18, 2023, STP was reopened. It was recorded as day 1, as we started supplying the sewage to the aeration tank. As mentioned earlier, we collected samples from an aeration tank to conduct MLSS test, observe floc characteristics, and determine sludge volume. This was done daily and whenever any undesirable deviations were found in the test results or floc characteristics, investigations were done to determine the root causes and rectify them. In order to determine the polluting potential of water being released from the clarifier (secondary sedimentation tank), COD test is conducted weekly. For this purpose, samples are collected from the equalisation tank and clarifier. COD values of sample obtained from the equalisation tank gives a measure of the organic and inorganic content present in the wastewater being fed into the aeration tank. The difference between the COD values from equalisation tank and clarifier helps us to know the efficiency of treatment to an extent. As per the general standards for discharge of environmental pollutants into surface waters (The Environment Protection Rules,1986), COD should be less than 250 mg/L.

The initial plan and construction of STP was based on theoretical design. As the plant was completely mixed, in theory the pump carrying effluent from the equalization tank can be provided at any section of the aeration tank. The aeration pumps in the tank would then mix the sewage from the equalization tank with microorganisms, to form flocs and settle. Therefore, the pump carrying effluent from the equalization tank was connected to a section near to the edge of the aeration tank (fig 4), from where the effluent from the aeration tank passes to the secondary settlement tank. From our findings, although the plant was designed as a completely mixed plant, in reality, it did not completely mix with the microorganisms. So, there was a need for redesign. As part of redesign, towards the end of month October, new manholes were opened and other minor construction works were also done. To increase the retention time of sewage at the aeration tank, the pump connecting equalization tank and aeration tank was removed. A new pump was attached which started from the end edge of the equalization tank and connected to the starting edge of the aeration tank (fig 5). This increased the retention time of sewage in the aeration tank and improved the biological processes occurring.

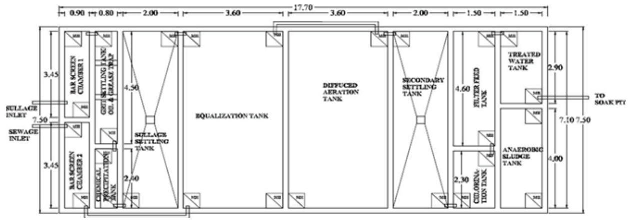

Fig. 4: Sewage Treatment Plant before correction

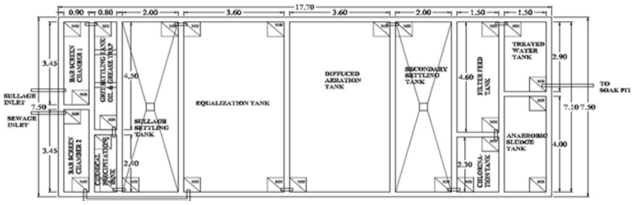

Fig. 5: Sewage Treatment Plant after correction

Due to the existing malfunctioning of the biogas plant and as the biogas produced by toilet waste is very low, the toilet waste from the buildings are directly fed into the sewage treatment plant. The amount of wastewater entering the STP exceeds its capacity during peak hours. The capacity of the STP is 100 KLD which is 100000 litres per day. But the sewage produced in the hostels add up to almost 150 KLD or 150000 litres per day. The Biogas plant is used to reduce the amount of incoming sewage as anaerobic degradation on sewage does take place before the effluent comes to the STP. But because of the existing malfunction of the biogas plant this anaerobic degradation was not taking place. And due to this resulting overloading of STP the microorganisms were not able to degrade the sewage to its potential. So in order to control that, a separate soak pit of capacity 50 KLD was constructed towards the end of December 2023 so that the overflowing sullage water can be fed into it. This was due to the fact that sullage water has less organic contaminants as compared to sewage water.

RESULTS AND DISCUSSIONS

Variation of MLSS per day

Change point 1: Peanut copra was fed into the aeration tank as feed for the facultative bacteria. The micro-organism was present due to the cow dung that was supplied as a slurry. Facultative bacteria acts as aerobic bacteria in the presence of oxygen which was supplied via aeration pumps. Two aerations pumps worked back to back in the tank for efficient working. When the supply of micronutrients i.e, peanut copra were stopped, it caused a drastic reduction in MLSS from 6500 to 1900.

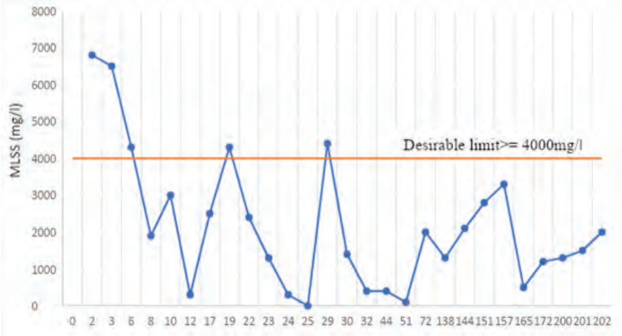

Fig. 6: Graph showing variation of MLSS per day

Change point 2: Although the STP was designed as a completely mixed aeration tank, in the real case it was not the same. Mixing was not uniform throughout. As a result, when we took samples from the aeration tank, it had not undergone proper mixing due to lack of retention time. This led to reduction to MLSS values.

Change point 3: Recirculation pump is the pump connecting the secondary settlement tank back to the aeration tank. It is used to carry activated sludge that is settled at the bottom of the secondary settlement tank. As activated sludge contains aerobic microorganisms that were formed from biological processes at the aeration tank, the sludge can be reused for the biological process. Therefore it is essential to ensure the proper working of the recirculation pump. In this case, the recirculation pump was not reaching the bottom of the secondary settlement tank where the sludge had settled.

Change point 4: The biological process in STP occurs in the presence of oxygen where the facultative bacteria that is present acts as aerobic bacteria. Aeration pumps supply oxygen to the microorganism, allowing them to metabolise and biodegrade organic matter more efficiently. One of the pumps broke down due to excessive heating.

Change point 5 & 6: A blockage in the recirculation pump of a STP can disrupt the flow of wastewater, leading to inefficiencies and potential system failure. Blockages can occur due to various reasons, including accumulation of debris, sediment build up, solid waste clogs, or mechanical failures within the pump itself.

Regular maintenance and monitoring can help prevent such issues.

Variation of COD per day

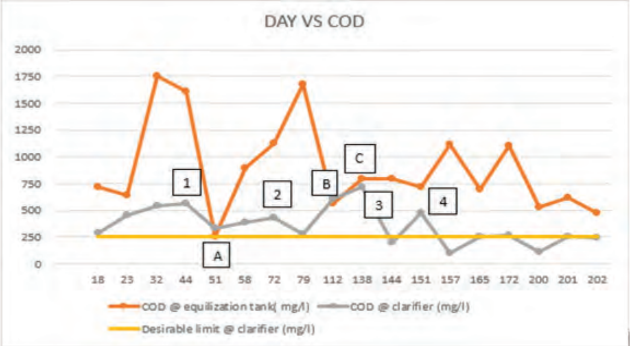

Fig. 7: Graph showing variation of COD per day

Change point 1: Recirculation pump is the pump connecting the secondary settlement tank back to the aeration tank. It is used to carry activated sludge that is settled at the bottom of the secondary settlement tank. As activated sludge contains aerobic microorganisms that were formed from biological processes at the aeration tank, the sludge can be reused for the biological process. Therefore it is essential to ensure the proper working of the recirculation pump. In this case, the recirculation pump was not reaching the bottom of the secondary settlement tank where the sludge had settled.

Change point 2: In an aeration tank, mixing plays a crucial role in facilitating the distribution of nutrients, microorganisms, and dissolved oxygen throughout the tank. Proper mixing ensures that all components are uniformly dispersed, allowing for efficient microbial activity and floc formation. Poor mixing can lead to uneven distribution of chemicals or particles, hindering floc formation. The biological process in STP occurs in the presence of oxygen where the facultative bacteria that is present acts as aerobic bacteria. Aeration pumps supply oxygen to the microorganism, allowing them to metabolise and biodegrade organic matter more efficiently. One of the pumps broke down due to excessive heating.

Change point 3 & 4 : A blockage in the recirculation pump of a STP can disrupt the flow of wastewater, leading to inefficiencies and potential system failure. Blockages can occur due to various reasons, including accumulation of debris, sediment build up, solid waste clogs, or mechanical failures within the pump itself. It's important to identify and remove the blockage promptly to maintain the smoothoperation of the plant and prevent any overflow or backups. Regular maintenance and monitoring can help prevent such issues. One of the major issues faced was the excess amount of sewage that was entering into the STP. A soak pit was constructed to collect the overflowing sullage water from the bar screen chamber.

Change points A,B and C were due to malfunctioning of oven, human error and low volume of dilution respectively.

CONCLUSIONS

Sewage management in itself is an important aspect in maintaining public health, environmental sustainability, community well-being and ecosystem. Activated sludge treatment plant is one of the methods in which a community can maintain healthy environmental management. The STP was monitored and observed for 7 months analysing the working of the selected STP, identifying feasible solutions for possible challenges that can occur, and improving the efficiency of STP. Important conclusions from the analysis are mentioned below.

- The maximum efficiency that was observed was 90.96%. This was observed on day 157. The MLSS value was sufficient that day at 3300 mg/l and the water at the clarifier was clear. This was after soak pit construction which reduced the overloading on the STP.
- Recirculation pump plays a major role in recirculating the sludge from secondary settlement tank to aeration tank. Problems in the recirculation pump can decrease the microorganisms returning to the aeration tank and thereby MLSS value. Major problems observed in the recirculation pump was pump not reaching the bottom of secondary settlement tank and sludge blockage. Regular monitoring and periodic cleaning of the pump is necessary for preventing sludge blockage.
- Aeration pump plays a role in mixing the wastewater and maintaining uniform conditions within the aeration tank. Moreover they supply oxygen to the microorganisms for the biological process. So it is

essential to ensure that the pumps don't overheat and the timer is synced properly.

- Overloading on STP can also lead to microorganisms not achieving their full potential. Therefore it must be ensured that the amount of sewage entering STP is not exceeding its capacity. As the incoming capacity of sewage to the considered STP was large, a soak pit was constructed for the overflowing sullage water.
- Theoretical knowledge can be different from practical cases. In the case study, the STP was constructed as per theoretical knowledge on a completely mixed sewage treatment plant. According to theoretical knowledge, the effluent from the equalisation tank can be supplied anywhere to the aeration tank. But in practice, sewage needs retention time even in completely mixed STP for it to degrade sewage.
- Moreover, continuous monitoring and periodic assessments are crucial for maintaining and enhancing the plant's performance over time. A comprehensive performance analysis not only ensures regulatory compliance but also underscores the plant's role in safeguarding public health and the environment.

REFERENCES

1. Karolinczak, B., Walczak, J., Bogacka, M., & Zubrowska-Sudol, M. (2024). Life Cycle Assessment of sewage sludge mono-digestion and co-digestion with the organic fraction of municipal solid waste at a wastewater treatment plant. Science of the Total Environment, 907. https://doi.org/10.1016/j.scitotenv.2023.167801
2. Monje, V., Junicke, H., Batstone, D. J., Kjellberg, K., V Gernaey, K., & Flores-Alsina, X. (2022). Prediction of mass and volumetric flows in a full-scale industrial waste treatment plant. Chemical Engineering Journal, 445. https://doi.org/10.1016/j.cej.2022.136774.
3. Kesari, K. K., Soni, R., Jamal, Q. M. S., Tripathi, P., Lal, J. A., Jha, N. K., Siddiqui, M. H., Kumar, P., Tripathi, V., & Ruokolainen, J. (2021). Wastewater Treatment and Reuse: a Review of its Applications and Health Implications. In Water, Air, and Soil Pollution (Vol. 232, Issue 5). Springer Science and Business Media Deutschland GmbH. https://doi.org/10.1007/s11270-021-05154-8.
4. Shao, Y., Liu, G. hua, Wang, Y., Zhang, Y., Wang, H., Qi, L., Xu, X., Wang, J., He, Y., Li, Q., Fan, H., & Zhang, J. (2020). Sludge characteristics, system performance and microbial kinetics of ultra-short- SRT activated sludge processes. Environment International, 143. https://doi.org/10.1016/j.envint.2020.105973
5. Blum, K. M., Andersson, P. L., Ahrens, L., Wiberg, K., & Haglund, P. (2018). Persistence, mobility and bioavailability of emerging organic contaminants discharged from sewage treatment plants. Science of the Total Environment, 612, 1532–1542.
6. Quraishi, T., Kenekar, A., Ranadive, P., & Kamath, G. (2018). Evaluation of Performance of Cowdung as Microbial Inoculum in Industrial Wastewater Treatment and its Environmental Implications. Indian Journal of Science and Technology, 11(20), 1–7. https://doi.org/10.17485/ijst/2018/v11i20/122616
7. Gautam, S. K., Sharma, D., Tripathi, J. K., Ahirwar, S., & Singh, S. K. (2013). A study of the effectiveness of sewage treatment plants in Delhi region. Applied Water Science, 3(1), 57–65. https://doi.org/10.1007/s13201-012-0059-9
8. Sundara Kumar, * K, Sundara Kumar, P., & Babu, M. J. R. (2010). PERFORMANCE EVALUATION OF WASTE WATER TREATMENT PLANT. In International Journal of Engineering Science and Technology (Vol. 2, Issue 12).
9. Yan, Shenshen & Sellamuthu, Balasubramanian & Surampalli, Rao & Narasiah, S. & Tyagi, R.. (2007). Isolation, Characterization, and Identification of Bacteria from Activated Sludge and Soluble Microbial Products in Wastewater Treatment Systems. Practice Periodical of Hazardous, Toxic, and Radioactive Waste Management. 11. 10.1061/(ASCE)1090-025X(2007)11:4(240).
10. Gernaey, K. V., Van Loosdrecht, M. C. M., Henze, M., Lind, M., & Jørgensen, S. B. (2004). Activated sludge wastewater treatment plant modelling and simulation: State of the art. Environmental Modelling and Software, 19(9), 763–783. https://doi.org/10.1016/j.envsoft.2003.03.005.

Development of Seaweed Based Bio-Composite Gel for Dye Removal

S. H. Anjali
PG Scholar
Department of Civil Engineering
College of Engineering, Trivandrum
Thiruvananthapuram, Kerala
✉ anjali513499@gmail.com

Sumi S
Assistant Professor
Department of Civil Engineering
College of Engineering Trivandrum,
Thiruvananthapuram
✉ sumis@cet.ac.in

ABSTRACT

Biosorption using natural materials has proved to have remarkable results in mitigating pollutants. Biosorbents developed from certain types of sea weeds are proven to be efficient in the removal of numerous pollutants, mostly dyes. In this study, the potential of a budget-friendly adsorbent processed from seaweed in the removal methylene blue dye from synthetic wastewater has been investigated. Preparation of biocomposite gel using a combination sodium alginate extracted from seaweed and egg shell has been investigated for its efficiency in dye removal. Prepared biocomposite gels were characterized using FT-IR spectroscopy. Various compositions of biocomposite gels were developed and were investigated for the dye removal efficiency. The maximum efficiency of gel without egg shell was found to be 79.37% whereas the maximum removal efficiency of the composite was only 77.56 % at a dosage of egg shell of 0.3g and contact time of 90 minutes. The results of the study indicate that biosorption using seaweed adsorbents can be a promising alternative to the existing technologies in the removal of as dyes from wastewater.

KEYWORDS: *Adsorption; Biocomposite gel, Seaweed; Dye removal.*

INTRODUCTION

Synthetic dyes are utilized in large quantities by many industries. These dyes have toxic nature and turn detrimental to the life of aquatic organisms. Malachite green, methylene blue and methyl orange are dyes commonly seen in wastewater. Adsorption, filtration, precipitation, chemical degradation, photo degradation and biodegradation are the various treatment methods which can be adopted individually or in combination for dye removal. Most of these methods either concentrates the colour into a medium or breaks down the colour molecule by means of chemical reactions. The common dyes used in the textile industries are non-biodegradable in nature and do not break down under aerobic conditions. Synthetic dyes such as azo dyes are manufactured such that they are do not undergo fading due to the attack of chemicals or light-induced oxidation. Hence the breakdown of such dyes under aerobic conditions is not possible. Moreover, high molecular weight and the water solubility of dyes prevent the degradation reactions through penetration of cell membranes. Basic dyes can be isolated from wastewaters by adsorption on to activated sludge. But acid dyes and reactive dyes possess less removal efficiency and hence cannot be effectively removed by activated sludge process. A comparison of various dye removal methods demonstrates that the advantages of biosorption outweigh the conventional dye removal techniques Table 1.

Biosorption

Biomolecules possess the capability to accumulate heavy metals from various media through metabolical or physico-chemical pathways [9]. Such materials can concentrate selected ions or other molecules from fluids and thus, take part in the treatment process. Biosorption is a quick mechanism of passive metal sequestration with the aid of adsorbents which are of biological origin. The process involves both liquid (solvent) and solid (sorbent) phases. In water treatment processes, solvent is normally the water/wastewater which contains the dissolved contaminants or adsorbate which are be eliminated. The higher affinity of the adsorbent for the adsorbate species allows the latter to get attracted and bound to the adsorbent either physically or chemically. This process continues as long as the amount of solid-bound adsorbate components and the portion that remains in the solution becomes equal. The rate of affinity of the adsorbent for the adsorbate controls its delivery between the solid and liquid phases [1]. Biosorbents can be either living cells or dead cells, either in raw form or in chemically modified form. The metal ion uptake by living and dead cells follows entirely different mechanisms.

Table 1. Comparison of various physicochemical methods [10]

Method	Advantages	Disadvantages
Electrodialysis method	Separation selectivity is very high; hence the quality of treated water is good	Membranes require replacement after a fixed number of cycles
Chemical precipitation	Process is cheap and easy to carry out	Sludge contains toxic contaminants. This results in extra expense for sludge handling and disposal
Ultrafiltration/ reverse Osmosis	High separation selectivity	Large amount of wastewater is produced
Membrane filtration	Separation selectivity is very high. The treatment plant can be set up in small space.	Not effective in removal of ions
Adsorption	Cheap and simple method, high efficiency	Separation selectivity is very low. Desorption requires additional processes and expense
Adsorption using biopolymers (Biosorption)	Low cost and high efficiency. Raw materials are easily available and are recyclable.	Biological process improvement has very less chances

Seaweed based biosorbents

Macroalgae, commonly known as seaweeds are natural polymers. They find applications innumerous industrial processes. Seaweeds are ideal candidates as adsorbents for the treatment wastewater [5,6]. The ability of macroalgae to bind pollutants can be attributed to the occurrence of sulphated polysaccharides in the walls of cells. Seaweed based adsorbents can be synthesised to replace the functional activated carbon in effluent treatment [2]. The major concept of extraction, preparation, properties and applications of alginates and its derivatives from brown algal mass has been reported by [3]. Alginate extraction is a time-consuming and complex process which involves the optimization of various process parameters such as the extraction temperature, alkali concentration and solvent concentration for alginate extraction. A study on response surface methodology to optimise the recoverability of the polysaccharide from S. muticum has been reported by [7]. In a laboratory study, the potential of Spongomorpha indica in the removal of Yellow 14 dye from synthetic effluent has been established by characterization studies and isotherm studies [4].

Natural and calcined eggshell have been found to enhance the treatment of strong wastewater through a reasonable uptake of heavy metal ions [8]. The present study attempts to explore the potential of alginate and eggshell powder in dye removal. A biocomposite gel based on sodium alginate – egg shell combination has been prepared and tested for its efficiency in the removal of dye from wastewater.

METHODOLOGY

Materials

Brown seaweed (Sargassum natans) was obtained from Vizhinjam, a natural port situatedin Kerala, India. The seaweed specimens were thoroughly rinsed with distilled water 4 times and dried and stored for further treatments. Eggshells of hen were collected from a local shop. Eggshells were thoroughly washed using distilled water and dried at 105 ˚C and stored for further treatments. Standard dye solutions of 0.1 mg/l were prepared from the solubilization of methylene blue in distilled water.

Preparation of samples

Seaweed specimens were washed thoroughly (Fig. 1. (a)) with distilled water 4 times and were dried for 24 hours. 5 g of dried samples were soaked in 2% formaldehyde for 24 h. The samples were again washed with distilled water and soaked in 0.2 M HCL for 24 hours. In the next step, sodium alginate extraction was carried out using 0.2% Na_2CO_3 solution. Alginic acid produces sodium alginate and solubilizes in the presence of sodium carbonate. The extraction was performed at 60˚C for 3 hours at 100˚C after washing again with distilled water. The sodium alginate was centrifuged using centrifuge by centrifuging for 10 minutes. Then methanol (3 times volume of soluble fraction) was added to the solution for the precipitation of sodium alginate. Sodium alginate obtained was washed with acetone twice and dried at 65˚C. Dried samples were then powdered using pistil and mortar into fine powder. Raw eggshell was rinsed with distilled water and dried at 105˚C for 10 minutes and powdered into fine powder.

1.5 g agar was dissolved in 50 ml distilled water. Various proportions of biocomposite gel (6 samples) were prepared with 10 ml of sodium alginate and varying proportions of egg shell powder (Table 2). The mixture was heated at 100 ˚C for 10 minutes. The mixture was then poured into 6 sterile petri dishes and was allowed to cool. 1cm x 1cm cubes were cut out from these composite gels for treatment as Fig. 1. (b).

Characterization and adsorption studies

The functional groups that make up the composite gels were identified by Fourier transform infrared (FT-IR) spectroscopy. The spectra of different samples were recorded using a Thermo Fisher Scientific Nicolet Is 50 FT-IR Spectrophotometer.

Adsorption efficiency of the composite gel was evaluated using methylene blue (basic dye) and effectiveness of the biocomposite gel in the removal of the dyes was carried out. Effect of egg shell proportion in the composite gel on the removal of methylene blue was investigated by using sodium alginate – egg shell biocomposite gel, while keeping the other parameters constant. Varying dosages of composite gel (6 samples) were added to 20 mL methylene blue of initial concentration 0.1 mg/L and was kept in mechanical shaker at 180 rpm for one and half hours at room temperature and the final absorbance of the dye was measured at maximum wavelength of 668 nm using UV-Visible Spectrophotometer. The optimized dosage of composite gel is the one that gave highest removal efficiency. The composite with optimized dosage was then added to 20 mL methylene blue and the samples were analyzed at specific time intervals for time optimization. The pH was maintained at 6 for the study. The removal efficiency was calculated using the equation as given below and graphs were plotted between (a) Dosage and Efficiency and (b) Contact time and Efficiency.

Removal efficiency = (Ci-Cf)/Ci

were, Ci - Initial absorbance of dye before addition of biocomposite gel and Cf- Final absorbance of dye after the addition of biocomposite gel

Fig. 1. (a) Washed seaweed(b) Sodium alginate gel

Table 2. Composition of biocomposite gel samples

Sample No	Seaweed (ml)	Egg shell (g)
1	10	0
2	10	0.1
3	10	0.2
4	10	0.3
5	10	0.4
6	10	0.5

RESULTS AND DISCUSSION

Characterisation and adsorption studies

FT-IR spectra of pure sodium alginate and synthesized sodium alginate are shown in Fig. 2. (a) and Fig. 2. (b) respectively. The similarity in the peaks at wavenumbers 1400 cm-1, 3000 cm-1, 1100 cm-1, 1700 cm-1, 1300 cm-1, 1100 cm-1 and 700 cm- 1 confirm the presence of sodium alginate and the various peaks indicate the characteristic functional groups in sodium alginate. The peak at 1100 cm- 1 corresponds to the

C-O-C stretching. The peak at 1400 cm- 1 corresponds to the COO− stretching, absent in sample 2. The peak at 3000 cm- 1 corresponds to C-H stretching band, absent in sample 1.

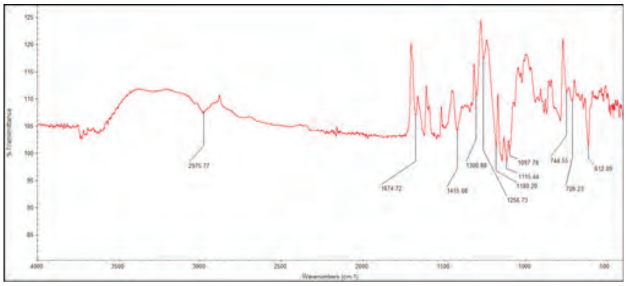

Fig. 2. (a) FTIR of pure sodium alginate

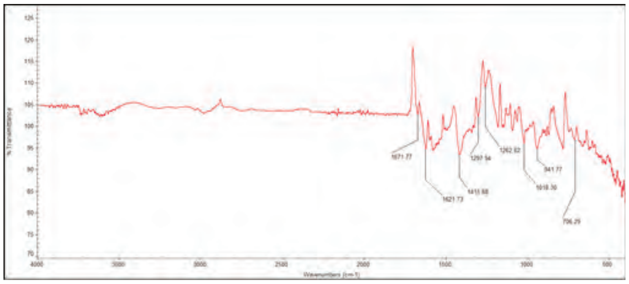

Fig. 2. (b) FTIR of synthesized sodium alginate

Effect of adsorbent dosage on removal efficiency for Methylene blue

The amount of adsorbent is a crucial factor that determines the ability of an adsorbent for a defined initial strength of sorbate. Fig. 3. shows the percentage removal of the dye with varying dosages of biocomposite gel. Removal efficiency increased with decrease in the egg shell dosage. The highest removal efficiency was obtained as 79.37% and among the tested dosages of egg shell in biocomposite gel, the highest removal efficiency (77.56%) was obtained for 0.3 gm of egg shell dosage.

Effect of contact time on removal efficiency for Methylene blue

The dye removal improved with the higher contact time of egg shell dosage. The highest efficiency was obtained at a contact time of 90 min as shown in Fig. 4. and thereafter remains constant. Rapid removal of dye took place in the first 15 min, and then gradual increase in removal efficiency was observed up to 90 min. Further increase in contact time caused no increase in the removal of dye. Table. 3 shows the removal efficiency obtained at specific time intervals.

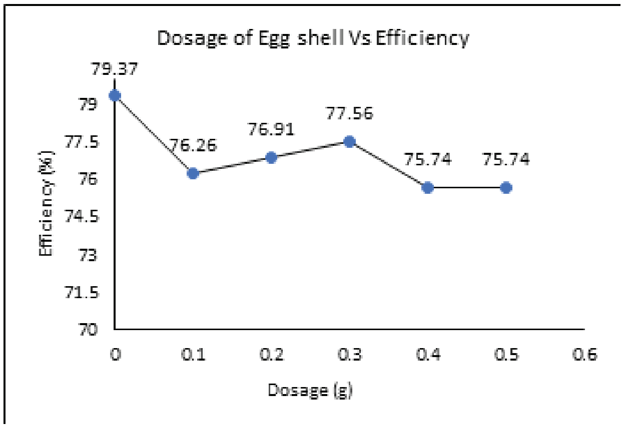

Fig. 3. Effect of adsorbent dosage on removal efficiency for various proportions of composite gel

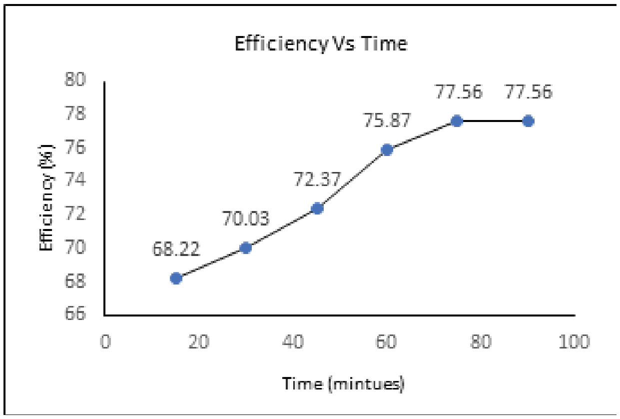

Fig. 4. Effect of contact time on removal efficiency

Various proportions of biocomposite developed using sodium alginate extracted from seaweed and egg shell was successfully studied for their dye removal efficiency. Removal efficiency increased with decrease in the egg shell dosage and increase in contact time. Egg shell composites exhibited relatively poorer results showing that either the process is to be modified or some other substitutes are to be attempted.

CONCLUSIONS

In the present study, sodium alginate was extracted from seaweed for the preparation of adsorbent and the same was characterized using FT-IR. Composite gel using sodium alginate and eggshell was also developed to selectively remove dye from wastewater. Sorption experiments were performed using methylene blue as the model of pollutant. Various proportions of sodium alginate – egg shell biocomposite gels were prepared and the removal efficiencies of dye from wastewater were determined. Maximum dye removal efficiency of the composite without egg shell was found to be 79.37% whereas, the maximum efficiency for composite was found to reduce to 77.56 % at dosage of egg shell of 0.3 g and contact time of 90 minutes. Decreased efficiency of egg shell composite compared to composite without egg shell indicates that inclusion of egg shell powder in present form did not contribute to dye removal significantly. Based on the present study, biosorbent prepared from naturally synthesised sodium alginate exhibited better results compared to biosorbent-eggshell biocomposites. The results indicate that either the process has to be modified or some other substitute has to be attempted.

REFERENCES

1. Al-Zaban, M.I., Alharbi, N.K., Albarakaty, F.M., Alharthi, S., Hassan, S.H., Fawzy, M.A. Experimental Modeling Investigations on the Biosorption of Methyl Violet 2B Dye by the Brown Seaweed Cystoseiratamariscifolia Sustainability 2022; 14(9): 5285. https://doi.org/10.3390/su14095285
2. Arumugam, N., Chelliapan, S., Kamyab, H., Thiru, S., Othman, N., Nasri, N.S. Treatment of Wastewater Using Seaweed: A Review. International Journal of Environmental Research and Public Health 2018;15(12): 2851. https://doi.org/10.3390/ijerph15122851
3. Bajpai, A.K., Agrawal, P., Singh, S.K., Singh, P. Alginate-Based Nanosorbents for Water Remediation. In: Bhardwaj Mishra, S., Mishra, A. (eds) Bio- and Nanosorbents from Natural Resources. Springer Series on Polymer and Composite Materials 2018. Springer, Cham. https://doi.org/10.1007/978-3-319-68708-7_5
4. Boddu, S, Babu, D.J., Alugunulla, V.N., Khan, A.A., Kolimarla, B.B., Jajula, S., Thumbeti, K.M. A prospective removal approach of reactive Yellow 14 dye using Spongomorpha indica. Materials Today Proceedings 2022; 67: 1235–1242. https://doi.org/10.1016/j.matpr.2022.08.379
5. El-Naggar, N.E., Rabei, N.H. Bioprocessing optimization for efficient simultaneous removal of methylene blue and nickel by Gracilaria seaweed biomass. Scientific Reports 2020; 10(1). https://doi.org/10.1038/s41598-020-74389-y
6. Hamd, A., Shaban, M., AlMohamadi, H., Dryaz, A.R., Ahmed, S.A., Al-Ola, K.A.A., El-Mageed, H.R.A., Soliman, N.K. Novel Wastewater Treatment by Using Newly Prepared Green Seaweed–Zeolite Nanocomposite. ACS Omega 2022; 7(13): 11044–11056. https://doi.org/10.1021/acsomega.1c06998
7. Mazumder, A., Holdt, S.L., De Francisci, D., Alvarado-Morales, M., Mishra, H.N., Angelidaki, I. Extraction of alginate from Sargassum muticum: process optimization and study of its functional activities. Journal of Applied Phycology 2016; 28(6): 3625–3634. https://doi.org/10.1007/s10811-016-0872-x
8. Park, H,. Jeong, S.J., Yang,J., Kim, B.S., Lee, S. Removal of heavy metals using waste eggshell. Journal of Environmental Sciences, 2007; 19(12):1436–1441. https://doi.org/10.1016/s1001-0742(07)60234-4
9. Shao, Z., Huang, X., Yang, F., Zhao, W., Zhou, X., Zhao, C. (2018). Engineering sodium alginate-based cross-linked beads with high removal ability of toxic metal ions and cationic dyes. Carbohydrate Polymers 2018; 187: 85–93. https://doi.org/10.1016/j.carbpol.2018.01.092
10. Sharma, R., Sapna, Dhillon, A., Kumar, D. Bio-and Nanosorbents from Natural Resources. In: Mishra SB, Mishra AK, editors. Springer Series on Polymer and Composite Materials,2018 Inc; Sringer International Publishing.

Design of Decentralized Treatment Systems for Canteen Waste Management

Aswathy KP
Assistant Professor
Department of Civil Engineering
NSS College of Engineering
Palakkad, Kerala
✉ aswathykp1992@gmail.com

Mariya Sebastian
Student
Department of Civil Engineering
NSS College of Engineering
Palakkad, Kerala
✉ nima291999@gmail.com

Nima Prem
Student
Department of Civil Engineering
NSS College of Engineering
Palakkad, Kerala
✉ mariyasebastian644@gmail.com

Niveditha K S
Student
Department of Civil Engineering
NSS College of Engineering
Palakkad, Kerala
✉ nivukavungal@gmail.com

ABSTRACT

This study revolves around creating a holistic framework for decentralized waste management by incorporating greywater treatment, solid waste management, recovery and reuse of treated waste for secondary applications such as flushing and biogas production. The goal of the proposed system is to deal with the current challenges of increasing level of waste generation as well as shrinking natural resources. The study proposed the design of decentralized systems such as settlers, anaerobic baffled reactor (ABR), anaerobic filter (AF) for the treatment of grey water and biogas digester for solid waste management. The on-site grey water treatment systems were selected depending upon the strength and characteristics of incoming waste water. Solid waste management comprises of source segregation of biodegradables and non- biodegradables. Biodegradable waste can be composted using anaerobic digestion processes, yielding biogas. Non- biodegradable waste undergoes recycling processes to recover valuable materials such as plastic, glass, and metal etc. Overall, the integrated system presented in this paper offers a sustainable solution for resource recovery and reuse, contributing to environmental protection and resource conservation.

KEYWORDS: *On-site treatment, Recovery & reuse, Environmental protection.*

INTRODUCTION

With global water scarcity concerns growing by the day, the need for sustainable water management has become crucial. The reuse of grey water leads to adaptability of local water systems, resilience and a sustainable future[1]. Positive shifts towards ensuring the proper treatment and reuse of wastewater point towards a ray of hope for a sustainable future. In such a scenario, decentralized systems are an attractive alternative option where wastewater can be treated and reused on-site. This method is a win/win as it increases efficiency and introduces a resource-responsible and resilient culture. Also, solid waste management indeed stands as a formidable problem in numerous locations, spawning environmental degradation and public health hazards[2]. But with proper segregation, waste can be substantially managed by adapting to change in practices. Recycling non-biodegradables and anaerobically oxidizing or composting biodegradables can have a good impact in this field. Researchers have explored the potential of bio-gas production from biodegradable food waste[3]. The paper clearly mentions the treatment and reuse strategy that can be adopted for both grey water and biodegradable solid waste.

BACKGROUND SUMMARY

A proper waste management facility can foster a healthy environment and a sustainable campus community. The current situation at the college shows a lack of a proper waste management system for the canteen. All generated waste is being discarded into the area behind the canteen leading to unhealthy surroundings and stagnant waste water. In India there is a large gap between waste collection and processing [4]. In this study, decentralized or on-site systems are preferred over centralized systems due to the improper functioning as well as the huge capital and maintenance costs involved with centralized systems. Objectives of the study are:

- To design grey water treatment modules and reuse the treated water for flushing
- To design a biogas unit to treat the biodegradable solid wastes to recover biogas as a valuable resource.

METHODOLOGY

The present study is divided into two parts: grey water treatment and solid waste management of the wastes generated in the college canteen. The grey water quantity is found from the average number of users visiting the canteen. The area of the canteen plot and characteristics of grey water were also measured to check the suitability of various treatment options. Lab tests including chemical oxygen demand (COD), biochemical oxygen demand (BOD), PH, DO, Sulphate, Solids, Conductivity, and Alkalinity was conducted at the laboratory as shown in Table 1. The treatment modules for grey water were selected based on the characteristics and quantity of grey water generated[5]. Similarly, the characteristics of biodegradable solid wastes were also conducted at the laboratory such as pH, total solids, conductivity and COD. A biogas unit was designed based on the quantity of biodegradable solid waste generated. The non-biodegradable waste is collected by the Panchayat on regular intervals.

Grey water treatment

Survey data

A survey was conducted for 5 consecutive days during peak hours from morning to evening to determine the number of people visiting the canteen to quantify the grey water generated[6]. The average number of users is found to be 350.

Study area

The college canteen backyard was selected for placing the modules. Levelling of plot was done using a dumpy level to find the ground level and reduced levels of various components of the grey water treatment system. Levelling of the backyard ensured that the grey water flows by gravity through various treatment units. Fig 1 shows the study area.

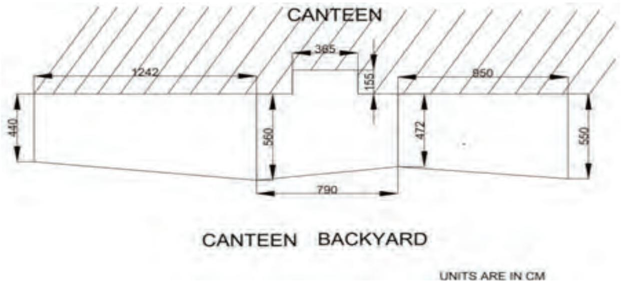

Fig. 1: Study area

Characteristics of grey water

Characteristics of grey water were determined using standard procedures in the Environmental Engineering laboratory. The range indicates the characteristics of treated grey water for reuse applications taken from the CPHEEO manual on sewerage and sewage treatment systems. The various characteristics along with their range are given in Table 1.

Table 1: Characteristics of grey water

Sl. No	Experiments	Result	Range
1.	Determination of PH	6.37	6.50 -8.50
2.	Determination of sulphates	0 mg/l	1000mg/l
3.	Determination of dissolved oxygen	8.6 mg/l	------
4.	Determination of BOD	620 mg/l	15 mg/l
5.	Determination of COD	1200 mg/l	100mg/l
6.	Determination of solids	TDS = 2400mg/l TSS =2751mg/l	TDS = 2100 TSS= 100mg/l

7.	Alkalinity	28 mg/l	----
8.	Conductivity	1400 microomh s/ cm	

Quantification of grey water

From the National Building Code of India 2005, as per the water requirements for buildings other than residences, the total per day demand for food courts is 35 l/capita[7]. The average number of persons visiting the canteen was worked out as 350 and the peak factor selected is 0.8. The quantity of grey water generated is considered to be 0.7 times the quantity of wastewater and is found to be 6860 l/day.

Design of grey water treatment units

The different units adopted for treating grey water were grease trap, settler, anaerobic baffle reactor and an anaerobic filter. All treatment units are designed using the DEWATS Design guide by BORDA 2009[8]. The treated water can be reused for toilet flushing[9]. The design of grey water treatment units is further explained in the subsequent sections.

Grease trap

The working of grease and grit chambers is similar to septic tanks, with lighter material rising to the surface and heavier material settling to the bottom, which is removed once a week. A grease trap requires a hydraulic retention time (HRT) of 30 minutes to allow the fats, oils, grease, and food solids to settle in the tank [8]. The flow rate into the grease trap was 4.76 l/minute. The volume of the grease trap was found to be 0.143 m^3. Assuming the depth as 0.45 m and length as 0.7 m, the width obtained was 0.45 m. The cross-sectional details of the grease trap are shown in fig 3.

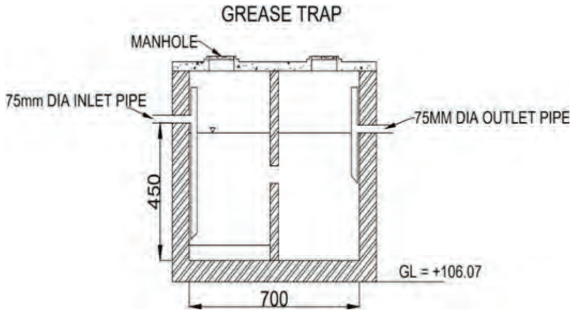

Fig 2: Cross-section of grease trap

Settler

A settler is a sedimentation tank where the sludge settles at the bottom and decomposed anaerobically. The particles heavier than water settle to the bottom and decompose anaerobically and the lighter particles float to the top and have to be removed periodically. The daily flow rate for the design is 6.86 m3/day. The retention time was assumed as 2 hrs. The HRT of a settler is a maximum of 2 hours[10]. The COD removal rate is determined as 0.38 based on the assumed HRT[2]. For BOD removal rate, factored BOD has to be determined. For a COD removal rate <0.5 factored BOD is 1.06[8].

COD out = (1– COD removal rate) × COD in = (1-0.38) x1200 = 746mg/l

BOD removal rate – Factored BOD × COD removal rate = 1.06 x 38% = 0.40

The effluent BOD was found to be 372 mg/l. The sludge accumulation rate is assumed to be 0.002. The desludging interval is chosen on an annual basis, assuming SRT as 18 months. The sludge volume was found using the equation below[8].

$$Sludge\ Volume = \frac{Fsl + V + COD\ removal\ rate}{1000} \times Q \times 30 \times SRT$$

The sludge volume obtained was 2.9 m3. The total volume was found to be 7.2 m3. The dimensions of the tank in length, breadth, and height are 3.3m x 1.1m x 2.2m, with two compartments. The cross-section of settler is shown in fig 3.

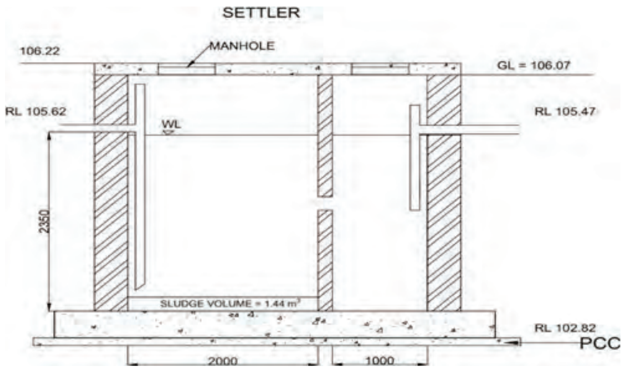

Fig. 3: Cross section of settler

Anaerobic Baffle Reactor

The Anaerobic baffled reactor (ABR) consists of alternate standing and hanging baffles which force the water to flow repeatedly through the sludge. Here, two mechanisms are responsible for the treatment: solids retention and anaerobic digestion. ABR is mainly used in remote areas where there is limited availability of electricity and oxygen. The up-flow velocity of ABR should not be larger than 1m/h. The ABR was designed as per the DEWATS Design guide by BORDA,2009[8].

The peak hourly flow rate for ABR was found to be 1.7 m^3/hr. Reactor dimensions are selected to meet the Upflow velocity and organic loading rate.

Assume L/W ratio as 0.4 and the Water depth is assumed as 2.50m[8]. Length of typical chamber = 2.5 x 0.4 = 0.8m ~ 1m.

$$Width\ of\ ABR = \frac{Peak\ hour\ flow}{(upflow\ velocity \times L)} = 2.1\,m$$

A Length/Depth ratio of 0.4 was considered and the depth obtained was 2.5 m. Three chambers are considered for ABR and the volume of ABR calculated was 20m3. HRT of ABR is calculated by dividing the volume of ABR by the daily flow rate. HRT obtained was 24 hrs. The COD removal efficiency was calculated by multiplying the design factors of HRT, strength, temperature and storm water. The storm water risk factor, feed concentration (strength) factor, and temperature factor was assumed as 1 and HRT factor was taken as 0.85. COD removal rate was found to be 85%. The BOD removal rate was calculated by multiplying COD removal rate with conversion factor obtained from the graph between COD removal efficiency and factor as shown in Fig 4. The cross-sectional details of ABR are shown in Fig 5.

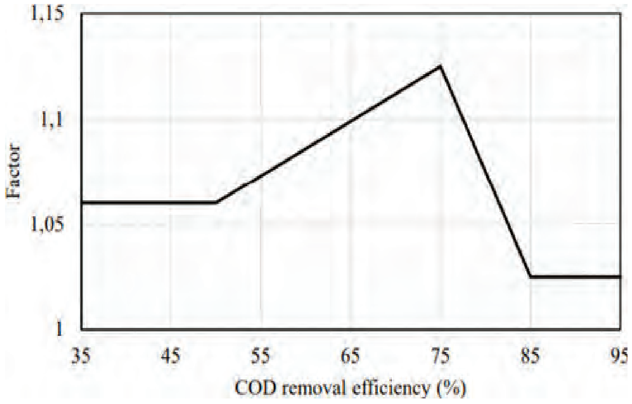

Fig. 4: Conversion factor for COD removal to BOD removal

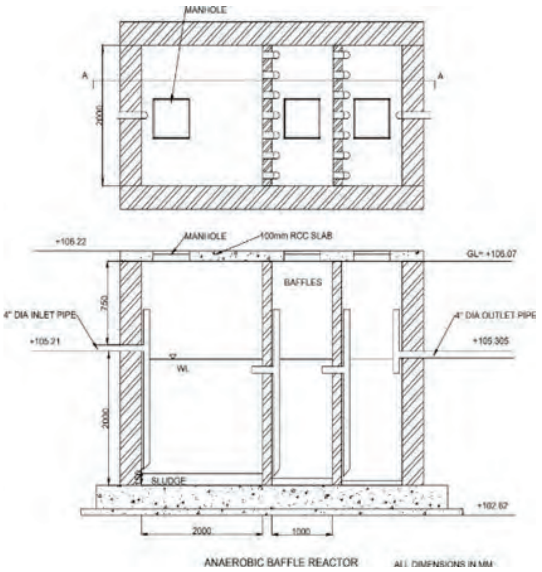

Fig. 5: Plan and cross section of anaerobic baffle reactor

Anaerobic Filter

An anaerobic filter is a contact process where the waste water comes in contact with the filter media carrying biological solids. The biomass is entrapped in the media which is made of gravel, rocks, cinder or specially formed plastic media. Anaerobic filter is widely used as a secondary treatment for household black or grey water systems. It helps in the efficient removal of solids unlike other treatment units. All assumptions and equations are taken from DEWATS Design guide by BORDA,2009[8]. The influent COD and BOD concentration was 112 mg/l & 48 mg/l. The depth of water was selected in the range of 1.8 m to 2.5 m. The depth of water above the filter material ranges from 0.2 m to 0.4 m and the depth of water below the filter material ranges between 0.3m to 0.6 m.

Water depth at the outlet (d_w) = 2 m

Water depth above filter (d_{af}) = 0.5 m

Water depth below filter (d_{bf}) = 0.5 m

Depth of filter (d_f)= d_w-d_{af}-d_{bf} = 1m

The inner length of AF chamber and the width of chamber is assumed to be 2 m. therefore, the total volume of AF assuming 2 chambers is 16m^3. The void space of the filter material typically ranges from 30% to 45%. The void space hence is assumed as 35%. The AF reactor volume considering the void space is found to be 2.8 m^3. The HRT is calculated as 9.8 hrs. The design COD removal efficiency (CODout) is calculated by multiplying the f_{HRT}, $f_{strength}$, $f_{surface}$, $f_{chamber}$ and $f_{stormwater}$ empirical design factors which is obtained from the graph. The COD removal rate was worked out as 63%. The BOD removal rate was determined using the same method applied for ABR. The effluent COD and BOD was found out to be 41mg/l and 15 mg/l. The cross-sectional details of AF is shown in fig 6.

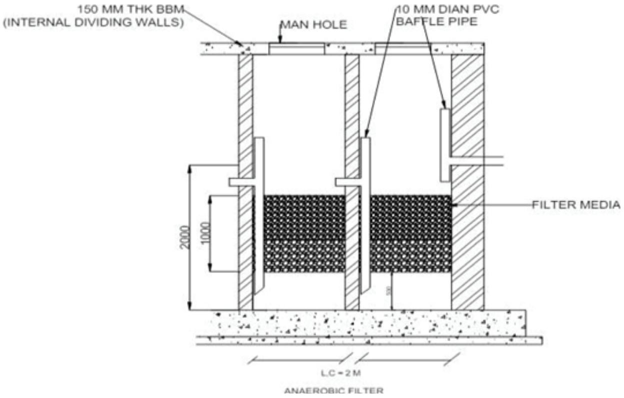

Fig. 6:Cross-section of anaerobic filter

Biogas digester

Biogas digester was designed to recover biogas produced as organic material degrades under anaerobic conditions within the reactor. The biogas can be recovered and can be used as a clean, renewable source of energy for cooking. A biogas digester is used for treating biodegradable solid waste generated from the canteen[11]. There are four main stages in anaerobic digestion: hydrolysis, acidogenesis, acetogenesis, methanogenesis[5]. The characteristics of biodegradable solid wastes was found out in the laboratory using standard procedures. The solid wastes are weighed manually to find its quantity. The results of the quantification and characterization is shown in table 2 and table 3.

Table 2: Quantification of solid wastes

Date	Bio-degradable waste (kg)	Non bio-degradable waste (kg)
5/2/2024	10.487	0.97
6/2/2024	10.25	0.823
7/2/2024	8.82	1.325
8/2/2024	8.32	0.932
9/2/2024	9.24	0.988

Table 3: Characterization of solid waste

Sl. No	Experiment	Result
1	pH	5.98
2	Total Solids	45%
3	Volatile Solids	31%

Step 1: Calculation of total solids and volatile solids

The total amount of waste collected per day is required for quantification of solids and volatile solids. Further heating the sample at high temperatures, volatile solids can be found.

$$Total\ Solids\% = \frac{Final\ weight}{Initial\ weight} \times 100 = 45\%$$

Step 2: Calculation of volatile solids

Approximate quantity of gas required for cooking = 0.3m^3

Percentage of volatile solids in 1kg of food waste (FW) = 31%

Amount of VS in 10kg FW = 10 x 0.31 = 3.1kg

Step 3: Calculation of biogas production from food waste

Amount of biogas production from food waste = 0.56m^3 /kg of VS = 0.56 x 3.1 = 1.736m^3/d

Amount of biogas production from food waste = 40 x1.736 = 6.94m^3

V_1= 6.94 m^3

Step 4: calculation of the volume and internal diameter of the dome Volume of the dome, $V_1 = 0.0827D^3$

internal diameter D_0 = 4.37m

Step 5: calculation of total volume, wall height, dome height, base depth, internal diameter of digester

$V_1 = 0.0827\ D^3_0 = 0.827 * 4.373 = 7\ m^3$

$V_2 = 0.0501\ D^3_0 = 0.0501\ D^3_0 = 4,26\ m^3_3$

$V_3 = 0.3142\ D^3_0 = 0.3142\ D^3_0 = 26.76\ m$

Total volume, = 38.02 = 38 m^3

$V = V_1 + V_2 + V_3$

Wall height = $H_0 = D_0/2.5 = 4.37/2.5 = 1.76$ m

Dome height= $f_1 = D_0/5 = 4.37/5 = 0.88$m

Base depth = $f_2 = D_0/8 = 4.37/8 = 0.55$m

Internal diameter of digester $R_0 = D_0/2 = 2.2m$

Total height = $f_1 + f_2 + H_0 = 3.91 = 3.2m$

Total volume = 38 m^3

The total height and total volume of the biogas plant was calculated as 3.2m and 38m^3. Fig 7 shows the cross-sectional details of biogas digester.

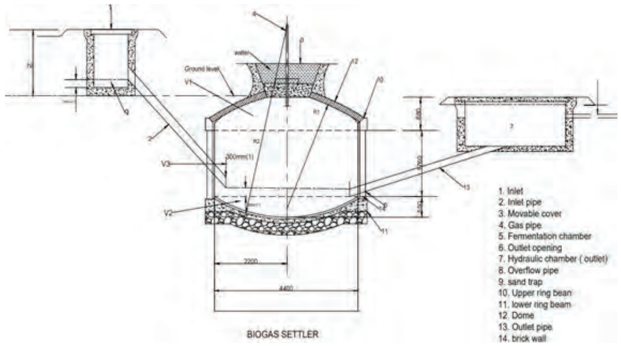

Fig. 7: Cross sectional details of biogas digester

RESULTS AND DISCUSSIONS

The objective of the study was to treat the grey water and solid wastes generated at the canteen facility. For treating grey water, four decentralized treatment modules were designed namely grease trap, settler, anaerobic baffled reactor, anaerobic filter. The influent BOD and COD of the grey water collected was 620 mg/l and 1200 mg/l. the final effluent BOD and COD was found to be 15 mg/l and 41 mg/l. The BOD removal efficiency of the system is found to be 97.58%. All treatment units were designed to work by gravity[12]. The treated water can be reused for toilet flushing in the canteen facility. The dimensions of the grey water treatment units are shown in table 4. The solid wastes were segregated first. The biodegradable wastes were anaerobically digested and the recovered biogas can be used as a valuable resource. The total volume of the biogas digester is found to be 38 m3. The non-biodegradable wastes will be collected by the municipality at regular intervals.

Table 4: Parameters and measurements of grey water treatment systems

Parameter	Grease Trap	Settler	Anaerobic Baffled Reactor	Anaerobic Filter
Length (m)	0.7	3.3	1	2
Depth (m)	0.45	2.2	2.5	2
Width (m)	0.45	1.1	2	2
Volume (m3)	0.143	7.2	20	16

CONCLUSION

The goal of this project was to install an integrated waste management system for the canteen facility. The canteen lacked a proper waste management facility. Grey water treatment units like grease trap, settler, anaerobic baffle reactor, anaerobic filter have been designed to treat and reuse it for toilet flushing. The solid waste generated has been segregated into biodegradables and non-biodegradables and the biodegradable part is digested and biogas is generated by using a biogas digester[13]. The BOD of the influent grey water was very high for it to discard it into open spaces. After the treatment the organic matter reduced to 97% of its initial content. The integrated system for total waste management at the canteen facility will provide cost savings, reusability of treated water and environmental benefits[5]. In future studies, the proposed system can be implemented in the site and the characteristics can be tested and further improvements can be made.

REFERENCES

1. A. Van de Walle et al., “Greywater reuse as a key enabler for improving urban wastewater management,” Oct. 01, 2023, Editorial Board, Research of Environmental Sciences. doi: 10.1016/j.ese.2023.100277.
2. R. Mahajan, “Environment and Health Impact of Solid Waste Management in Developing Countries: A Review,” Current World Environment, vol. 18, no. 1, pp. 18–29, Apr. 2023, doi: 10.12944/cwe.18.1.3.
3. A. Krishnaveni, C. Sivakumar, D. Shanmugapriya, S. Shobana, M. Siva, and M. Pandiayan, “Evaluation of Biogas Potential of Students Hostel Kitchen Food Wastes,” Int J Curr Microbiol Appl Sci, vol. 9, no. 1, pp. 457–467, Jan. 2020, doi: 10.20546/ijcmas.2020.901.050.
4. V. Ramakrishna, Ch. N. Subrahmanyam, S. Bhanuchand, B. S. Rao, and A. N. V. A. Kumar, “Municipal Solid Waste Quantification, Characterization and Management in Mylavaram,” IOSR Journal of Mechanical and Civil Engineering, vol. 13, no. 05, pp. 77–87, May 2016, doi: a. 10.9790/1684-1305047787.
5. M. Oteng-Peprah, M. A. Acheampong, and N. K.

deVries, "Greywater Characteristics, Treatment Systems, Reuse Strategies and User Perception—a Review," Water Air Soil Pollut, vol. 229, no. 8, Aug. 2018, doi: 10.1007/s11270-018-3909-8.

6. "Manual: Greywater Management."
7. "Central Ground Water Authority, Government of India Estimation of water requirement for drinking and domestic use (Source: NBC 2016, BIS) Central Ground Water Authority Jam Nagar House, New Delhi."
8. A. Ulrich, S. Reuter, B. Gutterer, L. Sasse, T. Panzerbieter, and T. Reckerzügel, "Decentralised Wastewater Treatment Systems (DEWATS) and Sanitation in Developing Countries A Practical Guide."
9. "Decentralized Wastewater Management Complementing Centralized Solutions for Achieving 100% Sanitation Coverage."
10. D. Pahwa, S. Rawat, B. Bhanot, and P. Shukla, "PART B: LEARNING NOTES INTEGRATED WASTEWATER AND SEPTAGE MANAGEMENT PLANNING MODULE TITLE Integrated

a. Wastewater and Septage Management-Planning Module (Part: B Learning Notes) PUBLISHER RESEARCH PROJECT Sanitation Capacity building Platform (SCBP) GRAPHIC DESIGN," 2021. [Online]. Available: www.niua.org,

11. R. L. K. Lokuliyana, C. Ambawatte, and W. V. D. L. Kumara, "Feasibility Study on Anaerobic Bio Gas Plants in Sri Lanka," SLEMA Journal, vol. 19, no. 1, p. 1, Mar. 2016, doi: 10.4038/slemaj.v19i1.12.
12. I. F. Purwanti, H. Sulistiyaning Titah, S. Budi Kurniawan, I. Fitri Purwanti, and B. Voijant Tangahu, "Article ID: IJCIET_09_13_174 Cite this Article: Ipung Fitri Purwanti, Harmin Sulistiyaning Titah, Bieby Voijant Tangahu and Setyo Budi Kurniawan, Design and Application of Wastewater Treatment Plant for 'Pempek' Food Industry," International Journal of Civil Engineering and Technology (IJCIET), vol. 9, no. 13, pp. 1751–1765, 2018, [Online]. Available: http://www.iaeme.com/IJCIET/index.asp1751http://www.iaeme.com/ijciet/issues.asp?JType=IJCIET&VType=9&IType=13http://www.iaeme.com/IJCIET/index.asp1752http://www.iaeme.com/IJCIET/issues.asp?JType=IJCIET&VType=9&IType=13
13. S. A. Iqbal, S. Rahaman, M. Rahman, and A. Yousuf, "Anaerobic digestion of kitchen waste to produce biogas," in Procedia Engineering, Elsevier Ltd, 2014, pp. 657–662. doi: 10.1016/j.proeng.2014.11.787.

Septic Tank Effluent Treatment Using Sand Shredded Plastic Mixture

Biju M S
Assistant Professor
Department of Civil Engineering
NSS College of Engineering
Palakkad, Kerala
✉ bijuced@nssce.ac.in

Mrudula K
B Tech Student
Department of Civil Engineering
NSS College of Engineering
Palakkad, Kerala
✉ mrudulakcpy@gmail.com

Nisha A S
Assistant Professor
Department of Civil Engineering
NSS College of Engineering
Palakkad, Kerala
✉ asnisha@nssce.ac.in

Varsha V
B Tech Student
Department of Civil Engineering
NSS College of Engineering
Palakkad, Kerala
✉ varshasajitha2000@gmail.com

ABSTRACT

As a sewage treatment unit, septic tank plays an important role in pollution control. Due to rapid urbanization, in states like Kerala, housing plots available for construction of residential units have become very small and consequently, adherence to norms pertaining to on-site disposal of domestic effluent has become very difficult. Taking this into account, treatment of septic tank effluent prior to disposal has become a necessity to prevent contamination of fresh water sources including dug wells. The contamination can be reduced to an extent by using a suitable filter media. This project focuses on the prospects of filters employing shredded plastic waste for the treatment of septic tank effluents. Shredded waste plastic is used as a partial replacement of sand in filters and its effectiveness in re- moving the contaminants is analyzed using column study. Coliform and BOD tests were conducted on the effluents by changing the height of the filter media and also by changing the proportion of sand and shredded plastic. Contaminant removal efficiency of sand-plastic filter media is higher when compared to sand. Using regression modelling, an equation has been suggested for finding the contaminant removal efficiency of sand-plastic filter media. The revealed that use of sand shredded plastic mixture can act as an excellent filter media for reducing the contaminant load from septic tank effluent.

KEYWORDS: *Septic tank, Shredded plastic, Dug well contamination.*

INTRODUCTION

The availability of land was not an issue in the past and dumping waste directly to the ground was an accepted practice. The progress of homo sapiens from hunter gatherers to farmers actually made their life worse[1]. Living in groups in permanent settlements required better sanitation facilities and pollution control. The rapid growth in many towns has led to a significant challenge, with available space proving insufficient for effective waste disposal. The cities and towns where centralized sewage treatment is still a dream, continues to use on site sanitation systems (OSSS). According to world health organization poorly managed septic tanks causes contamination to the drinking water sources especially in dense low income and informal areas.

BACKGROUND SUMMARY

The Central Public Health and Environmental Engineering Organization (CPHEEO) of India recommends maintaining a minimum distance of 15 meters between On-Site Sanitation Systems (OSSS) and drinking water sources such as dug wells. In the northeastern states of India, where heavy rainfall is prevalent, this distance is increased to 20 meters. However, it is noteworthy that in Kerala, a region that also experiences intense monsoons, this distance can be reduced to as little as 7.5 meters. Studies in specific areas in Kerala, suggests that horizontal distance more than 21 meter between well and soak pit is re-quired to avoid microbial contamination [2,3]. Furthermore, in high-population-density states like Kerala, achieving even the 7.5-meter separation often proves challenging. The Solution of this complex issue lies in reducing the contaminant load in the septic tank ef-fluent.

Preliminary operation of the coir geotextiles filter shows considerable amount of organics removal (up to 97%) and faecal coliform removal up to 99% from septic tank effluent [4]. A pilot study conducted in Bhutan with shredded waste plastic bottles as biofilter media for waste water treatment showed that effluent meets three out of four of the effluent dis-charge limits of Bhutan [5]. Along with such studies hundreds of innovations are being filed every year in the area related to septic tanks. A study which examined 889 patents filed in the last two decades revealed the need of continued improvements in septic tank technology to address the drinking water contamination problem of under developed populations [6].

SAND -SHREDDED PLASTIC MIXTURE AS FILTER MEDIA

The literature review revealed that the effluent conventional septic tanks require a secondary treatment, and the same should be economical. This objective of this paper is to show case the efficiency of sand- shredded plastic mixture filter in reducing the contaminant load in septic tank effluent.

Materials and Methods

River sand passing through 20mm and retaining on 90micron IS sieves was thoroughly washed with water to remove the dust, clay and attached organic impurities and was dried under sun. Shredded plastic was collected from the Grama panchayat waste management plant, Akathethara, Palakkad. The maximum dimension of shredded plastic sheets was 15 mm (figure 1) . The inlet water sample used to conduct the experiment need to have Escherichia coli content. The bacterium mainly inhabits the lower intestinal tract of warm-blooded animals, including humans, and is often discharged into the environment through faeces or wastewater effluent. Cow dung is utilized in this research to mix with water to make influent water to the column studies.

Fixed bed column study, which is an efficient method in the removal of various contaminants including dye, metal and hazardous waste is carried out to conduct the experiment. In this research, column study is conducted by using two PVC pipes. Each one having 20cm diameter and 90cm height. A permeable textile layer is used to support the sand at the bottom of each PVC column as depicted in figure 2. Sand is filled in the one pipe. Sand and shredded plastic with varying plastic content is filled in the other pipe.

Sample is diluted to the required concentration and sample collected from that was kept for the coliform concentration determination and BOD analysis. Sample is passed through both the pipes until a steady, continuous flow is attained. After reaching the steady flow, flow rate is calculated by noting the time. The effluent from both the pipes are collected. Both MPN and BOD tests are conducted as per Indian standards, IS 1622:1981 and IS 3025 (Part 44): 1993 respectively.

Fig. 1: Shredded waste plastic sample

Column study is repeated by varying the height of filter media such as 25cm, 50cm and 75cm. One of the pipes is filled with sand up to 25cm and other pipe with sand and plas-tic filled up to 25cm.Experiment is conducted by varying the sand- plastic ratio. Similarly, the experiment is conducted for 50cm and 75cm height

Fig. 2. Set up for column study

RESULTS AND DISCUSSIONS

Properties for the materials filled in the column are as shown in Table 1. In Table 1&2, S refers to sand and P to plastic. It can be observed from the table that there is a decrease in the packing density as the proportion of plastic is increasing. In the case of porosity, it is seen that percentage of porosity is increasing, when plastic is increased. Similar variation can be seen for the co-efficient of permeability as well. So it can be concluded form the readings that the percentage of plastic is directly proportional to porosity and coefficient of permeability.

Table 1: Properties of 25 cm high column

Height of column	Mix proportion	Packing density (kg/m³)	Porosity (%)	Flow rate (m³/s)	Coefficient of permeability (m/s)
25 cm	S	1414.3	45.65	4.9×10^{-6}	0.94×10^{-4}
25 cm	S + 75g P	1282.79	50.73	5.25×10^{-6}	1.04×10^{-4}
25 cm	S + 150g P	1165.01	55.20	8.56×10^{-6}	1.64×10^{-4}
25 cm	S + 300g P	509.3	80.41	49.9×10^{-6}	9.56×10^{-4}
50 cm	S	1411.26	45.7	0.17 × 10-5	0.44×10^{-4}
50 cm	S+150g P	1346.45	48.18	0.38 × 10-5	0.95×10^{-4}
50 cm	S + 300g P	1228.67	53.27	0.52 × 10-5	1.31×10^{-4}
50 cm	S + 600g P	972.75	64	0.97 × 10-5	2.43×10^{-4}
75 cm	S	1273.24	50.98	0.60 × 10-6	1.76×10^{-5}
75 cm	S+ 225g P	1270.06	51.15	1.08 × 10-6	3.20×10^{-5}
75 cm	S + 450g P	1078.01	58.54	1.57 × 10-6	4.65×10^{-5}
75 cm	S + 900g P	674.82	74	2.66 × 10-6	7.98×10^{-5}

The results of coliform tests on the effluent are shown in Table 2. The MPN value obtained for influent was more than 2400. As the concentration of plastic in the mixture increases, MPN value also increases. For 150g and 300g plastic in sand-plastic mixture, MPN value is found to be 110 and 210 respectively. This shows a direct relationship between percentage of plastic and MPN.

Table 2: results of coliform test

Height of the column	Sample	MPN index
25 cm	Sand	240
25 cm	Sand+ 75g Plastic	28
25 cm	Sand+ 150g Plastic	110
25 cm	Sand+ 300g Plastic	210
50 cm	Sand	110
50 cm	Sand+ 150g Plastic	14
50 cm	Sand+ 300g Plastic	28
50 cm	Sand+ 600g Plastic	110
75 cm	Sand	64
75 cm	Sand+ 225g Plastic	15
75 cm	Sand+ 450g Plastic	20
75 cm	Sand+ 900g Plastic	28

Regression modelling was carried out to find the percentage of contaminant removed.

$$Y = 98.2139 - 3.7306 * X_1 + 0.1153 * X_2 + 0.2569 * X_1^2 + 0.0252 * X_1 * X_2 - 0.001 * X_2^2$$

where; Y = Percentage of Contaminant Removed, X1 = Percentage of Plastic, X2 = Height in cm.

This equation can be used to find the contaminant removal efficiency for any values of plastic content and height. Hence greater removal efficiency can be attained for the optimum plastic content and height.

The results obtained by conducting BOD test presented in table 3. The BoD of influent is 550 mg/l. The results obtained by conducting BOD test show a linear trend between plastic percentage and the BOD value. That is, when the percentage of plastic in the mix is increases, BOD value also increases. This shows the contaminant removal efficiency is higher for sand plastic mix ratio having least percentage of plastic.

Table 3: BOD levels in the effluent

Height of the column	Sample	BoD mg/l
25 cm	Sand	144
25 cm	Sand+ 75g Plastic	130
25 cm	Sand+ 150g Plastic	148
50 cm	Sand	134
50 cm	Sand+ 150g Plastic	130
50 cm	Sand+ 300g Plastic	150
75 cm	Sand	128
75 cm	Sand+ 225g Plastic	118
75 cm	Sand+ 450g Plastic	122

CONCLUSIONS

This paper mainly focuses on introducing a sand-shredded plastic mixture as filter media for effective contaminant removal. Results obtained from the experiments shows that sand with least amount of plastic content shows greater contaminant removal efficiency.99% contaminant removal efficiency is obtained for 0.75% plastic. This is mainly because of the in-crease in porosity and flow rate with increase in plastic content. Hence the sand- shredded plastic mixture with least percentage of plastic have lower porosity and flowrate, causing the particles to get entrapped in the filter media. The entrapping rate is higher as the influent flows through a greater length. Experiments shows that the filtration rate is higher for 75cm column as compared to 25cm and 50 cm. Using regression modelling, an equation has been found out for finding the contaminant removal efficiency for any values of plastic content and flow length. A filter fabricated with sand shredded plastic mixture will cause a reduction in the contaminant load in the septic tank effluent. Hence the filtration requirement in the land will reduce. The requirement of higher distance between septic tank and dug well can be effectively reduced by employing this filtration technique. As the suggestion is to use shredded plastic from the waste management facilities of local self-government agencies this technique will help in finding a new area to use waste plastics. From all these perspectives the suggestion for using sand-shredded plastic mixture for septic tank effluent treatment can be considered as a sustainable technique.

REFERENCES

1. Harari, Y. N. “Sapiens: A Brief History of Humankind”. Random House. New York City, U.S. 2014.
2. .M. S. Biju, Irfan Khursheed Shah. and George K. Varghese. “An investigation into the safe distance between well and onsite waste disposal systems: A case study from Kerala, India”’ International Journal of Chemical and Environmental Engineering Systems, 2011, 0976-37, Vol 2(1)
3. P.U. Megha, S. Murugan and P.S. Harikumar. “Estimation of safe setback distance be-tween well and contamination source using bacteriophage – a Case study”, Asian Journal. of Microbiology and Biotechnology.; 2017, Vol. 19, No. (1): 2017: 176-184
4. Gopan Mukkulath, Biju. M. S and Santhosh.G.Thampi, “Dug Well Contamination by Sep-tic Tank Effluent and Remediation using Coir Geotextiles”, International Journal of Earth Sci-ences and Engineering”, 2011. Vol. 04, No. 03, June 2011, pp. 532-538.
5. Dorji, U., Dorji, P., Shon, H., Badeti, U., Dorji, C., Wangmo, C., Tijing, L., Kandasamy, J., Vigneswaran, S., Chanan, A. and Phuntsho, S., “On-site domestic wastewater treatment system using shredded waste plastic bottles as biofilter media: Pilot-scale study on effluent standards in Bhutan”, Chemosphere, 2022, 286, p.131729.
6. Rafie, R., Hardy, A., Mohamad Zain, N., Gödeke, S. and Abas, P.E., “The Future of Septic Tanks: Uncovering Technological Trends through Patent Analysis” Inventions, 2024, 9(4), p.77.

Spatio-temporal Variations in Water and Vegetation for Alappuzha

Akshay Ranjith
Department of Civil Engineering
Indian Institute of Science
Bangalore, Karnataka
✉ rakshay@iisc.ac.in

ABSTRACT

Water is a vital natural resource essential for sustaining life on Earth. It plays a critical role in the Earth's integrated system, alongside its various forms. Vegetation is a fundamental component of ecosystems, existing in multiple forms and serving as a key indicator of environmental health and ecosystem changes. Vegetation cover can be easily monitored and quantified using various remote sensing techniques. Consequently, both water and vegetation are crucial elements in regional ecosystems, significantly influencing local flora and fauna. However, human activities are increasingly impacting these natural resources. Expanding human settlements often lead to the depletion of large water bodies and deforestation as land is converted for development. Alappuzha, a district in Kerala renowned for its abundant water bodies and its nickname as the "rice bowl" of Kerala, is the focus of this study.

Over the past few decades, remote sensing data has been extensively utilized to study natural resources like water and vegetation. This study employs optical satellite imagery to analyze surface water and vegetation cover in Alappuzha from 2017 to 2021. By examining temporal variations over this five-year period, the study aims to enhance our understanding of biodiversity and land productivity in the region. Satellite images facilitate the derivation of various indices for mapping and monitoring vegetation, with the Normalized Difference Vegetation Index (NDVI) being a widely used tool to assess vegetation intensity. Additionally, the study involves detecting surface water and tracking its temporal changes, which is crucial for informing sustainable human development activities.

KEYWORDS: *Spatio-temporal variations, Kerala floods 2018, Remote sensing and GIS.*

INTRODUCTION

General

The introduction of remote sensing technology has made immense development human civilization making it possible to monitor and track anything under the sky. Over the past several years, the scientific community have looked into the possibilities of remotely sensed photographs for analysing natural resources including vegetation and water. Such research have attracted a lot of interest since vegetation and water are valuable natural resources that need to be maintained. An efficient method to investigate the qualitative and quantitative variations occurring to surface water bodies and vegetation over time can be constructed by using appropriate digital image processing techniques on images taken from remote sensing satellites or aerial sensors.

Study area

The land known for its immense water networks consisting of a large network of canals, lakes, fresh water rivers and lagoons, is district of Alappuzha in Kerala. Due to the same reason, the district is called the "Venice of the East". The district also houses the well-known "Rice Bowl" of Kerala, which is known for its paddy cultivation. The paddy is grown with flood irrigation and a large part of the farm lands are portions reclaimed for the lake. The location of Alappuzha is 9° 24' N and 76° 24' E. The place has an average elevation of 1 m above Mean Sea Level (MSL). Some of the areas like Kuttanad is also known that has areas with elevation below mean sea level. Alappzuha covers an area of 1414 km2 and out of which 13 % of the district constitute of water bodies [1].

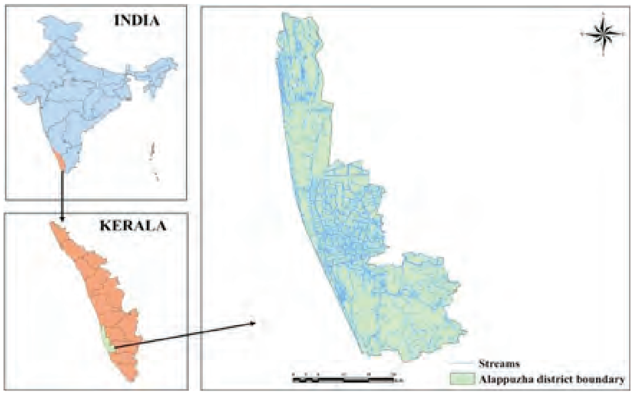

Fig. 1. The study area

Vegetation and water

The electromagnetic spectrum is used to understand the vegetation cover and surface water in the study area. Remote sensing data contains information reflected from the Earth's surface, using Electro-Magnetic Radiation (EMR). Each radiation of specific wavelength will have its unique interaction with the surface of the Earth. Different satellites will have large number of sensors on- board. These sensors will collect data in different bands of the EMR spectrum. For a particular feature like the vegetation or water body, each band will have different reflectance, thereby it becomes easier to differentiate each feature and also the properties of the feature. Further trying to improve the number of outputs that can be produced from a satellite image, the use of analytical techniques come into picture. One such is the use of Normalized Difference Vegetation Index (NDVI), which has the capability to differentiate vegetation into classes based on the intensity. Surface water can be easily identified as the reflectance in many of the bands are very low, as sparsely any of the radiation reaches the sensor. Hence, the availability of data natural resources helps towards evaluating and monitoring changes, thereby leading towards better planned operation.

Need for the study

A variety of methods in remote sensing helps collect data of different surface features over a large spatial extent. Water and vegetation indirectly objects as to the ecosystem of a region is widely required to be understood its condition and growth. Water, can be easily quantified as the surface water available in a region using remote sensing. Quantity of water is required to plan and execute various developmental activities like watershed planning, irrigation, etc. Vegetation in its various forms as forested areas, plantations, agricultural fields and the intensity of vegetation varies depending on factors like density, type of flora, etc. Vegetation directly and indirectly indicated the health of the environment and land productivity. For sustainable development, forecasting and planning lies in as a key stone. For all this to happen, the information or data on natural resources is an essentiality.

LITERATURE REVIEW

General

Remote sensing is widely used for monitoring, mapping, and evaluating natural resources, enabling the analysis of regional changes. As reviewed by Nagesh and Reshmidevi, 2013, its applications span areas like resource mapping, flux estimation, and resource management [2].

Study on vegetation and water

Assessing vegetation cover is crucial for understanding hydrology and climate, and is often done using remote sensing indices like NDVI, Soil Adjusted Vegetation Index (SAVI), Enhanced Vegetation Index (EVI), and Atmospherically Resistant Vegetation Index (ARVI) [3]. These indices help classify vegetation from dense to sparse, aiding land and resource analysis [4]. Similarly, monitoring surface water changes provides insight into environmental shifts due to natural or human factors. While optical imagery can be obstructed by clouds or vegetation, combining it with Synthetic Aperture Radar (SAR) allows for better detection, especially in wetlands, as SAR can penetrate such obstructions [5]. This integrated approach enhances the monitoring and management of water resources.

Concluding remarks

The best and compatible solution to understand the hydrological and ecological characteristics of an area would be to monitor and map the surface water and vegetation along with the spatio-temporal variations. Detection of vegetation and water can be done by processing satellite images along with use of an analytical derived product such as the various vegetation indices. By mapping out the temporal variations and comparing the variations between different locations within the study area helps us to get the spatial variations of the objects of interest. Based on the study of literature, the following objectives were formulated to be done in the study area, i.e., to find the spatio-temporal variations of surface water and vegetation cover.

METHODOLOGY

General

The study involves the use of satellite derived images to obtain the spatio- temporal variations of surface water and vegetation cover in the study area. The study is divided into five parts, namely, satellite imagery, image processing, delineation of area of interest and spatio-temporal variations.

Satellite imagery

General

An efficient and easily accessible procedure to efficiently assess vegetation cover and surface water over a 1,414 km² district, satellite-acquired optical imagery with adequate spatial resolution, minimal cloud cover, and consistent temporal availability is essential. LANDSAT 8, launched on February 11, 2013, from Vandenberg Air Force Base as part of the Landsat Data Continuity Mission (LDCM), meets these criteria. It carries two key sensors, namely, the Operational Land Imager (OLI) and the Thermal Infrared Sensor (TIR) which offers a temporal resolution of 98.8 minutes. The radiometric resolution of the OLI sensor is 12 bits which are scaled to 16 bit integers.

Downloading satellite images and shape file

The LANDSAT 8 images are freely available on the USGS Earth Explorer website (https://earthexplorer.usgs.gov). The required study area is found out. The scene cloud cover for the image is specified that it should be less than 10 % of the area. Similarly, the land cloud cover of the images should be less than 10 % of the area. The images for the time period of past five years is required. The preview of the images helps to check whether the area of interest is cloudy. The shape file for the area of interest is obtained from the revenue department website.

Image processing

QGIS

An efficient and robust image processing software for satellite imagery is Quantum Geographic Information System (QGIS). Initially, the downloaded images are corrected using DOS1 (Dark Object Subtraction 1) by inserting the appropriate metadata file corresponding to the satellite image [6]. During DOS1 correction, pixels with no data must be assigned a value of zero. The shapefile for the area of interest is inserted and used to clip the required area from the satellite image, applied to each required band image.

Mosaicing

The different satellite images for the area of interest is mosaicked using SAGA

2.3.2 processing toolbox. The toolbox houses various algorithms for interpolation at different cell sizes. The available algorithms are: Nearest neighbor, bilinear interpolation, inverse distance interpolation, bicubic spline interpolation and B spline interpolation. The data storage type is also available in different formats till a maximum of 8 byte floating point.

Delineation of area of interest

Surface Water

The surface water in a satellite image can be delineated using the characteristics of the EMR reflectance. Water bodies have very low reflectance in the near infrared band, i.e., band 5 for LANDSAT 8. The low reflectance values can be taken use of to threshold the image assign all the pixels below which a certain value represents surface water bodies. The reflectance for water body is shown in figure 2. The GRASS GIS 7 commands toolbox can be used to generate a report showing the area of surface water in the satellite image.

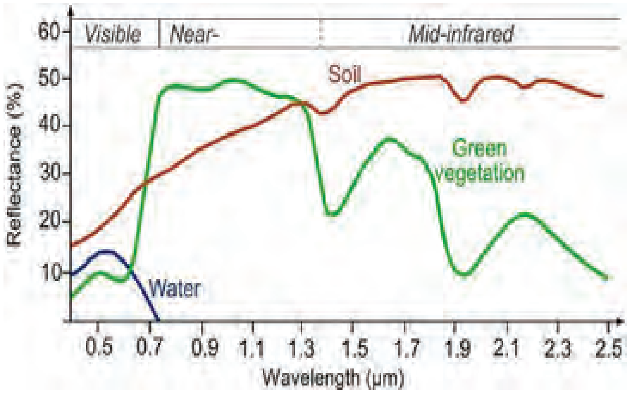

Fig. 2. Spectral signatures for water, soil and vegetation [7]

Vegetation cover

The vegetation cover for an area of interest can be delineated using the characteristics of an analytically derived product from satellite image. For this, the NDVI can be made use of. NDVI image for an area of interest is calculated as shown in Equation 1.

$$NDVI = \frac{NIR - R}{NIR + R} \tag{1}$$

where, NIR represents the pixel value in the near infrared band, i.e., band 5; and R represents the pixel value in the red band, i.e., band 4.

NDVI can be used to differentiate various intensities of vegetation using the details given in figure 3. The image can be then density sliced and the appropriate colour for the corresponding intensity of vegetation can be used. The GRASS GIS 7 commands toolbox can be used to generate a report showing the area of different intensities of vegetation in the satellite image.

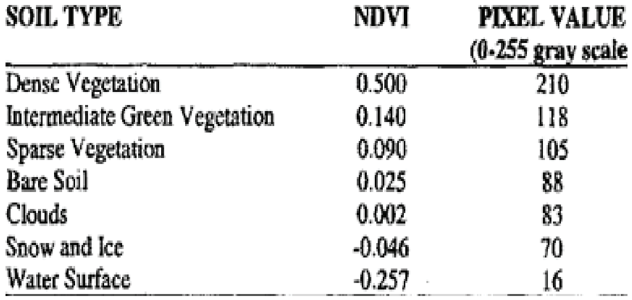

SOIL TYPE	NDVI	PIXEL VALUE (0-255 gray scale
Dense Vegetation	0.500	210
Intermediate Green Vegetation	0.140	118
Sparse Vegetation	0.090	105
Bare Soil	0.025	88
Clouds	0.002	83
Snow and Ice	-0.046	70
Water Surface	-0.257	16

Fig. 3. Classification of vegetation using NDVI [4]

Spatio-temporal variation

General

The spatio-temporal variation can be studied using the generation of appropriate images, i.e, for surface water and vegetation; for a sufficiently long time period and within the area of interest the changes in the different characteristics can be shown.

RESULTS AND DISCUSSION

General

The required study area was located, and the shape file downloaded. The required satellite images are downloaded and processed using QGIS software. The spatio-temporal variations are plotted and studied.

Satellite imagery

The satellite images for the area of interest were download from USGS EarthExplorer website. A total of 10 images were downloaded. Each two images are required to encompass the entire study region. The images are from the path 144 and the corresponding rows are 53 and 54. To capture the temporal variations, the images are downloaded for a span of five years, i.e., 2017 to 2021. All the images used are taken from the first half of the year as during the second half, it would be cloudy.

Image processing

The images are processed in QGIS software where by DOS1 correction was applied for each band image. The shape file for Alappuzha district was used to clip out the area of interest from the satellite image. The clipped out portions from two different satellite images are mosaicked using SAGA 2.3.2 toolbox. The interpolation algorithm used is nearest neighbour algorithm and the data is stored as a 4 byte floating point type.

Delineation of area of interest

The surface water was processed using a band 5 image, i.e., near infrared image. This image was then applied a threshold was applied to differentiate the surface water as they would be having very low reflectance values. The vegetation cover was assessed by deriving an NDVI image using the satellite images. The NDVI values are used to assign a pixel to a corresponding intensity of vegetation as per the criteria given in figure 3. These images are then density sliced create a vegetation intensity map for the study region.

Spatio-temporal variations

Surface Water

The variations of surface water for the period of five years is given in figure 4. It is clearly visible that the area under water for the year 2019 is large, which is due to the after-effect of 2018 flood. The area of surface water calculated is shown in the figure 5.

Vegetation cover

The variations of vegetation cover for the period of five years are given in figure 6, and it is clearly visible that a denser category of vegetation is less in case of the year 2019.

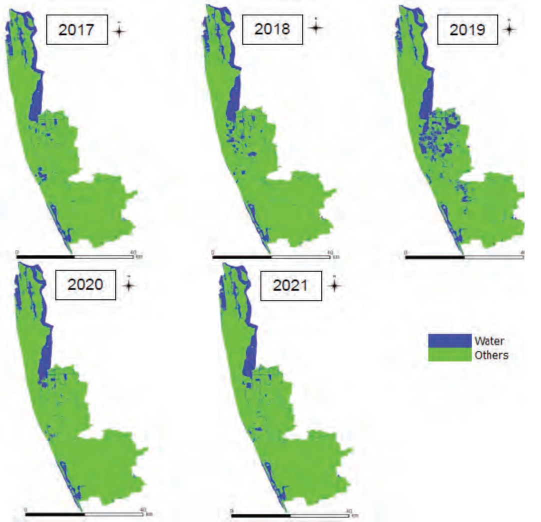

Fig. 4. The surface water changes for a span of five years

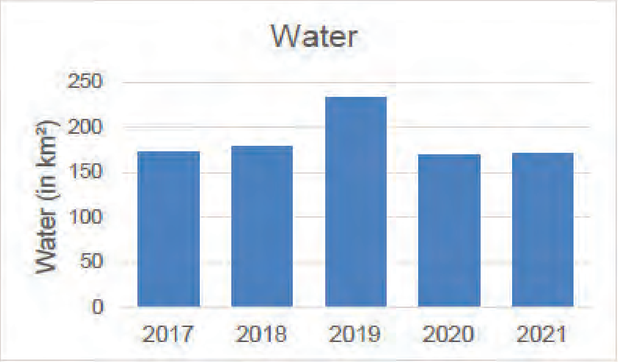

Fig. 5. Area of surface water

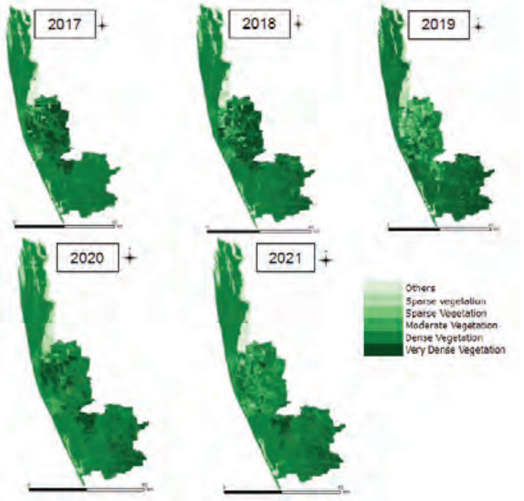

Fig. 6. The vegetation cover changes for a span of five years

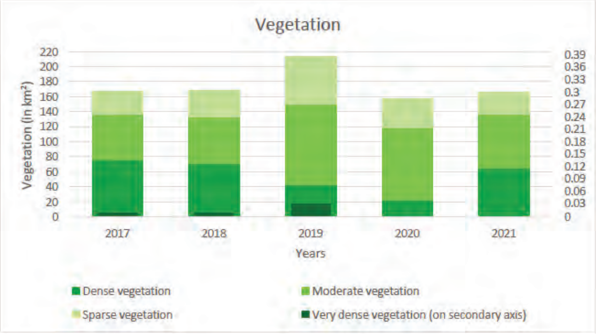

Fig. 7. Area of vegetation

It is clearly visible that the area under dense vegetation for the year 2019 is low and much lower in 2020, which is due to the after-effect of 2018 flood. The decrease in dense vegetation resulted in corresponding increase in moderate and sparse vegetation in 2019, which also further reduced in 2020. The area of vegetation calculated is shown in the figure 7.

CONCLUSION

The study demonstrates the use of remote sensing data to analyze spatio- temporal changes in water and vegetation cover in Alappuzha district, Kerala, India. It reveals the significant impact of the 2018 Kerala floods, marked by an increase in water area and a reduction in dense vegetation in 2019, followed by further vegetation decline in 2020, resulting in more moderate and sparse vegetation. Using open-source data and image processing tools, the study effectively illustrates core principles of remote sensing and Geographic Information Systems (GIS). To enhance accuracy, the methodology can be extended by incorporating additional satellite imagery and Digital Elevation Models (DEMs). Statistical tools and advanced methods like time series analysis and Monte Carlo simulations enhance model accuracy and alignment with real-world data.

REFERENCES

1. District environment plan for Alappuzha, Kerala state, 2021. Technical report by the Office of District Administration.
2. Kumar, D. N., and Reshmidevi, T.V., 2013. Remote Sensing Applications in Water Resources, Journal of the Indian Institute of Science, 93(2): 163 – 167.
3. Almalki, R., Mehdi K, Patricia M. S. and Jose F. R., 2022. Monitoring and Mapping Vegetation Cover

Changes in Arid and Semi-Arid Areas Using Remote Sensing Technology: A Review, Remote sensing, 14, 5143.

4. Dalezios, N., Domenikiotis, C., Tzortzios, S., & Kalaitzidis, C., 2001. Cotton yield estimation based on NOAA/AVHRR produced NDVI. Physics and Chemistry of the Earth, Part B: Hydrology, Oceans and Atmosphere. 26(3): 247-251.
5. Huang, Z., et al., 2020. Deep SAR-net: learning objects from signals. ISPRS Journal of Photogrammetry and Remote Sensing, 161: 179–193.
6. Chavez, P. S., 1996. Image-Based Atmospheric Corrections - Revisited and Improved. Photogrammetric Engineering and Remote Sensing, 62(9): 1025- 1036.
7. Lillesand T, Kiefer RW, Chipman J., 2015. Remote sensing and image interpretation. Wiley, New Jersey.

Long Term Trends in Rainfall and Extreme Indices Over Central Kerala

Krishnapriya K B
Department of Civil Engineering
Mar Athanasius College of Engineering
Kothamangalam, Kerala
✉ krishnapriyakb002@gmail.com

Riya Uday
Department of Civil Engineering
Mar Athanasius College of Engineering
Kothamangalam, Kerala
✉ riyauday02@gmail.com

Ashly Sara Issac
Department of Civil Engineering
Mar Athanasius College of Engineering
Kothamangalam, Kerala
✉ ashlysaraissac1142002@gmail.com

Alka Abraham
Department of Civil Engineering
Mar Athanasius College of Engineering
Kothamangalam, Kerala
✉ alka.ezrin@gmail.com

ABSTRACT

The intensification of human activities has caused global warming and increasingly dramatic climate changes, leading to an increase in the amount of extreme precipitation and temperature, resulting in destructive floods and landslides. The study discusses the trend analysis of rainfall, and extreme indices in the Ernakulam district of Kerala, India. Gridded precipitation data from the Indian Meteorological Department is utilised for the study. The monthly, seasonal, and annual rainfall of the district are studied based on the data of the past 72 years (1951-2022). Mann-Kendall test is used for trend analysis. In the current scenario, it is very important to study the trends in rainfall and extreme indices. The study emphasizes the patterns in yearly, seasonal, and monthly precipitation in the region. The study of extreme events high lights the susceptibility of climate change impacts in the area.

KEYWORDS: *Climate change, Mann Kendall test, Rainfall, Trend.*

INTRODUCTION

Climate change is the umbrella term for the wider range of effects caused by global warming. Global warming raises atmospheric humidity, while surface evapotranspiration accelerates the water cycle and causes more intense precipitation (Zhang et al., 2020). High frequency and intensity of precipitation events cause flash flooding (Singh et al., 2016). Recent trends in rainfall and climate patterns raise concerns about climate change and its potential impact. Rainfall events have been the subject of numerous studies conducted at larger spatial domains, such as national and regional scales, but relatively few researches have been conducted at the local level. By assessing these trends, We can make sensible choices to reduce risks and respond to increasing environmental conditions, so upholding the sustainability of our ecosystems and communities. More flash floods might arise due high frequency and severity of precipitation. (Singh et al., 2016). It is challenging to assign risk and socioeconomic vulnerabilities across state and national lines due to the cumulative effects of extreme events (Yaduvanshi et al., 2020). In India, precipitation has decreased during the past thirty years, while extreme precipitation events have increased in some areas (Zhang et al., 2020). The majority of the research examined rainfall patterns as well as maximum and minimum time series; however, with the current discussion of climate change, a greater emphasis is being placed on extreme events.

STUDY AREA

Ernakulam district, located in Kerala, India is selected for the study. Relatively few studies have been done at the local level on rainfall events, in contrast to the substantial amount of research conducted on broader geographical scales such as national, river basin, and larger regional levels, including Central India and urban areas of India. As a result, the current study is focused on examining rainfall patterns in the selected area. The study region spans from 9.90 to 10.070 N latitudes and from 76.20 to 76.40E longitudes, covering an approximate area of 3068 square kilometres.

Fig. 1 Ernakulam district (source: - https://www.mapsofindia.com/maps/kerala/districts/ernakulam-district-map.jpg)

METHODOLOGY

In order to analyse and evaluate rainfall patterns in the examined region, this study analyses daily rainfall data for 12 grids (0.25°x0.25°) during a 72-year period (1951–2022). Trend analysis is done using the Mann-Kendall (MK) test. "R Studio," a data analysis tool that lets you import, compile, modify, analyse, model, and produce machine learning predictions, is used to conduct the trend test. The MK test is a statistical tool adopted for identifying trends in time series data. It determines if a dataset's trend is continuously rising or declining over time. Because it is non-parametric and does not presuppose a certain distribution for the data, it can be applied to a wide range of situations. The slope of a linear trend in time series data can be identified via Sen's slope, a non-parametric method. Theil-Sen estimator or Sen's estimator are additional names for it.

RESULTS AND DISCUSSION

Trend analysis of rainfall

Rainfall trends for the Ernakulam section have been reviewed using 72 years of IMD rainstorm data, from 1951 to 2022. Sen's Slope (SS) estimator and the MK test were applied to ascertain the trend in rainfall. Trend analysis at yearly, seasonal, and periodic time way takes into account the diurnal rainfall data. For trend analysis, a aggregate of 12 grids are taken into account throughout the area. Figure 2 displays a plot for a sample grid, while Tables 1 and 2 display the periodic, yearly, and seasonal values illustrating significant trends for the area at each grid.

Trend analysis of extreme rainfall indices

Extreme indices are statistical measures used to assess extreme events such as heat waves, heavy rainfall, or droughts. These indices help quantify the intensity, duration, and frequency of extreme weather conditions, providing valuable information on climate change. For a climate change study in Kerala, the extreme indices defined by the Expert Team on Climate Change Detection and Indices (ETCCDI), such as Maximum daily rainfall (Rx1day), Maximum 5-day rainfall (Rx5day), Consecutive Dry Days (CDD), Consecutive Wet Days (CWD), Number of heavy rainfall days (R10), Number of very heavy rainfall days (R20), and Simple Daily Intensity Index (SDII) are considered.

Table 1: Trend analysis results of rainfall for Grids 1 to 6

Parameter: Rainfall Annual	Grid 1		Grid 2		Grid 3		Grid 4		Grid 5		Grid 6	
	z	SS	z	SS	z	SS	z	SS	z	SS	z	SS
	0.515	2.15	-0.58	-2.26	0.4	1.74	2.43	10	0.88	-2.63	-1.53	-6.17
Pre-Monsoon	0.12	0.16	-0.41	-0.55	-0.45	-0.76	2.34	1.78	-1.08	-1.26	-0.87	-1.58
Monsoon	0.46	1.22	-0.7	-2.08	0.79	3.28	1.61	5.04	-1.11	-2.65	-1.75	-5.13
Post- Monsoon	0.95	1.155	0.22	0.36	-0.88	-1.17	2.88	2.59	0.7	0.75	-0.62	-0.86
Winter	-0.41	-0.16	-0.102	-0.02	-1.123	-0.36	1	0.32	1.11	0.34	-0.52	-0.15
January	0.42	0	0.02	0	-1	-0.05	1.02	0	0.07	0	-0.86	-0.01

February	-1.24	0	-1.76	-0.14	-1.09	-0.097	1.79	0.06	-034	0	-1.37	-0.08
March	1.29	0.22	0.66	0.16	0.097	0.01	1.15	0.56	0.2	0.02	0.41	0.07
April	-0.194	-0.06	-1.05	-0.59	-1.03	-0.036	2.25	0.7	-1	-0.42	-1.53	-0.81
May	-0.23	-0.21	0.05	0.07	-0.47	-0.43	2.45	1.05	-0.66	-0.59	-0.54	-0.54
June	0.034	0.05	-0.69	-0.82	-0.52	-0.72	0.51	0.470	-2.21	-3.18	-1.4	-1.8
July	0.15	0.18	-1.61	-2.199	-0.07	-0.19	0	-0.01	-1.69	-2.12	-2.05	-2.82
August	0.73	0.75	-0.03	-0.06	1.38	2.08	2.04	2.29	0.27	0.2	-0.52	-0.51
September	1.1	0.78	0.13	0.12	1.33	1.27	2.86	1.6	0.43	0.41	0.25	0.31
October	0.58	0.36	-0.79	-0.75	-0.81	-0.69	2.6	1.45	0.19	0.78	-1.52	-1.28
November	1.41	0.76	1	0.77	-0.45	-0.25	1.35	0.64	10.6	0.54	0.45	0.36
December	-0.73	-0.08	0.35	0.06	-1.05	-0.18	0.42	0.09	0.72	0.96	0.1	0.02

Table 2: Trend analysis results of rainfall for Grids 7 to 12

Parameter: Rainfall Annual	Grid 7		Grid 8		Grid 9		Grid 10		Grid 11		Grid 12	
	z	SS	z	SS	z	SS	z	SS	z	SS	z	SS
	-2.49	-12.82	1.56	5.6	-1.04	-3.63	-2.9	-10.96	-0.04	-0.57	5.35	20.6
Pre-Monsoon	-2.78	-2.94	-0.37	-0.3	-2.12	-2.65	-3.45	-3.74	-068	-0.65	2.69	1.59
Monsoon	-1.414	-5.34	1.42	4.59	-1.14	-2.55	-1.93	-6.09	0.24	1.47	5.52	17.21
Post- Monsoon	-2.318	-2.85	0.34	0.3	0.35	0.35	-2.71	-2.91	-1.21	-1.35	-014	-0.08
Winter	-2.114	-0.692	-0.13	-0.04	0.22	0.06	-0.34	-0.097	-1.05	-0.35	-0.68	-0.25
January	-1.62	-0.05	-0.22	0	-0.51	0	-1.21	-0.005	-1.19	0	0.47	0
February	-1.61	-0.117	0.23	0	-0.55	0	-0.87	-0.007	-0.42	0	2.26	0.04
March	-0.01	0	0.38	0.08	-0.7	-0.06	-0.19	-1.03	0.64	0.09	3.1	0.34
April	-1.998	-0.79	-0.74	-0.29	-1.86	-0.73	-2.82	-1.07	-1.33	-0.45	2.72	0.71
May	-2.8	-2.28	-0.3	-0.17	-1.42	-1.36	-2.9	-2.37	-1.08	-0.62	1.02	0.45
June	-2.22	-3.2	-028	-046	-1.78	-2.59	-2.79	3.76	-0.57	-0.96	4.31	4.04
July	-1.22	-2.57	0.17	0.35	-1.33	-1.94	-1.93	-3.36	-0.84	-1.97	3.41	4.05
August	-0.063	-0.12	2.45	3.25	0.04	0.06	-0.98	-1.08	1.08	1.93	5.38	5.02
September	0.7	0.777	2.18	1.68	0.52	0.56	-0.12	-0.15	0.43	0.51	4.17	2.83
October	-2.26	-1.873	0.54	0.37	0.35	0.29	-2.74	-1.96	-1.35	-0.92	2.18	1.33
November	-1.54	-0.98	0.01	0.006	0.09	0.08	-1.27	-0.73	-1.27	-0.74	-0.14	-0.08
December	-0.88	-0.172	-1.15	-0.01	0.1	0	-0.03	0	-1.04	-0.16	-0.79	-0.22

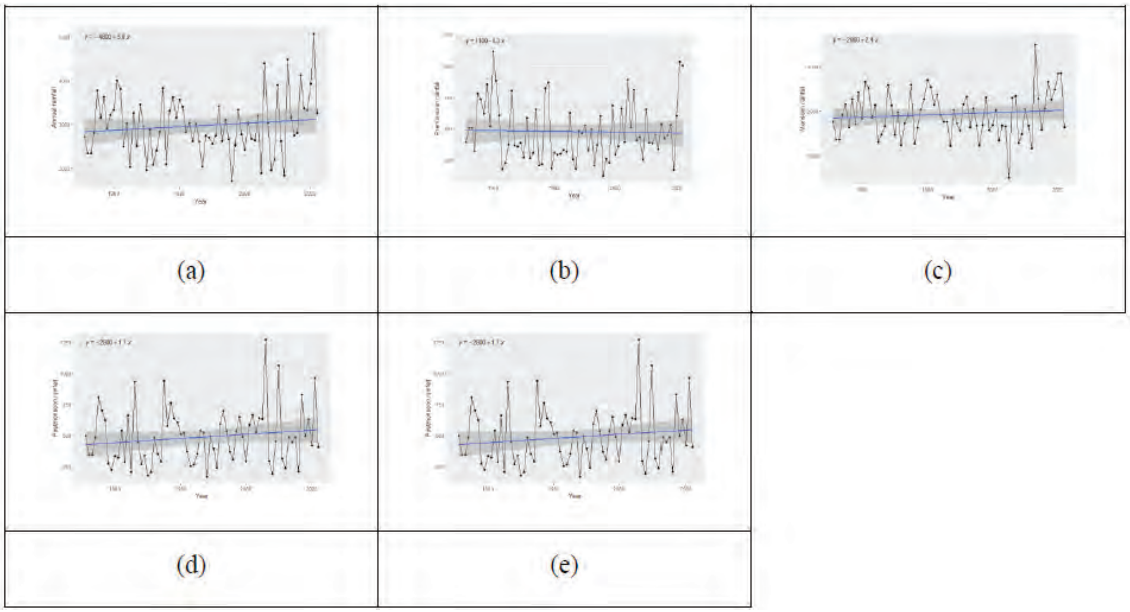
(a) (b) (c)

(d) (e)

Fig. 2: Trend of rainfall for sample grid (lat-10°0'N and long- 76°45' E) (a)Annual (b)Pre-Monsoon (c)Monsoon (d) Post-Monsoon (e)Winter

RX1day focuses on extreme precipitation events, which are characterized by unusually high amounts of rainfall within a short duration, often leading to flooding, landslides, and other hazards. The index identifies the single day within the measurement period that recorded the highest amount of precipitation. This maximum value represents the intensity of the most extreme precipitation event during that time frame. Increasing trends in Rx1day values over time can provide insights into climate variability and change. RX5day focuses on identifying extreme precipitation events that occur over multiple days, capturing prolonged periods of heavy rainfall. These events can have significant impacts on flooding, agriculture, infrastructure, and ecosystems. Increased Rx5day measurements reflect more severe and sustained extreme precipitation happenings. Monitoring changes in Rx5day values over time can provide valuable information on frequency and intensity of multi-day heavy rainfall, which are crucial for understanding climate variability and change. The index is also exhibiting an increasing trend in the study area.

When there is no precipitation for several days in a row, it is referred to as consecutive dry days. This phrase is frequently used in weather forecasting and monitoring, particularly in areas where water scarcity or drought conditions may be an issue. The CDD is found to be rising in the region. The duration of continuous wet weather periods is measured in climatology using the consecutive wet day's extreme index (CWD). CWD is especially helpful in determining how long and how severe rainfall events are, as these factors can have a big impact on a lot of different industries, such as infrastructure planning, agriculture, and water resource management. The CWD is showing a declination.

The extreme precipitation indices are also essential for comprehending flood and drought-like circumstances (Karki et al. 2017). The R10 extreme index typically refers to the number of days within a specific period where the daily minimum temperature exceeds a predefined threshold, often calculated as the 10th percentile of the climatological distribution for that location. In simpler terms, it represents the frequency of relatively warm nights compared to historical data for a given area. The R20 extreme index is similar to the R10 extreme index but focuses on a different threshold. It represents the number of days within a certain period where the daily minimum temperature exceeds the 20th percentile of the climatological distribution for that location. The index R10 and R20 are exhibiting a mixed trend in the region.

The extreme precipitation index SDII is a metric used in climate science to assess the intensity of precipitation over a given period. This allows for the focus on the intensity of precipitation events rather than the frequency of rainy days. SDII is calculated by dividing the total precipitation on all wet days by the total number of wet days during the measurement period. This provides the average daily precipitation intensity for the period under consideration. Higher values of SDII indicate greater average daily precipitation intensity during wet days. This metric is useful for understanding the intensity of precipitation events and their potential impacts on various sectors such as agriculture, water resources, infrastructure, and ecosystems. The extreme precipitation index SDII is observed to show an increasing trend in the district. The results is shown as a sample grid in Figure 3.

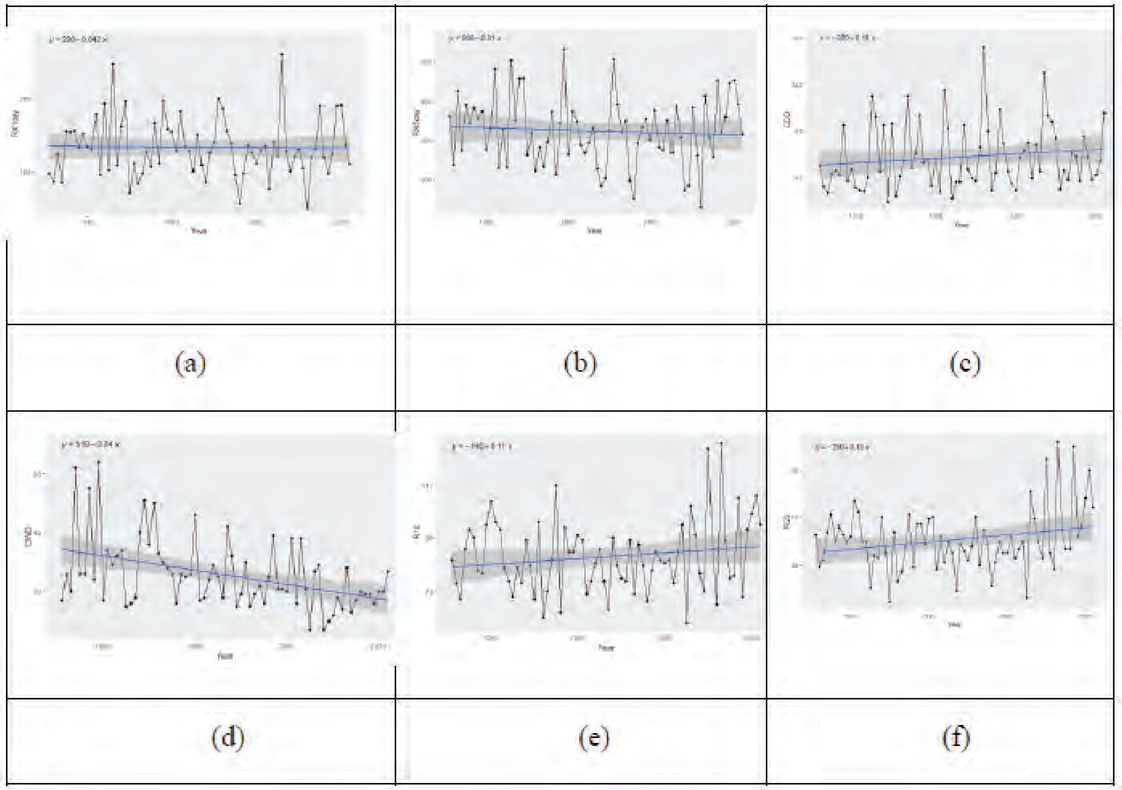

(a) (b) (c)

(d) (e) (f)

Fig. 3. Plot showing trend of Extreme indices for Grid 1(a) RX1day (b) RX5day (c) CDD (d) CWD (e) R10 (f) R20

CONCLUSIONS

Analysis of rainfall trend has been done for Ernakulam district of Kerala by collecting daily gridded data of the past 72 years (1951- 2022) for 12 grids using the IMD, using the Mann-Kendall test method. The findings showed varied pattern of trends for monthly, seasonal, and yearly rainfall. The computation of seven precipitation extreme indices revealed a substantial lowering trend in CWD and a growing trend in RX1day, RX5day, and SDII. The long-term trend analysis of rainfall and extreme precipitation indices reveals valuable insights into climate patterns. We can make better decisions on adaptation and mitigation approaches in a range of areas, particularly infrastructure planning, agriculture, and water resource management, by looking at these trends.

REFERENCES

1. Singh, D., Jain, S. K., Gupta, R. D., Kumar, S., Rai, S. P., & Jain, N. (2016). Analyses of observed and anticipated changes in extreme climate events in the Northwest Himalaya. Climate, 4(1), 9.
2. Karki, R., Hasson, S. U., Schickhoff, U., Scholten, T., & Böhner, J. (2017). Rising precipitation extremes across Nepal. Climate, 5(1), 4.

3. Zhang, D., Wang, W., Liang, S., & Wang, S. (2020). Spatiotemporal variations of extreme precipitation events in the Jinsha River Basin, Southwestern China. Advances in Meteorology, 2020, 1-13.

4. Yaduvanshi, A., Kulkarni, A., Bendapudi, R., & Haldar, K. (2020). Observed changes in extreme rain indices in semiarid and humid regions of Godavari basin, India: risks and opportunities. Natural Hazards, 103, 685-711.

5. Chahal, M., Bhardwaj, P., & Singh, O. (2021). Exploring the trends and pattern of rainfall extremes over the semiarid Sahibi basin in Rajasthan, India. Arabian Journal of Geosciences, 14, 1-16.

Design of Experiment – Time Taken to Boil 20 mL of Water

Akshay Ranjith
Department of Civil Engineering
Indian Institute of Science
Bangalore, Karnataka
✉ rakshay@iisc.ac.in

Rajinikanth B
Department of Aerospace Engineering
Indian Institute of Science
Bangalore, Karnataka
✉ rajinikanthb@iisc.ac.in

Sumanth S P
Dept. of Instrumentation and Applied Physics (IAP)
Indian Institute of Science
Bangalore, Karnataka
✉ sumanths@iisc.ac.in

Lakshminarayana Rao
Department of Aerospace Engineering
Centre for Sustainable Technologies (CST)
Interdisciplinary Center for Water Research (ICWaR)
Department of Materials Engineering
Indian Institute of Science
Bangalore, Karnataka
✉ narayana@iisc.ac.in

ABSTRACT

Unlocking the secrets of efficient experimentation lies at the heart of the Design of Experiments (DOE), where every trial holds the key to optimizing outcomes and unraveling the intricate dance of variables. The study investigates the application of DOE through a straightforward yet illustrative example of boiling a certain quantity of water, employing a comprehensive framework of experimental design and analysis. Initial phases encompass the creation of a fishbone diagram, a structured test plan, and instrument calibration to meticulously identify and categorize factors influencing water boiling time. Utilizing full and fractional factorial designs alongside blocking methodologies, the study aims to ascertain the most suitable model and ensure consistency in experimental outcomes. Quantification and analysis of variable effects through ANOVA and linear regression techniques aid in determining individual impacts, interactions, and the development of a robust regression model. Validation experiments, including OFAT studies and optimization through Response Surface Methodology (RSM), streamline the boiling process and identify optimal conditions effectively. The study's findings underscore the significance of structured methodologies in understanding and optimizing the water boiling process, paving the way for future explorations in refining optimization techniques and expanding the applicability of findings in diverse settings.

KEYWORDS: *Design of experiments, Analysis of variance (ANOVA), Factorial designs.*

INTRODUCTION

The efficiency of boiling water, a seemingly simple task, is influenced by numerous factors that intricately intertwine to define the time required to reach this threshold. This study employs factorial design of experiments to investigate the time it takes to boil 20 mL of water, aiming to identify conditions that minimize boiling time. By analyzing six key response variables, the study distinguishes between controllable and uncontrollable factors, isolating those directly impacting boiling time. This comprehensive investigation not only quantifies the effects of variables but also sheds light on the intricate interplay between factors affecting the boiling time of water by meticulously exploring factorial designs, regression analyses, and optimization experiments.

LITERATURE REVIEW

General

Design of Experiments (DOE), such as factorial designs, allow for the simultaneous manipulation of multiple variables at different levels. This enables the study to understand not only the individual effects of factors but also their interactions. One-Factor-at-a-Time (OFAT) experiments, on the other hand, alter one variable at a time while keeping others constant. Conducting a comprehensive array of OFAT experiments can be time- consuming and resource-intensive. Designed experiments, through fractional factorial or full factorial designs, reduces the number of experimental runs needed to gather comprehensive data. Designed experiments are rooted in statistical methodologies, allowing for robust analysis using tools like analysis of variance (ANOVA) and regression analysis. By utilizing a series of designed experiments, typically employing factorial or central composite designs, Taguchi methods, Robust Parameter Methodology (RPM), particularly the Response Surface Methodology (RSM) constructs mathematical models that depict the complex interactions between factors and their influence on the response [1]. RSM's iterative and methodical approach allows for the identification of the true optima, enabling researchers to fine-tune processes or systems for maximum performance or desired outcomes. These are widely used for performance studies such as adsorption performance of Zeolite by Imessaoudene et al., Optimization studies by Kassimi et al., and improvement of the traditional OFAT through DOE by Wahid and Nadir [2,3,4].

OFAT experiments might lack the statistical rigor required to accurately determine the relationship between variables. The structured nature of factorial designs also mitigates the domino effect seen in OFAT experiments, where an inconclusive result from one step can disrupt the entire study. OFAT experiments suffer from low precision and the risk of false optima, designed experiments transcends this pitfall by considering multiple factors concurrently [5]. However, despite its proven efficacy, the widespread adoption of DOE faces significant barriers. DOE also relies on statistical assumptions, and deviations from these assumptions might compromise the accuracy of conclusions drawn from experiments. For instance, assumptions related to normality or homogeneity of variance might not always hold true in practical settings, affecting the reliability of DOE outcomes [6]. Designed experiments, particularly with orthogonal designs, facilitate predictability and conclusiveness, enhancing the reliability and robustness of scientific conclusions [7].

Need for the study

In experimental research, the simplicity of the OFAT approach often leads to its widespread use despite its disadvantages. For instance, when measuring the time required to boil water, factors such as heat intensity, water volume, container size, and atmospheric pressure interact in ways that OFAT cannot adequately capture. Designed experiments, particularly factorial designs, allow for the simultaneous manipulation of multiple variables, facilitating a comprehensive understanding of their individual and combined effects. Utilizing statistical tools like ANOVA (Analysis of Variance) and regression analysis, these experiments provide nuanced insights and optimize processes more effectively than sequential OFAT methods.

Based on the study of literatures, the following objectives were formulated to be done in the study area would be to develop a comprehensive analysis framework through the creation of a fishbone diagram, a structured test plan, and instrument calibration to identify, categorize, and ensure precision in measuring factors influencing water boiling time. To perform full and fractional factorial model comparisons, the efficiency of the fractional model, to ascertain the most suitable model and ensure consistency in experimental outcomes.

METHODOLOGY

General

The study involves the use of an simple experiment such as the time required to boil 20 mL of water; to demonstrate the DOE as well as OFAT set of experiments and various tools associated with them. The study is divided into four parts, namely, fish bone diagram, test plan and instrument calibration; OFAT, fractional and full factorial design; ANOVA and linear regression; Main effects, interactions and surface plots.

3.2 Fishbone diagram, test plan and instrument calibration

A fishbone diagram categorizes potential causes of a problem into design factors (manipulated variables), held constant factors (unchanged variables), uncontrollable factors (external influences), and nuisance factors (secondary variables), aiding in systematic root cause analysis. A test plan comprises exploratory experiments to identify variables, screening experiments using factorial designs to determine significant factors, and optimization experiments employing Response Surface Methodology (RSM) for optimal conditions. The rotameter is to be calibrated for accurate measurement of air flow. The master instrument used for the calibration is the Mass flow controller which is factory calibrated and has a response time of 30 ms. The calibration should cover the entire range of the experiment.

OFAT, fractional and full factorial design

In OFAT design, one factor is varied while others are kept constant. Fractional factorial design efficiently explores multiple factors by examining a selected subset of factor combinations, significantly reducing the number of experimental runs required while still providing valuable insights into the most influential variables and their interactions. Here, the fractional factorial design keeps one factor constant with the other three factors being varied across the ranges. Full factorial design systematically examines all possible combinations of the design factors and their levels, offering a comprehensive exploration of how each factor and their interactions impact the outcome. Their results are then compared with that of the fractional factorial design.

ANOVA and linear regression

ANOVA

ANOVA assesses whether there are statistically significant differences between group means, aiding in understanding the impact of various factors on the observed outcomes. It enables the partitioning of total variability into components attributed to different factors, to quantify the significance of these factors influencing the response variable. The significance of the factors is estimated using the F value (Equation 1) and compared to the value from the F distribution [8]. ANOVA is done using R studio as well as Microsoft excel.

$$F = Mean\ Squares\ Between/Mean\ Squares\ Error \quad (1)$$

Linear regression

Linear regression elucidates relationships between variables by modeling how one or more predictors relate linearly to an outcome, aiding in understanding the directional impact of factors on the observed response. Here, for each of the designs, the time required to boil is modelled as a linear combination of response variables. Linear regression is done using R studio as well as Microsoft excel.

Main effects, interactions and surface plots

Main effects plots illustrate the individual impacts of different factors on the response variable, while keeping others constant. Interactions plots reveal the combined effects of multiple factors, highlighting whether the effect of one factor depends on the level of another, which explains the complex relationships and synergies between variables. Surface plots extend this understanding by visually representing the three-way interactions among factors, offering a comprehensive view of how variations in two factors affect the response, helping to identify optimal conditions or regions within the experimental space.

RESULTS AND DISCUSSION

The experimental study is to find the time required to boil 20 mL of water. For this, a fish bone diagram and the calibration of the instrument used in the study are done. Fractional and full factorial designs are done. Each design undergoes ANOVA and linear regression analyses. Subsequently, the exploration of main effects, interactions, and surface plots provides a comprehensive understanding of the experimental outcomes.

Fish bone diagram, test plan and instrument calibration

The fish bone diagram for the experiment with various types of factors on the backbone is shown in Figure 1.

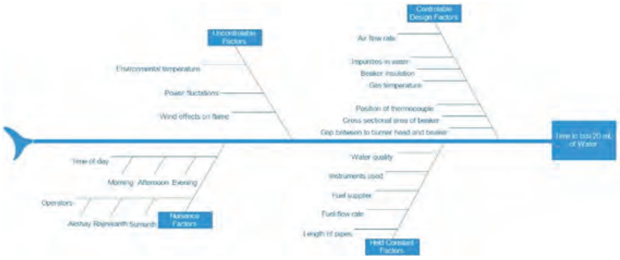

Fig. 1: Fish bone diagram for the experiment

The test plan consists of objectives, the exploratory experiments, screening experiments and results. For a test, each of the factor is kept at a high (+) and a low (-) value. The six response variables are [A] percentage excess air over fuel (CH_4) which ranges from -75 % (-) to 0 % (+). The plus and minus symbols in brackets indicate the ranges and the alphabets in box brackets indicate the same factor; [B] fuel – air mixture gas temperature which ranges from Room temperature (-) to 50 °C (+); [C] average water hardness (TDS) which ranges from 50 NTU (-) to 950 NTU (+); [D] beaker to burner surface area ratio which ranges from 2.8 (-) to 6.6 (+); [E] Beaker Insulation which are without or No insulation (-) and with insulation (+); and [F] the height difference between burner and beaker which ranges from 38 mm (-) to 16 mm (+). For all the factors two levels are considered. The experimental set up is shown in Figure 2 (a). The calibration of the rotameter is done using mass flow controller (MFC) as the standard. The gas used is 99.9% pure nitrogen. The entire range of the experiment is covered. The R2 value between the MFC and rotameter readings are 0.99.

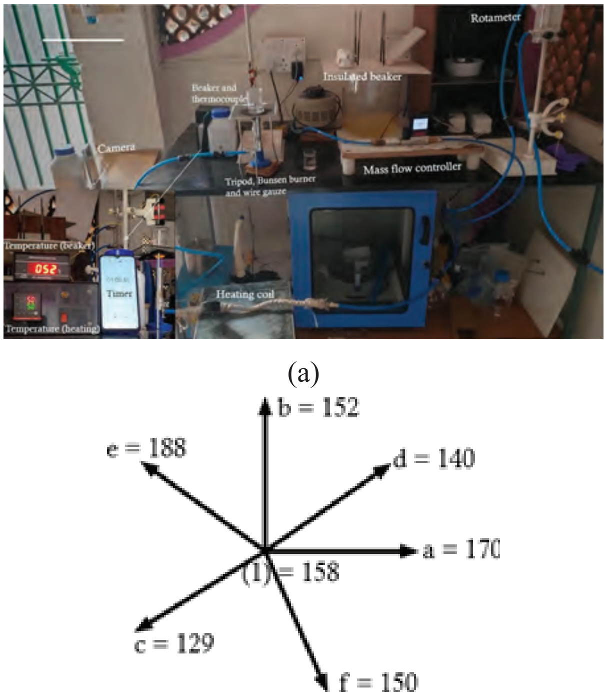

(a)

(b)

Fig. 2. (a) The experimental setup and (b) OFAT design

OFAT, fractional and full factorial design

The OFAT design is done such that each of the factors is kept constant while only one is varied. The OFAT design is shown in Figure 2 (b), where the lines for each factor represents the experiments for each of its high and low points, the time taken to boil 20 mL of water in seconds is denoted at each point.

The fractional factorial design is done for both the positive (+) and the negative (-) values of the F factor and it consists of all the combinations of A, B and C factors. The fractional factorial design of F – is shown in Figure 3 (a). For example, in Figure 3 (a) the vertex 'a' denote the experiment where, the factor A is high while all else are at low. The full factorial design consists of all combinations of A, B, C and F factors which is shown in Figure 3 (b).

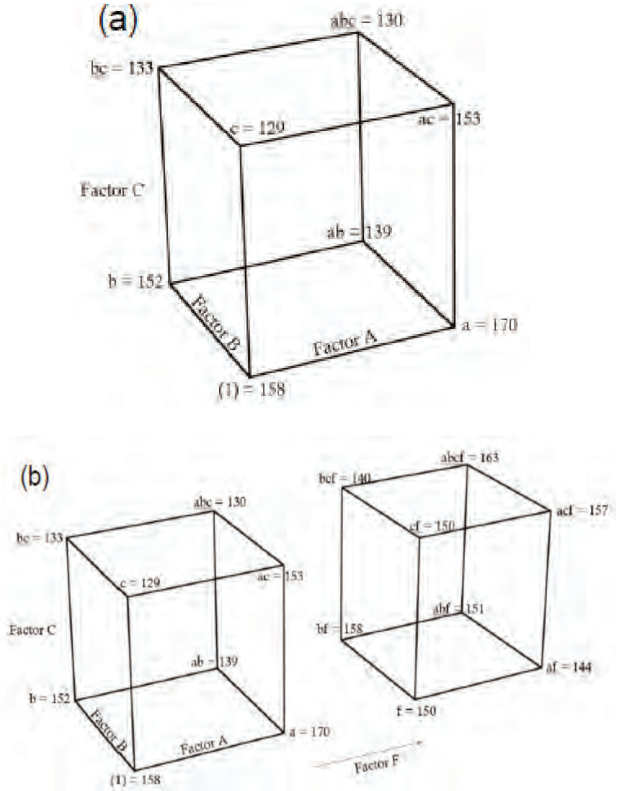

Fig. 3. The fractional factorial designs of (a) F - and (b) A full factorial design of 4 factors and 2 levels

ANOVA and linear regression

OFAT Design

ANOVA brings out the factors C and E being statistically significant at 0.05 level, while A and D being statistically significant at 0.1 level. The ANOVA table is given in Table 1.

Table 1. ANOVA table and regression results for OFAT design

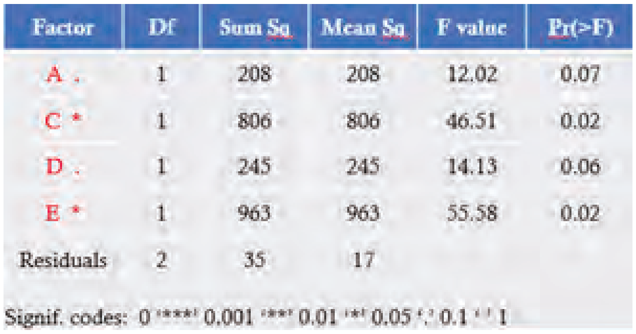

Factor	Df	Sum Sq	Mean Sq	F value	Pr(>F)
A .	1	208	208	12.02	0.07
C *	1	806	806	46.51	0.02
D .	1	245	245	14.13	0.06
E *	1	963	963	55.58	0.02
Residuals	2	35	17		

Signif. codes: 0 '***' 0.001 '**' 0.01 '*' 0.05 '.' 0.1 ' ' 1

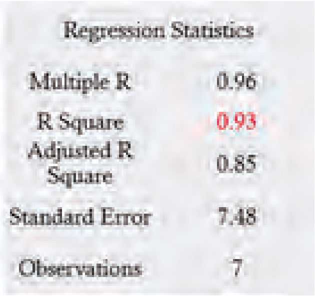

Regression Statistics	
Multiple R	0.96
R Square	0.93
Adjusted R Square	0.85
Standard Error	7.48
Observations	7

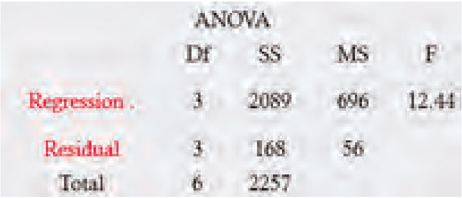

ANOVA	Df	SS	MS	F
Regression .	3	2089	696	12.44
Residual	3	168	56	
Total	6	2257		

A linear regression (Equation 2 in coded variables and Equation 3 in actual variables) using the significant terms from the ANOVA gives the best fit in consideration with parsimony. ANOVA on the regression reveals that the linear fit is statistically significant to 0.025 level using F test. The details are given in Table 1.

$$t = 168.5 + 10.0(ExcessAir) - 10.5(TDS) + 19.0(Insulation) \quad (3)$$

$$t = 170.17 + 0.27(ExcessAir) - 0.02(TDS) + 19.00(Insulation) \quad (4)$$

Fractional factorial design with F

ANOVA brings out the factors B, C and the interaction AB being statistically significant at 0.05 level. The ANOVA table is given in Table 2. A linear regression (Equation 4) using the significant terms from the ANOVA gives the best fit in consideration with parsimony. ANOVA on the regression reveals that the linear fit is statistically significant to 0.025 level using F test. The details are given in Table 2.

$$t = 145.50 - 7.00(MixTemp) - 9.25(TDS) - 6.50(ExcessAir * MixTemp) \quad (4)$$

Table 2. ANOVA table and regression results for fractional factorial design with F –

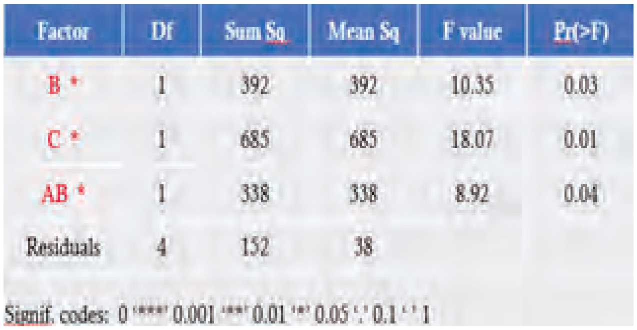

Factor	Df	Sum Sq	Mean Sq	F value	Pr(>F)
B *	1	392	392	10.35	0.03
C *	1	685	685	18.07	0.01
AB *	1	338	338	8.92	0.04
Residuals	4	152	38		

Signif. codes: 0 '***' 0.001 '**' 0.01 '*' 0.05 '.' 0.1 ' ' 1

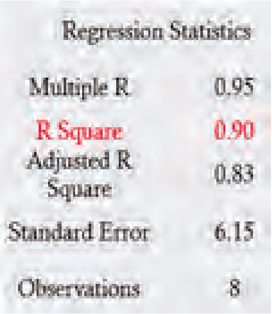

Regression Statistics	
Multiple R	0.95
R Square	0.90
Adjusted R Square	0.83
Standard Error	6.15
Observations	8

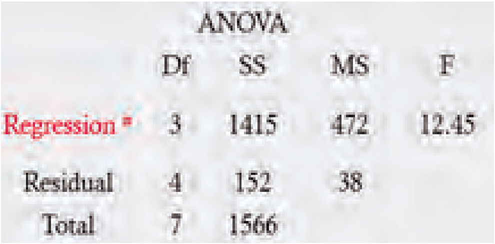

ANOVA	Df	SS	MS	F
Regression *	3	1415	472	12.45
Residual	4	152	38	
Total	7	1566		

Full factorial design with A, B, C and F

ANOVA brings out the factors B, C, F and the interaction AB, CF and ABF being statistically significant at 0.01 and 0.05 level, respectively. The ANOVA table is given in Table 3. A linear regression (Equation 5) using the significant terms from the ANOVA gives the best fit in consideration with parsimony. ANOVA on the regression reveals that the linear fit is statistically significant to 0.01 level using F test. The details are given in Table 3. The residual plot as shown in Figure 4, reveals that the residuals are random.

$$t = 139.19 - 4.94(MixTemp) - 5.69(TDS) - 6.31(Height) - 3.31(ExcessAir * MixTemp) + 2.94(MixTemp * TDS) + 3.56(TDS * Height) + 3.19(ExcessAir * MixTemp * Height)$$

Table 3. ANOVA table and regression results for full factorial design with A,B,C and F

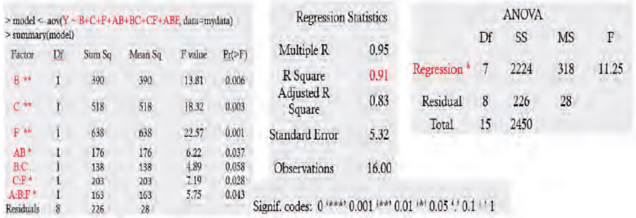

```
> model <- aov(Y ~ B+C+F+AB+BC+CF+ABF, data=mydata)
> summary(model)
```

Factor	Df	Sum Sq	Mean Sq	F value	Pr(>F)
B **	1	390	390	13.81	0.006
C **	1	518	518	18.32	0.003
F **	1	638	638	22.57	0.001
AB *	1	176	176	6.22	0.037
B:C .	1	138	138	4.89	0.058
C:F *	1	203	203	7.19	0.028
A:B:F *	1	163	163	5.75	0.043
Residuals	8	226	28		

Regression Statistics	
Multiple R	0.95
R Square	0.91
Adjusted R Square	0.83
Standard Error	5.32
Observations	16.00

ANOVA

	Df	SS	MS	F
Regression *	7	2224	318	11.25
Residual	8	226	28	
Total	15	2450		

Signif. codes: 0 '***' 0.001 '**' 0.01 '*' 0.05 '.' 0.1 ' ' 1

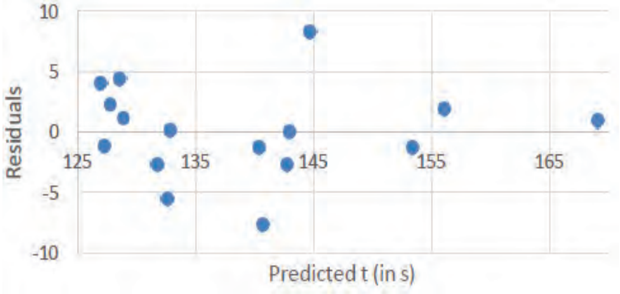

Fig. 4. Residual plot of full factorial design

Comparison of fractional with full factorial design

Comparing the results of the full and fractional factorial experiments, which have a similar R2 value of 0.91 and 0.90, standard error of 5.32 s and 6.15 s respectively. This shows that only fractional factorial experiments are adequate and advantages that more of the design space was explored with minimum effort.

Main effects, interactions and surface plots

Main effects

The plots of effects as shown in Figure 5, the factors B,C and F have a decreasing trend, which means that the time to boil water decreases as the factors such as the gas temperature and water hardness increases; and the height difference between burner and beaker increases. The normal probability plot of effects as shown in Figure 6 helps us to determine the significant factor, which does not lie on the straight line (dotted line).

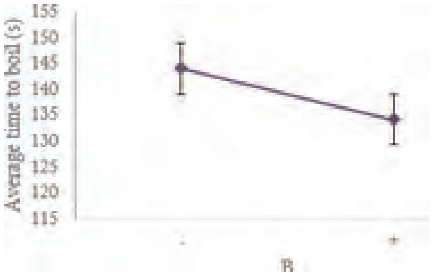

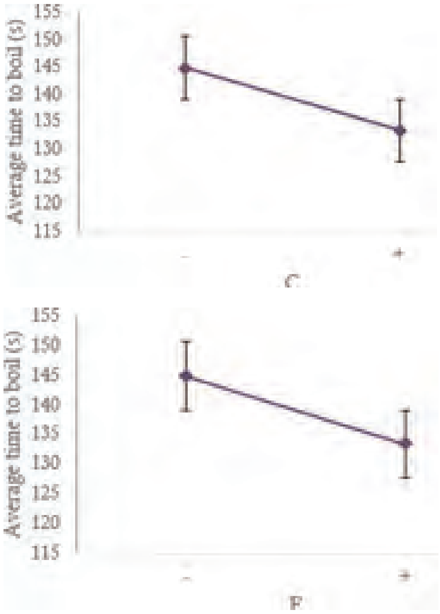

Fig. 5. Main effects

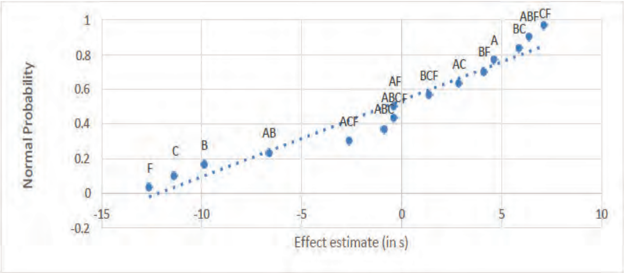

Fig. 6. Normal probability plot of effects

Interactions

The plots of interactions reveal that in AB has a decreasing effect as B = - and B = + has different trends while in the case of BC and CF, they have an increasing effect on the response. The interaction plots are shown in Figure 7 (a). Therefore, B, C and F factors can be increased for a lesser time to boil water.

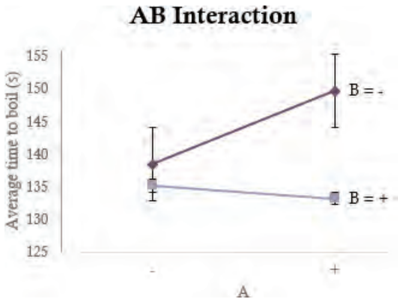

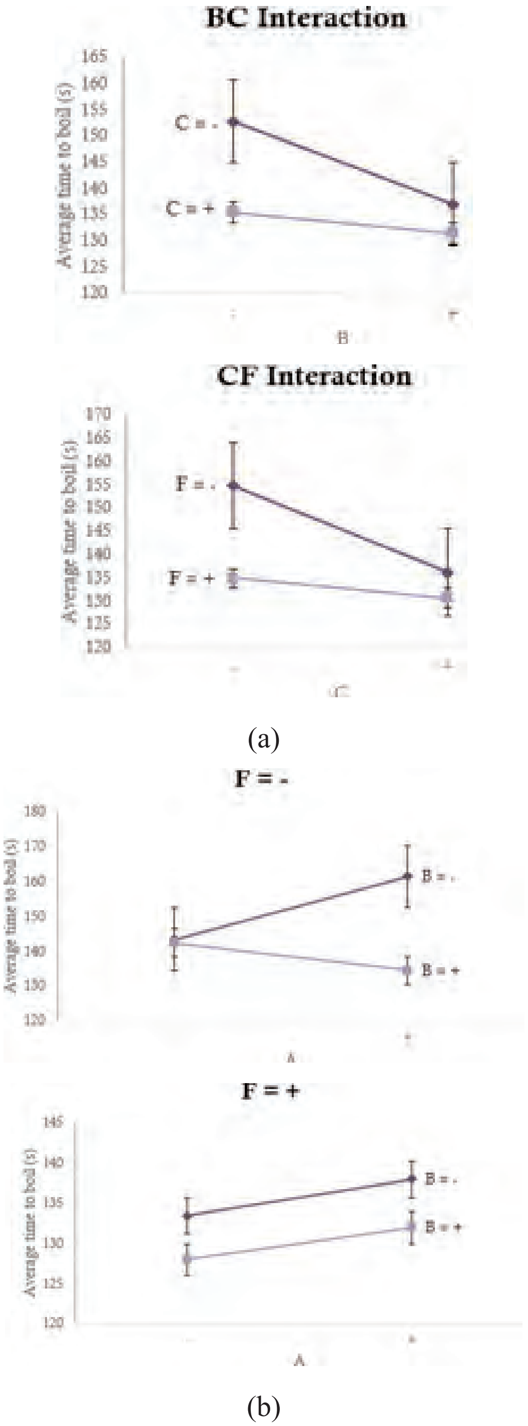

(a)

(b)

Fig. 7. (a) Two factor and (b) Three factor interaction plots

The three-factor interaction as shown in Figure 7 (b), suggests that increasing the factor F affects to increase the time taken to boil water. Therefore, factor F should be increased in an incremental manner while other factors A and B are increased.

Surface plot

The analysis done on the entire dataset was used to produce the surface plot as shown in Figure 8. The surface plot represents the modelled surface of response in the present design space for a hypothetical boiling time of 50 seconds and 15 seconds.

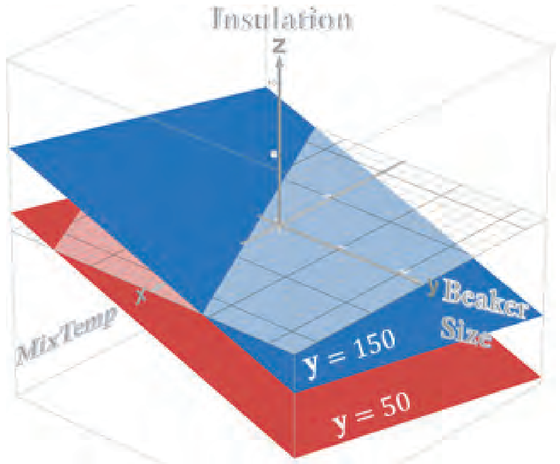

Fig. 8. Surface plot of modelled response

CONCLUSION

The study presents an example of using design of experiments to effectively conduct experiments and to get the most out of the resources. In conclusion, the study employed a comprehensive approach to unravel the intricacies affecting water boiling time. The minimum boiling time was found to be 126 ± 1 s. In the example presented in the study, a higher gas temperature, smaller non-insulated beaker would produce a smaller boiling time. The utilization of a structured analysis framework, encompassing the creation of a fishbone diagram, a meticulously planned experiment, and instrument calibration, facilitated the identification and precise measurement of influential factors. The comparison between full and fractional factorial models, coupled with the implementation of blocking design methodologies, ensured consistency and reliability in experimental outcomes. The thorough quantification and analysis of variable effects through ANOVA and linear regression techniques, complemented by the visualization of relationships via surface plots, culminated in the development of a robust regression model, could be explored further using advanced optimization methodologies, such as genetic algorithms or machine learning-based approaches. This multifaceted approach provided invaluable insights into understanding and optimizing the water boiling process, showcasing the significance of a structured methodology in experimental design and analysis.

REFERENCES

1. Czitrom, V. 1999. One-Factor-at-a-Time Versus Designed Experiments. The American Statistician, 53 (2): 126–131.
2. Deaconu, S., and H. W. Coleman. 2000. Limitations of Statistical Design of Experiments Approaches in Engineering Testing. Journal of Fluids Engineering, 122 (2): 254–259.
3. Helberg, C. 1996. Pitfalls of Data Analysis (or How to Avoid Lies and Damned Lies) The problem with statistics. Practical Assessment, Research, and Evaluation, 5 (5).
4. Imessaoudene, A., S. Cheikh, A. Hadadi, N. Hamri, J. C. Bollinger, A. Amrane, H. Tahraoui, A. Manseri, and L. Mouni. 2023. Adsorption Performance of Zeolite for the Removal of Congo Red Dye: Factorial Design Experiments, Kinetic, and Equilibrium Studies. Separations, 10 (1). https://doi.org/10.3390/separations10010057.
5. El Kassimi, A., Y. Achour, M. El Himri, M. R. Laamari, and M. El Haddad. 2023. “Optimization of preparation conditions of highly efficient activated carbon for use in water treatment–experimental design approach.” International Journal of Environmental Analytical Chemistry, 103 (3): 491–513. https://doi.org/10.1080/03067319.2020.1861261.
6. Montgomery, D. C. 2013. Design and analysis of experiments. Tempe, Arizona: John Wiley & Sons, Inc.
7. Tanco, M., E. Viles, M. Jesus Álvarez, and L. Ilzarbe. 2010. Why is not design of experiments widely used by engineers in Europe? Journal of Applied Statistics, 37 (12): 1961–1977. https://doi.org/10.1080/02664760903207308.
8. Wahid, Z., and N. Nadir. 2013. Improvement of one factor at a time through design of experiments. World Applied Sciences Journal, 21 (SPECIAL ISSUE1): 56–61. https://doi.org/10.5829/idosi.wasj.2013.21.mae.99919.

Uplifting the Efficiency of Water Distribution Network and Design of Water Tank in Peruvamba Panchayat

Pooja Suresh
Assistant Professor
Department of Civil Engineering
NSS College of Engineering
Palakkad, Kerala
✉ poojasuresh@nssce.ac.in

ABSTRACT

A detailed planning is required for the construction of an overhead water tank to ensure optimal operation and structural integrity. Tank capacity, material selection for longevity, and the installation of a sturdy support structure are all factors to consider. Seismic resistance and water pressure are critical factors to consider when assuring the tank's stability and safety. Proper inlet and outlet layouts, as well as overflow mechanisms, all contribute to effective water usage and maintenance. Overall, a well-designed overhead water tank strikes a balance between practicality, safety, and lifespan in order to carry out the specific requirements of the community or facility it serves.

A pipeline network requires a complete approach to carry fluids or gases efficiently. It takes into account things like pipeline material selection, route optimization, and hydraulic analysis to ensure optimal flow rates. Pressure control, corrosion prevention, and adherence to safety regulations all play important roles in the design process. Furthermore, the integration of control systems for monitoring and maintenance improves the pipeline network's reliability. The entire design seeks to achieve a balance between cost-effectiveness, environmental impact, and long-term sustainability while meeting the different needs of fluid or gas transportation within a particular infrastructure.

KEYWORDS: *Water distribution, Reinforced concrete structure, EPANET.*

INTRODUCTION

In Peruvamba Panchayat, enhancing the water distribution network's effectiveness is not only a technical challenge but also a social and environmental imperative. The design of water tanks should not only consider current population needs but also account for anticipated growth and fluctuating water demand patterns. The choice of durable materials for tank construction, such as reinforced concrete, is critical for withstanding environmental stresses and ensuring the longevity of infrastructure. Efficient inlet/outlet configurations and overflow mechanisms not only prevent operational issues within the tanks but also contribute to water conservation and safeguard against potential damage. Conducting a comprehensive hydraulic analysis of the distribution network is fundamental to identifying inefficiencies and pressure losses. Optimizing pipeline routes based on this analysis improves water flow, reduces energy consumption, and enhances the overall reliability of the system. The integration of modern technologies, such as sensor-based monitoring systems and remote sensing, transforms the water distribution network into a smart and responsive infrastructure. Real-time data on water flow, pressure, and quality enables timely detection of leaks and inefficiencies, facilitating rapid response and preventive maintenance. By amalgamating these technical advancements with community engagement and awareness initiatives, Peruvamba Panchayat can establish a comprehensive and sustainable model for water resource management.

BACKGROUND SUMMARY

The study area, peruvemba is a village and grama panchayat in Kollengode block in the Palakkad district of Kerala, India. The total area of the village is 2029. 0132 hectors which is divided into 14 wards. According to 2011 Census the Village contains 19312 People of which 9471 are males and 9841 are females. The primary source of water distribution for the entire panchayat is the Kannadipuzha, also known as the Shokanashini, which rises in the foothills of the Anamalai hills on the eastern outskirts of Kerala's Palakkad district. By utilizing the current water supply scheme out of 14 wards 8 of them (3,4,5,6,8,9,10,11) being fully supplied and 2 (12,13) of which are partially supplied. Rest of the people in the panchayat rely on public wells, borewells and public water supply scheme for their needs.

ESTIMATING WATER NECESSITY: TO ESTIMATE THE WATER DEMAND BY CONDUCTING POPULATION FORECASTING

To ascertain the area's overall water demand, the populace of the area at the conclusion of the design period must be projected. Therefore, it is necessary to forecast the population at the conclusion of the design period using the current demographic statistics. The arithmetic mean approach is one of the population forecasting techniques mentioned here. 2. The method of geometric increase 3. The method of incremental increase

Population Forecasting and Water Demand Calculation

For population forecasting, the Geometrical Increase Method is employed. This approach assumes that the population growth rate from decade to decade stays constant. Future population growth is predicted using geometric mean increase. This strategy should be applied to a young industrial town that is only a few decades old because it produces higher values. According to estimates, the population by the end of the nth decade, "Pn," will be as follows:

Pn= 19312(1+6.90/100)3.7 = 24719.78 ≈ 24800

Per capita water demand = 70 l/day (As per IS 1172:1193) Total water demand=24800×70=1736000litres

Table 1: Direct shear test Result

Normal Load (KN)	Proving ring reading at failure or at 20% strain whichever occurs first	Shear load P(KN)	Normal stress N/mm2	Shear stress N/mm2
1.8	54	18.36	0.0245	0.050
3.6	67	22.78	0.049	0.060
5.4	82.50	28.08	0.073	0.076

DESIGN OF WATER TANK AT DESIRED CAPACITY

Details of designed water tank for modelling

Dimensions of water tank are 15.8 X 8 X 4 m with 5 lakhs litres capacity. Step 1: Analysis of Moment

Long wall (Moment calculation- As per IS 3370 part 4)

- Maximum vertical moment = Mx wa3=-80.64 kNm
- Maximum horizontal moment = Mywa3 =-52.48 kNm Short wall (Moment calculation)

- Maximum vertical moment = Mxwa3 =-55.04 kNm
- Maximum horizontal moment = Mywa3 =-38.4 kNm Step 2: Design constants
- Modular ratio (m) = 280 (3 σcbc) = 9.33
- Permissible stress in concrete(σcbc) = 10 N/mm2 (As per IS code 456:2000, Table 21)
- Permissible stress in steel (σst) = 130 N/mm2 (As per IS 3370, Part 2, Table 4)
- Critical neutral axis depth (nc) = mσcbc (mσcbc+σst)- Lever arm (j) = 1 − nc 3 = 0.86 = 0.4178 Step 3: Calculation of thickness of wall

-Maximum bending moment from long and short walls for vertical moment = 80.64 kNm

- M=.5 σcbc nc j b d2
- Effective depth(d) = 220 mm
- Effective cover = 30 mm
- Overall thickness(D) = 250 mm

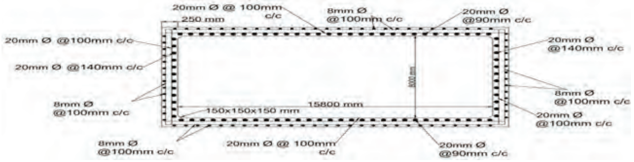

Fig. 1: Reinforcement detailing of water tank (top view)

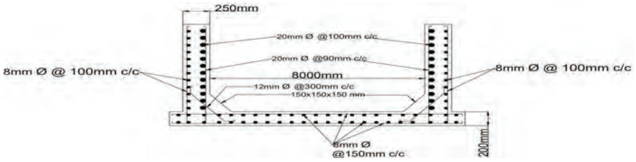

Fig. 2: Sectional view along long wall

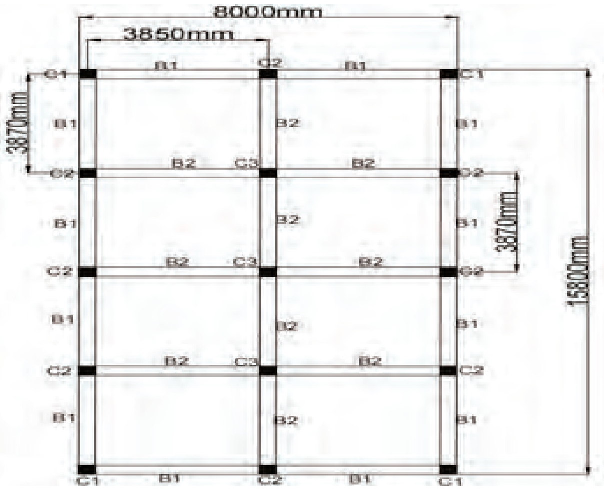

Fig. 3: Beam and column layout

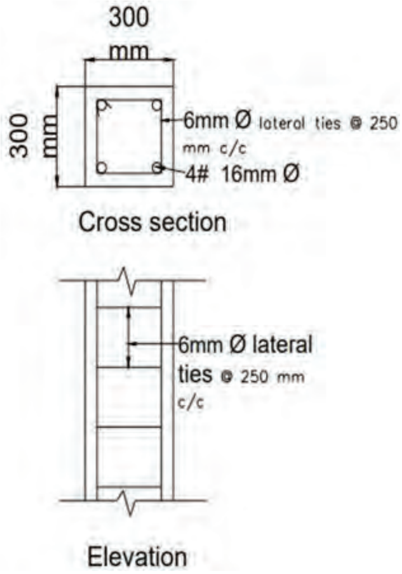

Fig. 4: column C1& C2

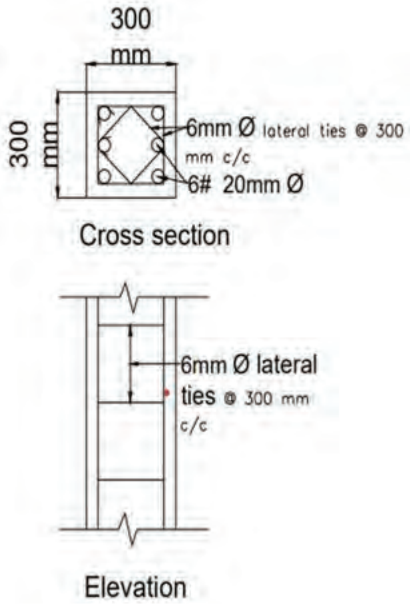

Fig. 5: column C3

Design of foundation Column load= 1530 kN

Selfweight of footing,10%=153 kN

Total load=1683 kN

Overall depth=450+75+16/2=533mm≈550 mm

Effective depth=550-75-16/2=467 mm

Area of reinforcement, Ast=2140.46mm2

Provide 16 mm ø bars at 170 mm c/c in each direction.

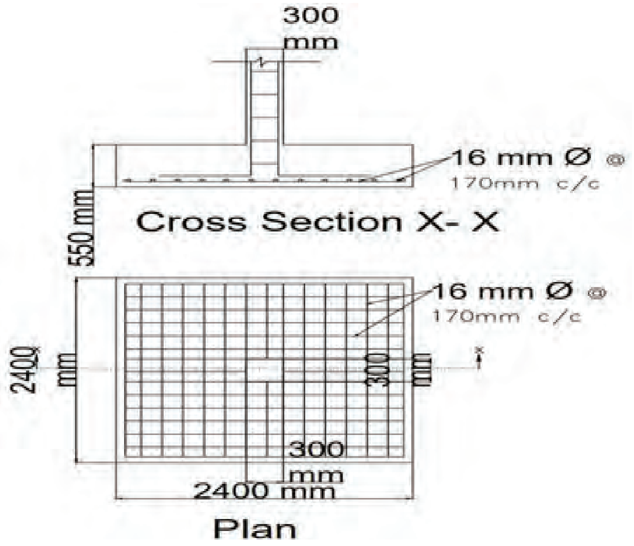

Fig. 6: Foundation

Analysis Of Water Tank

Analysis was done by sing STAAD Pro software.

Material property

Following material properties shows in Table 1 considered

Table 2 Material properties

Properties	Values
Concrete Compressive Strength fck	30N/mm2
Reinforcing yield stress fy	415N/mm2
Concrete modulus of Elasticity	20000N/mm2

Fig. 7: Front view of water tank

Fig. 8: Side view of water tank

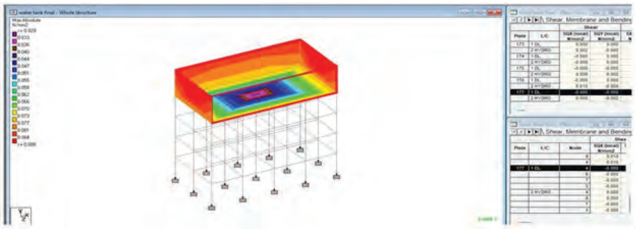

Fig. 9: Plate stress diagram

Using EPANET for Distribution Network Design

The Water Supply and Water Resources Division of the US Environmental Protection Agency (EPA) created a computer program known as EPANET. to model the behavior of hydraulic systems and water quality in pressurized pipe networks over extended periods of time. Pipelines, reservoirs or storage tanks, pumps, valves, nodes (pipe junctions), and storage tanks comprise a network.. Every tank's water level, every node's pressure, and every pipe's water flow are all tracked by EPANET. In order to better understand the flow and ultimate destination of the components that comprise drinking water inside distribution networks, EPANET is intended to serve as a research instrument. It can be used for many different analytical tasks related to distribution systems. Calibration of hydraulic models, consumer exposure evaluations, chlorine residual studies, and sampling program design are a few examples. Alternative management techniques for enhancing water quality across a system can be evaluated with EPANET.

When used on Windows, EPANET offers a complete platform for controlling hydraulic and water quality simulations in multi-source systems. This includes the capacity to alter source utilization, pumping and tank operations, incorporate satellite treatments such as re chlorination, and carry out maintenance tasks like as replacing and cleaning pipes. By providing an integrated workspace where users may update network input data and analyze outcomes using a variety of visualization formats, such as contour plots, The software expedites these operations via tables of information, historical graphs, and assigned colors network maps.

Hydraulic Modeling Capabilities

Precise fluid modeling forms a crucial foundation for efficient water utilization analysis. EPANET features an advanced hydraulic analysis engine offering the following functionalities like unrestricted capacity for analyzing network sizes, Using the Hazen-Williams, Darcy-Weisbach, or Chezy-Manning formulae to calculate friction headloss, Incorporation of minor head losses for bends, fittings, and similar components, Simulation of both constant and variable speed pumps, Computation of pumping energy consumption and associated costs, Representation of diverse valve types, Flexibility in tank design, allowing for tanks of varying shapes, such as those with variable diameters relative to height, Support for handling various demand segments at nodes, each with its unique time variation pattern, Representation of pressure-driven flow from sources like sprinkler heads, Modeling of demand induced by pressure at network nodes.

Physical Components

A water distribution system is represented by EPANET as a group of links that are joined to nodes. The linkages represent control valves, pumps, and pipes. The nodes represent reservoirs, tanks, and junctions.. Junctions are the points where water enters or leaves a network and linkages join together.

Nodes known as reservoirs provide the network with an infinite external water source or sink.. Models of lakes, rivers, ground water aquifers, and connections to other systems are among the objects they are used to simulate. Additionally, reservoirs can be sources of high-quality water. A reservoir's primary input qualities for water quality analysis are its hydraulic head, which is equivalent to the water surface height when the reservoir is not under pressure, and its initial quality. Since a reservoir is a boundary point, events that take place within the network have no effect on its head or water quality. Because of this, it does not have computed output properties. On the other hand, its head can be made to alter over time by providing it with a temporal pattern.

Tanks are nodes that have the ability to store water, and during a simulation, the amount of water in them can change over time. Tanks must run between their minimum and maximum capacities. When a tank reaches its minimal level, EPANET ceases out flow; when it reaches its maximum level, it stops in flow. Additionally, tanks can be used as sources of water quality. Devices called emitters, which are connected to junctions, simulate the flow through an aperture or nozzle that releases gas into the atmosphere. Sprinkler systems and irrigation networks use emitters for imitating the flow. As long as a leak's pressure exponent and discharge coefficient fracture or joint can be computed, additionally they can be utilized to mimic leaks. in a pipe linked to the junction or to determine a fire flow at the junction (the flow available at some minimal residual pressure). Emitters are not treated as distinct network components by EPANET, but rather as a characteristic of a junction. Pipes are links that carry water from one place in the network to another. EPANET always assumes that all pipelines are filled. Flow is directed between the end with the lower hydraulic head and the end with the higher hydraulic head (internal energy per weight of water).

Basic Steps to be Followed

1. Elevations of points are given as input file (elevation in meters- Tank and nodes are given separately).

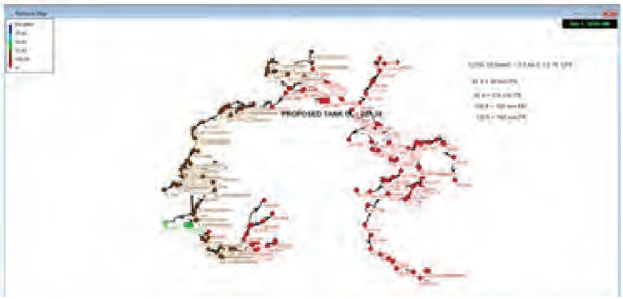

Fig 10: Step 1

2. Million liters per day converted to litres per second and which divided by no of nodes provides base demand, check run successfully.

Fig. 11: Step 2

3. Initially diameter is set to 90 mm, Roughness coefficient given in between 130-140, loss coefficient as 3, followed by 'Run' operation. (run will not be successful due to provided uniform diameter).

Fig. 12: step 3

4. Changing the diameter accordingly like, diameter keeps on decreasing from source to branches. Check for pressure (70-120 Kpa) and velocity (below 1 m/s)

Fig. 13: step 4

CONCLUSIONS

- Implementation of a 5-lakh litres water tank combined with the design of a water distribution network using EPANET software offers a promising solution to uplifting water distribution efficiency.
- A crucial storage component thereby helps regulate supply and demand fluctuations, especially during peak usage periods or in case of emergencies such as maintenance or unexpected outages.
- Leveraging EPANET software allows for meticulous design and analysis of the distribution network, considering factors like pressure and flow rates. This advanced modelling ensures optimal pipe sizing, layout, and operational parameters, leading to minimized water losses.

REFERENCES

1. Ashwini B T, Chethan V R, Bhavya D R (2018). “Design of overhead RCC rectangular water tank by using working stress method”. International Research Journal of Engineering and Technology (IRJET), Volume: 05 Issue: 06.
2. Kumar, A., Kumar, K., Bharanidharan, B., Matial, N., Dey, E., Singh, M., & Malhotra, N. (2015). “Design of water distribution system using EPANET”. International Journal of Advanced Research, 3(9), 789-812.
3. Latha M. S. (2021). “Comparison of Analysis between Rectangular and Circular Overhead Water Tank”. Applied Research on Civil Engineering and Environment, 2, 77-95.
4. Maryam Abareshi, Seyed Mahmood Hosseini, Ahmad Aftabi Sani,2017” A simple iterative method for water distribution network analysis,” Applied Mathematical Modelling, Volume 52.

Effect of Gradation on the Performance of Bituminous Mixes

Atheena Bhai A V
B.Tech Student
Department of Civil Engineering
NSS College of Engineering
Palakkad, Kerala
✉ atheenabhaiav@gmail.com

Aleena Johnson
B.Tech Student
Department of Civil Engineering
NSS College of Engineering
Palakkad, Kerala
✉ aleenajohn1224@gmail.com

Ambuja P V
B.Tech Student
Department of Civil Engineering
NSS College of Engineering
Palakkad, Kerala
✉ ambujapv17@gmail.com

Rejani V U
Professor
Department of Civil Engineering
NSS College of Engineering
Palakkad, Kerala
✉ rejanivu@nssce.ac.in

ABSTRACT

Aggregates significantly influence the properties of bituminous mixes, comprising about 94–95% of the total composition. Beyond their chemical, physical, and mechanical characteristics, the size and gradation of aggregates notably impact the quality of pavement, performance, and service life. To assess the effect of gradation, upper, mid-point, and lower gradation limits are selected for both Bituminous Concrete (BC) Grade I and II. The Marshall mix design method is employed for evaluation, with Marshall Tests conducted to analyze variations in strength and other Marshall characteristics.

KEYWORDS: *Gradation, BC, Bituminous mix, Marshall test.*

INTRODUCTION

A pavement is a layered structure built above natural soil (sub-grade) to distribute vehicle loads and prevent stress from exceeding sub-grade capacity. It must provide good ride quality, skid resistance, light reflection, and low noise. There are two main types: flexible and rigid pavements.

Flexible pavements, made with bituminous materials, lack flexural strength and distribute loads through grain-to-grain contact in multiple layers. The surface layer, made of high-quality aggregate and bitumen, bears the most stress and wear. Aggregate gradation, the size distribution of particles in bituminous mixes, is crucial for pavement strength and durability. Gradation affects cohesion, drainage, and friction, and is governed by specifications that vary by use, climate, and traffic.

The present study aims to compare the strength of bituminous mixes with different aggregate gradations and to investigate the influence of aggregate gradation on the performance of Bituminous Concrete (BC) grade I and II. To achieve the objectives, three gradations viz. lower limit, middle limit and upper limit, are tried for mix design. The gradation structure (percent passing through each sieve) was determined based on the acceptance criteria outlined by Ministry of Road Transport and Highways(MoRTH, 2013).

BACKGROUND SUMMARY

The gradation of bituminous mixes significantly impacts road performance, affecting workability, compaction, stability, and resistance to rutting and cracking. Poor gradation can lead to early road failure, higher maintenance costs, traffic disruption, and safety risks, making it a key socio-economic concern. Gradation also affects construction cost and efficiency. Properly graded mixes optimize binder and material use, lowering costs and minimizing waste. This not only enhances performance and durability but also reduces the environmental impact and long-term maintenance needs.

Various researchers have evaluated the mechanical properties of bituminous mixes, focusing on the interrelationship between aggregate gradation, mix composition characteristics and structural response. The effect of mix parameters, including gradation, compaction levels, and filler variations, on cold bituminous mixes (CBM) were studied by Dash et al. (2018). Both Dense Bituminous Concrete and gap-graded SMA were compared with hot mixes using Marshall and gyratory compaction methods. Variations in aggregate gradation (lower, upper, and adopted ranges) and binder types (CMS bitumen for CBM and VG30 for hot mixes) were analyzed. Marshall, coating, dry stability, and soaked stability tests revealed that excessive compaction reduced air void content and stability in SMA. It was found that both dense and gap gradations achieved satisfactory performance with a 2% cement replacement by aggregate weight. Lira et al. (2020)assessed the deformation resistance characteristics of asphalt mixtures using a gradation-based framework. This framework identified primary and secondary structures within aggregates. Mixes were prepared with crushed aggregates, and rut depth was measured using a wheel-tracking apparatus. Compression tests assessed compaction effects and rutting susceptibility. The study found limitations in using a gradation-based framework to evaluate mixtures with varying gradations. Garcia et al. (2020) investigated the interrelationship between aggregate gradation, mix composition characteristics and structural response in Superpave mixes. Following the Superpave design method, the study evaluated voids in mineral aggregate (VMA) and voids filled with asphalt (VFA). The Hamburg Wheel-Tracking Test was used to evaluate rutting resistance and moisture susceptibility. Aggregate gradation's influence on volumetric and mechanical performance was explored by systematically modifying coarse and fine fractions of the gradation. Results were analyzed using Bailey's ratio, showing that optimal gradation selection can effectively balance mix composition characteristics and structural response without arbitrarily changing the optimum asphalt content (OAC).Khairandish et al. (2021) conducted a study to evaluate the mechanical properties of BC and DBM based on variations in aggregate gradation and morphology. Morphological characteristics were assessed using 3D scanning and image processing techniques. The study included the determination of volumetric and Marshall characteristics, as well as indirect tensile strength (ITS) and tensile strength ratio (TSR) tests to assess mechanical performance. The results indicated that BC II and DBM II mixtures exhibited higher values compared to BC I and DBM I mixtures. Yue et al. (2022) investigated the effect of aggregate gradation variations (ranging from +4% above the upper limit to −2% below the lower limit) on the performance of asphalt mixes. Using Marshall testing, wheel tracking, and indirect tensile strength tests, they evaluated the impact of these gradation shifts on Hot Mix Asphalt (HMA) properties. Their findings indicated that mixes with gradations within the +4% to −2% range exhibited the lowest rutting depths and the highest resistance to moisture-induced damage in hot climates, outperforming conventional asphalt mixtures.

In the present study, the performance of BC grades I and II is evaluated using lower, middle, and upper aggregate gradations combined with varying bitumen contents. The Marshall mix design method is employed to assess the effect of gradation on the characteristics of BC grade I and II mixes. Key Marshall characteristics including Stability, Flow Value, Air Voids, Voids Filled with Bitumen (VFB), and VMA are determined, and variations in performance are analyzed accordingly.

METHODOLOGY

Various types of aggregates, including crushed stone, sand, and filler materials, are selected based on their physical properties, availability, and the performance requirements of the asphalt mix. The appropriate grade of asphalt binder is determined by considering factors such as anticipated traffic loads, climatic conditions, and the desired characteristics of the final pavement. Laboratory-scale asphalt mix samples are then prepared by blending the selected aggregates with the chosen binder. These samples are compacted using a Marshall compactor under controlled temperature and pressure conditions to replicate the compaction process during actual road construction.

Once compacted, the samples undergo stability and flow tests. Stability measures the mix's resistance to deformation under traffic stresses, while flow indicates the extent of deformation or the mix's resistance to deformation at a specific temperature. The process aims to identify the combination of aggregate and binder that achieves the optimal balance of performance characteristics. Once the ideal mix proportions are determined, the final mix design is established, specifying the exact aggregate gradation and asphalt binder content. To evaluate performance, the variation in Marshall characteristics across lower, middle, and upper gradations is analyzed, helping to determine the most suitable mix for achieving the best performance.

PHYSICAL PROPERTIES OF MATERIALS

The selection of various materials for the preparation of Marshall specimen is determined based on the physical properties of materials. Materials have high stability, temperature susceptibility, long life etc. are selected from this method. The materials consist of aggregates of sizes 20mm, 12mm, 6mm, quarry dust and VG-30 bitumen. The suitability of materials for conducting Marshall test is determined by using the results obtained from the physical property tests.

Aggregate physical characteristics were determined, with the corresponding results summarized in Table1.

Table 1 Physical properties Aggregates

TESTS	RESULT
Impact Value	23%
Crushing Value	28%
Specific Gravity &Water Absorption	2.69
0.7%	
Los Angeles Abrasion Value	25%
Grain Size Analysis	2%

The results indicate that the aggregate properties comply with the specifications for BC as outlined in MoRTH 5th Revision (Table 500-16).

Tests were carried out to determine the physical characteristics of bitumen with the corresponding results summarized in Table2.

Table 2 Properties of Bitumen

Property	Tests	Result	Specifications for VG 30 As Per IS 73: 2013
Softening	Softening point	51°C	Min 47° C
Elongation	Ductility	62 cm	Min 40cm
Temperature Susceptibility	Flash and Fire Point	230° C	Min 220° C
Adhesion	Stripping	0%	Max 5%
Resistance to flow	Absolute Viscosity	2687.49 Poise	2400 – 3600 Poise

PROPERTIES OF BITUMINOUS MIX

Bituminous concrete which is a common pavement layer used in road construction is selected for the present study. They are asphalt mixtures used to provide durable and smooth riding surface for roads. Bituminous concrete (BC) provides a smooth driving surface that reduces vehicle wear and tear. The Marshall method of mix design as per the specifications outlined in ASTM D6927 (2006) is used to determine the optimum bitumen content. The method involves testing various combinations of aggregate materials, asphalt binder to determine the mix design that provides the desired performance characteristics as per MoRTH. These characteristics include stability, flow, density, and durability.

The specification in MoRTH (2013)outlines the design and construction processes for BC intended specifically for use in base, binder, and profile corrective courses. The work involves the construction of a single layer of Bituminous Concrete (BC), with a thickness ranging from 30 mm to 50 mm, placed over a previously constructed bituminous layer. Bituminous concrete grades I and II refer to different types or specifications of bituminous concrete mixtures commonly used in road construction. These grades are typically defined by specific requirements for the asphalt binder and aggregate properties.

RESULTS AND DISCUSSIONS

In accordance with ASTM D6927–06, the Marshall mix design procedure was conducted, and the resulting data were analyzed.

Marshall Characteristics

Marshall Specimens at lower limit, middle limit, upper limit with varying bitumen contents 5%, 5.2%, 5.4%, 5.6%, are prepared for BC grade I and bitumen contents of 5.2%, 5.4%, 5.6%, 5.8% are used to prepare specimen for BC grade II. Prepared specimens are tested in Marshall test apparatus and Marshall characteristics such as bulk specific gravity of compacted specimen (Gm), theoretical specific gravity of specimen (Gt), percentage air voids (Vv), percentage volume of bitumen (Vb), VMA, VFBare calculated.

The optimum binder content refers to the ideal amount of binder material to be used in a particular application or process. It depends on factors such as the binder type, the properties of the materials being bound, and the desired outcome. To determine the optimum binder content, it is typically necessary to conduct experiments or tests. These tests involve varying the amount of binder used and evaluating the resulting properties of the bound material. The goal is to find the binder content that provides the best balance of desired characteristics, such as strength, durability, flexibility, or adhesion. Bitumen content corresponding to maximum stability (B1), maximum Gm (B2), and 4% air voids (B3) are determined and by taking average, optimum bitumen content for each limit can be calculated.

Optimum Binder Content of BC Grade I

For the lower gradation limit, the bitumen content corresponding to maximum stability and maximum bulk specific gravity (Gm) was found to be 5.2%, while the bitumen content corresponding to 4% air voids was 5.25%. Based on these values, the OBC for the lower limit gradation was determined to be 5.21%.

For the middle gradation limit, maximum stability was achieved at 5.2% bitumen content, maximum Gm at 5.4%, and 4% air voids at 5.25%, resulting in an OBC of 5.28%.

In the case of the upper gradation limit, both maximum stability and maximum Gm occurred at 5.4% bitumen content, while 4% air voids were achieved at 5.2%. Consequently, the OBC for the upper limit gradation was established as 5.33%.

Optimum Binder Content of BC Grade II

For the lower gradation limit, the bitumen content to attain maximum stability was 5.4%, maximum bulk specific gravity (Gm) was 5.6%, and 4% air voids was 5.47%. Based on these values, the Optimum Bitumen Content (OBC) for the lower limit was determined to be 5.49%.

For the middle gradation limit, maximum stability and Gm were observed at 5.4% and 5.6% bitumen content, respectively, while 4% air voids were achieved at 5.52%. The resulting OBC for the middle limit was 5.50%.

For the upper gradation limit, both maximum stability and Gm occurred at 5.6% bitumen content, while 4% air voids were attained at 5.42%, leading to an OBC of 5.54%.

6.4 Effect of Gradation on Marshall Characteristics

The variation in gradation of aggregate affects the Marshall characteristics to a great extent. To study the effect of gradation and to find better mix, Marshall characteristics of specimen prepared at optimum binder content need to be determined. For that, Marshall specimens are prepared at OBC for BC grade I&II and test results are analyzed.

Test results of grade I is shown in table 3and grade II is shown in table 4. With the obtained results, graphs are plotted to study the variation in properties with respect to gradation.

Table 3 Marshall test results for BC grade I at OBC

Marshall characteristics	Lower limit	Middle limit	Upper limit
Gm	2.41	2.47	2.45
Gt	2.54	2.55	2.56
Vv (%)	4.01	3.9	3.12
Vb (%)	12.83	12.88	12.98
VMA (%)	16.43	16.73	12.97
VFB (%)	77.12	74.83	80.89
Stability (KN)	10	10.9	8.56
Flow value (mm)	4.3	3.2	3.8
OBC	5.21	5.28	5.33

Table 4 Marshall test results for BC grade II at OBC

Marshall characteristics	Lower limit	Middle limit	Upper limit
Gm	2.44	2.47	2.46
Gt	2.56	2.58	2.56
Vv (%)	4.69	4.5	3.9
Vb (%)	13.2	12.61	13.53
VMA (%)	17.89	17.12	17.13
VFB (%)	73.8	74.2	78
Stability (KN)	8.9	9.5	9.2
Flow value (mm)	3.5	3.9	5.4
OBC	5.49	5.50	5.54

The results for BC Grade I and Grade II were analyzed and the following observations were made.

For Grade I:

- The mix with middle gradation exhibited the highest stability, while the mix with upper gradation had the lowest stability.
- Lower gradation showed the highest flow value, whereas middle gradation had the lowest flow value.
- Lower gradation had the lowest unit weight, while middle gradation had the highest unit weight.
- Middle gradation exhibited the highest air voids and lowest VFB, whereas lower gradation had the lowest air voids and highest VFB.
- The Optimum Binder Content was lowest for lower gradation and highest for upper gradation.

The Marshall characteristics for middle gradation were within the acceptable range as per MoRTH specifications. Based on the results, the middle gradation demonstrated superior performance compared to the other gradation limits.

For Grade II:

- The mix with middle gradation exhibited the highest stability, while the mix with lower gradation showed the lowest stability.
- Upper gradation had the highest flow value, whereas lower gradation had the lowest flow value.
- Middle gradation showed the highest unit weight, while lower gradation had the lowest unit weight.
- Lower gradation exhibited the highest air voids and lowestVFB, while upper gradation had the lowest air voids and highest VFB.
- The Optimum Binder Content was lowest for lower gradation and highest for upper gradation.

The Marshall characteristics for the middle gradation fell within the permissible limits outlined by MoRTHspecifications, indicating compliance with national standards for bituminous mix design.

CONCLUSIONS

From the experimental findings, the following conclusions are derived:

Higher stability indicates the greater resistance to rutting and deformation. It ensures the structural integrity and long – term performance of the pavement. Factors affecting stability includes aggregate gradation, binder type, compaction level and temperature. For both the mixes middle gradation has higher stability compared to other two gradations.

Excessive flow can lead to rutting, while insufficient flow can result in poor compaction and decreased durability. Optimal flow ensures proper construction and long- term performance of pavement. Flow value ranges from 2-4 as per MoRTH. Flow value for middle gradation of both the mixes are within the limit and while it is outside the limit for upper gradation of BC Grade II.

Percentage of air voids affects the durability permeability and resistance to moisture damage. Excessive air voids can result in decreased strength, increased permeability and accelerated aging. Percentage of air voids ranges from 3-5 as per MoRTH. The values for Middle gradation of both the mixes are within the limit and while it is outside the limit for the lower gradation of BC Grade I.

Proper density ensures sufficient interlocking of particles and improved resistance to moisture intrusion aging. Achieving the specified density during construction is the critical for the long – term performance of pavement.

Maximum density is achieved for middle gradation of both the mixes.

Filling voids with bitumen in the bituminous mixes improves the durability, stiffness, stability, flexibility and temperature variation. It helps in creating more long–lasting pavement structure. Value of VFB ranges from 65-75 as per MoRTH. The values for the middle gradation of both the mixes are within the limit and that for the lower gradation of BC Grade I, and upper gradation of both the mixes are outside the limit.

Among the different gradation limits evaluated—typically representing fine, middle, and coarse gradations—the middle gradation exhibited superior performance. This was evidenced by higher stability values, optimal flow, and favorable volumetric properties, suggesting enhanced resistance to deformation, better load-carrying capacity, and improved durability. The results underscore the importance of adhering more closely to the middle gradation in flexible pavement construction to achieve optimal performance characteristics.

In case middle limit cannot be achieved the performance of the upper and lower gradation can be improved by adjusting aggregate proportion, optimizing gradation curve, considering aggregate properties, using additives or modifiers.

REFERENCES

1. American Standard Test Method for Marshall Stability and Flow of Bituminous Mixtures. ASTM D6927 – 06, 2006.
2. Dash, S, S, & Panda,M, Influence of mix parameters on design of cold bituminous mix, Construction and Building Materials 2018, vol 191, 376-385.
3. Garcia, V. M., Barros, L., Garibay, J., Abdallah, I., & Nazarian, S., “Effect of aggregate gradation on performance of asphalt concrete mixtures”, Journal of materials in Civil Engineering 2020, vol 32(5), 2249-2258.
4. Khairandish, M, Chopra, A, Singh, S, Chohan, J & Kumar,” Effect of Gradation and Morphological Characteristics of Aggregates on Mechanical Properties of Bituminous Concrete and Dense Bituminous Macadam”, Iranian Journal of Science and Technology-Transaction of Civil Engineering 2021, Vol 46(1), 293-307.
5. Lira, B., Ekblad, J., & Lundström, R., “Evaluation of asphalt rutting based on mixture aggregate gradation”, Road Materials and Pavement Design 2019, Vol 22(5), 1160-1177.
6. Ministry of road Transportation and Highway (MoRTH) – Specification for road and bridge Works, Fifth revision 2013, Indian Roads Congress, New Delhi.
7. S K Khanna, C.E.G Justo & A. Veeraragavan, “Highway Engineering Revised 10th Edition” 2015, Roorkee: Nem Chand and Bros.
8. Yue, Yanchao & Abdelsalam, Moustafa & Eisa, Mohamed. Aggregate Gradation Variation on the Properties of Asphalt Mixtures 2022. Coatings. 12(11). 1608. 10.3390/coatings12111608.

N S S COLLEGE OF ENGINEERING

Palakkad 678008, Kerala, India
(A Government Aided Institution Established in 1960)
Affiliated to APJ Abdul Kalam Technological University and approved by AICTE
An Institution of Nair Service Society
www. Nssce.ac.in
Email: nssce@nssce.ac.in

DEPARTMENT OF CIVIL ENGINEERING

Vision of the Department

To be recognized as a Centre of Excellence in Civil Engineering, Education, Research and Consultancy, contributing to Sustainable Development and growth of the Nation.

Mission of the Department

1. To impart high quality education in Civil Engineering, inculcating professional, managerial and leadership skills to meet the changing and challenging needs of the society.
2. To provide excellent learning inputs, through appropriate pedagogical practices, for successful career and scholarly endeavours.
3. To foster social commitment and professional ethics through planned curricular and extra curricular activities, for sustainable development.

Program Educational Objectives

Within a few years of graduation, the graduates of the program will

1. Develop theoretical and practical knowledge in Civil Engineering, by practicing in various sectors, focusing on sustainable solutions, professional ethics and social accountability.
2. Perform effectively both as leader and team member in a professional environment utilizing managerial and life skills to achieve the goals of engineering projects.
3. Pursue higher studies and research and recognize the need for updating engineering solutions and practice, to meet the changing professional requirements.

Motto: GROW TO SHARE & SHARE TO GROW

GROW TO SHARE
SHARE TO GROW

VOLUME 48 • SPECIAL ISSUE • NO. 1 • September 2025

ISSN 0971-3034

N S S
COLLEGE OF
ENGINEERING
Palakkad, Kerala, India

GROW TO SHARE
SHARE TO GROW

N S S COLLEGE OF ENGINEERING PALAKKAD, KERALA

N S S College of Engineering, Palakkad, one of the oldest engineering educational institutions in Kerala, was founded in 1960 by Nair Service Society under the leadership of the late **Bharatha Kesari Mannathu Padmanabhan**, during the second five-year plan with the assistance of the Central and State Governments under the Grant- in-Aid Scheme. The college is now affiliated to the APJ Abdul Kalam Technological University, Kerala, offering six B.Tech Programmes (Civil Engineering, Mechanical Engineering, Electrical and Electronics Engineering, Instrumentation and Control Engineering, Electronics and Communication Engineering and Computer Science Engineering) and six M. Tech Programmes.

DEPARTMENT OF CIVIL ENGINEERING

The Department of Civil Engineering in N S S College of Engineering was established in 1960 and remains as one of the best Civil Engineering Departments in the state. The department offers B. Tech programme in Civil Engineering and M.Tech programme in Structural Engineering. To provide high quality education and training in Civil Engineering, the department treasures a strong team of sincere and dedicated faculty members, and has all the facilities needed to cater with high end training in both theoretical and practical aspects of Civil Engineering. B.Tech Programme of this department is accredited by the National Board of Accreditation (NBA).

PUBLISHED BY
INDIAN SOCIETY FOR TECHNICAL EDUCATION
Near Katwaria Sarai, Shaheed Jeet Singh Marg,
New Delhi - 110 016

Printed at: Compuprint, Flat C, Aristo, 9, Second Street, Gopalapuram, Chennai 600 086.
Phone : +91 44 2811 6768 • www.compuprint.in